Monolayer Polymers grown on Surfaces via Ullmann Coupling and Plasma Polymerisation

Alessio Quadrelli

Thesis submitted for the degree of

Doctor of Philosophy

Physics Department

Lancaster University

October 2023

Declaration

This thesis is my original work and has not been submitted, in whole or in part, for a degree at this or any other university. Nor does it contain, to the best of my knowledge and belief, any material published or written by another person, except as acknowledged in the text.

Abstract

Surfaces are the interfaces between materials and the surrounding environment and, thus, play a significant role in technological applications, ranging from catalysis to medical implants, electronics, and fundamental studies. The properties of surfaces can be tailored by functionalising them without affecting the bulk material, resulting in enhanced performances or new properties. Among the many available options, the use of organic molecules for surface functionalisation offers unique advantages. First, the functional groups of organic molecules can be engineered, allowing exquisite control over their chemical, electronic, and optical properties down to the single-atom level. Additionally, organic molecules can be stabilised by covalent bonds into polymers that are robust against a wide variety of *stimuli*, such as heat, light, pressure, and chemicals, and thus suitable for real-life applications. This thesis focuses on studying the growth of nanoscaled polymers on surfaces through on-surface catalytic reactions and plasma polymerisation.

Plasma polymerisation is a technologically relevant process to coat surfaces with thin functional films of organic molecules with a host of applications, ranging from biomaterials to energy materials. The fundamental understanding of plasma polymerisation, however, lags behind its applications. In particular, the role of the surface in the formation of the polymer is still underexplored. This thesis investigates the effect of different surfaces on the formation of nitroxide-containing polymers using a monomer with anti-microbial activity, (2,2,6,6-tetramethylpiperidin-1-yl)oxyl (TEMPO), employing surface-sensitive techniques such as atomic force microscopy (AFM) and X-ray photoemission spectroscopy (XPS). The results reveal that, contrary to the widespread assumption of surface independence, the chemical and morphological properties of the plasma polymers depend on the surface in the early stages of plasma polymerisation. Finally, the anti-bacterial properties

of TEMPO are investigated by showing that the use of TEMPO plasma polymers as a matrix to host TEMPO molecules improves the performance.

One of the most studied on-surface polymerisation reactions, Ullmann coupling, is usually carried out on noble metal surfaces that catalyse it. The intended applications for 1D and 2D surface polymers typically require insulators or semiconductors as substrate materials. Developing a method for polymerisation on insulators is, thus, essential. However, molecules sooner desorb from insulating surfaces before the reaction can be thermally activated. This thesis investigates the use of atomic quantum clusters (AQCs) as catalysts for Ullmann coupling on non-metal surfaces with AFM and XPS. First, the AQCs are characterised and then their role as catalysts in the polymerisation of halogenated porphyrin molecules on non-metal surfaces is investigated. Silver and copper AQCs are found to catalyse the on-surface polymerisation. These results represent a major step towards growing 2D polymers directly on technologically relevant surfaces, such as silicon wafers.

Acknowledgements

I would like to thank Dr Samuel Jarivs of Lancaster University and Prof Rob Short of the University of Sheffield for giving me the possibility to join such a fascinating research project and for their supervision throughout the PhD. They provided me with guidance, support, and amazing opportunities beyond their duty.

I would like to extend my gratitude to the members of my research group: Dr Alex Robson for the training on the use of XPS, Dr Javad Naderi for his guidance on the fabrication of plasma polymers, Amy Crisp for training me on microbiology experiments and Craig Williams for providing me access to the pathology laboratory at Royal Lancaster Infirmary, Leonardo Forcieri for sharing his knowledge on the use of UHV equipment, Dr Sophie Au-Yong, and Edward Dunn for introducing me to the use of AFM.

I would like to thank all the people involved in the projects: Dr David Buceta, Prof Manuel Arturo Lopez-Quintela, Prof Neil Champness for providing the materials used in the research project, Dr David Duncan for sharing his knowledge on X-rays-base techniques and helping me analyse the NIXSW data, and Prof Philip Moriarty for giving me the possibility of using his STM. I am grateful to Prof Colin Lambert, Dr Qingqing Wu, and Dr Ali Ismael for their simulations that provided invaluable insight into the experimental results.

Finally, I would like to thank my parents, Mrs Lorella Lorenza and Mr Marco Quadrelli, for supporting me throughout my whole education. This PhD is just the end of a long journey that would have not been possible without them.

Contents

Chapter 1

Introduction

Surfaces are the interfaces between materials and the surrounding environment and thus are extremely relevant to the performances and functionalities of materials. Surfaces play a significant role in technological applications, ranging from catalysis to biocompatibility to electronics, and in the fundamental understanding of the physical world. The striking difference between the properties of the bulk and the surface derives from the different energetic landscape of the atoms at the topmost layer, resulting in completely new and fascinating physical and chemical phenomena. The understanding and engineering of surfaces are inherently related to nanoscience and nanotechnology as they are only a few nanometres thick, requiring specialised tools to probe materials at the nanoscale. In particular, two of the most powerful tools for studying surfaces are scanning probe microscopy (SPM) and X-ray photoemission spectroscopy (XPS), described in Chapter 3.

Given the importance of the surface in the overall performance of a material, there is a significant interest in enhancing the existing properties or adding new functionalities to it while retaining the bulk properties. The use of organic molecules for functionalisation is driven by their versatility as building blocks that can be tailored to allow exquisite control over their chemical, electronic, and optical properties down to the single-atom level. Furthermore, coatings of organic molecules are potentially biocompatible, enabling their use in biological settings, including the human body. Individual organic molecules are, however, unstable as they easily desorb from surfaces, hindering their use for real-life applications. Nonetheless, stability can be improved through the polymerisation process by linking the molecules into a polymer via covalent bonds. The resulting functionalised

surfaces can be used to address a variety of problems.

Microbial infections are an enormous burden for society in general in terms of suffering, loss of quality of life, and economic damage. Although the use of antibiotics greatly reduces the burden of microbial infections, it results in a selection of resistant strains that pose a pressing challenge for healthcare systems [1, 2]. In particular, bacteria form organised communities when they adhere to a surface, called biofilms, surrounded by an extracellular polymeric matrix, making them more resistant to treatments. Developing anti-bacterial surfaces that prevent, reduce, or delay the growth of bio-films in medical implants is one of the many options to tackle the problem of bacterial infections with less or without antibiotics [3]. Among the possible methods to functionalise surfaces to this end, plasma polymerisation has emerged as a single-step, solvent-free, green, and efficient method to coat a wide variety of substrates with polymers of organic molecules [4], especially for biomedical use [5]. A brief background on this topic is presented in Chapter 2. Although nitric oxide is an effective anti-bacterial and anti-biofilm agent, it is inherently unstable, raising the interest in a class of analogous molecules, the more stable nitroxide radicals [6]. In Chapter 4, the growth of nitroxide-containing polymers from (2,2,6,6-tetramethylpiperidin-1-yl)oxyl (TEMPO) during plasma polymerisation is investigated and the antibacterial properties are tested.

The discovery of new and more effective catalysts has the potential to improve the efficiency of industrial-scale reactions [7], thus, reducing energy and materials usage. Scaling the dimensions of catalysts down to the sub-nanometer regime holds the promise to enhance efficiency by increasing the surface-to-volume ratio, so that most of the atoms are involved in the reactions, achieving enhanced performances with the same or less amount of material [8]. In this context, atomic quantum clusters (AQCs), made of only a few noble metal atoms, combine the catalytic properties of metals with the advantages of nanometric or sub-nanometric dimensions [8, 9]. They exhibit an exceptional catalytic activity that can be tuned by the choice of the metal and the number of atoms, providing a flexible platform for a host of reactions [9]. A brief background on AQCs is presented in Chapter 2. The understanding of the chemical and morphological properties of AQCs is extremely elusive due to their sub-nanometric dimensions. However, SPM and X-ray-based techniques offer the possibility to characterise their properties down to the atomic level once supported by a surface, as shown in Chapter 5 and 6 with AQCs of just five copper and silver atoms. Furthermore, they

can be used as catalysts for a variety of reactions occurring on solid surfaces. In the context of this thesis, the potential of AQCs to catalyse the on-surface polymerisation via the formation of C-C bonds from halogenated monomers is explored in Chapter 6. At the moment, this kind of reaction is mainly carried out on noble metal surfaces due to their catalytic activity, greatly limiting the application of the resulting polymers. The possibility of producing polymers directly on a variety of surfaces, including semiconductors and insulators, could enhance their application as catalysts [10, 11] and building blocks for molecular electronics [12].

Chapter 2

Background

In this chapter, the literature relevant to this thesis is reviewed. Some aspects of on-surface polymerisation are discussed in Section 2.1, focusing on the efforts of extending the process to insulating and semiconducting surfaces. Atomic quantum clusters (AQCs) are discussed in Section 2.2, highlighting the gap in the current knowledge, and the questions addressed in this thesis, and pointing to the potential use in on-surface polymerisation. Finally, plasma polymerisation is introduced in Section 2.3, the scant literature on the early stages of the process is reviewed and the research questions addressed by this thesis are introduced.

2.1 On-surface polymerisation

Nanostructures have historically been produced with top-down approaches, such as lithography and the etching of semiconductors. However, this is not the only option. Research pivoted toward bottom-up methods to assemble nanostructures from smaller units [13]. These processes are widespread in nature and can be precise down to a single atom, such as the assembly of amino acids into proteins, polypeptides into DNA, and the growth of crystals.

In nanotechnology, the bottom-up paradigm consists of assembling building blocks on a surface to create a structure with new emerging properties. Among the building blocks, organic molecules possess both functional properties and the possibility to tailor their functionalities efficiently by

modifying their structure. Molecular assemblies are promising candidates for molecular electronics, photonics, spintronics, and selective chemistry [14, 15]. However, molecular layers are easily disrupted by heat, light and exposure to the environment, which limits their application in real life unless they are stabilised. This thesis focuses on linking molecules with covalent bonds through polymerisation on inert surfaces as a first step to extend the process to technologically relevant materials, such as SiO_2.

2.1.1 Molecular interactions

The interaction between molecules can be broadly categorised as non-covalent and covalent.

In the non-covalent case, the interactions between building blocks are reversible, such as hydrogen bonds, halogen bonds, Van der Waals forces [16], and metal-ligand coordination [17]. For example, trimesic acid molecules assemble into a kagome lattice on Cu(100) in UHV [18] and in solution [19] due to the hydrogen bonding between the carboxylic groups. 1,3,5,-(tris-bromophenyl) benzene (TBB) molecules assemble in different patterns on Cu(111) and Ag(111) at 80 K due to the halogen bonding [20]. Metal ligand coordination involves the interaction between electrons of single atoms of a transition metal with molecules such as polyphenyl-dicarbonitrile with cobalt centres to form a porous matrix [21].

The hydrogen bond derives from the partial transfer of electrons from a hydrogen atom to a more electronegative species within a molecule, forming an electric dipole. The dipoles of neighbouring molecules tend to align, forming a hydrogen bond, with a typical energy of approximately 0.25 eV [22]. It is a directional interaction because it is stronger between the axis connecting the electronegative atom to the hydrogen, but its intensity falls off quickly. Van der Waals forces occur between the permanent, induced or instantaneous dipole of neighbouring molecules so that even neutral molecules interact with one another. The permanent dipole-permanent dipole, permanent dipole-induced dipole and instantaneous dipole-induced dipole interactions, called Keesom, Debey and London forces, align molecules with an energy lower than 0.25 eV [22]. These interactions are all proportional to $\frac{1}{r^6}$ and are generally attractive. Pauli repulsion caused by the overlapping of the electronic clouds prevents the molecules from collapsing. The balance between attractive and repulsive interactions causes molecules and atoms to assume well-defined equilibrium positions. This topic is further discussed in Chapter 3. Metal-ligand coordination involves the bond between a transition metal and one or more molecules called ligands. The energy of the interaction can be as

high as a few eletronvolt [22]. These interactions are crucial when molecules assemble on a metallic surface or in the presence of an adsorbed metal atom.

The reversibility of non-covalent interactions allows for self-assembly, self-healing, self-recognition and self-selection as the molecules can reach the equilibrium while exploring the phase space [23]. On the other hand, molecules bound by these interactions are unstable against light, heat, and chemicals, making them unsuitable for most real-life applications.

Covalent interactions involve the linking of molecules with energy of a few electronvolt into complex structures, such as nanowires [24], nanoribbons [25], and 2D polymers known as covalent organic frameworks [26]. The irreversibility of this interaction makes these structures stable against a wide range of stressors, and, thus, suitable for real-life application but can significantly reduce the quality of the structure as defects cannot be avoided. Furthermore, covalent links allow electron transport across the structure opening the way to molecular electronics [27]. Although the growth of covalent structure occurs at a variety of interfaces, this thesis deals with the growth at the boundary between solid surfaces and vacuum.

2.1.2 On-surface polymerisation

The covalent linking of organic molecules on solid surfaces in ultra-high vacuum (UHV) is known as on-surface polymerisation [14]. Compared to polymerisation in solution, the monomers are confined in a bidimensional space by the surface resulting in new 1D and 2D products that cannot be otherwise synthesised [28]. The development of this field is inherently connected to the rise of scanning probe microscopy (SPM), in particular, STM and non-contact AFM (see Section 3.3.3), which enabled the imaging of the reaction products at the nanoscale [14].

The growth of nanostructures derives from the balance between energy and entropy. Energy favours the polymerisation of molecules on the surface. The loss of the monomers' translational and rotational degrees of freedom upon immobilisation into the polymer causes an entropic loss. Surface confinement reduces these degrees of freedom, shifting the balance towards the energetic term compared to polymerisation in solution [14].

Growth processes, such as polymerisation, rarely take place in equilibrium, thus a kinetic description is needed to account for the energy barriers. There are three steps involved in on-surface

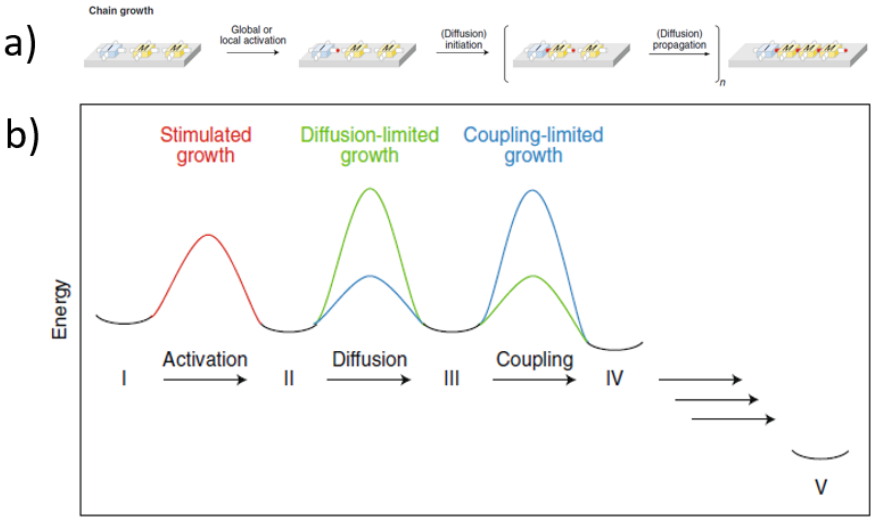

Figure 2.1: (a) Schematic representation of on-surface polymerisation showing the activation, diffusion, and coupling of monomer. (b) Activation, diffusion, and coupling barriers in the on-surface polymerisation. The images are reproduced from [14].

polymerisation (Figure 2.1): activation of the monomers, diffusion, and coupling.

Activation Monomers on the surface are usually not reactive by themselves. Activation requires heat or light to cleave specific bonds in monomers (stimulated growth) forming radicals. This step usually involves a high-energy barrier (a few eV), potentially causing the monomers to desorb from the surface before the activation. This issue is overcome by lowering the activation energy with a catalytic surface [29, 30]. Not all reactions require an activation step. For example, the polycondensation of aldehydes and amines on Au(111) is spontaneous at room temperature [31,32]. Monomers with a single reactive group form dimers; with two reactive sites, grow into wires; with three or more reactive groups, form 2D polymers.

Diffusion Radicals and molecules diffuse across the surface and react forming increasingly long chains. The surface has a relevant role since the diffusion coefficient varies depending on the surface chemistry, atomic landscape, and the coordination of atoms. For example, molecules exhibit a higher diffusion coefficient on terraces than at step-edges, where the surface atoms are less coordinated and thus more reactive [13]. Diffusion is also influenced by the chemistry, geometry, and orientation

of the monomers [33].

Coupling As the radicals and monomers diffuse, they react and form increasingly long chains with a reactive radical at their edge. They become slower due to the increased mass and are less reactive since new monomers can link only at the edges. The polymerisation ends when two different chains merge, neutralising the radicals at their sides (the dimerisation of two radicals is the most trivial case). For the system to reach equilibrium, the chains should explore the phase space i.e. their coupling should be a slow process compared to the diffusion due to a high energy barrier [29]. In this case, the growth is called 'coupling-limited' and the number of defects is low. Otherwise, it is named 'diffusion-limited' and results in defective polymers (Figure 2.1b) [14].

Several mechanisms of on-surface polymerisation have been studied. The following list is a non-exhaustive summary of some of them:

- Dehalogenative homocoupling studied on porphine molecules on Ag(111) [34]
- Dehydrogenative cycloaddition [25]
- Decarboxylation of naphthalene dicarboxylic acid on Ag(111) and Cu(111) [35]
- Ring-opening polymerisation of melamine on Cu(111) [36]
- Bergman cyclisation of ethynyl substituted benzenes [37]
- McMurry-type reductive coupling of aldehydes [38]
- Condensation of aldehydes with amines on Au(111) [31, 32]
- Trimerisation of acetyls [39]
- Ullmann coupling [24, 25, 40–46].

2.1.3 Ullmann coupling

Fritz Ullmann discovered the coupling between aryl halides, organic molecules with carbon-halogen bonds, with copper in solution to form biphenyls and copper salts in 1901 (Figure 2.2) [47]. In 2007, Grill and colleagues induced on-surface Ullmann coupling of halogenated molecules using a coinage

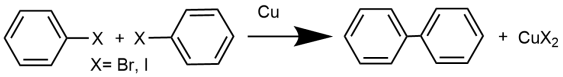

Figure 2.2: Ullmann coupling of aryl halides in solution.

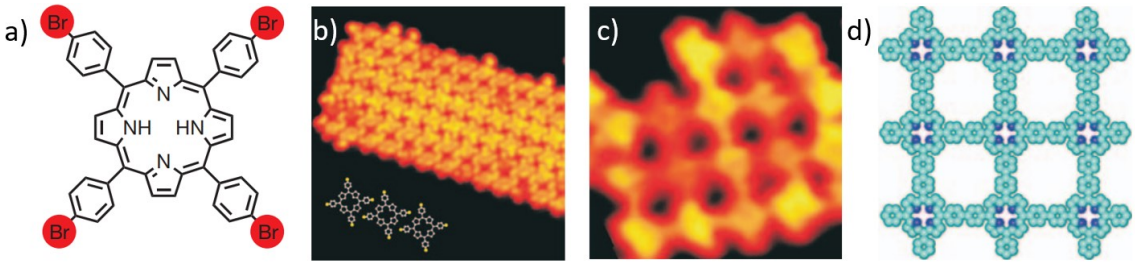

Figure 2.3: (a) Schematic representation of tetra(4-bromophenyl) porphyrin (Br_4TPP), consisting of a porphyrin core with four phenyl groups where hydrogen 4 has been replaced by a bromine atom. (b) STM image of Br_4TPP island on Au(111) before the polymerisation with a molecular model. (c) STM image and (d) schematic of TPP polymer. The images are reproduced from [33].

metal surface to confine the monomer in 2D and catalyse the reaction at the same time. Different kinds of halogenated phenyl porphyrins (an example is shown in Figure 2.3) can be polymerised upon annealing in UHV on an Au(111) surface, forming nanowires and 2D polymers [33].

Afterwards, the coupling of other halogenated organic molecules on coinage metals has been achieved, such as halogen-substituted 1,3,5-tris(phenyl)benzene [40,41], 1,4-dibromo phenyl benzene [42], ciclohexaiodo-m-phenylene [43], diphenyl–10,10'-dibromo-9,9'-bianthracene [25, 44], fluorene [24, 45], and 4,4"-dibromo-m-terphenyl [46].

Several papers cover the theoretical, computational, and experimental aspects of Ullmann coupling of aryl halides in detail due to the widespread interest [20, 29, 30, 33, 40–43, 48–52]. The activation of the Ullmann coupling consists of the thermal dehalogenation of the monomer (Figure 2.4a), resulting in the formation of radicals that are stabilised by the surface (Figure 2.4b). The halogen-carbon bond cleavage depends on geometric and electronic considerations [20]. The C-Cl bond is the strongest, C-I is the weakest, while C-Br strength lies between them. Consequently, each bond can be activated at a unique temperature [24, 29], providing exquisite control over multi-step reactions [24, 25].

The surface plays an important role in catalysing the activation step, too. At each atomic site,

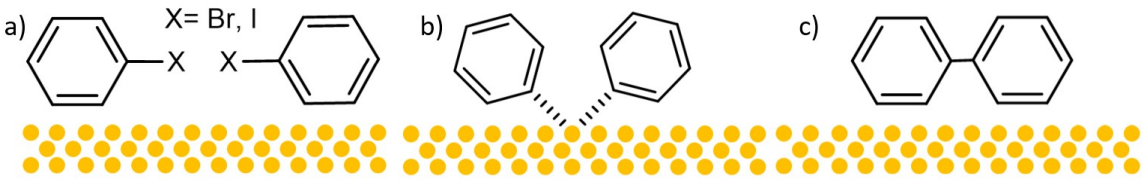

Figure 2.4: (a) Schematic representation on-surface Ullman coupling of halogen-substituted benzene. (a) Two halogen-substituted benzenes on a coinage metal surface. (b) Two dehalogenated benzenes radicals form a metal-organic bond with the same metal atom. (c) Coupling of the radicals into a polymer (dimer).

the coinage metal d orbitals overlap with the molecular one, causing an electron transfer to the $\pi^\star$ level. This excitation shifts to the $\sigma^\star$ halogen-carbon bond breaking it [20]. The energy required for this step decreases from Au to Ag to Cu [29]. Indeed, the dehalogenation is spontaneous at room temperature on Cu(111) [20, 40, 41] but requires activation on Au(111) [33]. Upon dehalogenation, the radical bond with the coinage metal surface (Figure 2.4b) forming the metal-organic phase [29, 30, 43, 53], that can be stable or unstable.

Radicals diffuse by hopping between metal atoms. The coupling occurs when two adjacent radicals eject the metal atom between them and form a covalent bond (Figure 2.4c) [29, 40, 43].This step is usually endothermic, requiring energy to be activated. The metal-organic intermediate state explains the observed anti-correlation between the activation and coupling barriers [29, 30, 43]. A molecule readily loses the halogen only if the energy gained in bonding with the metal is substantial. Thus, the metal atom ejection in the coupling step requires a significant amount of energy.

2.1.4 Ullmann coupling on insulators

On-surface Ullmann coupling is mainly studied on coinage metal surfaces as a catalyst is required to initiate the polymerisation at a temperature below the desorption point. The growth of the nanostructure for integration into devices on technologically relevant substrates, such as semiconductors and insulators, is non-trivial as they lack the catalytic activity of noble metals. In the literature, different approaches have been highlighted to transition from noble metal to other surfaces. First, the growth happens directly on an insulator. The second method consists of using a thin decoupling

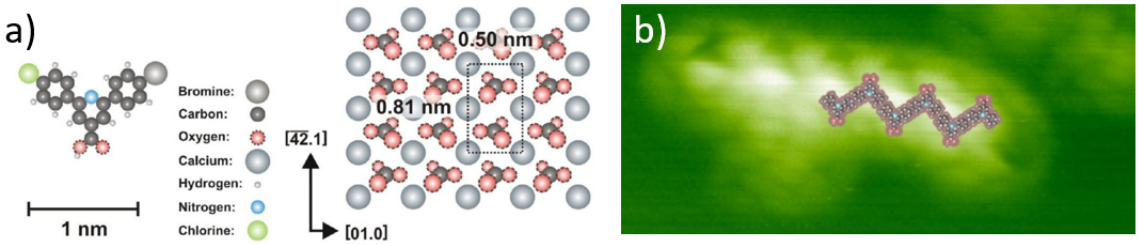

Figure 2.5: (a) 2-(4-bromophenyl)-6-(4-chlorophenyl)pyridine-4-carboxylic acid (BPCPPCA) monomer and calcite surface. (b) BPCPPCA oligomer forming after annealing at 610 K for 1h. The images are adapted from [56].

layer grown on top of the noble metal surface to confine the monomer while retaining the catalytic activity of the underlying metal. Finally, an extrinsic catalyst can be deposited on the noble metal surface to control the activation. Each approach is discussed in the following paragraphs.

Insulators Gutzler and coworkers tried to induce Ullmann on graphite(001), a zero-bandgap semiconductor, to pivot away from metal surfaces [41]. However, the molecules desorbed before the activation occurred due to the absence of a catalyst. Kittlemann and colleagues overcame the desorption problem by attaching a carboxylic group to a variety of monomers to anchor them strongly to a calcite surface and activating the reaction without a catalyst [54, 55]. A variety of halogen-substituted benzoic acid monomers and 2-(4-bromophenyl)-6-(4-chlorophenyl)pyridine-4-carboxylic acid (BPCPPCA) monomer (Figure 2.5a) were shown to undergo debromination and dechlorination forming a polymer (Figure 2.5b). Although this research proved that Ullmann coupling on a bulk insulator is feasible, the approach of Kittlemann and colleagues is limited to a single class of monomers with a specific anchor group suitable for a calcite surface. This method is not easily generalised to a variety of surfaces and monomers, which would be of interest to the technological application of 2D polymers.

Decoupling layers Morchutt and coworkers coated Ni(111) with a hexagonal boron nitride (h-BN) and graphene decoupling layer to reduce the monomers-metal interaction [51], instead of replacing the metal surface. In this configuration, the activation of 1,3,5,-(tris-bromophenyl)benzene Ullmann coupling takes place before the desorption but it exclusively yields oligomers (Figure 2.6), suggesting that the underlying Ni(111) still interacts with the monomer limiting the diffu-

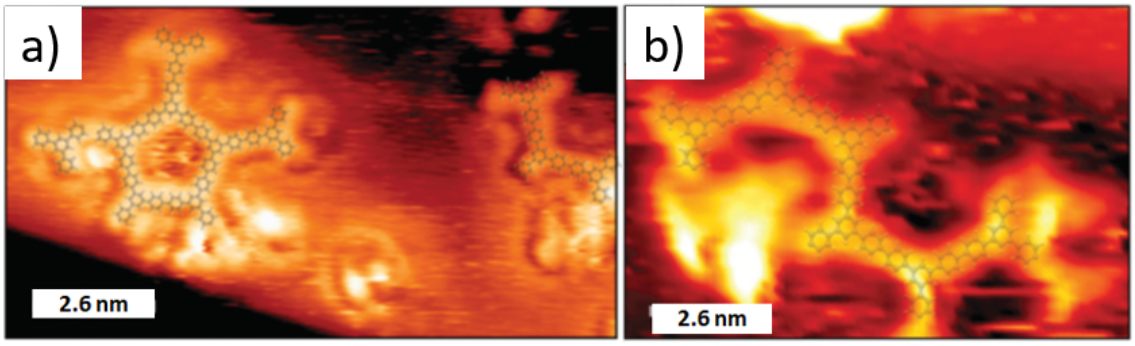

Figure 2.6: STM image of 1,3,5-tris-(bromophenyl) benzene (TBB) oligomers on (a) Ni(111)/h-BN and (b) Ni(111)/graphene. The images are reproduced from [51].

sion [51]. Similarly, Ullmann coupling of 1,8-dibromobiphenylene has been induced on h-BN grown on Rh(111) by Zhang and colleagues [57]. Bombis and coworkers demonstrated that it is possible to grow dibromoterfluorene (DBTF) polymers on an Ag(111) surface partially covered by a NaCl insulating layer [58]. While this method provides information on the properties of the polymer on an insulating surface, the catalytically active noble metal surface is still required for the polymerisation to occur, limiting the practical applications. Rastgoo-Lahrood and coworkers used a different approach [59]. First 1,3-bis(p-bromophenyl)-5-(p-iodophenyl)benzene (BIB) molecules were linked into a polymer through Ulmmann coupling on Ag(111) surface. Successively, the resulting polymer was decoupled from the noble metal surface through the intercalation of iodine atoms between the porous structure and the surface.

Although decoupling layers have shown some success, it is not possible to rule out the possibility that the underlying surface or metal adatoms are not influencing or catalysing the growth. Moreover, these decoupling layers cannot be integrated into current device architectures, such as CMOS, hindering their practical application.

Extrinsic metal catalysts In the context of on-surface Ullmann coupling, the surface supports the diffusing molecules and catalyses the reaction. Separating these two processes could enhance control over the reaction by tuning the energy barrier of activation, diffusion, and coupling independently. The substrate influences the diffusion barrier, while an extrinsic catalyst affects the activation and coupling barrier. Noble metals are a natural choice for this purpose as Ullmann

coupling occurs on coinage metal substrates. Shi and coworkers used single Cu atoms as extrinsic catalysts on Au(111) in a two-step reaction (Figure 2.7 a) as copper is the most reactive of the noble metals [50]. The first reaction step involves the C-Br activation leading to dumbbell-shaped dimers. Then, the Cu atoms catalyse the C-Cl bond cleavage (Figure 2.7a). Overall, the covalently bonded polymer grows (Figure 2.7b-c) but it is limited by the formation of Cu islands. In addition, other metals, such as Pd and Dy, have been studied. Pd is a well-known catalyst in Ullmann coupling [60], while Dy is a promising candidate [61]. In this context, single atoms are used as catalysts because they are extremely reactive and highly mobile. Early studies on porphyrins show that Cu and Pd atoms catalyse the Ullmann coupling on noble metal surfaces reducing the activation temperature and increasing the reaction yield [36, 60]. Zhao and colleagues tested Cu and Pd atoms as extrinsic catalysts on TBB supported by an h-BN monolayer grown on top of Ni(111) [62]. Cu atoms catalyse the reaction only when the surface covered by the TBB layer is heated. Pd is a worse catalyst than Cu, even if it is active at room temperature. Extrinsic catalysts result in the formation of oligomers improving the results on bare h-BN on Ni(111), as previously discussed [51].

Extrinsic metal catalysts are a general way to induce Ullmann coupling of a plethora of halogenated monomers on technologically relevant surfaces as they can efficiently initiate the reaction. Furthermore, the activation and coupling barrier could be controlled by the choice of the metal catalysts, as demonstrated for the coinage metal surfaces [29]. Although single metal atoms have been shown to induce Ullmann coupling, the quality of the resulting polymers is generally poor as the individual atoms sinter together and are trapped into the polymer, poisoning the surface and the polymer and, hence, disrupting the polymerisation [50, 62]. A suitable replacement should be as highly catalytically active and mobile as single atoms but it should also be resistant to sintering. A natural choice would therefore be small metal clusters comprising just a few atoms that retain high catalytic activity but are more stable than individual atoms.

The work in this thesis aims to induce Ullman coupling of Br_4TPP on inert surfaces, such as mica and HOPG, using small atom clusters as an extrinsic catalyst. This method could enable the polymerisation of a variety of monomers on different surfaces without the need for a specific anchor group.

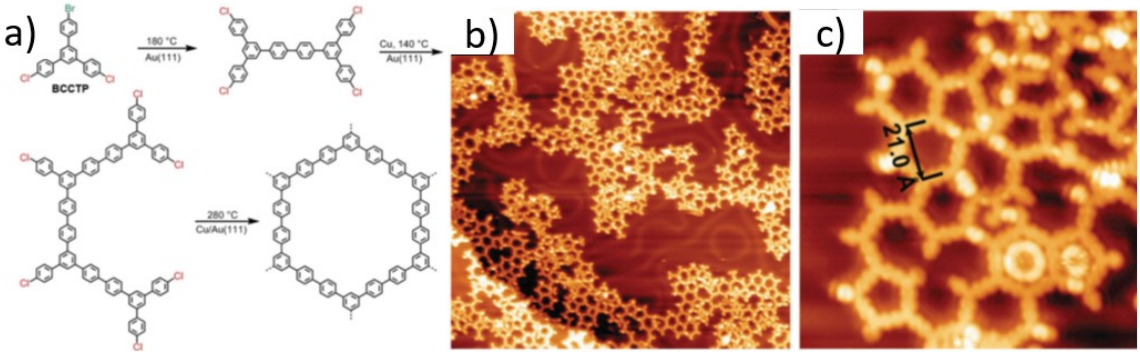

Figure 2.7: (a) DCTP monomer sequential Ullmann coupling: the Au(111) surface activates debromination, and single extrinsic copper atoms activate dechlorination. (b) 65 nm × 65 nm STM scan of the network of covalently bonded DCTP molecules. (c) High-resolution, 14 nm × 14 nm STM image of the polymer. The images are reproduced from [50].

2.2 Atomic Quantum Clusters

2.2.1 Introduction

Atomic quantum clusters (AQCs) are assemblies of a few atoms (e.g. Ag_3 [63], Pt_4 [64], and Cu_5 [65]) with sub-nanometer or nanometre dimensions, that can be thought of as molecules. Indeed, discrete energy level and localised orbital emerge from confinement as the size is comparable to or lower than Fermi length (< 1 nm). For instance, Cu_n ($n < 10$) exhibits fluorescence (Figure 2.8) implying a non-metallic electronic structure. On the contrary, Cu_{309} is not an AQC as it has a surface plasmon due to a collective electron behaviour as observed in nanoparticles and solids but not in small molecules [66]. AQCs properties significantly differ from nanoparticles or bulk counterparts and depend on the number of atoms, namely atomicity.

AQCs have drawn significant attention as nanoscaled and efficient catalysts with high selectivity and activity in several reactions [9,67–70]. They are highly reactive because the atoms are in a low-coordination state and the orbitals are easily accessible. This topic is further discussed in Section 2.2.3. Furthermore, potential application as anti-cancer agents [71], anti-bacterial materials [72], and fluorescent markers [73] has been highlighted. A discussion of the properties of AQCs is relevant to this thesis, as the structure and chemical composition of Cu_5 clusters stabilised by an

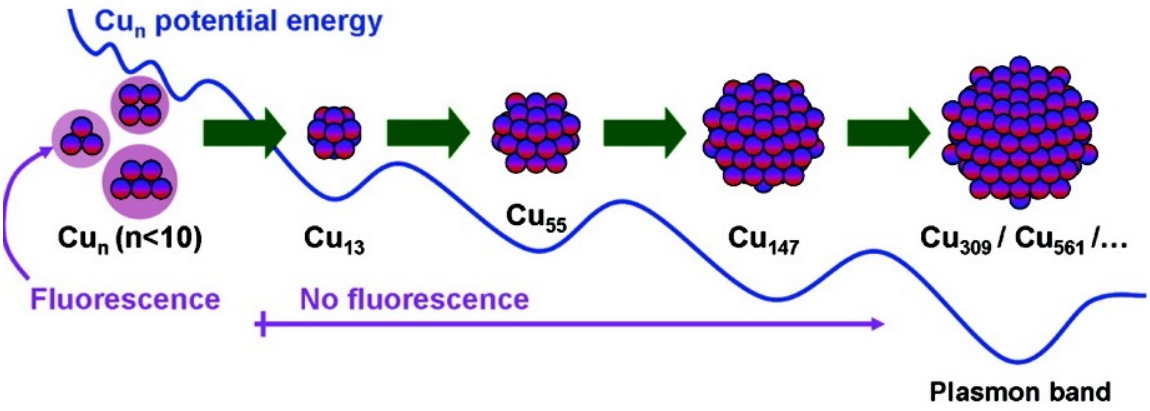

Figure 2.8: Difference in the optical properties and potential energy in Cu_n. Small clusters ($n < 10$) are fluorescent, while bigger nanoparticles exhibit plasmons. The image is reproduced from [74].

oxygen layer, $Cu_5[O_2]_n$, is analysed and they are used to catalyse the on-surface polymerisation of tetra(4-bromophenyl)porphyrin (Br_4TPP).

2.2.2 Electronic properties

The fascinating properties of AQCs derive from the molecular-like electronic structure that can be investigated with theoretical models and numerical simulations. The jellium model is the most simple theoretical framework to understand AQCs. Each atom in the cluster is approximated by free electrons from the valence band attracted by a short-range, spherical potential generated by the *nucleus* screened by core electrons [75–77]. This kind of Hamiltonian entails discrete energy levels analogous to the nuclear shell model (e.g. 1s, 1p, 1d, 1f, etc.) where the azimuthal quantum number, l, is not smaller or equal to the principal quantum number, n. The closure of a shell gives rise to stable configurations, that are dominating in mass spectra, such as Na_2, Na_8, Na_{18}, Na_{20} shown in Figure 2.9a. As sodium atoms have a single electron in the valence shell, the 1s level is filled by two electrons in a cluster comprising two atoms (Na_2), giving rise to a stable configuration. Analogously, the 1p level is full in Na_8 (Figure 2.9a). The number of atoms in a cluster necessary to close a shell is called the "magic number". Other potentials explain the shell structure and magic numbers [78]. For example, q-deformed oscillator approximation is in excellent agreement

with experimental magic numbers of alkali and noble metals up to 1500 [79, 80]. It is, however, possible to synthesise clusters with open shells using wet chemistry or electrochemical methods that are extremely reactive and, thus, suitable for catalysis.

Discrete electronic structure results in the loss of metallic behaviour of AQCs due to a gap between the highest occupied molecular orbital (HOMO) and the lowest unoccupied molecular orbital (LUMO). This gap, $\Delta E_{HOMO-LUMO}$, derived from the jellium model for noble metals agrees with the measured trend [82]:

$$\Delta E_{HOMO-LUMO} = E_F n^{-\frac{1}{3}}, \tag{2.1}$$

where E_F is Fermi energy of the bulk noble metal and n is the atomicity. The atomicity-dependent $\Delta E_{HOMO-LUMO}$ is exploited for catalytic applications as discussed in Section 2.2.3. In addition, the shift of the Fermi energy,$E_{F,AQC}$, with respect to the bulk counterpart, $E_{F,bulk}$, reads:

$$E_{F,AQC} = E_{F,bulk} + An^{-\frac{1}{3}}, \tag{2.2}$$

where A is a constant that depends on the material [83].

2.2.3 Catalytic activity

AQCs have drawn attention as catalysts since all or most of their atoms are accessible and low-coordinated, making them reactive and unstable. Their activity, the possibility to catalyse reactions, and selectivity, the catalysis of a specific reaction, differ from the bulk counterparts and depend on their atomicity [83–85]. Indeed, spatially localised orbitals are suitable for interacting with other species [70,82,86] as well as the HOMO-LUMO band gap and position affect the selectivity [82]. For example, only Cu_5 is active in methylene blue reduction to leucomethylene by hydrazine (Figure 2.10) among Cu_n ($n = 5, 13, 20$). The alignment between LUMO and the tail of methylene blue reduction energy favours a weak interaction [83]. On the contrary, Cu_{13} interacts too strongly with the molecules and the LUMO of Cu_{20} does not align with the reduction energy.

Although AQCs can be synthesized without ligands, they are usually surrounded by a layer of oxygen or supported by surfaces to improve their stability and prevent sintering, changing their catalytic properties from ideal clusters presented above [87]. Even if theoretical models account for the additional complexity in specific cases [88], DFT calculations and molecular dynamics simulations are widely used to provide in-depth information on energy and kinetics [70,85,89] such as Cu_5

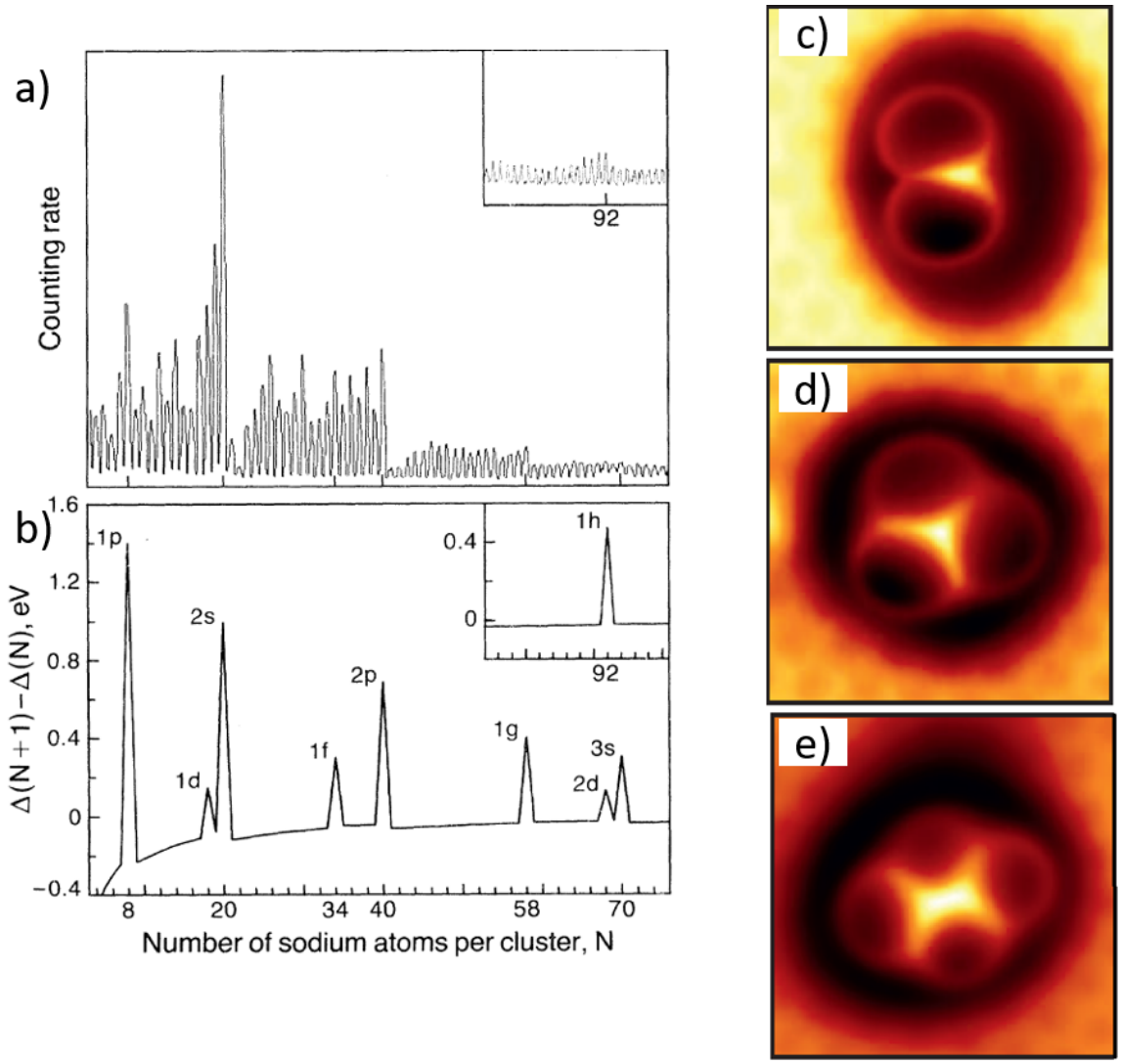

Figure 2.9: (a) Mass spectrum of Na AQCs and (b) electronic energy difference between cluster with N+1 and N atoms. Non-contact AFM image of (c) Fe_2, (d) Fe_3, and (e) Fe_4 on Cu(111), respectively. Panels a,b and c-e are reproduced from [75] and [81], respectively.

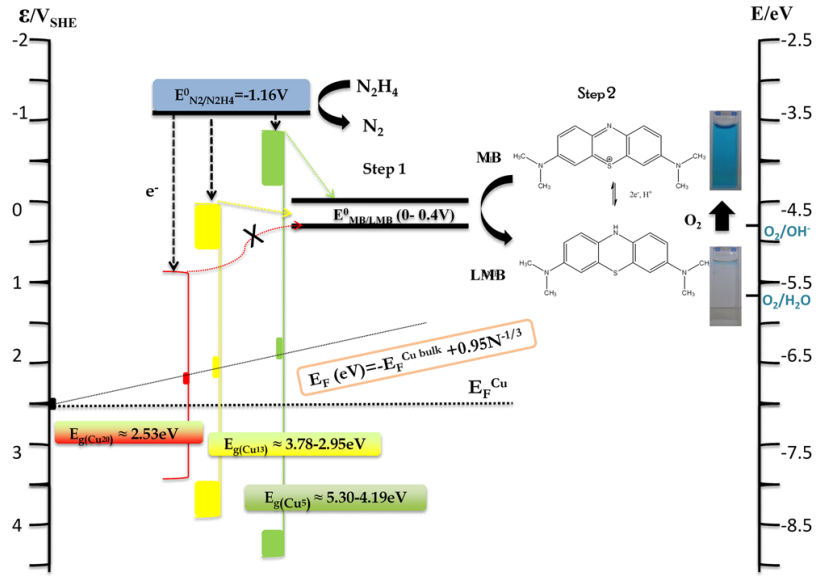

Figure 2.10: $\Delta E_{HOMO-LUMO}$ and $E_{F,AQC}$ versus n of Cu_n $(2 < n < 20)$ clusters involved in methylene blue (MB) to leucomethylene blue (LMB) reduction by hydrazine (N_2H_4). The energy alignment between the catalysts and the reactant is also shown. The image is reproduced from [83].

oxidation [90] and iodobenzene adsorption on Pd_3, Pt_3 and Au_3 [91].

AQCs catalyse a wide variety of reactions. The following list is a non-exhaustive summary of some of them:

- CO oxidation by Au [92] and Pt on TiO_2 [84]
- Propane dehydrogenation by Pt [93]
- Oxygen reduction by Pt [94]
- Dehydration [69] and hydration [95] of alkenes
- Olefin hydrogenation by Ir [96] and Cu [97]
- Selective oxidation of alkanes by Au [98], alkenes by Ag [99], alcohols by Pt and Pd [100], and thiols by Au [101]
- C-C coupling (Heck, Sonogashira, Stille, and Suzuki coupling) by Pt and Pd [89, 102]
- Dehalogenation of iodo and bromobenzene by Au [91]
- Assistance in the photocatalytic processes on TiO_2 by Cu_5 [103] and Ag_5 [104]
- Selective oxidation of glutathione and thioredoxin by Ag_5 in biological settings [71].

2.2.4 Structure and isomers

Density functional theory (DFT) is the standard approach for the *ab initio* calculation of AQCs properties, accounting for the discrete nature of *nuclei* and core electrons. In general, small clusters are predicted to be 2D while bigger ones are 3D [105], as their structure resembles that of a nanoparticle.

Experimental characterisation of the AQCs structure is lagging behind simulations due to the sub-nanometric dimensions of clusters, which are comparable to small organic molecules, such as benzene. Only with the recent development of high-resolution scanning probe microscopy, small surface-supported clusters have been imaged [81, 106]. Emmrich and coworkers managed to image Fe_2, Fe_3, and Fe_4 on Cu(111) (Figure 2.9b) with non-contact AFM [81]. Adachi and colleagues

imaged 3D gold clusters on rutile TiO_2 [106].

DFT simulations predict that noble metal AQCs comprising a few atoms exhibit 2D and 3D isomers [105,107–109] (middle row of Figure 2.11a) with different electronic and catalytic properties [90,110–112] due to the localisation of the molecular orbitals in different parts of the clusters [111]. For example, 2D and 3D Cu_5 exhibit different band gaps of 1.6 eV and 1.25 eV, respectively, as shown in Figure 2.11b. The HOMO and LUMO are located on the side of 2D Cu_5 and the top and bottom of the 3D isomer. The different electronic properties affect the mechanisms of CO oxidation [112] and water splitting on TiO_2 [103].
The isomers have hardly been experimentally characterised due to the sub-nanometric dimensions. For example, Imakoa and coworkers resolved a Pt_4 cluster evolution into different isomers (Figure 2.11c) using a high-angle annular dark-field scanning transmission electron microscope [64].

It could be possible to distinguish between isomers in at least two ways. First, 2D and 3D isomers have different adsorption heights on a surface that could be measured with an Atomic Force Microscope (AFM) or normal incidence X-ray standing waves (both techniques are discussed in Chapter 3). Second, the difference in electronic properties could be identified by measuring the band gap or mapping the orbitals with a scanning tunnelling microscope (STM).

Cu_5 is 2D in gas phase [112] and potentially when supported by a surface [65]. It is predicted to be 2D when negatively charged and to become 3D upon donation of an electron (Figure 2.11a) [105, 113, 114]. This suggests that the structure could change when catalysing reactions that involve charge donation such as dehalogenation of aryl halides coupling [115]. This possibility is explored by inducing the on-surface polymerisation of Br_4TPP using oxygen-stabilised copper clusters, $Cu_5[O_2]_n$.

2.2.5 $Cu_5[O_2]_n$

This thesis focuses on characterising the properties of $Cu_5[O_2]_n$, kindly provided by D. Buceta and M.A. López-Quintela at the Univeristy of Santiago de Compostela.

Compared to other small atom clusters, $Cu_5[O_2]_n$ have been synthesised without a capping layer to stabilise them [65], they are thus a suitable system to study the properties of naked clusters. As $Cu_5[O_2]_n$ are synthesised in water solution, it is assumed that dissolved molecular oxygen absorbs onto them, according to DFT simulations and experimental evidence [103, 116].

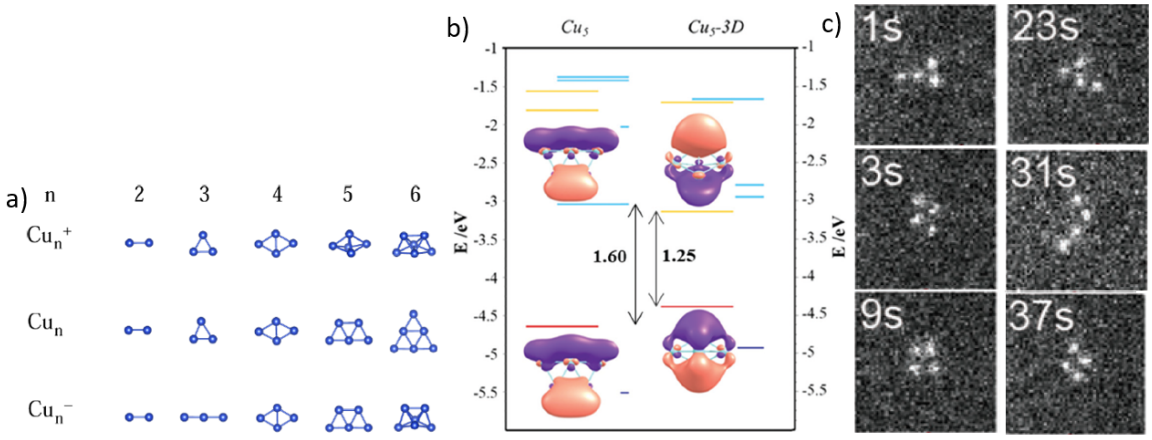

Figure 2.11: (a) DFT predicted structures of (top row) positively charged, (middle row) neutral, (bottom row) negatively charged Cu_n. (b) DFT calculation of the electronic structure of (left) 2D and (right) 3D Cu_5 with the HOMO and LUMO orbital structure and energy gap. (c) High-angle annular dark-field scanning transmission electron microscope of a Pt_4 isomer evolution over time. Panels a, b, and c are reproduced and adapted from [105], [112], and [64], respectively.

$Cu_5[O_2]_n$ in water solution have been proven to be stable against ageing, temperature up to 60 °C, UV exposure up to 24 h, and pH through emission spectroscopy (Figure 2.12). Additionally, DFT simulations show that small Cu AQCs are resistant to the dissociation of O_2 into atomic oxygen ($O_2 \rightarrow 2O$), suggesting that Cu_5 should be resistant to oxidation [110]. At the moment, experimental evidence that $Cu_5[O_2]_n$ are resistant to oxidation is inconclusive [65] and the question is addressed in this thesis.

I aim to understand (1) the chemical state of copper in the clusters, (2) whether surface-supported $Cu_5[O_2]_n$ is 2D or 3D, (3) test their capability to catalyse the on-surface polymerisation of Br_4TPP on different surfaces, and (4) verify if the structure changes during the process.

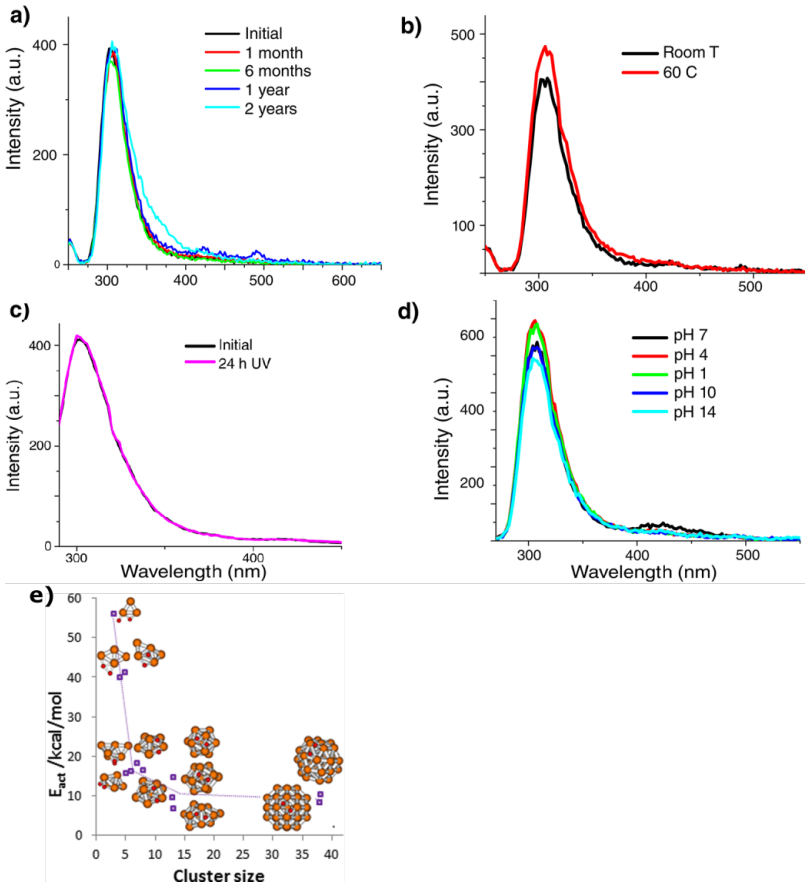

Figure 2.12: Emission spectra of $Cu_5[O_2]_n$ excited with a 224 nm laser tested against (a) ageing, (b) temperature, (c) UV exposure and (d) pH. (e) Computed activation energy of Cu_n AQCs oxidation. Panels a-d and e are reproduced from [65] and [110], respectively.

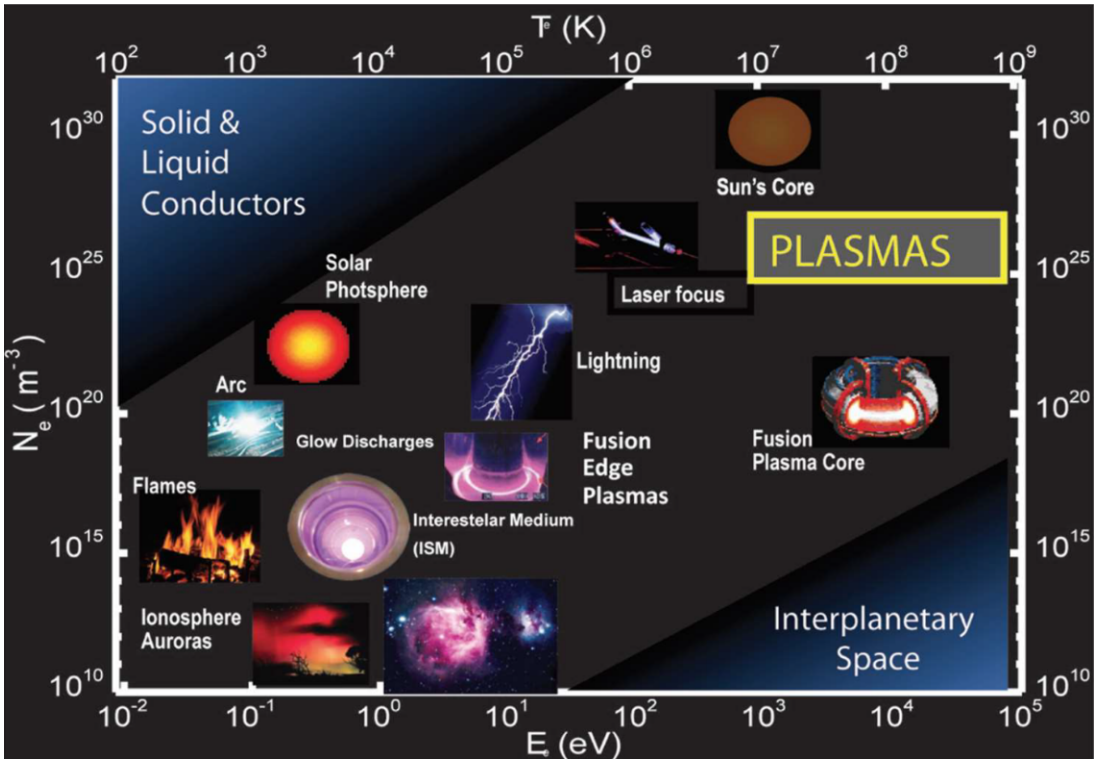

Figure 2.13: Types of plasma categorised by the electron density (N_e) and temperature (T) or energy (E). The image is reproduced from [117].

2.3 Plasma polymerisation

In the following sections, plasma polymerisation as an additional method to grow covalently stabilised molecular layers is discussed.

2.3.1 Plasma

Plasma is the fourth and the most abundant state of matter [117] found, for instance, in lightning, flames, auroras, stars, lasers, electron beams, fusion reactors, and arc discharges (Figure 2.13). Plasma is an ionised gas with a complex mixture of electrons, ions, radicals, atoms and molecules in excited states, neutrals, and photons.

Conventionally, there are two categories of plasma depending on the average temperature or kinetic energy of its constituents: thermal and non-thermal plasma. In thermal plasmas, electrons

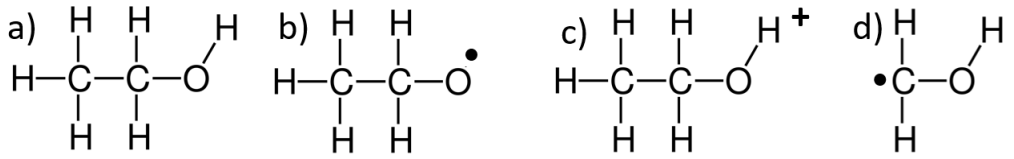

Figure 2.14: Example of species in an ethanol plasma comprising (a) a neutral, (b) a radical, (c) an ion, and (d) a fragment.

and heavy particles (radicals, ions, neutrals) are in thermal equilibrium. On the contrary, the plasma is non-thermal or cold if heavy particles have a lower temperature or kinetic energy than electrons. Cold plasma offers the possibility to modify the surface property of solid materials while preventing thermal damage to the bulk, as Hollahan and coworkers showed for the first time in 1969 [118].

2.3.2 Plasma polymerisation

An electric field is an effective way to generate cold plasma at low pressure. While the ions gain a small fraction of the electric energy remaining close to room temperature, the temperature of electrons rises due to the low mass (1836 times lighter than the nucleons). One application of cold plasma generated through glow discharge at low pressure ($0.01-0.5$ mbar) is plasma polymerisation (PP).

PP is the process of forming a polymeric coating on a substrate from the plasma of a monomer gas [119]. Most of the monomer gas is neutral (Figure 2.14a) (density $n_n = 10^{19-21}\mathrm{m}^{-3}$), a small fraction becomes radicals (Figure 2.14b) (density $n_r = 10^{17-19}\mathrm{m}^{-3}$), and just a negligible part is ionised (Figure 2.14c) (density $n_i = 10^{13-16}\mathrm{m}^{-3}$) [120]. Due to charge neutrality, the density of electrons, n_e, equals n_i. Moreover, plasma is rich in photons, as the glow observable during the polymerisation process suggests. Their wavelength ranges from the ultraviolet (UV) to the infrared (IR) spectrum as they derive from molecular de-excitation, electron-ion or radical recombination.

Electrons are the 'powerhouse' of plasma polymerisation as they absorb most of the power from the electric field above kHz because they can respond to the change in the electric field direction while the heavy ions cannot react readily enough (see Section 3.4.2 for pp reactor description). The energy of electrons usually ranges from 1 to 10 eV with a peak between 1 and 4 eV (Figure 2.15).

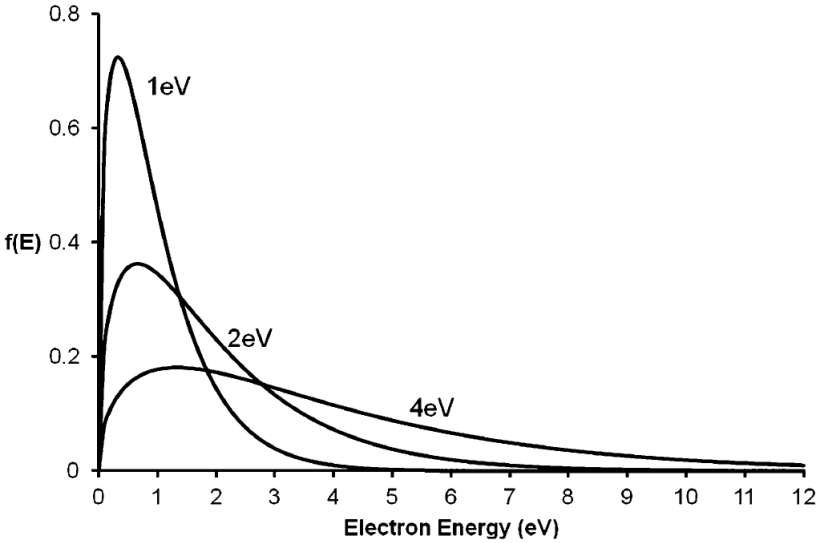

Figure 2.15: Electrons energy distribution function (EEDF) at different mean energies. The image is reproduced from [120].

Electrons initiate the polymerisation by damaging the monomers as they possess enough energy to break covalent bonds (energy ranges from 3 to 5 eV), creating radicals or molecular fragments (Figure 2.14d). These extremely reactive species can take part in reactions in the plasma phase, land on the substrate and further react. The resulting coating can have little resemblance to the original molecule but it is highly cross-linked and thus stable. Moreover, the incorporation of interesting functional groups of the monomers, such as hydroxyl (OH) [121], amine (NH_2) [118,122], carboxylic (COOH) [123], and nitroxide (NO) groups [124,125], drives plasma polymers applications, as discussed in Section 2.3.3.

Ions or radicals?

There is an ongoing debate about whether radicals [126] or ions [120] contribute the most to plasma polymer formation. It was widely believed that radicals are the main film-forming species, in analogy with radical polymerisation, as their density is $10^3 - 10^4$ times the electrons in the bulk of the plasma [120]. However, the electric field arising when a substrate is in the plasma has a significant impact on the deposition. The fast-moving electrons negatively charge the substrate, generating a potential difference with respect to the plasma. The resulting electric field accelerates

the positive ions towards the substrate enhancing their flux and increasing the likelihood of sticking to the substrate (sticking coefficient). It has been shown that, at high pressure, the ion flux can account for most of the mass flux to the surface [127–129]. Appendix A examines this fascinating topic in detail.

External parameters

Many external factors influence the properties of final plasma polymers such as power, pressure, monomer flow rate, and continuous or pulsed discharge [130]. Although correlating the external parameters to the process in the plasma is extremely complex [131], the properties of plasma polymers as a function of the external parameters have been studied, providing some experimental insight [126]. Here, the role of power and pressure are briefly discussed as they are relevant to this thesis.

- Power: the higher the power provided to the plasma, the more energy the electrons gain, increasing the molecular damage. Consequently, a lower power ($< 5-10\,\mathrm{W}$) improves functional group retention.

- Pressure: at higher pressure ($> 0.1-0.2$ mbar), a collisional sheath forms around the surfaces in the plasma reducing the energy of ions traversing it through collisions. This process reduces the molecular damage by slowing the ions before they collide with the substrate. This topic is discussed in detail in the Appendix A.

In general, low power and high pressure are ideal conditions to retain functional groups of the monomers [128, 129].

2.3.3 Applications of plasma polymers

The interest in plasma polymerisation derives from the possibility of cross-linking organic molecules into a film even if they cannot undergo conventional radical polymerisation. Thus, it extends the stabilisation of polymerisation to unsaturated monomers with interesting functional groups (hydroxyl, amine, carboxylic, and nitroxide) at the cost of some molecular damage. For the same reason, plasma polymerisation is suitable for depositing multi-layered or patterned coatings of hydrophilic and hydrophobic monomers that would be challenging using wet chemistry methods.

The monomers involved are mainly gasses (e.g. perfluorocyclobutane) and liquids of low molar mass (e.g. ethanol, propionic acid, allylamine), even though solids with a suitable vapour pressure are available (e.g. 2,2,6,6-tetramethyl-1-piperidinyloxy (TEMPO)).

Another advantage is the wide selection of substrates to coat, ranging from silicon to paper, no matter their shape or size. The process is scalable, the coatings area being limited only by the chamber size, and requires a single step. Additionally, it is regarded as green as it is solvent-free, material- and energy-efficient [4]. For these reasons, plasma polymerisation is suitable for industrial applications [132–135], although reproducibility among different reactors is a well-known issue in the research field [136].

Biomedicine is one of the main drivers of plasma polymer application [5]. Indeed, plasma coatings have been shown to improve biocompatibility by enhancing or preventing the adhesion of proteins and cells to surfaces. They can also prevent the attachment of bacteria or kill them [137] as well as sense both biomolecules and biological entities. Functionalising surfaces with specific chemistries naturally leads to selective absorption of organic and inorganic compounds in liquids, while the cross-linked structure favours their entrapment. Thus, water purification from heavy metals and dyes can benefit from plasma polymerisation [138]. Furthermore, pp could be applied to electronics, as the recent investigation into perovskite solar cells [139] and wearable devices suggest [140].

Biofouling and anti-bacterial coatings

Biofouling is the attachment of proteins, viruses, or microorganisms to a surface. It causes significant harm due to the resulting infections, accounting for 400 billion dollars in healthcare expenses worldwide [141]. Biofouling of catheters alone results in 250000 blood infections each year in just the U.S. [142].

Once bacteria adhere to a surface, they form an organised community, called the biofilm, potentially comprising several pathogen species at the same time. The biofilm is surrounded by an extracellular polymeric matrix that protects it from treatments, making it extremely hard to eradicate. Biofilm eradication requires higher doses of antibiotics compared to treating bacteria in the planktonic state [141], creating an evolutionary pressure to select drug-resistant strains that are even more difficult to treat [1, 143]. The rise of antimicrobial resistance calls for new approaches to

address bacterial colonisation of surfaces alongside antibiotics [3].

Among the many possibilities offered by nanomaterials, one option is protecting surfaces with coatings. PP is suitable for tuning the chemical and physical properties of surfaces for antimicrobial purposes.

One option is preparing surfaces with anti-biofouling chemistry from molecules or functional groups such as hydroxyl [144], poly(ethylene glycol) [143], amine, and oxazoline [5]. Beyond chemistry, the morphological and physical features of coatings are available. For instance, nano-spikes embedded in hydrophilic coatings are proven to kill bacteria [5]. Furthermore, steric and electrostatic repulsion physically obstruct bacterial adhesion [143]. Another option consists of avoiding bacterial adhesion in the first place or disperseing the biofilm. Nitric oxide and nitroxides have recently drawn attention as they prevent bacterial adhesion to the surface or disperse a biofilm [145, 146] and they can potentially undergo plasma polymerisation [124, 147].

Antibacterial activity of nitric oxide and nitroxides

Nitric oxide (NO) is an antimicrobial agent with a dose-dependent effect (Figure 2.16a). It is a killing agent in high concentration, causing nitrosative and oxidative stress against cell walls and DNA due to the reaction between NO and reactive oxygen species to form N_2O_3 and $OONO^-$ [148]. However, nitric oxide can damage non-bacterial cells, too. In low concentrations, NO induces biofilm dispersion by reducing the second messenger c-di-GMP concentration that, in turn, triggers the transition to the planktonic state [149,150]. Bacteria in this state are more vulnerable to antibiotics and treatments. The biofilm dispersal potentiality of nitric oxides has been highlighted for different bacterial species [151], including *Pseudomonas aerugionsa* and *Staphylococcus epidermidis*.

Although nitric oxide is a promising antimicrobial agent, it has two drawbacks. NO can interact with the biological environment, readily degrading, and the half-life in tissues is about 5s [152], resulting in a short efficacy window. To overcome these limitations, nitric oxide delivery platforms, such as polymeric matrices and nanoparticles loaded with NO or stimulated release of NO from donors [147, 152], have been developed to slow the release for a long-lasting action and keep a sub-lethal NO dose. A thorough review of these applications is beyond the scope of this thesis, but more information is available in reference [148] and references therein.

Another option is switching to molecules with a stable NO functional group, the nitroxides.

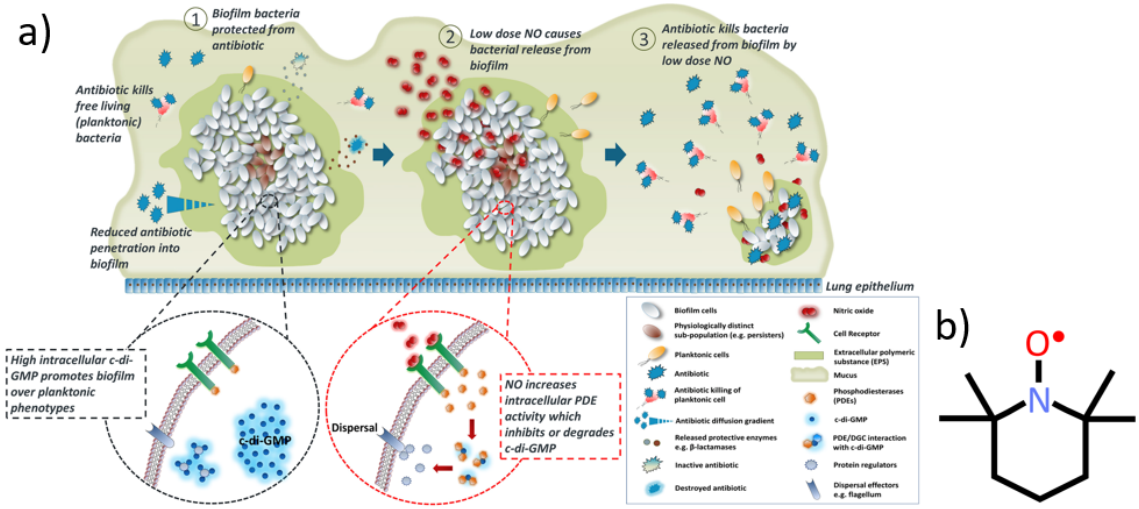

Figure 2.16: (a) Proposed mechanism of the disruption of antibiotic tolerating biofilms by nitric oxide. (1) The extracellular polymeric matrix reduces antibiotic penetration into biofilms, (2) NO at low concentrations induces biofilm dispersal, and (3) antibiotics are more effective against planktonic bacteria. (b) Diagram of 2,2,6,6-tetramethyl-1-piperidinyloxy (TEMPO). Panel a is reproduced from [154].

Among them, TEMPO (Figure 2.16b) and its derivatives are of interest because the steric hindrance of methyl groups protects the nitroxide radical, resulting in a long half-life. TEMPO and its derivatives in solution exhibit antimicrobial properties akin to nitric oxide, causing biofilm dispersion and preventing its formation [146,153]. Plasma polymerisation has been shown to offer the possibility of stabilising TEMPO on a variety of substrates [124], potentially coating catheters and other surfaces in contact with the human body. Furthermore, Michl and coworkers showed that TEMPO plasma polymers exhibit anti-biofouling properties against *Staphylococcus Epidermidis* [125]. This thesis aims to understand how the substrate affects the growth of TEMPO coatings in the early stages of plasma polymerisation and test the anti-microbial activity. In the following section, the literature on the early stages of plasma polymerisation is reviewed.

2.3.4 Early stages of plasma polymerisation

Recent studies challenge the typically held belief that plasma polymerisation is a surface-independent process. The properties in the early stages of plasma polymerization differ from thicker films in terms of chemistry [122, 123, 155–157], morphology [123, 156–158], growth rate [123], and adhesion [156, 159]. The state-of-the-art in the early stages of plasma polymerisation is briefly reviewed here.

The early stages of plasma polymerisation are defined as the first few nanometres of the film, i.e. the region significantly affected by the substrate, as shown schematically in Figure 2.17a. In the early stages, the deposition rate [123, 156, 159], adhesion [159–161], cross-linking [159, 160], chemistry [122, 123, 155–158, 162], and morphology [122, 156, 163] differ from the bulk counterpart. Initially, the monomers deposit from the plasma onto the substrate and, after the first layers are grown, they land on the already deposited film. The probability of sticking to the surface (sticking coefficient), the type and strength of interaction with it, and diffusion changes when the monomer lands on the substrate or the already deposited plasma polymer film (Figure 2.17b). Furthermore, energetic particles generated in the plasma, such as ions and photons, constantly bombard the film providing energy for processes taking place on the surface. Studying what happens in the early stage is relevant for designing nano-scaled coatings [120], their application to bio-materials [5], as well as energy and material savings as we transition to a greener economy. Additionally, tuning the properties of the first few nanometres of the film can significantly improve the overall performance of films, for instance, by enhancing the adhesion in biological environments [156] and stability in water [160]. Moreover, studying the early stage of plasma polymerisation is a step forward in the fundamental understanding of plasma polymer formation. Surface-sensitive, averaging techniques (e.g. XPS, water contact angle, ellipsometry, and profilometry) convey precious information about the early stages of plasma polymerisation. Yet, they cannot provide spatially-resolved measurements nor probe the morphology and detailed molecular structure of the coatings. Thus, SPM is required to provide important insights. In particular, AFM is suitable since it gives access to morphology, down to the sub-molecular resolution [164, 165], and other local features of the surface, such as chemistry [158], mechanical [166] and electronic properties, and interfacial forces [167].

This section aims to organise and critically review the available information about the early stages of plasma polymerisation. First, the growth rate and cross-linking, and then the chemistry

of the films are examined. Finally, the AFM analysis of the film morphology and structure, which is comparatively underexplored, is discussed.

Deposition rate, sticking coefficient and cross-linking

Vasilev and coworkers showed that the deposition rate of n-heptylamine, allylamine, propionic acid and acrylic acid increases during the early stages and then levels off. They highlight that the deposition rate depends on the substrate since the coatings are consistently thicker on a self-assembled monolayer (SAM) of mercaptoundecanoic acid (MUA) than on gold. Since the flow of particles to the surface is the same, then the sticking coefficient of different surfaces accounts for the different deposition rates. Similarly, the ellipsometric measurements by Akhavan and colleagues show that the deposition rate of C_2H_4, N_2, and Ar stabilises after an initial drop (Figure 2.18 a). However, ellipsometric measurements may not precisely estimate the film thickness when the first few nanometres are rough and discontinuous, so the deposition rate is affected by significant uncertainty. Vandenbossche and colleagues showed that the growth rate of C_2H_4/NH_3 plasma, as measured by profilometry, is lower in the early stage and saturates to a constant value after 0.6 minutes (Figure 2.18 b). Assuming that the flux of particles to the surface is constant, it suggests that the sticking coefficient is initially lower. This assumption may not be entirely justified as plasma is out of equilibrium in the first seconds of polymerisation and it may contribute to the change in the deposition rate. Waiting until the plasma is in equilibrium before coating the substrates could improve the reliability of the above-reported results.

Working on the above-mentioned C_2H_4/NH_3 plasma, Hegemann and coworkers noticed that the coating left in water detaches from the silicon, yet a few nanometres thick films remain on the substrate [160] (Figure 2.18c). The authors assign the lower solubility of this interface layer to the enhanced cross-linking due to the energy excess provided by the particles impinging from the plasma that do not stick to the surface. Initially, the sticking coefficient is low, so many particles release energy to the surface when bouncing off. As the film grows thicker, more particles stick to the film and are available to absorb the energy from the molecules that do not stick.

To sum up, the film grown in the early stages exhibits unique properties due to its interaction with the surface that affects the sticking coefficient and thus the energy released to the surface by the impinging molecules. Different cross-linking degrees in the early stages and the interaction of

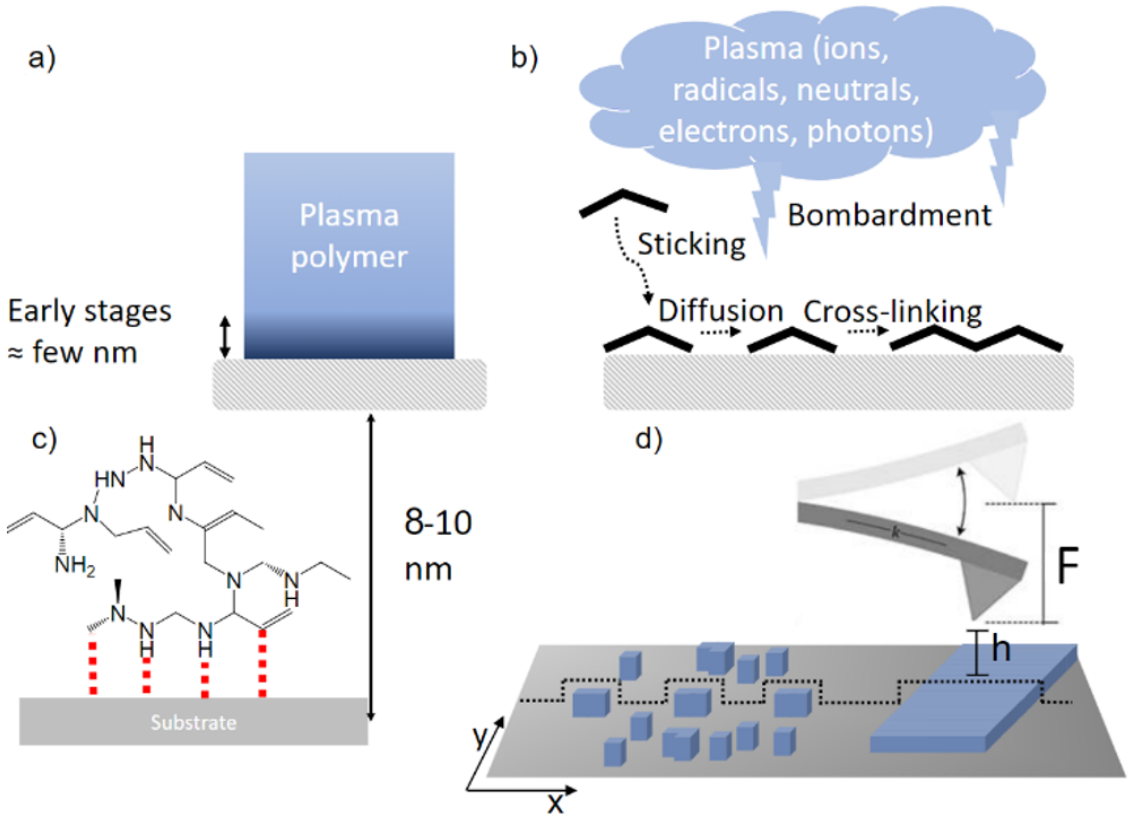

Figure 2.17: (a) The first few nm of the coating film can be considered the early stages of plasma polymerisation. (b) Sticking of a molecule, diffusion on the surface and cross-linking under energetic particles bombardment from the plasma. (c-d) Characterisation of the early stages of plasma polymerisation. (c) XPS provide information on the chemistry of the polymer such as the molecular structure, damage, and binding with the surface as sketched for an allylamine plasma polymer. (d) AFM provides information on the morphology of the polymer (h(x,y)) such as island-like growth (left) or layered growth (right), roughness, mechanical properties (F(h)), and chemistry (e.g. F(h, pH)).

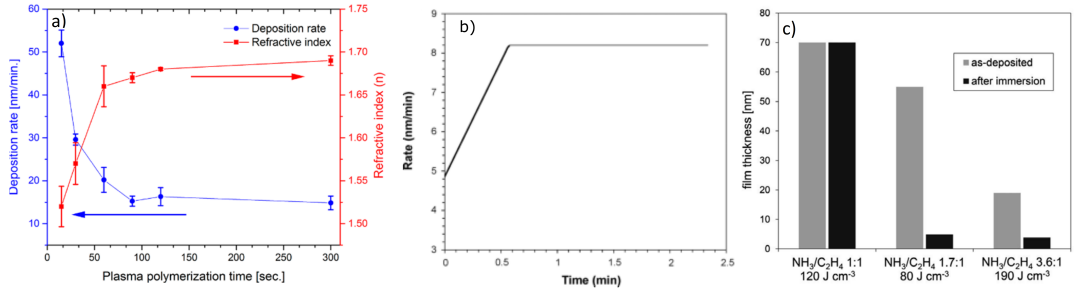

Figure 2.18: (a) Deposition rate and refractive index of C_2H_4, N_2, and Ar plasma polymer measured by spectroscopic ellipsometry at a wavelength of 630 nm. (b) Deposition rate as a function of deposition time C_2H_4/NH_3. (c) C_2H_4/NH_3 film thickness as-deposited on Si wafer and after 2 h immersion in bi-distilled water depending on the energy density during the deposition. Panels a, b, and c are reproduced from [156], [159], and [160], respectively.

the first few nanometres of the film with the surface suggest that the chemistry should be different in the interface region.

Chemical composition of plasma polymer films

X-ray photoelectron spectroscopy (XPS) is the most common averaging technique to analyse the surface chemistry of plasma polymers since the signal from the first few nanometres of the material is detected. Moreover, XPS conveys information on the chemical environment of molecular species and is generally a non-invasive technique. Furuya and coworkers highlighted the difference in the chemistry of 70 nm thick perfluorocarbon plasma polymers deposited onto Si, Ag and Al (Figure 2.19a) [168]. On Si, the C-CF_x peak is relatively intense, suggesting that the main alkyl backbone has several branches. A strong CF_3 signal on Ag hints at short chains terminated by a carbon atom bonded to three fluorine; while the dominating CF_2 peak on Al suggests long chains of carbon atoms. When the film is 1.4 µm thick, no difference in the XPS spectra is detected. These results show that the substrate drastically affects the chemistry in the early stages and that XPS can provide essential information. Akhavan and colleagues investigated plasma polymers' interaction with Zr, Ti, and SiO_2 surfaces, finding evidence of covalent bonds between the transition metals and the coating [156]. Indeed, the carbide (Zr-C or Ti-C) component of Zr 3d and Ti 2p peaks increases after 15 seconds of plasma polymerisation (components T_5 and T_6 in Figure 2.19c) compared to

the bare substrate (Figure 2.19b). Additionally, carbide and oxycarbide (ZrO_xC_y and TiO_xC_y) components of the C 1s spectrum (Figure 2.19d) are lower after 120 s of deposition than after 15 s, showing that the interaction takes place at the film-substrate interface. Paulino and coworkers further prove the different chemical compositions of the first layers of triethyl phosphate (TEP) films. They performed XPS measurements of coatings deposited on glass, aluminium oxide, and nylon6,6 before and after 1 hr immersion in water [161]. The polymer detaches from the glass (silicon oxide) while only a thin layer remains on the aluminium and does not detach from nylon. The evidence suggests that the bonding with each substrate is different. These observations agree with other studies of TEP immersed in solvents revealing weak physisorption on silicon oxide [169] and metal-ligand interaction on metal oxides. Additionally, the coating on aluminium oxide has a soluble layer on top of an insoluble one hinting at a chemical gradient in the sample, according to reference [160].

Even when no covalent bonds with the surfaces are detected, remarkable differences in the XPS peaks may occur. References [122] and [123] describe the polymerisation of N-containing monomers (n-heptylamine and allylamine) on gold and self-assembled MUA as well as a silicon wafer, respectively. The absence of a chemical shift in the Au 4f, Si 2s, and Si 2p peaks points to a weak coating-substrate interaction, while it is impossible to identify any MUA-polymer interaction. Nonetheless, the N 1s peak evolves as the deposition time increases from a few to tens of seconds on all the substrates (Figure 2.19e-g). A handful of initially detected chemical environments disappear in thicker films. In addition, the substrates affect the chemical environments as NO_x appears at 407 eV on silicon (Figure 2.19e), isocyanide at 397.6 eV on Au (Figure 2.19f) and quaternary amines/protonated amines at 401.6 eV on Au and MUA (Figure 2.19f-g). Interestingly, there is no evolution of the C 1s peak of O-containing monomers (acrylic acid and propionic acid) on gold and MUA with the deposition time, suggesting that they are unaffected by the substrate [123]. As previously noticed, plasma being out of equilibrium in the first few seconds after the ignition could account for some differences in the XPS spectra in the early stages in the absence of covalent bonds with the substrate. Indeed, Li and colleagues noticed that the substrate-polymer interface has different chemical properties from the top layer of the same film of di(ethylene glycol) dimethyl ether when the pressure changes by 40 Pa in the first ten seconds [162].

In conclusion, the chemistry of plasma polymers may be altered in the early stages, likely due

to the film-surface interaction as shown by the results of n-heptylamine and allylamine on different substrates. To further characterise the early stages of plasma polymerisation, information about the local nanoscale properties of the surface, such as structure, morphology, chemistry, and electronic properties, is required. As discussed below, scanning probe microscopy (SPM) is ideally suited for this task.

Nanoscale characterisation with scanning probe microscopy

The interplay between molecule and substrate chemistry directs the coating morphology in a complex way. Monomers, impinging on the substrate, are physisorbed or chemisorbed onto it. They diffuse at a rate (mobility) dictated by the strength of the interaction with the substrate. Radicals cross-link with diffusing or impinging ones via radical polymerisation or fragmentation-recombination, forming the film. Additionally, energetic particles bombarding the surface activate adsorption sites and provide energy to overcome diffusion barriers and intensify coupling, enhancing sticking, diffusion and cross-linking. SPM, and particularly AFM can provide qualitative and quantitative information about the structure and morphology of plasma polymers on a wide variety of surfaces (metal, semiconductor, insulators).

AFM is ideally suited for nanoscale characterisation, capable of resolving structures down to single molecules [164, 165]. However, and somewhat surprisingly, there is scant literature on this topic, which is reviewed below. The role of the surface in the morphology of plasma polymers is first analysed, then the role of the monomer chemistry is presented; finally, the effect of plasma parameters on the roughness is discussed. AFM measurements defy the commonly held view that plasma polymerisation is surface-independent. For example, perfluorocarbon plasma polymer morphology is smoother on Ag and Al than on Si in the early stages, but there is no remarkable difference when the films are 1.4 µm thick [168]. Additionally, Hegeman and coworkers ascribe increased roughness of 5 nm C:H:N coatings on PET than on Si wafer to the lower sticking coefficient of the latter substrate that causes a higher degree of cross-linking [160]. This example highlights not only the relevant role of the interplay between the energetic particle bombardment but also the substrate chemistry in the early stages of plasma polymerisation [160]. C_2H_4, N_2, and Ar polymerisation on Zr, Ti and silicon point out the role of the adsorption onto the substrate. AFM measurements reveal a smooth polymeric layer on the transition metals (Figure 2.20a,b), likely caused by the high density of nucleation sites due to carbide and oxycarbide bonds between the substrate and

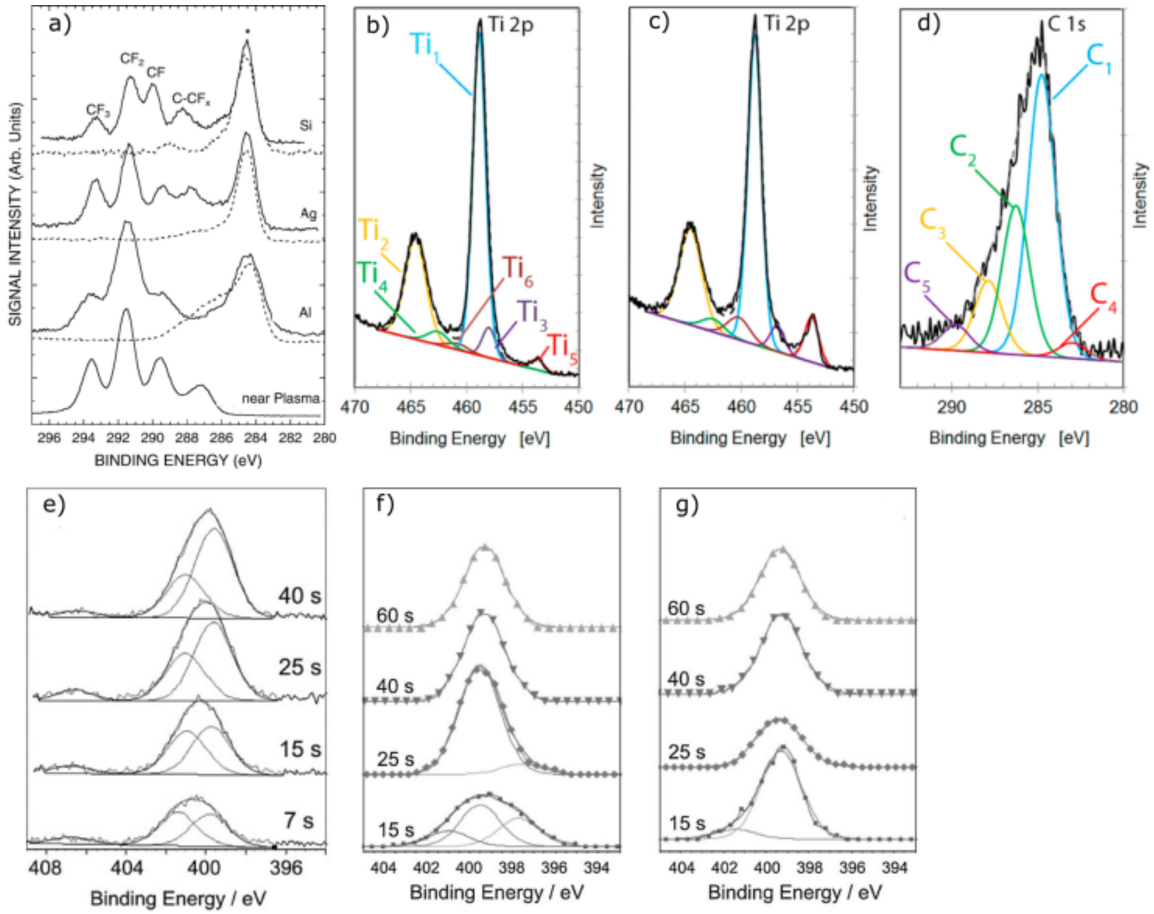

Figure 2.19: High-resolution XPS measurements collected (a) in the C 1s region of perfluorocarbon coatings deposited 50 cm (Si, Ag, Al) and (near plasma) 10 cm from the plasma. High-resolution XPS measurements of C_2H_4, N_2, and Ar collected in the Ti 2p region after (b) 15 and (c) 120 s of polymerisation fitted with three doublets: Ti_1: $(TiO_2)_{3/2}$, Ti_2: $(TiO_2)_{1/2}$, Ti_3: $(TiO_x)_{3/2}$, Ti_4: $(TiO_x)_{1/2}$, Ti_5: $(Ti/Ti\text{-}C)_{3/2}$, and Ti_6: $(Ti/Ti\text{-}C)_{1/2}$. (d) C 1s environment fitted by five components: C_1: C-C/C-H, C_2: C-O/C-N, C_3: C=O/N-C=O, C_4: TiC, and C_5: titanium oxycarbides. High-resolution XPS measurements of n-heptylamine collected in the N 1s region for different deposition times on (e) a silicon wafer, (f) gold, and (g) MUA self-assembled monolayer with the following components: isocyanide at 397.6 eV, amine/imines/amides at 399.7 eV, quaternary amines/protonated amines at 401.6 eV, NO_x at 407 eV. Panels a, b-d, e and f-g are reproduced from [168], [122], and [123], respectively.

the coating. On the other hand, the polymer forms 6 nm high islands on silicon (Figure 2.20c), suggesting that the cross-linking is more favourable than the adhesion to the surface. Indeed, no chemical bond with the surface was identified by XPS. Le and coworkers studied the substrate role in maleic anhydride film by depositing it onto pristine (hydrophilic), hydroxyl-functionalised (hydrophilic), and alkyl-functionalised (hydrophobic) silicon oxide layers (Figure 2.20d) [163]. The authors attribute the smooth morphology to the affinity of hydrophilic maleic anhydride with SiO_2 and a hydroxyl-functionalised surface that enhances the adsorption. Conversely, maleic anhydride forms small circular clusters on the hydrophobic surface that merge into rod structures after 2 minutes of polymerisation. In this case, the lack of nucleation sites and weak adhesion to the surface favour diffusion and cross-linking. After the early stages, the effect of the surface on the morphology could be negligible [168] or prime the growth of the successive layers as shown in reference [163]. Michelmore and colleagues studied the role of the monomer in the early stages by depositing n-heptylamine (saturated) and allylamine (unsaturated) onto a silicon wafer [122]. While the former grows into clusters 10-12 nm thick (Figure 2.20e, f) that merge into a uniform layer (Figure 2.20g), the latter grows layer-by-layer from the beginning (Figure 2.20h-j). Allylamine double bond could account for the different morphology since it could increase the cross-linking degree due to radical polymerisation [122]. In addition, the long, hydrophobic carbon backbone of n-heptylamine could reduce the nucleation density on the hydrophilic silicon surface, according to reference [163].

The difference in the plasma parameters is also responsible for varying morphologies in the early stages. Indeed, allylamine films (8-10 nm thick) are rougher when the pressure of the gaseous monomer increases from 25 to 100 Pa [170]. Furthermore, Akhavan and colleagues noticed that increasing the energy per monomer in a 1,7-octadiene plasma causes a roughening of the coating surface in the early stages due to the bombardment of energetic particles (Figure 2.20k-n) [155].

Brioude and coworkers exploited the vast characterisation possibility offered by AFM to study maleic anhydride chemistry [158]. They analysed the force experienced by the tip coated by the same polymer when approaching and retracting from the surface in a wide pH range (chemical titration force) to determine the acid dissociation constant of the two carboxylic groups in the monomer (pK_{a1} and pK_{a2}). They discovered that Pk_{a1}= 4 and Pk_{a2}=9.5 after 2 min of plasma polymerisation (Figure 2.20o).

In conclusion, the examples confirm that AFM is suitable to characterise the morphology of

plasma polymers in the early stages. It provides evidence that the interplay between substrate and monomer chemistry as well as the energetic particle bombardment influence the coating morphology and roughness. However, some degree of post-deposition reconstruction may affect the results, as suggested in references [122, 156]. Yet, AFM is a versatile technique that can provide information beyond morphology, a still underexplored area of research.

Outlook

In the last 15 years, significant but non-systematic evidence of the difference between the early and subsequent stages of plasma polymer in terms of growth rate, chemistry and morphology emerged. Indeed, the change in the deposition rate suggests that the sticking coefficient varies as monomers initially land on the surface and then on the pre-deposited polymeric layer, resulting in different properties. XPS further proves this point as the adsorption of monomers on the surface affects their chemistry, highlighting chemical bonding at the interface or the presence of several chemical environments. Additionally, AFM reveals a variety of morphologies and roughnesses in the early stages. They emerge from the complex interplay between surface and monomer chemistry that determines the sticking coefficient, diffusion, and cross-linking. Moreover, plasma parameters affect the monomer flux to the surface and the energetic particles bombardment, which are involved in the polymer formation, too.

A critical literature review shows that there are some shortcomings in the study of the early stages. First, monomer pressure may change in the early stages since plasma is out of equilibrium in the first few seconds after the ignition. Hence, the transition in the experimental conditions may contribute to the observed peculiar properties of the first few nanometres of the coatings. Exposing substrates to the plasma only when pressure is stable could rule out this contribution. Second, the assessment of the morphology from AFM scans might not be straightforward as surface reconstruction may occur after the deposition [122, 156]. Third, ellipsometry is not suitable for measuring thicknesses in the early stages, especially when coatings are significantly rough or composed of islands. Indeed, the average thickness measured in a 1 mm^2 area may not represent well the underlying distribution due to substantial variance.

In conclusion, combining plasma polymerisation with nanotechnology opens the possibility of further tuning the coating properties, especially for bio-materials [5,171]. Producing a few nanometres thick films could further reduce energy and material consumption enhancing manufacturing

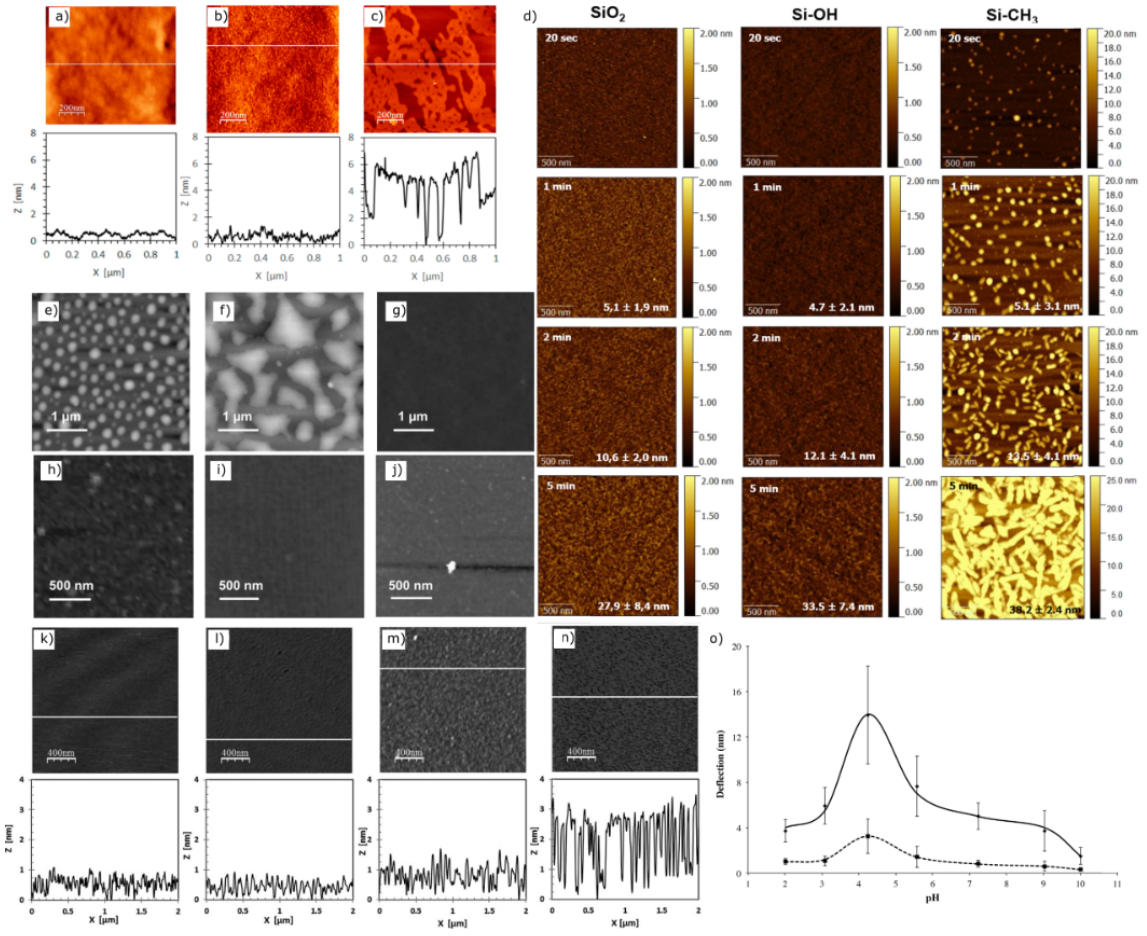

Figure 2.20: AFM topography images of C_2H_4, N_2 and Ar mixture plasma polymer on (a) titanium (b) zirconium (c) silicon wafer deposited or 15 s with a representative line profile. (d) AFM topography images of maleic anhydride plasma polymers on SiO_2, OH-terminated SiO_2 (Si-OH) and alkyl-terminated SiO_2 (Si-CH_3) polymerised for 20 s, 1, 2, 5 min with the corresponding thickness as measured by ellipsometry. AFM topography images n-heptylamine plasma polymer (e) 2.4 nm, (f) 4.2 nm, (g) 8 nm and allylamine plasma polymer (h) 1.6 nm, (i) 2.4 nm, (j) 7.5 nm thick as measured by ellipsometry. AFM topographic images of (k) silicon and 1,7 octadiene coatings on silicon polymerised for 2 minutes at (l) 0.12, (m) 0.45, and (n) 1.05 kJ cm^{-3} energy density. Chemical titration force curve of maleic anhydride plasma polymers deposited for 2 minutes. Panels a-c, d, e-j, k-n, and o are reproduced from [123, 155, 156, 158, 163], respectively.

efficiency and reducing the environmental impact. Furthermore, studying the coating-substrate interface has relevant applications in optimising the film properties, such as adhesion in liquid [160] and biological [156] environments. A set of spatially-resolved characterisation techniques is needed for thin plasma polymers. In particular, scanning probe microscopy offers a new host of possibilities to study the local morphological and nanomechanical properties of films in air or liquid [167]. Conductive AFM (c-AFM) could provide relevant information about electronic properties, while high-resolution AFM can further elucidate the structural order in the coatings. Time of flight secondary ions mass spectroscopy (ToF-SIMS) can provide punctual information about the mass composition by sampling a 2-5 nm surface layer but it is seldom used. Akhavan and colleagues discovered the surface morphological and chemical inhomogeneity in the early stages of 1,7-octadiene plasma polymers using ToF-SIMS [155].

The early stages of plasma polymerisation are still an underexplored topic. There is a significant lack of understanding and modelling waiting to be filled by experiments and simulations. This knowledge could be transferred to the rational design of functional coatings. Additionally, while thick plasma polymers have well-established applications, further research is needed to test the properties of nano-scaled counterparts and their stability over time.

Chapter 3

Materials and Methods

This chapter briefly summarises the methods used to characterise the molecular layers and atomic quantum clusters in this thesis. Section 3.1 introduces X-ray photoelectron spectroscopy (XPS) for the characterisation of surface chemistry, followed by a discussion on the normal incidence X-ray standing wave (NIXSW) in Section 3.2 to characterise the adsorption geometry. More information on both topics is available in books and articles [172–176]. Section 3.3 describes scanning probe microscopy (SPM), focusing on imaging molecular layers and soft materials using atomic force microscopy (AFM). More information is available in references [164, 165, 177, 178].

3.1 X-ray photoelectron spectroscopy (XPS)

X-ray Photoelectron Spectroscopy (XPS) is a surface-sensitive technique used to determine the elemental composition and the chemical environments of the first few atomic layers of materials. XPS was first developed in 1954 by Kai Siegbahn [179], who received the Nobel prize in 1981, and it is now a standard method to obtain qualitative and quantitative information on surfaces.

3.1.1 Working principles

XPS works via the photoelectric effect (Figure 3.1a). X-rays, with energy E_{ph}, cause the emission of electrons from an orbital. The kinetic energy K is recorded by the analyser and then converted

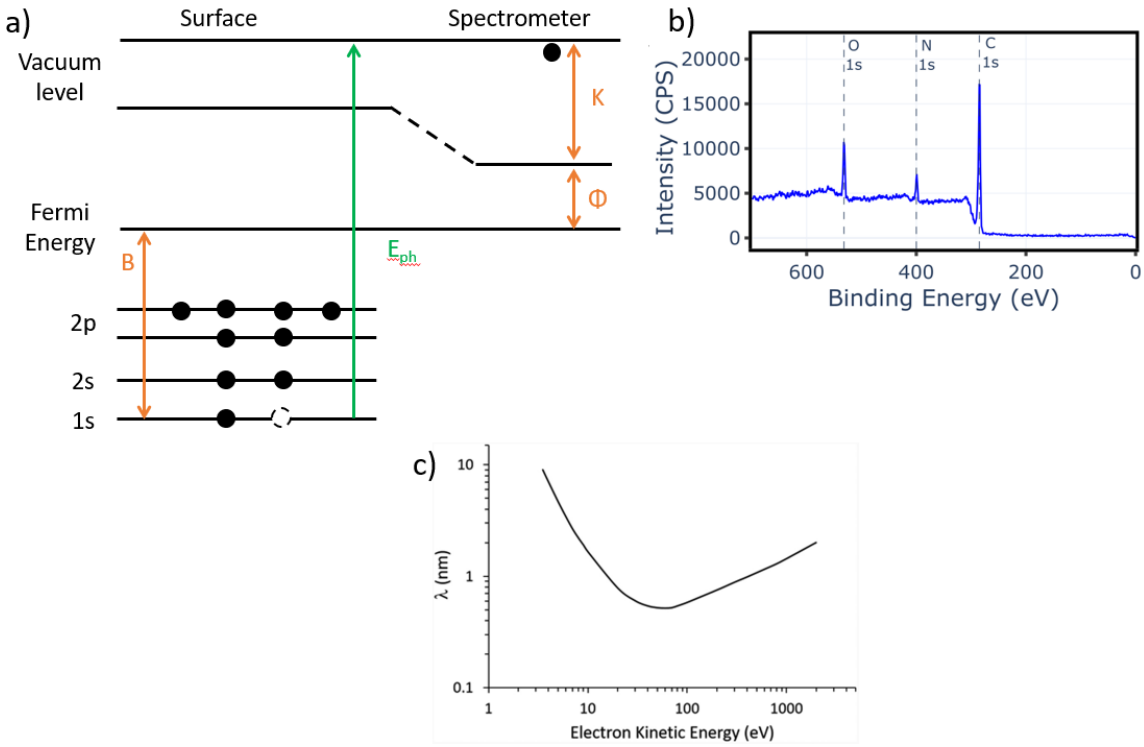

Figure 3.1: (a) Diagram to illustrate the XPS equation, including the X-ray source photon (E_{ph}), the binding energy of the electron (B), the measured kinetic energy of the electron (K), and the work function of the spectrometer (Φ). (b) Example of XPS survey spectrum of a TEMPO plasma polymer showing the O 1s, N 1s, and C 1s peaks. (c) Inelastic mean free path λ of electron versus kinetic energy. Panel c is reproduced from [173].

to the binding energy B using the conservation of energy

$$B = E_{ph} - K - \Phi, \tag{3.1}$$

where Φ, the work function of the instrument, is a constant value [173]. The binding energy is the work required to remove an electron from a specific atomic orbital of a given element to the vacuum level, therefore providing a unique "fingerprint" for the atomic species present in a material. Only hydrogen and helium are undetectable by XPS [173]. XPS can probe only the occupied electronic states up to E_{ph}. For example, the common X-ray energy used in laboratory instruments is 1486.6 eV (Al K_α) that allows the measurement of elemental core lines from 0 eV, (Fermi energy) to 1486.6 eV (E_{ph}). XPS data are a spectrum displaying the intensity (number of electrons counted by the analyser in a second) versus the electron energy, as shown in Figure 3.1b where each peak indicates the photoemission from a specific orbital such as O 1s, N 1s, or C 1s [175].

X-rays cause photoemission several µm deep in material depending on their energy, but only the electrons from the top atomic layers can escape the material without further interactions. Indeed the intensity of the unscattered electron, I, as a function of the distance from the surface z has an exponential behaviour

$$I(z) \propto e^{-\frac{z}{\lambda}}, \tag{3.2}$$

where λ is the inelastic mean free path (Figure 3.1c). λ is in the range of $1 - 3$ nm for $K = 100 - 1000$ eV, the typical kinetic energy range due to the excitation with lab-based X-ray sources. The unscattered electrons emitted within 3λ ($3 - 9$ nm) from the surface account for more than 95% of the total intensity, resulting in the surface sensitivity of XPS [172].

However, a fraction of the photoemitted electrons lose kinetic energy to the material, resulting in lower kinetic energy and thus higher binding energy. Due to the wide spread of energies, they do not appear as a single peak but contribute to the continuous background. For example, the background in Figure 3.1b increases sharply on the left-hand side of the C 1s peak due to the inelastic scattering of the carbon electrons.

The area under the peaks, A, conveys information on the concentration of each element, c_a, as it reads

$$A = j c_a \sigma \lambda H, \tag{3.3}$$

where j is the incoming flux of photons, λ is the mean free path of the electron, and H is the transfer function of the instruments used for the measurement. The photoemission cross-section or sensitivity factor, σ, is the probability of the photoemission of the electron from a given orbital of a given atomic species by an X-ray with energy E_{ph}. The sensitivity factor is commonly referenced to the C 1s by assuming that σ_{C1s} is unity and all the others are multiples of the carbon sensitivity factor (e.g. $\sigma_{N1s} = 1.8$). In this thesis, the sensitivity factors in the Casa XPS software library (Casa Software Ltd, UK) are used. As the sensitivity factors and the inelastic mean free path are estimated from available data of similar materials, the ratio between the area under two peaks is proportional to atomic concentration [175]. It is thus possible to determine the relative abundance of all the elements on the surface down to 0.05% [172]. For example, the O, N, and C relative concentrations in Figure 3.1b are 10.47%, 82.30%, and 7.23%, respectively.

3.1.2 Chemical shifts in core level spectra

XPS is highly sensitive to the bonding environment of the elements as the interaction between atoms changes the electronic structure of the valence orbitals which, in turn, affects the core levels [174, 175]. This phenomenon, known as the chemical shift, is shown in Figure 3.2 for the N 1s and C 1s peaks of (2,2,6,6-tetramethylpiperidin-1-yl)oxyl (TEMPO). In the case of carbon, the chemical shift is related to the electronegativity of the atoms bonded to it as they withdraw the electron density reducing the electron-electron repulsion and thus increasing the binding energy. Figure 3.2b shows that the binding energy increases as the atom bonded to carbon becomes more electronegative from 285.0 eV for C-C/H component to 286.0 eV for C-N, to 286.5 eV for C-O, to 289.0 eV for O-C=O, to $293 - 294$ eV for CF_3. It should be noted that the relationship between binding energy and electronegativity is not always applicable. For example, the valence electrons are often screened from the core electrons in heavy atoms. Similarly, the binding energy of transition metals is primarily influenced by their oxidation state. As the oxidation state increases, the binding energy also increases due to the loss of electron density. However, a transition metal with the same oxidation state but bonded to different atoms can give rise to different peak shapes, as for Ti, which is not explained by this simple model [180].

Not only chemical shifts but also interaction within an atom or material can cause a peak to shift or split. The photoemission of an electron from a closed shell leaves a hole behind, resulting

in spin-orbit coupling. The interaction splits the energy level into multiple states, detected in the XPS spectrum as multiplets. The intensity of these peaks is proportional to the j quantum number, $2j + 1$. For example, the 2p orbital is split into a doublet consisting of the $2p_{1/2}$ and $2p_{3/2}$ levels with a fixed intensity ratio of $2\frac{1}{2} + 1 : 2\frac{4}{2} + 1 = 2 : 5$.

Furthermore, the photoelectron can lose a small but finite amount of kinetic energy to the surrounding material by exciting another electron to an empty state, called the shake-up process, or ejecting another electron, called the shake-off process, or exciting quasi-particles, such as plasmons in metals. The resulting peaks appear at higher binding energies with respect to the main peak due to the loss of kinetic energy. In metals, photoelectrons can lose part of their kinetic energy by exciting valence electrons to a continuum of higher energy states in the valence band resulting in an asymmetry of the peak at higher binding energy.

Identifying shifts often relies on fitting functions representing each component that is assumed to be part of the peaks [174]. A convolution between a Lorentzian and Gaussian function, namely the Voigt function, is commonly used for peak fitting [174]. The Lorentzian function describes the broadening of the electron energy in the orbitals due to the finite lifetime of the core hole [181]; the Gaussian function accounts for the spread of the X-ray energy depending on the instrument used, namely monochromaticity. In this thesis, the components of the peaks are fitted to asymmetric Voigt functions using CASA XPS after linear or Shirley background subtraction [182].

3.1.3 Auger peaks for chemical analysis

The Auger effect refers to the emission of an electron during the relaxation of atoms from an ionised state in a three-body process as shown in Figure 3.3a [173]. The photoemission of a first electron from a core level leaves a hole behind that is filled by a second electron from a higher orbital. The energy released in this process causes the emission of a third electron of an even higher orbital, namely the auger electron. As Auger electrons come from outer orbitals, they are generally more sensitive to the chemical bonding of the element, as shown in Figure 3.3b for copper [183]. In the example in Figure 3.3a, the X-rays cause a hole in the K level that is filled by an electron in the L_1 shell causing the emission of another one from the L_3 orbital. The kinetic energy of the auger electron K depends only on the binding energy of the orbitals involved, it is thus constant and

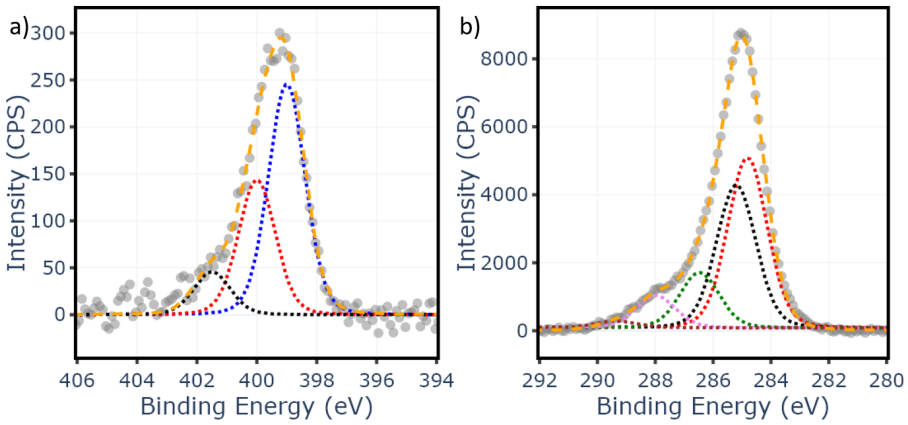

Figure 3.2: (a) N 1s core-level photoemission spectrum of TEMPO plasma polymer fitted to three components NH_2^+ (black), NO (red) and N (blue). (b) C 1s core-level photoemission spectrum of TEMPO plasma polymer fitted to five components C-C/H (red), C-N (black), C-O (green), C=O (pink), O-C=O (purple).

reads:

$$K = B_K - B_{L1} - B_{L3}. \tag{3.4}$$

3.2 Normal Incidence X-ray Standing Waves (NIXSW)

The need for characterising surfaces with atomic precision led to the development of analytical techniques taking advantage of the surface's long-range order, such as low-energy electron diffraction or surface X-ray diffraction. However, these techniques fail in disordered systems, such as molecular adsorbates, or when studying heterogeneous catalysis. These limitations led to the development of the normal incidence X-ray standing wave (NIXSW), a tool that takes advantage of bulk periodicity. NIXSW combines X-ray absorption with X-ray photoemission spectroscopy or Auger spectroscopy to provide chemically-resolved and surface-sensitive information on the adsorption geometry with picometer precision [176, 184, 185]. The implementation of NIXSW usually requires synchrotron light, which is described below.

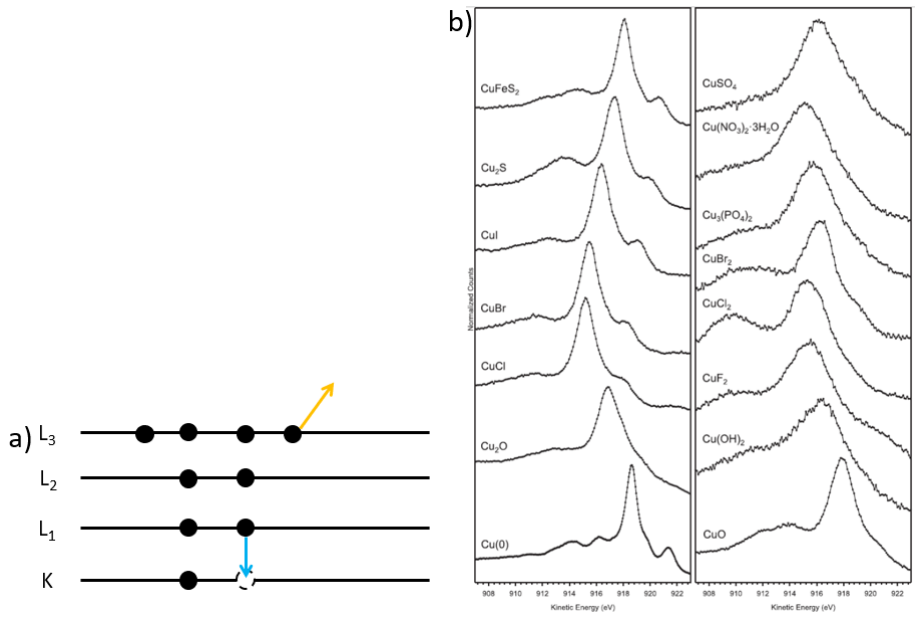

Figure 3.3: (a) Diagram of KL_1L_3 Auger peak showing a hole in the K level that is filled by an electron in the L_1 shell causing the emission of another one from the L_3 orbital. (b) LMM Auger peaks of copper in different compounds. Panel b is reproduced from [183].

3.2.1 Synchrotron light

A thorough discussion of synchrotrons, though fascinating, is beyond the scope of this thesis (see reference [186]), so only the working principle is discussed. Synchrotrons are circular particle accelerators where electrons are accelerated in a radio-frequency cavity to a speed, v, close to the speed of light, c. Magnets force the electrons in a circular trajectory so that they remain in the accelerator, creating a high-energy and high-flux beam of particles. In synchrotrons, X-rays are generated in an undulator via the bremsstrahlung. The magnets of the undulator generate a spatially periodic field perpendicular to the trajectory of electrons, periodically accelerating the electrons. The wavelength of the light they emit is proportional to the periodicity of the magnetic field divided by $2\gamma^2$ where $\gamma = \frac{1}{\sqrt{1-\frac{v^2}{c^2}}}$. It is possible to select an X-ray energy from approximately 1 eV to approximately 20 keV by changing the magnetic field periodicity [172]. Compared to lab-based sources, the energy is changeable, the X-ray flux is higher, and the X-ray energy spread is lower, making synchrotrons the ultimate X-ray source.

Three factors contribute to the broadening of spectral lines in XPS: the energy spread of the X-rays, the resolution of the instrument, and the broadening of the energy level. In synchrotrons, the energy spread of X-rays can be as low as 0.1 eV, compared to 0.85 eV of conventional Al K_α lab-based sources [172], due to the different way to excite the X-rays and possibility of filtering out more photons with the monochromators given the high incident flux. Furthermore, these large facilities are commonly equipped with excellent analysers, further improving the energy resolution. An example of the improvement of the XPS spectra quality is shown in Figure 3.4 where the components of the N 1s core-level spectrum are resolved with the synchrotron light and not with the Al K_α lab-based source.

In the context of this thesis, synchrotron radiation was used as a suitable method to collect normal incidence X-ray standing wave (NIXSW) data to study the absorption geometry of clusters of five copper atoms. Indeed, the possibility of changing X-ray energy and the low energy spread of the photons are ideal for NIXSW compared to lab-based sources. NIXSW practical implementation and data analysis are so complex that the expertise is available only in a few synchrotrons around the world. The data discussed in this dissertation has been acquired at the Diamond Light Source (UK), beamline I09. The energy of the electron in the ring, excited by a 499.680 MHz radiofrequency, is 3 GeV [187]. The undulators of beamline I09 produce soft and hard X-rays from 100 eV to 20 keV [187].

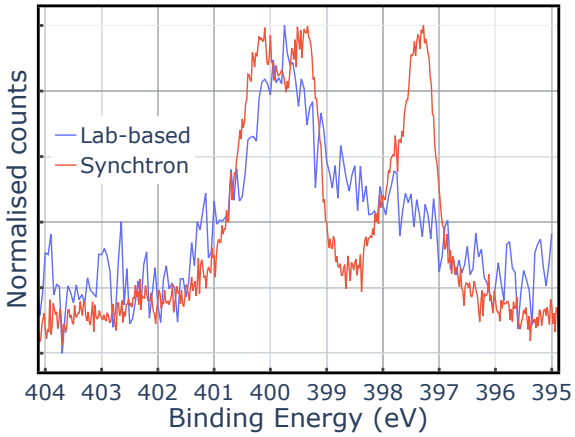

Figure 3.4: N 1s core-level photoemission spectrum of tetra(4-bromophenyl) porphyrin molecules acquired with lab-based Al K_α and synchrotron X-ray sources at $E_{ph} = 600\,\text{eV}$.

3.2.2 Working principles of NIXSW

X-ray standing waves arise from the interference between the normally incident radiation and the wave reflected from the bulk of a perfect monocrystal when the light wavelength matches the crystal layer spacing d (Figure 3.5a). This condition, called Bragg reflection or diffraction, is met only at a specific photon energy, Bragg energy, under the assumption of no absorption. In a more realistic situation, the standing wave field exists in a small but finite energy range due to multiple scatterings (dashed line in Figure 3.5b). On the low-energy side of the reflectivity range, the wave has a nodal plane on the atomic sites so that no absorption takes place (0.0 Å line in Figure 3.5b). On the opposite side of the energy range, the antinodal planes align to the crystal layers minimising the absorption of X-rays [176]. As the energy sweeps through these extremes, the absorption decreases to zero and reaches a maximum. Outside the reflection range, there is no significant change in absorption and the reflectivity is normalised to unity.

An interstitial layer in the middle of two crystal planes exhibits a reversed absorption profile (1.0 Å line in Figure 3.5b). The interstitial layer lies in an antinodal plane of the X-ray field at the lower energy side of the range corresponding to a maximum in absorption. As the photon energy increases, the absorption reaches zero. It is thus possible to reconstruct the position of the interstitial layer compared to the crystal spacing from the absorption versus photon energy profile.

The X-ray absorption can be detected through the photoemission or Auger emission, providing

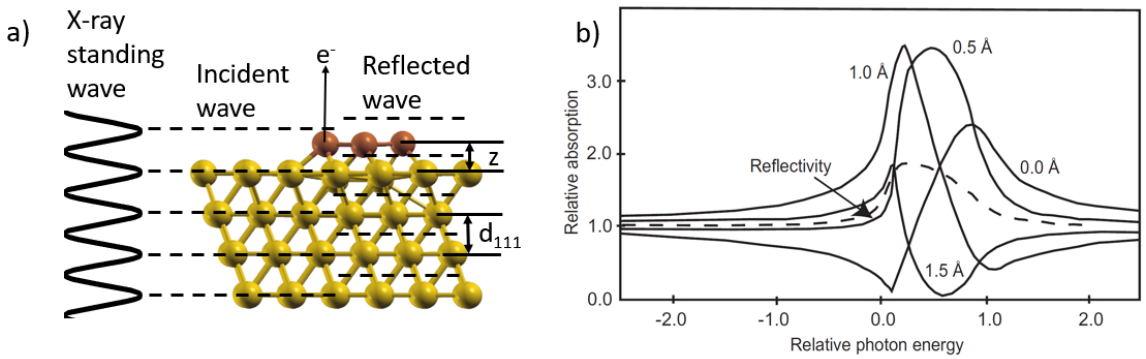

Figure 3.5: (a) Diagram of NIXSW showing the X-ray standing waves field created by the superposition of the incident and reflected wave on Au(111) with an adsorbate on top of the surface.(b) Simulated photoemission intensity for a layer of adsorbate in different coherent positions. Panel b is reproduced from [176].

chemical and surface sensitivity to the technique. It is thus possible to measure the position of a given chemical species with respect to the surface (Figure 3.5b) once the correction for the angular dependency of the emission is applied (further information on this topic is available in reference [188]). Being a diffraction technique, NIXSW conveys information on the distribution of atoms in space. Indeed, the photoemission intensity versus the photon energy curve is the Fourier transform of the absorbate distribution in space $\rho(r)$:

$$f_H e^{\frac{i2\pi p_H}{d}} = \int_0^d \rho(r) e^{\frac{i2\pi z}{d}} dz \tag{3.5}$$

where p_H is the coherent position and f_H is the coherent fraction. From the coherent position, the position of the absorbates is derived

$$z = d \cdot p_H + n \cdot p_H \qquad n = 0, 1, 2, 3, ... \tag{3.6}$$

The coherent fraction represents the fraction of elements in the same position. The value ranges from 0 to 1, corresponding to all the adsorbates being at different or identical distances from the crystal, respectively. When the same chemical species exhibit distinct adsorption geometries, the coherent fraction and position measured are the sum of different vectors in the Fourier space. In this case, the derivation of the adsorbate position from the coherent position is not straightforward due to the interference pattern and assumptions are made to reconstruct $\rho(z)$.

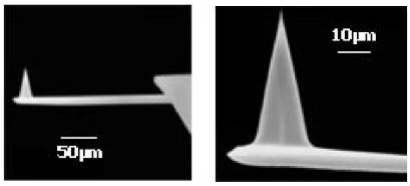

Figure 3.6: SEM image of an AFM tip and cantilever (left) and a zoom-in of the tip (right). The image is reproduced from [191].

3.3 Scanning Probe Microscopy and Atomic Force Microscopy

Scanning probe microscopy (SPM) is a widely-used tool in nanoscience and nanotechnology to analyse the surface of materials down to the atomic level. It works by sensing the local interaction between a surface and a probe. The first breakthrough happened in 1982 when Binning and Rohrer invented the Scanning Tunnelling Microscope (STM) [189]. This instrument images the tunnelling current between a metal tip and a conductive surface. As STM is limited to conductive samples only, Binnng and Gerber designed the Atomic Force Microscope (AFM) four years later [190]. This instrument senses the force between a surface and a probe at the atomic scale. AFMs are nowadays widely used for their versatility and adaptability. Furthermore, the probe can be modified to detect specific interactions, such as electric, magnetic, and chemical forces.

3.3.1 Working principles of AFM

AFM consists of mapping the local properties of a surface through the interaction with the edge of the tip (a few nm) hanging from an elastic cantilever (Figure 3.6). AFM is based on a feedback system to keep a variable constant by adjusting another one, resulting in a map of the latter. For example, the force acting on the tip is kept constant by changing the distance from the surface, resulting in the topography map.

The first step in AFM measurement is sensing the force acting on the tip. The most common approach is measuring the bending of the cantilever Δz caused by the force acting on the tip from Hooke's law:

$$F = -k\Delta z, \tag{3.7}$$

where k is the cantilever spring constant. The tip and the cantilever displacements are at the

nanometer scale, so the issue of measuring such small displacements arises. The most common configuration exploits the reflection of a light beam onto a detector (Figure 3.7a). A laser is positioned at the end of the flexible cantilever and is reflected onto a quadrant photodiode detector (Figure 3.7b). The beam activates one photodiode, and the current flow is detected. As the tip-sample interactions are negligible when the tip is far from the surfaces, the cantilever reflects the beam in the centre of the detector. When the tip approaches the surface, the forces cause the cantilever to bend (eq. 3.7). The reflected beam hits a different part of the detector, causing a current to flow (Figure 3.7b). The out-of-plane forces (z-axis) cause a difference between the signal of the two topmost photodiodes and the other two. The in-plane interactions torque the cantilever, inducing a difference between the current of the right and left photodiodes.

A feedback system enables the control of the interaction. In the previous example, the force is kept constant by adjusting the tip-surface distance. A voltage signal, controlled by the detector current, drives the piezoelectric scanner that moves the sample closer or apart from the surface, as shown in Figure 3.7b.

In contact mode, the deflection of the cantilever is kept constant through a feedback system that regulates the tip-surface distance. In contrast, the addition of a piezoelectric motor to drive the cantilever motion enables the non-contact (dynamic) mode where the variables are the resonant frequency and oscillation amplitude.

3.3.2 Forces involved in AFM

Figure 3.8a summarises the most common forces to consider when studying AFM dynamics. There is a long-range attraction between the tip and the surface due to van der Waals forces, counterbalanced by the short-range repulsion caused by the electrons overlapping. These interactions are the most important factors involved in high-resolution AFM. Once the tip is in contact with the surface, adhesion forces arise due to the sample's response to the deformation induced by the probe. This enables the measurements of the nano-mechanical properties of the surface as discussed in further detail in reference [178]. Additionally, as a layer of water covers the samples in ambient conditions, the tip experiences the capillary force of the liquid with two consequences. First, the force drags the tip toward the surface during the approach causing the snap into contact when it exceeds the restoring elastic force of the cantilever. Second, additional energy is needed to retreat the tip from the surface due to the formation of a meniscus between the surface and the tip, resulting in a

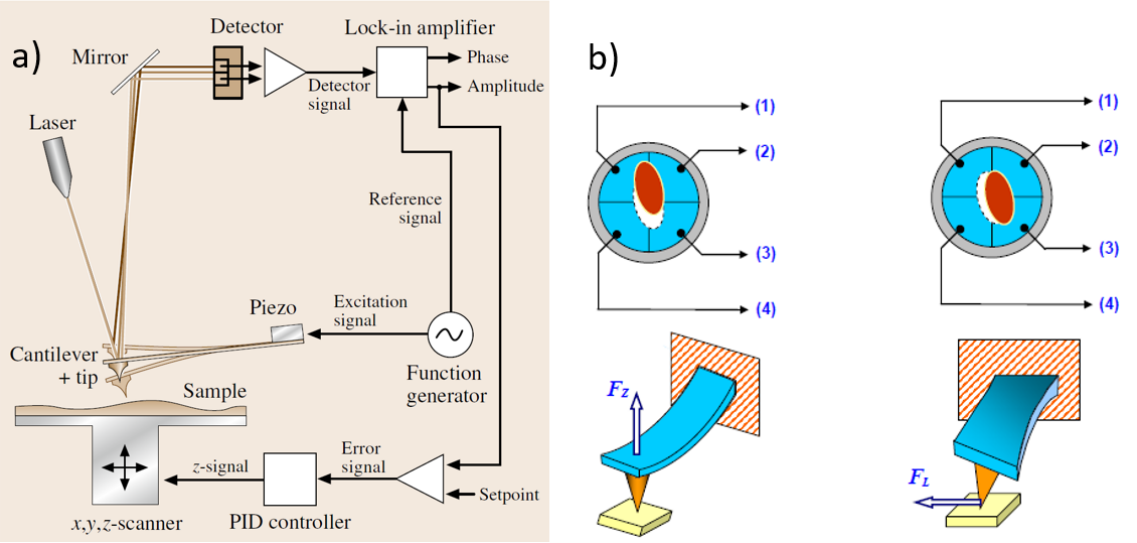

Figure 3.7: (a) AFM setup consists of a tip connected to a cantilever whose bending is measured by the detector. Piezos, connected to the scanner and the cantilever, control the sample-tip and cantilever motion, respectively. The feedback electronics connected to the AFM keep the system stable during the measurements. (b) Schematic representation of the laser and the detector when an out-of-plane (left) and in-plane (right) force acts. The four photodiodes are labelled 1,2,3 and 4. Panels a and b are reproduced from [191] and [192], respectively.

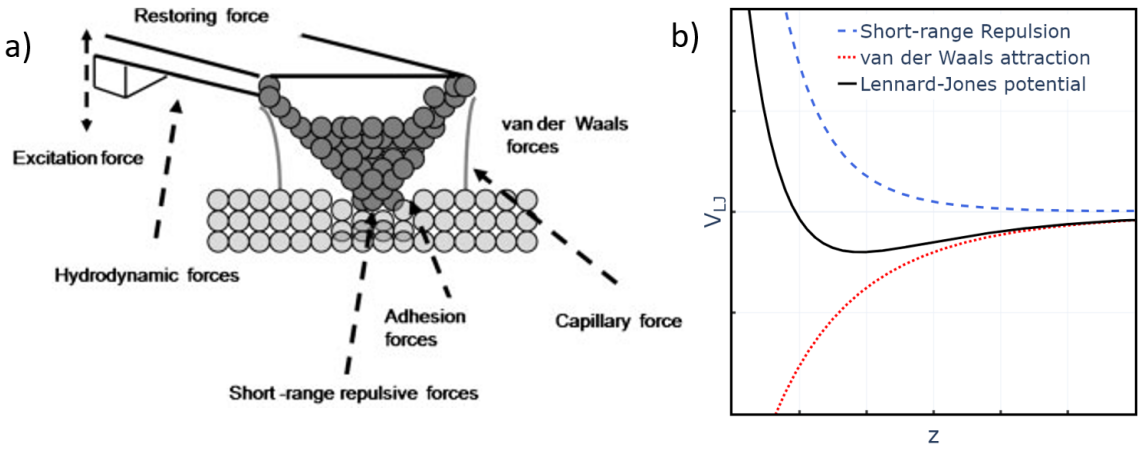

Figure 3.8: (a) A schematic description of the forces involved in AFM operations and measurements. (b) Lennard-Jones potential, V_{LJ}, as a function of the tip-surface distance z. Panel a is reproduced from [177].

hysteresis phenomenon between approach and withdrawal. Though the capillary forces are relevant to interpret the forces detected using an AFM in air, it disappears when the cantilever is immersed in a liquid or kept in a vacuum.

In non-contact AFM, the excitation force driving the cantilever and the hydrodynamic damping adds further complexity. The sum of these forces equals the cantilever restoring elastic force and can thus be measured.

The dominating interactions between the tip and surface at nanometric separation are the attractive van der Waals forces and the ionic and Pauli short-range repulsion. The former derives from the dipole-dipole, dipole-induced dipole, and induced dipole-induced dipole interactions [22]. While van der Waals forces are always attractive and drag the tip toward the surface, the overlapping of electron shells causes short-range repulsion due to the electrostatic interaction and the Pauli exclusion principle. The sum of these interactions as a function of the distance z is modelled by the Lennard-Jones potential (Figure 3.8b) with a well-depth ϵ and zero-potential distance σ:

$$V_{LJ} = \epsilon[(\frac{\sigma}{z})^{12} - 2(\frac{\sigma}{z})^{6}]. \tag{3.8}$$

van der Waals forces co-exist with other long-range interactions. In ambient conditions, the probe interacts with the water layer that condenses on the surfaces. Furthermore, the medium

affects the motion of the cantilever in non-contact AFM as it damps the oscillations or can screen the electromagnetic interactions.

3.3.3 AFM modes

Contact mode

In contact mode, the force between the tip and the surface, or their relative distance, is kept constant by adjusting the other. In the former case, the relative distance between the tip and the surface z must change locally $z = z(x, y)$. The value of z depends on the voltage of the feedback electronics required to keep the force constant. In the latter case, z is kept constant through the feedback system to keep the out-of-plane current at a fixed value. As such, the force acting on the tip can be locally computed $F = F(x, y)$.

The tip can easily be damaged or broken due to surface-tip collisions in contact mode measurements on rough surfaces. Additionally, the force applied might damage soft samples and the molecular layers studied in this thesis.

Non-contact mode

Non-contact mode measurements overcome the contact mode issues by oscillating the tip away from the surface. However, the mathematical description of the system becomes even more complicated since the force depends on the displacement of the cantilever that changes over time. In the non-contact AFM (NC-AFM) setting, frequency and amplitude modulation modes proved suitable for molecular imaging as the lateral resolution is enhanced by the absence of contact with the surface [164,193,194]. However, the time scale involved in the change of the amplitude in a vacuum makes amplitude modulation (AM-AFM) impractical for high-resolution imaging. The tip and the elastic cantilever form a complex oscillating system defined by a precise resonance frequency that depends on the geometry and physical properties of the system. So, detailed modelling of the system is required to compute it. This is a challenging mathematical problem as the resonance frequency depends on the Young's modulus, the cross-section, the density and the inertia moment of the cantilever.

The frequency modulation mode consists of measuring the shift in the tip-cantilever resonant frequency caused by force acting on it while keeping the amplitude constant through the feedback

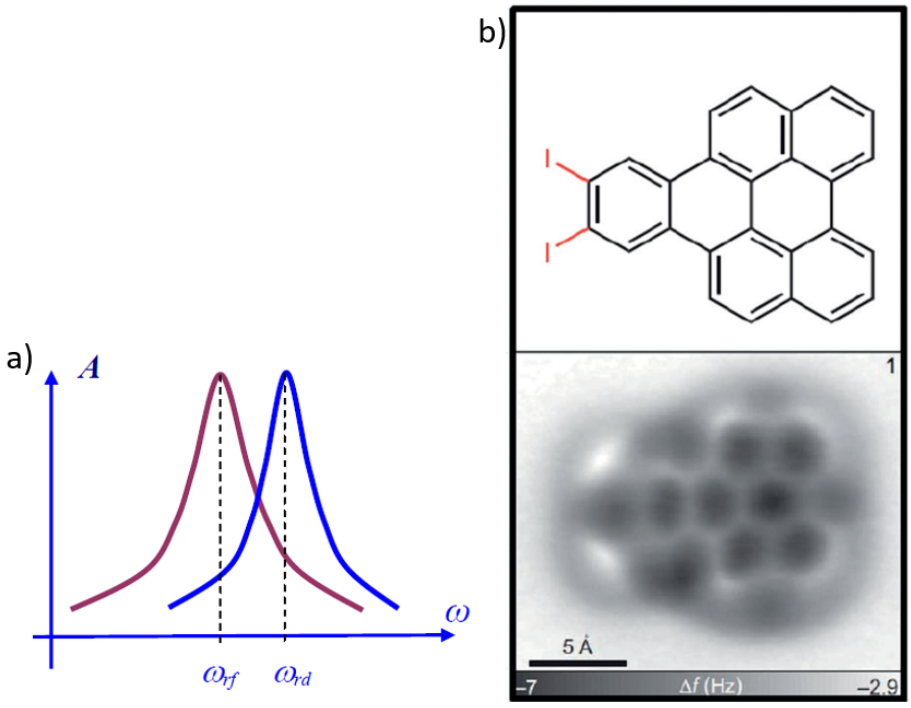

Figure 3.9: (a) The Lorentzian shape oscillation amplitude and the resonance frequency when no forces act on the tip (red) and when the tip is interacting with the surface (blue). (b) (Top) Schematic of an aryne molecule and (bottom) its frequency modulation AFM image. Panels a and b are reproduced from [191] and [165], respectively.

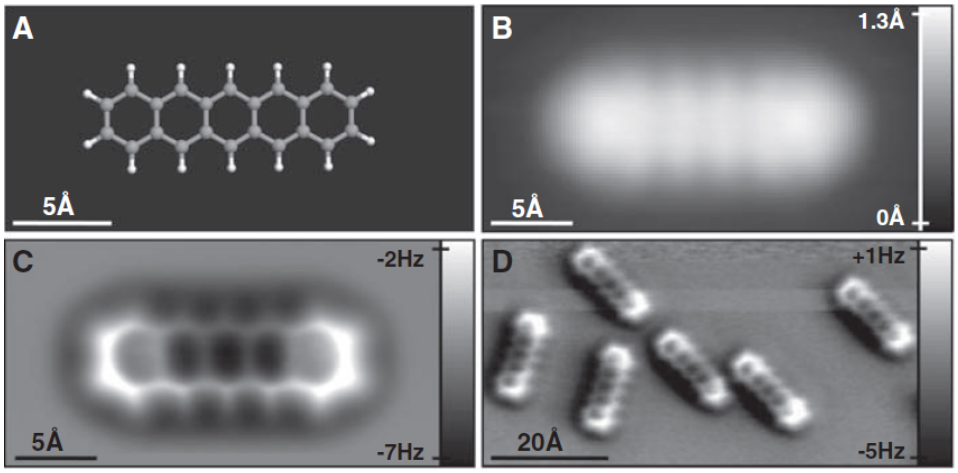

Figure 3.10: (A) Schematic of a pentacene molecule, (B) STM image and (C and D) submolecular resolution AFM of pentacene molecules on Cu(111). The image is reproduced from [193].

system [192]. It is worth noticing that z-dependent forces shift the resonance, while constant ones modify only the equilibrium position [191]. The amplitude profile versus the frequency has a Lorentzian shape where the resonant frequency corresponds to the maximum amplitude (Figure 3.9a). The frequency shift, Δf, is the difference between the resonant frequencies of the tip close and apart from the surface. The result of a scan is map $\Delta f(x, y)$ as shown in Figure 3.9b.
The frequency shift conveys information on the surface-tip force [192, 193]. Frequency modulation mode using a qPlus setup provided one of the first sub-molecular resolution images. In 2009, Gross *et al.* showed the internal bonds of pentacene (Figure 3.10) kept in UHV at 5 K using a CO-functionalised tip [193]. The working principle of submolecular imaging with functionalised tips is the measurement of the Pauli repulsion of chemical bonds with a probe smaller than the molecule and highly flexible [164]. The repulsion tilts the molecule highlighting the bond but exaggerates the length and gives rise to spurious features that can be confused with intermolecular interactions [164]. However, lower energy features, such as inter-molecular interaction, cannot be detected since they involve no electron delocalisation [164]. Besides CO functionalisation, the attachment of other small molecules to the probe enables atomic resolution [164].

In amplitude modulation mode the measurements are like the ones described in the previous paragraph. However, the feedback system keeps the frequency constant while the oscillation ampli-

tude changes [177]. The result is a map of the oscillation amplitude or the tip-surface distance such that the force equals a set point. The amplitude modulation mode is suitable for high-resolution images in air and liquids [192] but it is less used compared to frequency modulation.

Peak force AFM

FM-AFM is not suitable for achieving sub-molecular resolution in ambient conditions due to the thermal gradients causing the tip-sample distance to change during the measurement. Furthermore, there is no way to prevent the tip from breaking on rough surfaces or sharp features as it sits at a constant height. Peak force (PF) or peak force tapping AFM could be used to achieve molecular resolution in ambient conditions characteristic of FM-AFM. PF consist of driving the cantilever oscillation away from the resonant frequency and moving the tip closer to the surface until the force equals a setpoint. This process enables the exploration of different regions of the force-distance curve with forces as low as 50 pN [195]. It is worth noting that, unlike FM-AFM, the tip continuously moves from contact to non-contact, namely tapping. The low force protects the tip from pushing too far into the surface during the approach resulting in damage and the adsorption of atoms or molecules from the surface that would spoil the quality of the images. At the same time, the low setpoint is suitable to probe the short-range repulsion analogously to FM-AFM with a CO-functionalised tip. Additionally, PF enables the direct force measurement (Figure 3.11) and provides quantitative information about the surface, such as surface-tip adhesion and the local Young's modulus of the sample [195]. Moreover, setting the force as the feedback parameter and the withdrawal following a sine wave (Figure 3.11) increases the control over the tip, reducing the damage and improving the resolution.

In the context of this thesis, PF is used to image molecular layers without damaging them. Compared to previous studies, the work is carried out under ambient conditions to measure the sample under more realistic conditions for their application, yet molecular resolution is achieved.

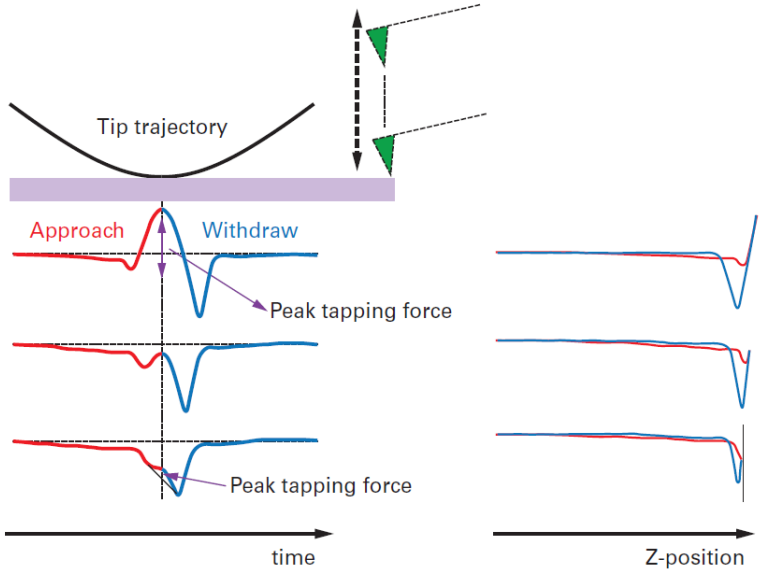

Figure 3.11: A schematic representation of the tip trajectory (top) and the force-time (left) and force-distance (right) curves measured when it approaches the surface (red) and withdraws (blue) in air. The image is reproduced from [195].

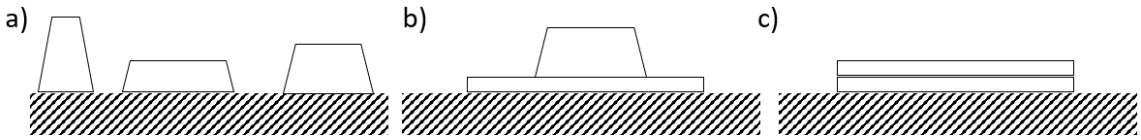

Figure 3.12: Schematic of film growth. (a) Volmer-Weber, (b) Straski-Krastanov, and (c) Frank-van der Merwe.

3.4 Sample preparation

3.4.1 Thermal evaporation in UHV

Thermal evaporation under UHV conditions is an exceptionally clean way to prepare thin molecular films, ranging from less than a monolayer to microns in thickness. It involves subliming a highly pure molecular powder to form a beam of pristine molecules directed toward a surface.

The resulting film grows epitaxially in three possible ways depending on the surface energy of the molecules and the surface, as shown in Figure 3.12. If the surface energy of the molecule-surface interface is lower than the molecule-molecule one, the molecules form a layer on the surface. This growth process is named Frank-van der Merwe. If the molecules-molecules interface energy is lower than the molecule-surface one, the molecules grow into clusters. This growth mechanism is named Volmer-Weber. Between these two extremities, there is Straski-Krastanov growth. After forming the first flat layer, the molecules grow into clusters as the molecule-molecule interface has lower energy than the molecule-vacuum one. The 4-tetra(bromophenyl) porphyrin, used in this thesis, grows into flat layers on Au(111) and on HOPG (Frank-van der Merwe) but into islands on mica (Volmer-Weber).

Thermal evaporation requires special equipment to keep UHV conditions and clean substrate to prevent any contamination. The UHV equipment used for this thesis (Figure 3.13) consists of a load lock and a main chamber pumped by a turbo and ion pump to maintain UHV (10^{-10} mbar). The load lock is regularly vented and pumped to mount a sample on the linear translator, which is then moved into the main chamber to clean it or deposit molecules. Molecular cells enable the thermal sublimation of the molecules. They are 2.5 cm long tubes of borosilicate glass containing the molecules, wrapped by a tantalum wire for resistive heating. A K-type thermocouple, composed of a chromel and an alumel wire, is in direct contact with the glass to control the temperature.

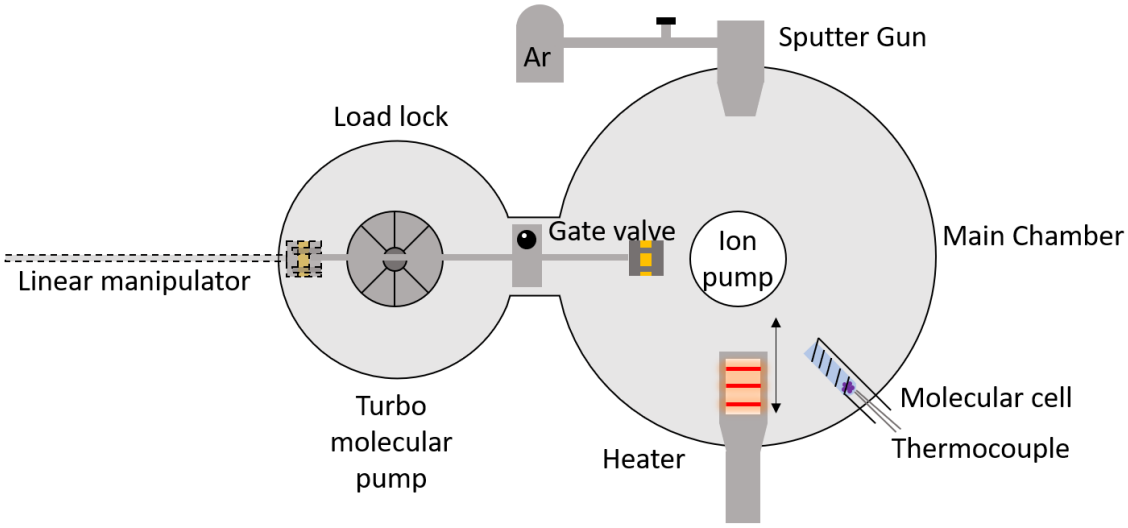

Figure 3.13: (a) Schematic of the UHV chamber used in this thesis. The chamber has a load lock to load the sample evacuated by a turbo molecular pump. The sample is connected to a linear manipulator to move it to the main chamber kept in a vacuum by an ion pump and isolated from the load lock by a gate valve. The sample can be annealed in a heater and sputtered with an Ar sputter gun. The molecules are stored in a molecular cell connected to a thermocouple.

After heating the cell and allowing for temperature stabilisation, the surface is rotated to face the molecular cells for deposition.

To remove contaminations from the surfaces before the deposition, they are cleaned in different ways. The highly oriented pyrolytic graphite (HOPG) and mica are exfoliated by scotch tape, as they are layered materials. The Au(111) surface on mica undergoes two cycles of sputtering at $5\,10 \times 10^{-6}$ mbar for 20 minutes and annealing at 400 °C for 30 minutes to clean it and form atomically flat terraces. The results are clean surfaces, displayed in Figure 3.14, that survive ambient conditions and are resistant to oxidation, unlike other commonly used surfaces such as silver and copper.

3.4.2 Plasma polymerisation

Plasma polymerisation is carried out in a custom build reactor (Figure 3.15), consisting of a glass barrel (50 cm × 10 cm) clamped between two stainless steel plates used as ground electrodes. To

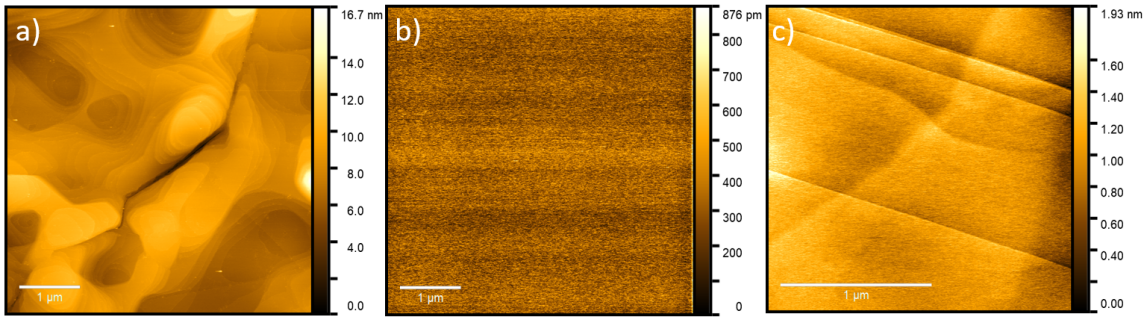

Figure 3.14: AFM topographic images of (a) flat Au(111) on mica after two cycles of sputtering and annealing, exfoliated (b) mica and (c) HOPG under ambient conditions.

generate the plasma, a 13.56 MHz radiofrequency generator produces the electric field applied to a copper wire wrapped around the barrel. The generator is connected to a matching network to compensate for the source and load impedance imbalance and maximise power transmission. The glass barrel is connected to a liquid nitrogen cold trap and a rotary pump to evacuate it (base pressure 5×10^{-5} mbar) as monitored by a Pirani gauge connected to an electrode attached to the pump. The electrode not connected to the pump is equipped with a door to insert the substrates, placed on a glass slide, into the barrel. In this thesis, the substrate sits 12 cm from the plate. 1 g of TEMPO is stored in a flask connected to the barrel by a needle valve and kept in a water bath at 25 °C to improve the vapour pressure. Using the needle valve and a valve connected to the pump, it is possible to control the monomer pressure.

To remove contaminations before the deposition, the silicon wafer is sonicated first in acetone and then in propan-2-ol (IPA) for 5 minutes. Poly-tetrafluoroethylene (PTFE) sheets are sonicated only in IPA. Au(111) on mica, HOPG and mica are treated as described in Section 3.4.1.

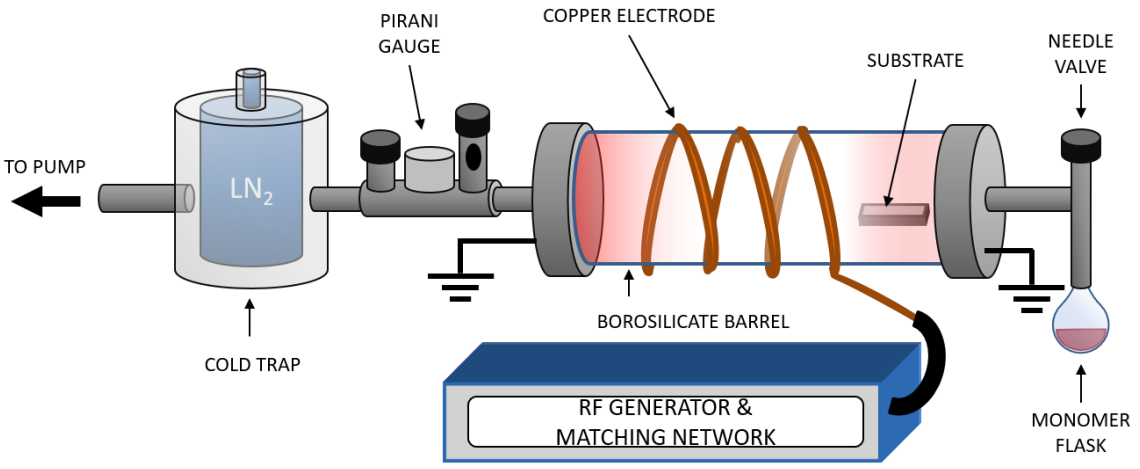

Figure 3.15: Schematic of a plasma polymerisation reactor. The reactor consists of a borosilicate barrel wrapped with a copper electrode connected to the radio-frequency generator and matching network. The sides of the barrel are enclosed by two grounded metal plates, one being connected to the monomer flask via a needle valve, the other one being connected to a Pirani gauge and a valve to the pump. The system is evacuated by a rotary pump connected to a cold trap filled with liquid nitrogen. Figure courtesy of Dr Alexander J. Robson.

Chapter 4

Surface Directed Growth of a Stable Free Radical Polymer Layer

4.1 Introduction

Nitric oxide (NO) plays an important role in several therapeutic processes, ranging from biofilm inhibition [145] to cancer treatment [196]. However, NO inherent instability has sparked interest in stable radicals with analogous behaviour, such as (2,2,6,6-tetramethylpiperidin-1-yl)oxyl (TEMPO). TEMPO has been reported as effective in anti-biofouling applications [124, 125, 146, 148, 153, 197] with its potential for use in chronic wound treatment also highlighted [125]. In high doses, TEMPO is lethal to bacterial cells and biofilms [148]. In low doses, it mimics nitric oxide behaviour as a signalling molecule able to induce biofilm dispersion, as discussed in Section 2.3.3. To use TEMPO as an anti-biofouling agent effectively, the ability to coat the surface of a wide range of materials and preserve the nitroxide moiety is required. Recently, plasma polymerisation has been shown to fulfil these requirements [124, 125, 129] and the low vapour pressure of the monomer imposes severe limits on the thermal deposition in UHV, such as operating at cryogenic temperatures.

Although plasma polymerisation is considered a mature technology, many fundamental questions remain around the initial growth stages, uniformity, and order within the polymer layers. The resulting polymers are assumed to be disordered, with little resemblance to the monomer due to fragmentation [119,198], as discussed in Section 2.3. However, high monomer pressure and low power

can reduce the damage [125, 127–129], improving functional group retention [120, 129], as discussed in Appendix A. These findings could be explained by assuming that the ions 'soft-land' on the substrate. Additionally, the flux of ions at the surface, consisting of mainly intact or protonated monomers and dimers, is often sufficient to account for the whole of the mass flux [127–129], although there is a significant debate about this topic [120, 126]. High pressure and low power are thus optimal conditions to deposit molecules as intact as possible to study their interaction with the surface and the order of the polymer.

Furthermore, recent studies challenge the belief that plasma polymerisation is a surface-independent process. The properties in the early stages of plasma polymerisation differ from thicker films in terms of chemistry [122, 123, 155–157], morphology [123, 156–158], growth rate [158], and adhesion [156, 159] because the monomers land on the pristine substrate rather than an already coated polymeric layer.

The hypothesis that (1) plasma polymerisation is surface-dependent and (2) the substrate can promote ordered growth by studying the early stages of TEMPO plasma polymerisation are tested. This chapter presents the growth and characterisation of TEMPO plasma polymers (TEMPO pps) on different substrates (HOPG, Au(111), SiO_2, and PTFE). The chemical and morphological properties of TEMPO pps were compared at various stages of the growth (5, 300, and 600 s) using XPS and AFM, respectively. The order of monolayer coatings is controlled through annealing and it is elucidated by comparing the experimental evidence with computational simulation performed by Bashayr Alanazi, Renad Almughathawi, Dr Ismael Ali, and Prof Colin J. Lambert at Lancaster University. Finally, the anti-antibacterial properties of TEMPO molecules and TEMPO pps are studied using colony-forming unit (CFU) assays and substantiated by electron paramagnetic resonance spectra collected by Chris Cook at Lancaster University.

4.2 Methodology

4.2.1 Plasma polymerisation of TEMPO

Plasma polymerisation of TEMPO (Alfa Aesar, purity $\geq 98\%$) is conducted using a borosilicate tube reactor, as described in Section 3.4.2. TEMPO plasma polymers are deposited on SiO_2 (Inseto),

HOPG (Mickromasch), Au(111) on mica (Georg Albert PVD), and PTFE (Goodfellow), which are placed on a glass slide 12 cm away from the electrode connected to the monomer flask. SiO_2 was selected due to its frequent use in characterising plasma polymers. HOPG and Au(111) are both atomically flat, but the former is chemically inert while the latter is reactive and typically utilised for self-assembly [13]. PTFE is chosen due to its application in medical devices and implants, such as catheters, where the antibacterial activity of TEMPO could be of interest.

After the reactor is evacuated to 5×10^{-5} mbar, the TEMPO pressure is adjusted to reach 0.1 mbar by partially closing the valve to the pump and keeping the monomer flask in a water bath at 25 °C. Due to the low vapour pressure of TEMPO powders and the design of the plasma reactor, stable pressure higher than 0.1 mbar could not be achieved. To test different stages of the polymer growth, TEMPO polymerisation is carried out for 5, 300, and 600 s after the plasma ignition at a nominal power of 5 W. SiO_2, HOPG, Au(111), and PTFE are coated simultaneously to prevent inconsistencies.

4.2.2 XPS

All the measurements are performed using a Kratos AXIS Supra spectrometer with monochromatic Al K_α x-ray source, operating at 15 kV, 15 mA, and equipped with an electron gun for charge neutralisation. The spectra are referenced to the C 1s peak centred at 285.0 eV.

4.2.3 AFM

AFM measurements are acquired with a Bruker MultiMode 8 equipped with a Nanoscope V controller in ambient conditions in an ultra-low-noise facility, IsoLab. The images are acquired in PeakForce mode using NuNano Scout 70 probes with a resonant frequency of approximately 70 kHz and nominal spring constant $2\,\mathrm{N\,m^{-1}}$ to minimise the interaction between the tip and the samples. Scratch tests described below are conducted in contact mode using the same tips.

4.2.4 DFT simulations

DFT simulations are carried out by Bashayr Alanazi, Renad Almughathawi, Dr Ismael Ali, and Prof Colin J. Lambert at Lancaster University. The optimal geometries of isolated TEMPO molecules are obtained using the density functional code SIESTA through the relaxation of the molecules

until all forces on the atoms were less than $0.01\,\mathrm{eV\,\AA^{-1}}$. A double-zeta plus polarization orbital basis set, norm-conserving pseudopotentials, and an energy cut-off of 3.401 keV that define the real-space grid are used and the local density approximation (LDA) is chosen to account for the exchange-correlation functional. The results obtained with general gradient approximation (GGA) are in agreement with those obtained using the LDA.

To calculate the optimal distance between any two TEMPO molecules or TEMPO-HOPG, DFT and the counterpoise method are used, which removes basis set superposition errors. The optimal distance, z, is defined as either the optimal TEMPO-TEMPO or TEMPO-HOPG separation. If one of the entities (TEMPO or HOPG) is named entity A and the other (HOPG or TEMPO) entity B, then the ground-state energy of the total system is denoted E_{AB}^{AB}. The energy of each entity is then calculated on a fixed basis, using ghost atoms in SIESTA, i.e. a basis set of functions that have no electrons or protons. The energy of entities A and B in the case of the fixed basis is defined as E_A^{AB} and E_B^{AB}, respectively. The binding energy is then the difference between the isolated entities and their total energy when placed at a distance z apart, calculated using the following equation:

$$\Delta(z) = E_{AB}^{AB} - E_A^{AB} - E_B^{AB}. \tag{4.1}$$

It is widely accepted that carbon systems, such as TEMPO and HOPG, are sensitive to the choice of density functional and it is important to consider the effect of van der Waals interactions to study the absorption height and energy. Therefore, the simulations below are conducted using GGA and Van der Waals functional and are found in agreement.

4.2.5 Bacterial attachment

To test the ability of TEMPO plasma polymers to prevent bacterial attachment, colony-forming unit assays are conducted using the rapid biofilm-forming strain of *S. epidermidis* (RP62A). Bacteria are first plated out onto a Columbia agar plate (CAP) and incubated for 24h at 37 °C, then a single colony is inoculated into 3 mL of nutrient broth and incubated for 24 more hours at 37 °C. The bacteria solution is diluted to $1 \times 10^6\,\mathrm{CFU\,mL^{-1}}$. The three treated and one control samples are immersed in 1 mL of bacterial solution and incubated at 37 °C for 1 h. Similarly, three more treated and one more control samples are incubated for 24 h. The samples are then washed with 1 mL of phosphate buffer solution (PBS) to remove planktonic bacteria and then sonicated in 1 mL of PBS for 5 min to detach the biofilm. After the solution is serially diluted from $d = 10^{-1}$ to

$d = 10^{-8}$, 20 µL of each dilution is inoculated into a Columbia blood agar (CBA) plate in triplicate and incubated for 24 h at 37 °C. The *S. epidermidis* colonies are counted to compute the average, a, and the standard deviation. The number of colony-forming units per mL, C, is calculated using the following equation:

$$C = a \frac{1\,\text{mL}}{20\,\mu\text{L}} \frac{1}{d} \tag{4.2}$$

4.2.6 Electron paramagnetic resonance (EPR)

EPR spectra were collected by Chris Cook at Lancaster University using a Bruker EMX, x-band spectrometer, with a centre field of 343.641 mT, sweep width of 40 mT, modulation frequency of 100 kHz, and microwave frequency of 9.7 GHz.

4.3 Characterisation of TEMPO plasma polymers

4.3.1 Chemistry

The chemical composition of TEMPO pps is characterised using XPS with wide scan and high-resolution measurements conducted on the same day of the deposition to minimise surface oxidation. Figure 4.1 shows typical wide scans for 5 s, 300 s, and 600 s of polymerisation. After 5 s of plasma polymerisation (blue lines in Figure 4.1), the XPS spectra are dominated by Au 4f, C 1s, Si 2p, and F 1s peaks of the substrates, indicating that the coatings are thinner than the XPS sampling depth ($\approx$ 10 nm). However, trace amounts of nitrogen, oxygen and carbon were detected. The presence of nitrogen suggests that after 5 s the substrates are coated by a thin layer of TEMPO pp. Although the detected oxygen and carbon could be assigned both to TEMPO and adventitious carbon, the nitrogen peak suggests that the former scenario is more likely.

After 300 s of plasma polymerisation (black lines in Figure 4.1), the peaks of the substrates disappeared, except for SiO_2, suggesting that the coatings are thicker than 10 nm. However, the background rises from 0 to 200 eV on Au(111) and SiO_2 (Figure 4.1 a and c), which could be attributed to the bremsstrahlung effect caused by the underlying substrate. The spectra exhibit N 1s, O 1s, and C 1s as expected for TEMPO pps. After 600 s, only carbon, nitrogen, and oxygen peaks were detected, suggesting that the substrates were coated with a pinhole-free film thicker than the XPS sampling depth.

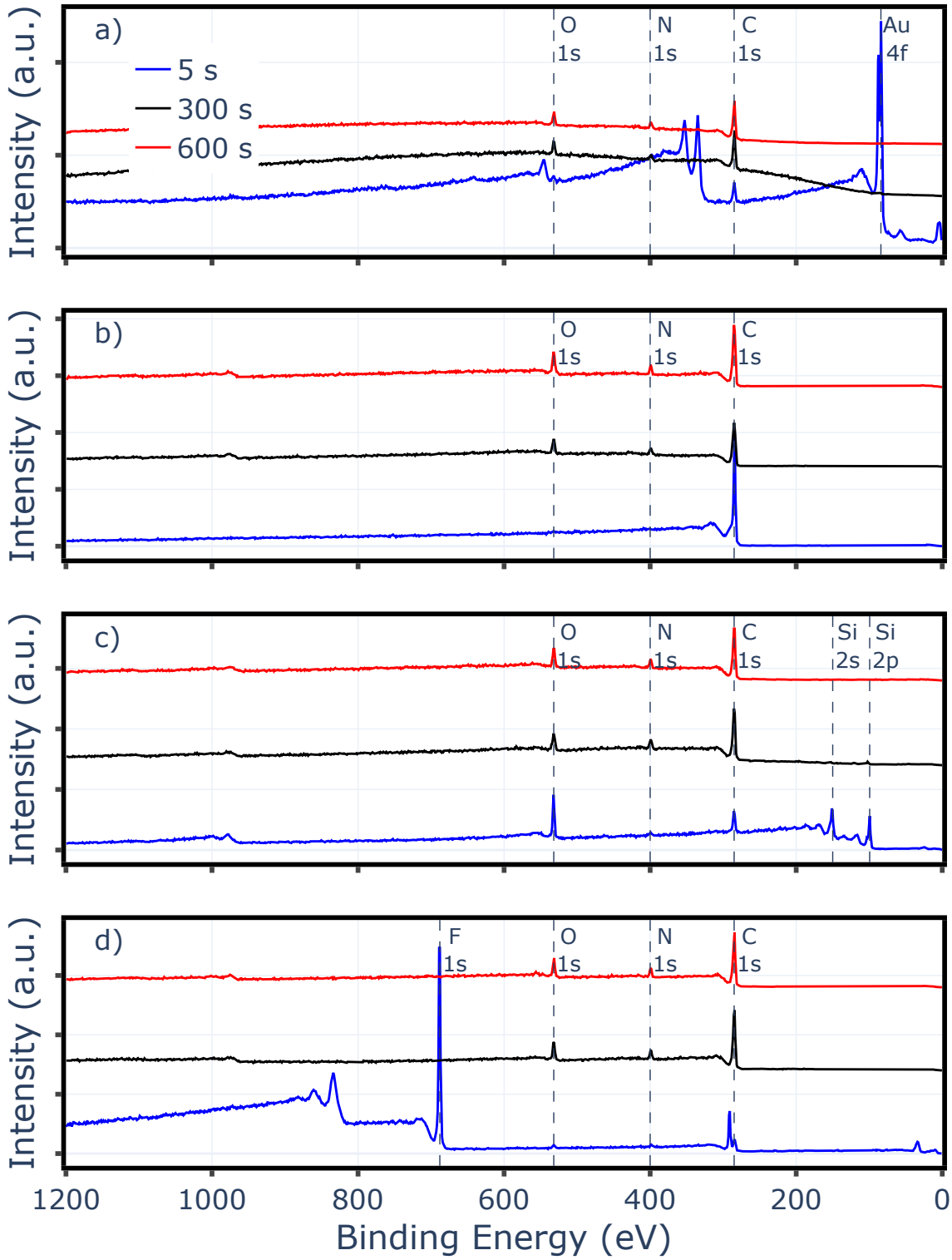

Figure 4.1: (a) Wide XPS spectra of TEMPO on (a) Au(111), (b) HOPG, (c) SiO_2, and (d) PTFE grown for 5 s (blue line), 300 s (black line) and 600 s (red line).

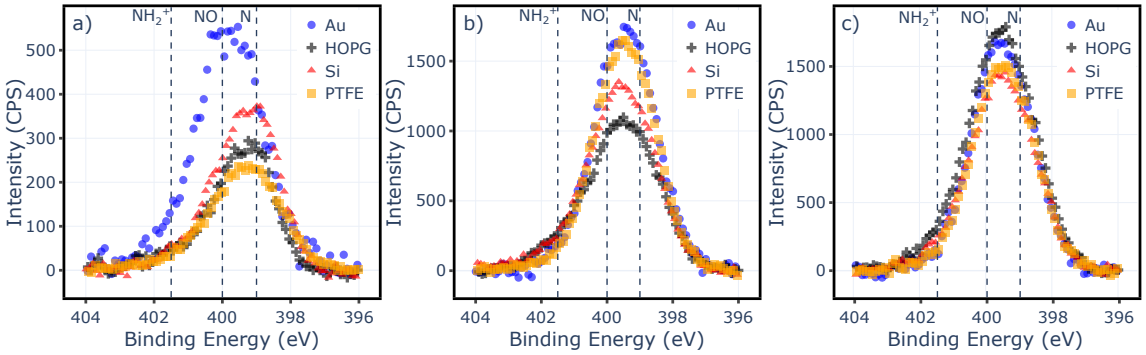

Figure 4.2: High-resolution XPS spectra of the TEMPO pps collected in the N 1s region after (a) 5 s, (b) 300 s and (d) 600 s of plasma polymerisation. Dashed lines indicate the approximate positions of common environments.

The presence of nitrogen, detected after 5 s deposition, indicates the formation of a thin film during the early stages of plasma polymerisation. The chemical composition of TEMPO pps was further examined using high-resolution measurements to gain a better understanding of the changes that occur due to interactions with the substrates. In particular, the N 1s peak was studied to test whether the NO functional group was retained as it is the biologically active part of the molecule.

Figure 4.2 and 4.3 present overlaid and fitted N 1s peaks, respectively. The dashed lines in Figure 4.2 indicate three common nitrogen environments, which were used for peak fitting in Figure 4.3. These three environments are the pristine molecule with the nitroxide functional group (NO), the damaged molecule without the NO moiety (N), and the damaged molecule with the nitroxide group replaced by a protonated amine moiety (NH_2^+). The peaks corresponding to N, NO, and NH_2^+ are observed at 399, 400, and 401.5 eV and attributed to the nitroxide group, amines (primary, secondary and tertiary), and protonated amine (NH_2^+), based on previous works [129].

Samples exposed to 5 s of TEMPO plasma exhibit an N 1s peak centred at 399.2 eV on SiO_2, HOPG, and PTFE, attributed to an intense N and NO components with a tail at higher binding energy because of the NH_2^+ environment (Figure 4.3a-d). This is consistent with previous observations [129]. The N 1s spectrum on Au(111) is centred at 400.0 eV, suggesting an increased relative abundance of NO in the TEMPO film, due to reduced molecular damage and higher functional group retention. Based on the fitting analysis presented in Figure 4.3, and the assumption that the methyl groups would provide a steric barrier for N-Au binding, an increase in NO retention is most

likely. Furthermore, the higher intensity of the N 1s peaks suggests that there is more TEMPO on Au(111) compared to the other substrates. As the deposition time is the same, the growth on Au(111) is faster. This observation is substantiated by AFM measurements discussed in Section 4.3.2.

XPS spectra measurements were conducted on thicker TEMPO films that were deposited for 300 s and 600 s. The N 1s region shows a similar structure, with a higher NH_2^+ percentage observed on SiO_2 and HOPG (Figure 4.2b,c). Conversely, the percentage of NO decreases in TEMPO pp on Au(111), while increasing on all the other substrates (Figure 4.3e-i). The ratio between NO and N components converges to 50 % suggesting that approximately half the nitrogen atoms are parts of the nitroxide group (Figure 4.3).

Based on the N 1s spectra analysis, it can be inferred that the TEMPO plasma polymerisation partially preserves the nitroxide functional group (NO component) of the monomer, with XPS sensitivity limited only to nitroxide groups, and not nitroxide radicals. Furthermore, the substrate influences the chemistry of the films during the initial 5 s of deposition, leading to an increase in NO retention on gold. After 300 s, the nitrogen chemistry reaches convergence, although the coating thickness remains substrate-dependent, as elaborated upon in Section 4.3.2.

4.3.2 Morphology

The morphology of the same TEMPO pps was characterised via AFM after 5 s, 300 s, and 600 s of polymerisation as shown in Figure 4.4. The characterisation of coatings on PTFE was not feasible due to the roughness of the substrate.

Figure 4.4a-c shows AFM measurements of TEMPO pps after 5 seconds of growth on SiO_2, HOPG, and Au(111), respectively. Each pp exhibits a distinct morphology. On SiO_2 (Figure 4.4a) the polymer grows unevenly as TEMPO collects in small aggregates (the brown and yellow parts of Figure 4.4a). The line profile shows that most of the surface has the same roughness as the pristine SiO_2 (blue line) suggesting that there are no densely packed molecules while the height of the aggregate is below 2 nm. On HOPG, TEMPO pp (highlighted in orange in Figure 4.4b) covers most of the substrate (highlighted in blue). The polymer forms large, flat islands, suggesting layer-by-layer growth. The thickness of the islands is 0.6 ± 0.2 nm and it is comparable to the monomer dimension, indicating that the molecules form a monolayer. This topic is discussed in detail in Section 4.3.3. The atomically flat Au(111) surface is completely covered by a conformal coating

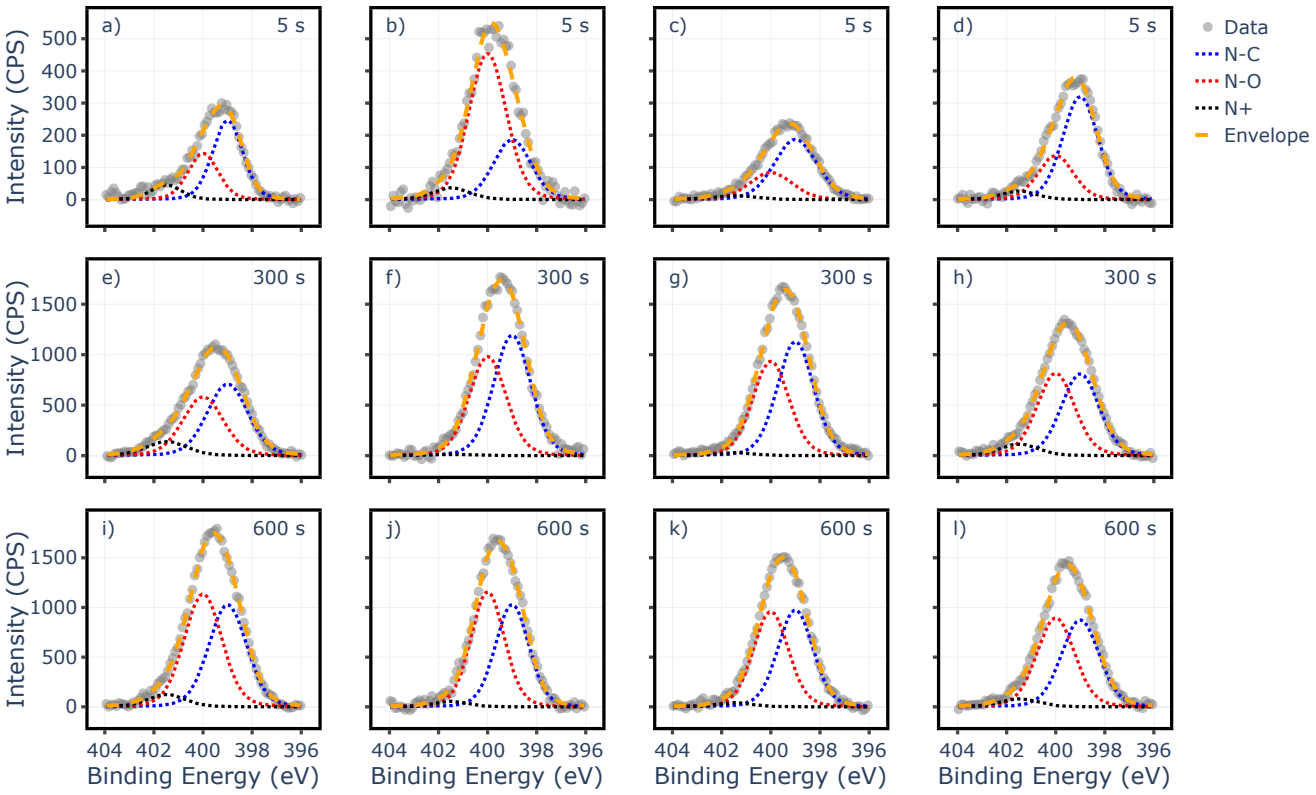

Figure 4.3: High-resolution XPS spectra of the TEMPO pps collected in the N 1s region after (top row) 5 s, (middle row) 300 s and (bottom row) 600 s of plasma polymerisation. TEMPO pp on (a,e,i) HOPG, (b,f,j) Au(111), (c,g,k) SiO_2, (d,h,l) and PTFE. Each spectrum is fitted with three symmetric Voigt functions representing the NO, N, NH_2^+ components at 399, 400, and 401.5 eV with the same full-width half-maximum (FWHM).

(Figure 4.4c), as suggested by the increase in roughness shown in the line profile. A scratch test was conducted (the method is described in detail below) by operating the AFM at a high loading force to measure the thickness. The layer is 3 ± 1 nm thick, exceeding the other coatings and supporting the XPS results of accelerated growth on Au(111) (Figure 4.2). Despite numerous attempts, it was not possible to prepare a sub-monolayer TEMPO pp on Au(111), likely due to the higher sticking coefficient of Au(111) compared to SiO_2 and HOPG, and the difficulty in preparing a stable plasma for deposition times shorter than 5 seconds.

After 300 s of plasma polymerisation, variations in the morphology of TEMPO pps persist (Figure 4.4d-f). TEMPO forms bigger aggregates on SiO_2, multilayer islands on HOPG, and a continuous coating on Au(111). The AFM images share similar characteristics to 5 s deposition, suggesting that the initial monolayer primes the growth of subsequent layers during the early stages of plasma polymer deposition. After 600 s of plasma polymerisation (Figure 4.4g-i), the morphology converges across all the imaged samples, with comparable root mean square (RMS) roughness of 276.5 pm, 333.7 pm and 288.9 pm for SiO_2, HOPG and Au(111), respectively. The morphology of TEMPO pps after 600 s of deposition is comparable to previously published results [125]. The convergence of both morphology and chemistry suggests that TEMPO coatings exhibit a transition from substrate-dependent to 'substrate-agnostic' around 600 s of plasma polymerisation.

To determine the critical thickness such that coatings transition from being from substrate-dependent to substrate-agnostic, a scratch test is conducted on the TEMPO pps that were deposited for 600 s, as shown in Figure 4.5. The coatings on SiO_2, HOPG, and Au(111) are scratched in a $2 \times 2\,\mu m^2$ area (Figure 4.5 a-c) using the AFM in contact mode with a deflection setpoint as high as 100 nm. The samples are scratched in contact mode and imaged in PeakForce mode in steps until the morphological features of the substrates are recovered, ensuring complete removal of the polymer (insets in Figure 4.5). SiO_2, Au(111), and HOPG are identified due to their smoother surface compared to the plasma polymer and their distinct features, such as terraces on HOPG and Au(111), and low roughness on SiO_2. The thickness of TEMPO pps is estimated as the difference in the height at the bottom of the pit and the unscratched layer displayed in the height histogram derived from the AFM images (Figure 4.5d-f). The additional peak associated with TEMPO at the edges of the pit is not shown. The height is estimated as the centre of the peaks with half of the full-width half maximum (FWHM) as the uncertainty. The difference between the centres of

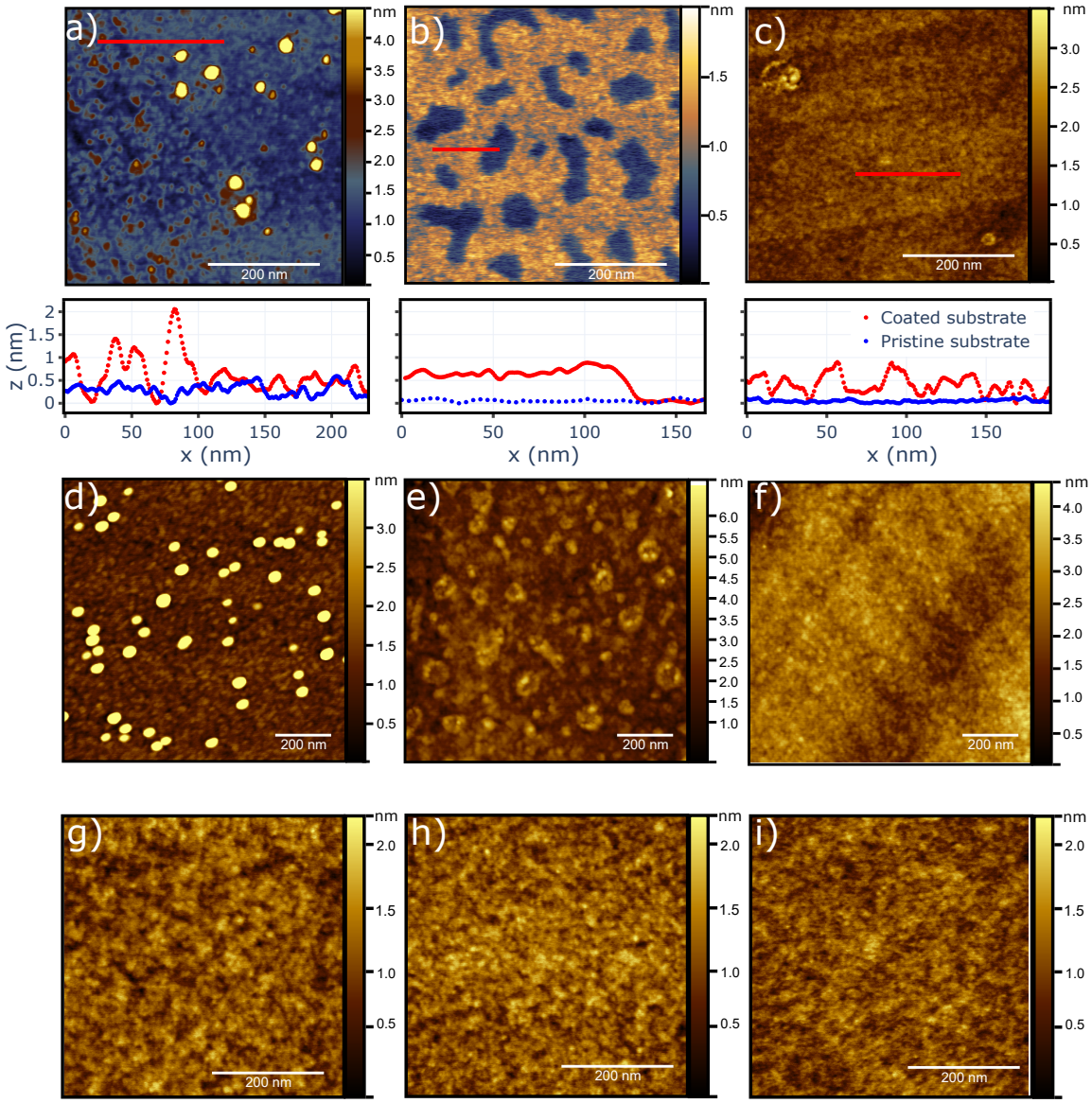

Figure 4.4: AFM topography images of TEMPO pp after 5 s of deposition on (a) SiO_2, (b) HOPG and (c) Au(111), shown with line profiles comparing TEMPO layers (red trace) to the pristine substrate (blue trace). AFM morphology images of TEMPO growth following 300 s of deposition on (d) SiO_2, (e) HOPG and (f) Au(111). AFM images of TEMPO pps growth after 600 s showing similar topography on (g) SiO_2, (h) HOPG and (i) Au(111).

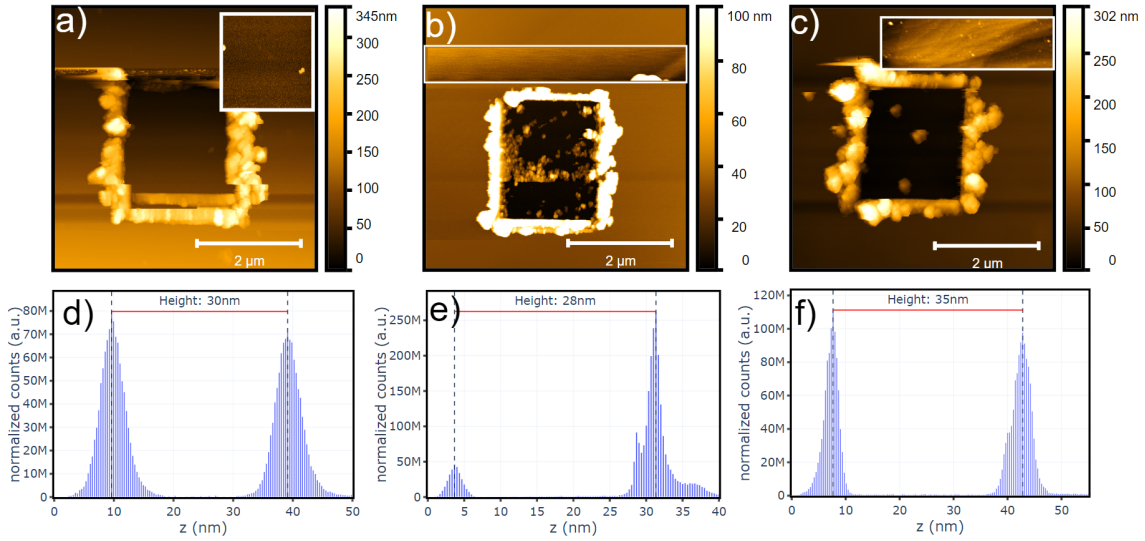

Figure 4.5: AFM images of TEMPO pps deposited for 600 s on (a) SiO_2 (b) HOPG and (c) Au(111) after being scratched in contact mode. The insets (white borders) show the flat SiO_2 substrate, a HOPG step and Au(111) steps inside the scratched area. (d-f) Height histograms derived from the figure (a-c), respectively, showing the thickness of the pps.

the peaks yielded the thickness of the polymer, and the sum in quadrature of the FWHM is the associated uncertainty. Following this procedure, thicknesses of 30 ± 2 nm, 28 ± 2 nm and 35 ± 2 nm were measured on SiO_2, HOPG and Au(111) (Figure 4.5d-f), respectively.

The properties of TEMPO pps grown by plasma polymerisation exhibit a strong dependency on the substrate in the first 30 nm. XPS reveals that the chemical composition is primarily affected in the first layer of growth. Beyond this point, molecules exhibit a consistent chemical structure in the N 1s region. AFM measurements reveal a significant variation in morphology up to a thickness of approximately 30 nm. Beyond this critical thickness, the plasma polymers become substrate-agnostic, converging to a flat, uniform layer of comparable roughness. These findings suggest that the substrate-TEMPO interaction is persistent during the early stages of growth, and it is completely screened when the pps reach a thickness of 30 nm. Moreover, the results after 5 s of deposition on HOPG indicate that it is possible to produce TEMPO monolayers using plasma polymerisation. This possibility is further explored below and may be applicable to growing molecular layers from liquid organic monomers that are incompatible with ultra-high vacuum conditions.

4.3.3 Order in TEMPO monolayers

The results obtained from the TEMPO pp grown by plasma polymerisation on HOPG after 5 s (Figure 4.2b) are of great interest due to the uniformity of islands' height, suggesting the ordered arrangement of molecules, unlike on SiO_2. Additionally, the height of 0.6 ± 0.2 nm is comparable to the dimensions of the monomer, indicating that it is indeed a monolayer. These observations led to the testing of the possibility to control the molecular ordering of TEMPO pp on HOPG by annealing the samples under atmospheric conditions at 50 °C. This temperature is above the melting point of the monomer, 34 °C, and it is likely to remove the surface coating unless the molecules are cross-linked. Therefore, annealing at 50 °C is sufficient to provide energy for the TEMPO monolayer to reach the minimum energy configuration.

AFM images of TEMPO monolayer on HOPG before and after annealing are shown in Figure 4.6. Before annealing (Figure 4.6a), the molecular layer (highlighted in orange in the figure) does not cover the entire HOPG substrate (highlighted in blue). The height of the molecules was measured by fitting the height histogram of the images within a single terrace to avoid any artefact due to the step edge of HOPG (Figure 4.6c). The graph displays two peaks corresponding to the top of the TEMPO layer and the substrate. The layer thickness was measured as the distance between the centres of the two Gaussian distributions with the sum in quadrature of the standard deviation as uncertainty (analogously to the method of scratch testing). The thickness of the TEMPO layer before the annealing is 0.6 ± 0.2 nm as shown in Figure 4.6c. After annealing the sample at 50 °C for 30 min, the TEMPO layer exhibited a similar morphology (Figure 4.6b), but the height was found to increase to 0.9 ± 0.1 nm.

XPS data of the same samples, collected in the N 1s region, (Figure 4.7) indicated that there was no significant difference in the area under the peak and the binding energy. As the layer is thinner than the XPS sampling depth, these spectra imply that the amount of TEMPO on the surface remained unchanged, suggesting that the molecules are at least partially cross-linked and, thus, not volatile.

The increase in height combined with the absence of molecular desorption suggests that annealing the sample induced a change in the ordering of the TEMPO molecules in the layer. It is likely that the arrangement of TEMPO molecules was affected by the electric field during the process of plasma polymerisation (see Section 2.3 and Appendix A for further details) and changed upon annealing as the system had enough energy to reach the equilibrium position in the absence of

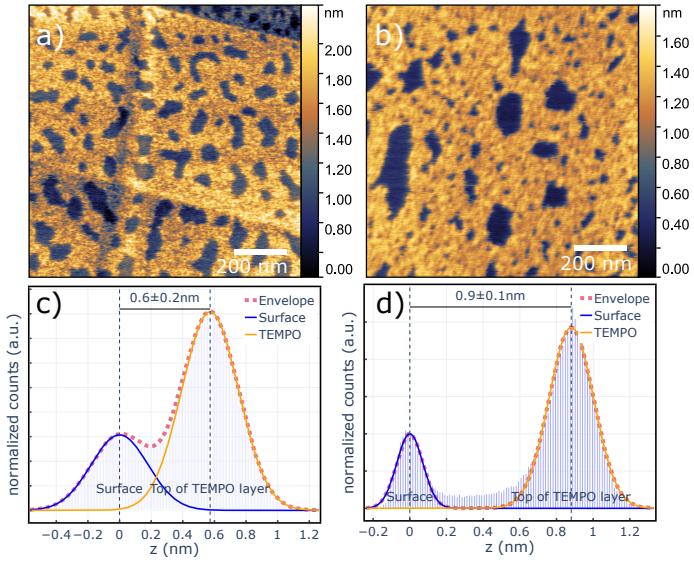

Figure 4.6: AFM images of TEMPO pp deposited on HOPG (a) before and (b) after annealing at 50 °C for 30 min under atmospheric conditions. The corresponding height histograms, before and after annealing, are shown in panels (c) and (d). Height histograms are analysed within a single terrace and are fitted to two Gaussian distributions to measure the layer thickness for each sample.

external perturbations.

These observations are further discussed within the context of computational modelling performed by Bashayr Alanazi, Renad Almughathawi, Dr Ismael Ali, and Prof Colin J. Lambert at Lancaster University. Although the author of this thesis did not perform any calculations, this work was a collaboration to explore the properties of TEMPO pp. It is, hence, worth presenting the results as they shed light on the experimental evidence. The study used DFT and counterpoise methods to investigate the behaviour of two TEMPO molecules, taken as a representative of the whole plasma polymer, assuming that monomers constitute most of the mass flux to the surface. In reality, the plasma polymerisation process generates a mixture of molecular species with a varying degree of resemblance to the monomer and cross-linking. However, mass spectrometry of TEMPO shows that the plasma conditions used in this thesis mainly produce a flux of pristine or protonated monomers with a relatively marginal contribution of damaged molecules [129]. Although the modelling does not capture the complexity of the TEMPO plasma polymerisation, it can still be

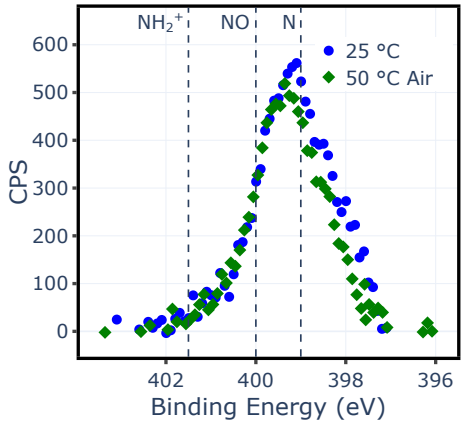

Figure 4.7: High-resolution N 1s XPS spectra of TEMPO on HOPG at 25 °C (circles) and after annealing at 50 °C for 30 minutes under atmospheric conditions (diamonds). Dotted lines indicate approximate positions of common environments.

considered a reasonable approximation.

First, the interaction between two isolated monomers was explored by comparing two orientations: parallel and anti-parallel NO groups as shown in Figure 4.8a. The latter was found to be the most energetically favourable due to the interaction between the dipole moments of the nitroxide groups no matter the lateral separation between the molecules. Additional simulations indicated that the TEMPO-TEMPO interaction is stronger than the TEMPO-HOPG interaction (Figure 4.8b) in the range of distance studied, suggesting that the substrate does not affect the anti-parallel orientation. Consequently, the lateral separation between the molecules is kept constant and a thousand different configurations of two anti-parallel TEMPO molecules on the HOPG surface were explored as shown in Figure 4.8c. The lowest-energy configurations are presented in Figure 4.8d. The upright configuration was identified as the most energetically stable, while the tilted orientation was found to be a local minimum. The height of the two configurations, measured from the top of the HOPG carbon to the top of the oxygen of TEMPO, was determined to be 0.87 nm and 0.65 nm, respectively. These values are directly comparable to the AFM measurements. Therefore, the monolayer 0.6 ± 0.2 nm in height observed before the annealing in Figure 4.6 is assigned to the tilted configuration; the TEMPO molecules after annealing are likely to stand upright as their height is 0.9 ± 0.1 nm and matches the simulated upright configuration. The transition from the tilted to the upright configuration suggests that the minimum energy configuration was prop-

erly identified by the simulations. In conclusion, these results demonstrate that annealing allows the ordering of TEMPO pp to be controlled and that ordered molecular layers can be deposited by choosing the substrate for the plasma polymerisation process, contrary to the assumption that plasma polymers are always disordered.

4.4 Anti-microbial properties of TEMPO

TEMPO anti-microbial properties are tested using colony-forming unit (CFU) assays after inoculation with a rapid biofilm-forming strain of *S. epidermidis* (RP62A) for 1 and 24 h to assess the inhibition of the bacterial attachment and biofilm formation, respectively, as described in Section 4.2. Four different kinds of samples, deposited onto $0.5 \times 0.5\,\mathrm{cm}^2$ PTFE sheets sterilised in ethanol 70%, are tested: (1) TEMPO polymerised for 50 min at 0.1 mbar and 5 W (TEMPO pp), (2) TEMPO molecules absorbed on PTFE from the exposure to the monomer vapour for 50 min at 0.1 mbar. Additionally, two samples consisting of TEMPO pps loaded with TEMPO molecules are prepared. (3) TEMPO molecules are absorbed on TEMPO pp produced by 5 steps of 10 min of plasma polymerisation at 0.1 mbar and 5 W followed by 10 min of exposure to TEMPO vapour at 0.1 mbar, namely vapour sample. (4) TEMPO powders (< 0.1 mg) are melted on TEMPO polymerised for 50 min at 0.1 mbar and 5 W and pumped at a pressure of 5×10^{-5} mbar for 10 min to remove the molecules that are not embedded into the polymer, namely powder sample. The performances of these samples are compared to controls consisting of a $0.5 \times 0.5\,\mathrm{cm}^2$ PTFE sheets sterilised in ethanol 70%.

The results of the CFU assays are shown in Figure 4.9. TEMPO pps perform worse than the PTFE control after 1 h and 24 h (Figure 4.9a). The concentration of colony-forming units of the control, c_c, and the sample, c_s, after 1 h and 24 h are $c_c = (1.5 \pm 0.7) \times 10^3\,\mathrm{CFU\,mL^{-1}}$ and $c_s = (11 \pm 5) \times 10^3\,\mathrm{CFU\,mL^{-1}}$, $c_c = (1.7 \pm 0.2) \times 10^7\,\mathrm{CFU\,mL^{-1}}$ and $c_s = (12 \pm 2) \times 10^7\,\mathrm{CFU\,mL^{-1}}$, respectively. The results suggest that TEMPO pp is significantly worse than the control in inhibiting the bacteria attachment, likely due to the loss of the nitroxide radical during plasma polymerisation and the enhanced adhesion of bacteria caused by the reduced hydrophobicity of the pp compared to PTFE as reported in the literature [199, 200].

TEMPO molecules absorbed on PTFE (Figure 4.9b) exhibit an anti-biofouling behaviour as the

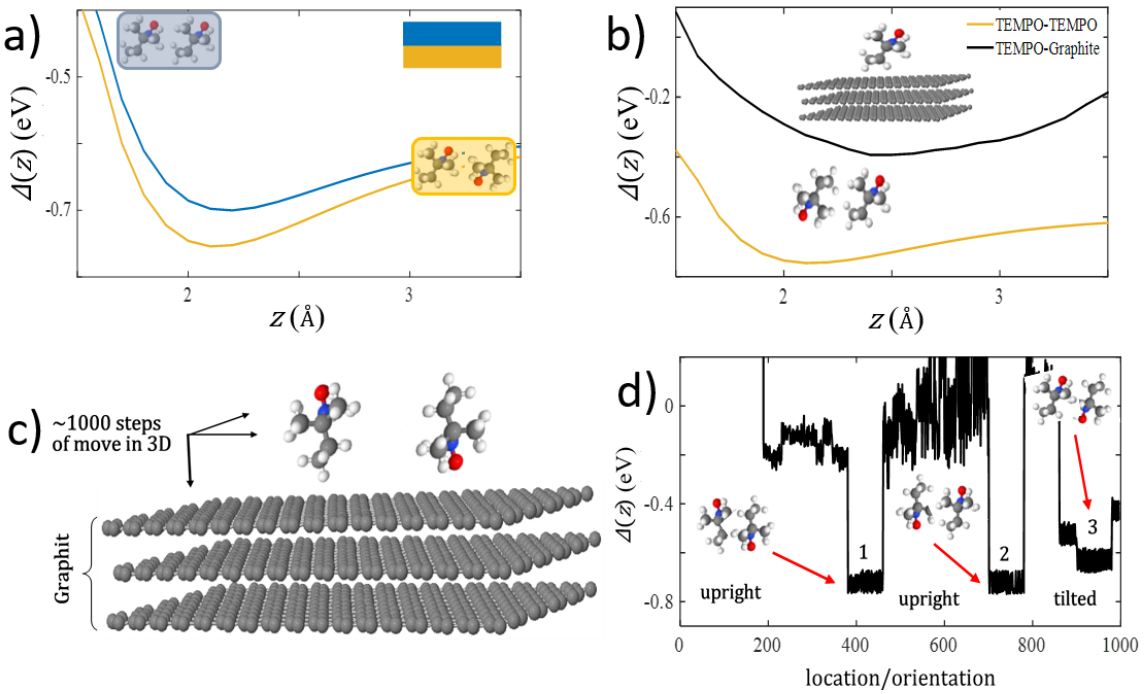

Figure 4.8: (a) Simulated energy, Δ, as a function of the distance, z, between two TEMPO molecules (red=oxygen, blue= nitrogen, grey=carbon, white = hydrogen) in a parallel (blue) and anti-parallel (orange) configuration. (b) Simulated energy, Δ, as a function (orange) of the lateral distance between two TEMPO molecules in the anti-parallel configuration and (black) of the vertical distance between TEMPO and a graphite surface. (c) Schematic diagram of two TEMPO molecules -graphite interaction. (d) van der Waals 3D energy spectrum of TEMPO-graphite interaction. 1, 2 and 3 minima are the most energetically favourable orientations between the TEMPO molecules and HOPG. Figure courtesy of Dr. Ismael Ali.

sample shows a significant reduction of colony-forming units compared to the control. After 1 h and 24 h the control and samples colony-forming unit concentrations are $c_c = (6.3 \pm 0.7) \times 10^3\,\mathrm{CFU\,mL^{-1}}$ and $c_s = (3 \pm 1) \times 10^3\,\mathrm{CFU\,mL^{-1}}$, $c_c = (25 \pm 4) \times 10^6\,\mathrm{CFU\,mL^{-1}}$ and $c_s = (4 \pm 1) \times 10^6\,\mathrm{CFU\,mL^{-1}}$, respectively. TEMPO molecules absorbed on PTFE exhibit an anti-microbial behaviour as reported in the literature [146, 153]. The presence of TEMPO on PTFE before the CFU assay is confirmed by the XPS spectrum collected in the N 1s region shown in Figure 4.10. Furthermore, the XPS data suggests that TEMPO molecules form a layer approximately 1 nm thick on PTFE. Given the small quantity of molecules absorbed on PTFE, the anti-microbial activity detected with the CFU assay is significant.

TEMPO pp is then used as a matrix to load TEMPO molecules. The vapour sample performs as the control PTFE in the CFU assay (Figure 4.9c). After 1 h and 24 h the control and samples colony-forming unit concentrations are $c_c = (1.6 \pm 0.2) \times 10^4\,\mathrm{CFU\,mL^{-1}}$ and $c_s = (1.3 \pm 0.3) \times 10^4\,\mathrm{CFU\,mL^{-1}}$, $c_c = (10 \pm 1) \times 10^6\,\mathrm{CFU\,mL^{-1}}$ and $c_s = (13 \pm 6) \times 10^6\,\mathrm{CFU\,mL^{-1}}$, respectively. Analogously to the vapour sample, the powder sample performs as the control PTFE in the CFU assay (Figure 4.9d). After 1 h and 24 h the control and samples colony-forming unit concentrations are $c_c = (2.5 \pm 0.4) \times 10^4\,\mathrm{CFU\,mL^{-1}}$ and $c_s = (2.1 \pm 0.5) \times 10^4\,\mathrm{CFU\,mL^{-1}}$, $c_c = (1.7 \pm 0.1) \times 10^7\,\mathrm{CFU\,mL^{-1}}$ and $c_s = (1.2 \pm 0.2) \times 10^7\,\mathrm{CFU\,mL^{-1}}$, respectively.

The results suggest that embedding TEMPO molecules improves the performance of the polymer. However, the anti-microbial properties of the sample are still worse than pure TEMPO molecules. This difference is assigned to the preferential attachment of *S. epidermidis* to the hydrophilic TEMPO pp compared to the hydrophobic PTFE [199, 200]. The XPS spectra of TEMPO pp and the vapour samples collected in the N 1s region (Figure 4.10) suggest that there is no significant difference between them, thus little TEMPO molecules are absorbed into the surface of the vapour sample. These results highlight the limited absorption of TEMPO molecules into the plasma polymer.

To assess the presence of the nitroxide radicals, which is the biologically active part of the molecules, electron paramagnetic resonance (EPR) spectra of TEMPO vapours absorbed on PTFE (Figure 4.11a) and TEMPO pp produced at 0.1 mbar and 5 W (Figure 4.11b) are acquired by Chris Cook at Lancaster University. The spectrum of TEMPO vapours absorbed on PTFE shown in Figure 4.11a exhibits six sharp peaks. They are the fingerprints of TEMPO radicals [124]. On the other hand, the spectrum of TEMPO pp shown in Figure 4.11b exhibits three sharp peaks

and it is remarkably different from the previous one, indicating that TEMPO pp contains little or no nitroxide radical. It is likely that the NO radicals, the biologically active part of TEMPO, do not survive the plasma environments used to create the polymer, explaining the absence of anti-microbial properties. On the contrary, the anti-microbial activity of TEMPO vapour absorbed on PTFE is substantiated by the presence of pristine nitroxide radicals.

In conclusion, the CFU assays show that TEMPO molecules are more effective against *S. epidermidis* biofouling compared to PTFE and TEMPO pp due to the presence of nitroxide radicals that are not detected in the plasma polymer, as substantiated by EPR data. This result is in disagreement with the study of Michl and coworkers that shows an anti-bacterial activity in TEMPO pp [125]. The difference could derive from the lower retention of undamaged TEMPO molecules due to the parameters used for the plasma polymerisation and the design of the reactor, a well-known issue in the context of plasma polymerisation [136]. However, TEMPO pp can be used as a matrix to absorb TEMPO molecules, improving the performance to the same level as the control.

4.5 Conclusions and future work

In this chapter, the hypothesis that the early stages of TEMPO plasma polymerisation are affected by the substrate was tested by depositing TEMPO plasma polymers on HOPG, Au(111), SiO_2, and PTFE for 5, 300, and 600 s. The results revealed a transition of morphology and chemistry from surface-dependent to surface-agonistic at approximately 30 nm of thickness. XPS data indicated that the interaction with the surface affects the chemistry of the monomer, resulting in increased retention of NO on Au(111). AFM images showed significant differences in the morphology of TEMPO pps on HOPG, Au(111), and SiO_2 after 5 s, which affected the growth up to 30 nm. Therefore, these results provide evidence that the substrate is an essential factor in the early stages of plasma polymerisation.

The observation of monolayer films of TEMPO on HOPG with different heights of 0.6 ± 0.2 nm and 0.9 ± 0.1 nm before and after annealing, respectively, prompted further investigation into understanding the molecule's ordering. DFT simulations of TEMPO on HOPG revealed that the NO functional group orientation is anti-parallel due to the dipole moment of the oxygen unpaired elec-

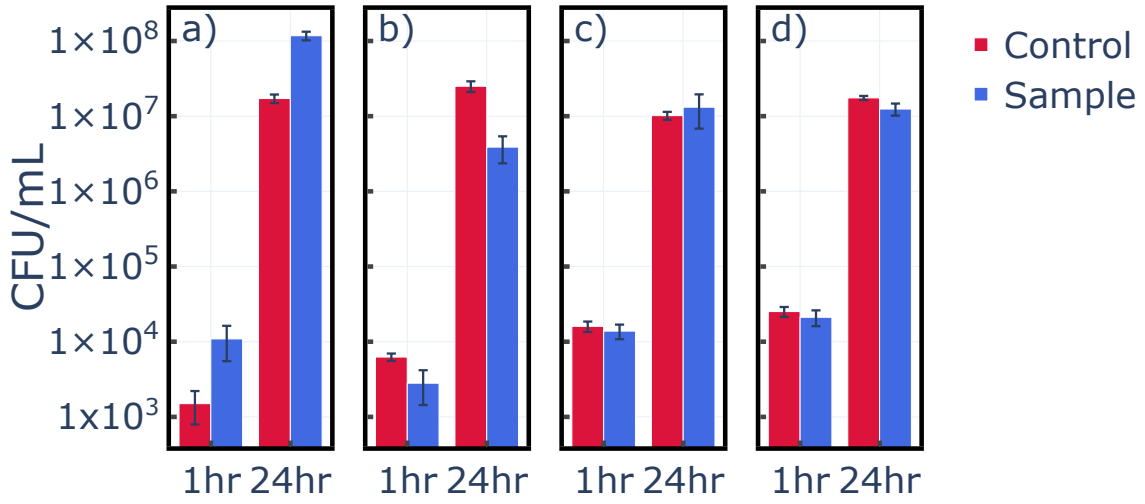

Figure 4.9: Colony forming unit assay after 1 h and 24 h of incubation in *S. epidermidis* solution of (a) TEMPO pp deposited on PTFE for 50 min at 0.1 mbar and 5 W, (b) TEMPO vapour absorbed on PTFE for 50 min at 0.1 mbar, (c) TEMPO vapour absorbed on TEMPO pp produced by 5 steps of 10 min of plasma polymerisation at 0.1 mbar and 5 W followed by 10 min of exposure to TEMPO vapour at 0.1 mbar. (d) TEMPO powders (< 0.1 mg) melted on TEMPO polymerised for 50 min at 0.1 mbar and 5 W and pumped at a pressure of 5×10^{-5} mbar for 10 min. Sterilised pieces of PTFE are used as the control in each case. The results are shown as mean ($n = 9$ for samples, $n = 3$ for control), and bars represent the standard error of the mean.

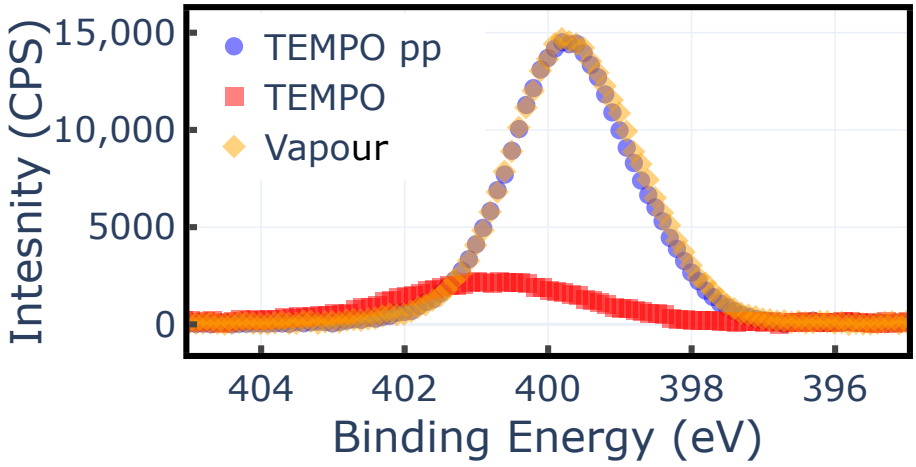

Figure 4.10: High-resolution N 1s XPS spectra of (blue dots) TEMPO pp deposited on PTFE for 50 min at 0.1 mbar and 5 W, (red squares) TEMPO vapour absorbed on PTFE for 50 min at 0.1 mbar, (orange diamonds) TEMPO vapour absorbed on TEMPO pp produced by 5 steps of 10 min of plasma polymerisation at 0.1 mbar and 5 W followed by 10 min of exposure to TEMPO vapour at 0.1 mbar.

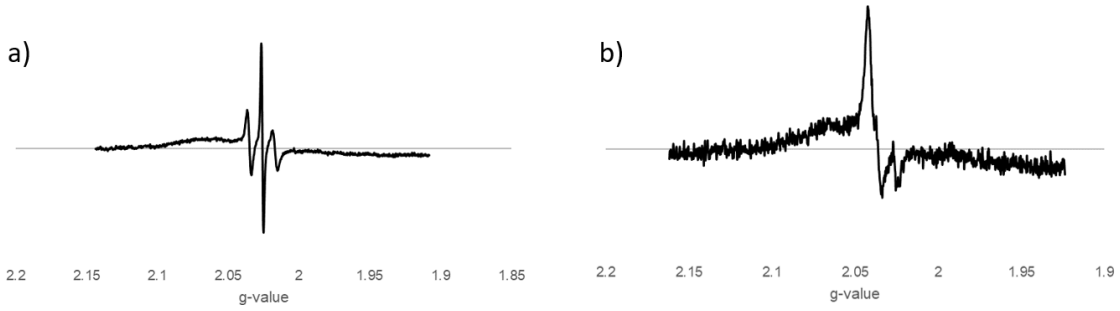

Figure 4.11: EPR spectra of (a) TEMPO vapours on PTFE and (b) TEMPO pp on PTFE produced at 0.1 mbar and 5 W. Figure courtesy of Chris Cook.

tron and the molecules can stand upright or tilted. These findings demonstrate that it is possible to deposit ordered molecular layers with a low degree of damage with plasma polymerisation, a feat not previously demonstrated. This possibility is relevant for the growth of molecular layers from liquid organic monomers incompatible with ultra-high vacuum methods. Furthermore, the study demonstrated the potential to control the order of TEMPO pp by annealing, contrary to the widespread assumption that plasma polymers are inherently disordered.

Finally, the anti-microbial activity of TEMPO pp, molecules, as well as the molecules absorbed into a TEMPO pp matrix was tested. The results show that TEMPO molecules on PTFE exhibit a significant anti-bacterial activity. However, TEMPO pp performs worse than the control, indicating that the active component of the monomer, the nitroxide radical, is lost during plasma polymerisation, as confirmed by EPR measurements. A possible strategy to improve the retention of nitroxide radicals in the plasma polymer consists of increasing the TEMPO pressure during the polymerisation process by heating the vial containing the monomer above 34 °C to melt it. Additionally, a pulsed plasma could improve the anti-microbial properties by trapping free TEMPO molecules during the growth of the polymer. While loading TEMPO molecules into TEMPO pp provided some improvement compared to pp alone, the performances are still inferior to those of pure TEMPO molecules. Other strategies to incorporate TEMPO molecules into the TEMPO pp could be devised, such as immersing the polymer into a TEMPO water solution.

Chapter 5

Isomerisation of $Cu_5[O_2]_n$ AQCs

5.1 Introduction

Atomic quantum clusters (AQCs) are assemblies of 2 to about 50 atoms [70] with sub-nanometric or nanometric dimensions. Noble metal AQCs have drawn significant attention as efficient catalysts due to high selectivity and activity in several reactions [9, 67–70], including C-C coupling [70, 102], C-N, P, O, S bonding reactions [201], CO oxidation [84, 92], and water splitting [103]. The catalytic activity of AQCs derives from the low coordination of the atoms and the high surface-to-volume ratio. The confinement of the atoms within the clusters in sub-nanometric or nanometric dimensions results in molecular-like electronic states with a HOMO-LUMO gap dependent on the atomicity [82] that can be tuned to catalyse specific reactions [82, 83]. This topic is discussed in more detail in Section 2.2.

Density functional theory (DFT) calculations show that noble metal AQCs of a few atoms exhibit 3D and 2D isomers [105, 107–109] with different electronic properties and catalytic activity [90,110–112] due to the localisation of the molecular orbitals in different parts of the AQCs [111] and different band gaps [82]. However, experimental characterisation of these isomers is sparse [64, 202] due to the challenge posed by the sub-nanometric dimensions [81, 106]. The properties of AQCs can be better studied if they are supported by a surface since a host of high-resolution techniques is available. In particular, scanning probe microscopy (SPM) [106, 202, 203] has been shown to provide detailed structural information down to the single atom level and X-ray photoelectron spectroscopy

(XPS) gives access to the chemical composition of AQCs [84, 92].

Cu_5 AQCs are predicted by DFT calculations to have 2D and 3D isomers [105, 112–114], which are expected to have a significant effect on the catalytic performances. The 2D structure is the most stable configuration in gas phase [112] and potentially when supported on a surface [65], but experimental confirmation is lacking. The isomers of $Cu_5[O_2]_n$ supported by an Au(111) surface are thus investigated in Section 5.3.1 using AFM, NIXSW, and the results are compared to DFT simulations performed by Dr Qingqing Wu and Prof Colin J. Lambert at Lancaster University. Furthermore, the oxidation state of $Cu_5[O_2]_n$ synthesised via electrochemistry method [65] is still debated [65, 116]. This question is addressed in Section 5.3.1 through XPS measurements of the Cu 2p core-level photoemission spectra and LMM Auger peak. Additionally, the unique properties of normal incidence X-ray standing waves (NIXSW) are used in Section 5.3.2 to study the isomerisation of $Cu_5[O_2]_n$ AQCs before and during the debromination of tetra (4-bromphenyl) porphyrin (Br_4TPP) molecules on Au(111). Indeed, NIXSW has been successfully used to measure the absorption height of molecules down to tens of picometers [184,185,204] by combining X-ray absorption and XPS. It also provides information on the uniformity of the absorption height [176]. Thus NIXSW offers the possibility to characterise the structure of AQCs with sub-nanometric resolution and correlate it with the chemical information.

5.2 Methods

5.2.1 Sample preparation

A high mosaicity Au(111) crystal used for NIXSW experiments performed at the Diamond Light Source and Au(111) on mica used for AFM measurements were both prepared by standard sputter-annealing cycles as described in Section 3.4.1. $Cu_5[O_2]_n$ AQCs, prepared following a previously reported method [65], were deposited as $4\,\mathrm{mg\,L^{-1}}$ solutions in Milli-Q water. The AQCs enclosed in a vial were first dispersed by ultra-sonication for 10 min in a water bath with a probe sonicator and then spin-coated on the Au(111) for 10 s at a speed of 500 RPM followed by 10 s at a speed of 2500 RPM. Br_4TPP molecules were deposited via thermal sublimation in UHV (better than 10^{-9} mbar) as discussed in Section 3.4.1.

5.2.2 XPS and NIXSW

Lab-based XPS data is acquired using a Kratos Analytical AXIS Supra spectrometer with a monochromatic Al K_α 1486.6 eV X-ray source, operating at 15 mA, 15 kV and equipped with an electron gun as charge neutraliser. Synchrotron light XPS data are collected at Diamond Light Source, beamline I09. I09 features a soft X-ray undulator, used for the acquisition of high-resolution Cu 2p, Br 3p, N 1s, C 1s, and a hard X-ray undulator, used for XSW measurements at the Au{111} Bragg energy of 2.6386 keV as measured from the reflectivity curve acquired at 77 K. The binding energy of the lab-based and synchrotron-based spectra are referenced to the Au $4f_{7/2}$ peak at 84.0 eV and Fermi edge of gold at 0 eV, respectively.

5.2.3 AFM

AFM measurements are acquired with a Bruker MultiMode 8 equipped with a Nanoscope V controller in ambient conditions in an ultra-low noise facility, IsoLab. The samples are scanned in PeakForce tapping mode using NuNano Scout 70 probes with a resonant frequency of approximately 70 kHz and nominal spring constant $2\,\mathrm{N\,m^{-1}}$ to minimise the interaction between the tip and the samples.

5.2.4 Simulations

Geometrical optimisations and Bader charge calculations of $Cu_5[O_2]_n$ on a non-reconstructed Au(111) surface were carried out by Dr Qingqing Wu and Prof Colin Lambert at Lancaster University using VASP 5.4.4 DFT codes at two levels of exchange-correlation functionals. The first one is based on the van der Waals density functional with the optimised PBE exchange functional (optPBE-vdWDF) [205, 206], the other is based on the spin-polarised Perdew-Burke-Ernzerhof (PBE) calculation plus the Becke-Jonson damping function in Grimme's D3 method [207] to include van der Waals corrections. Bader analysis method was applied to the results of spin-polarised calculation for atomic charge distributions [208–210]. The optimised structures are displayed using VESTA [211].

5.3 Results

5.3.1 2D or 3D isomer of $Cu_5[O_2]_n$ AQCs?

Simulations suggest that Cu_5 AQCs in gas phase exhibit a 2D and 3D isomer, the latter being the most energetically favourable [65, 105, 112–114]. In reality, the synthesised copper AQCs are not in gas phase but dispersed in solution or supported by a surface and, additionally, they are protected by an oxygen layer. These additional interactions could potentially affect the chemical composition and structure. Here, the isomers of $Cu_5[O_2]_n$ supported on Au(111) surface are studied using AFM and NIXSW measurements and compared to DFT simulations.

Structural properties

The structure of 2D and 3D $Cu_5[O_2]_1$ AQCs on a non-reconstructed Au(111) surface, calculated using DFT, is shown in Figure 5.1a and b, respectively. The optimised structure of 2D $Cu_5[O_2]_1$ shows that the height of the copper atoms above the surface is approximately constant, although it increases by 0.2 Å from left to right due to the weakening coupling between atoms in the cluster and gold substrate originating from the partial charge transfer to oxygen dimer from the right Cu atom [212]. No stable 2D isomers with more than one oxygen molecule are found. In the case of the 3D configuration shown in Figure 5.1b all the atoms sit at different heights above the surface with a copper atom on top of the cluster.

To experimentally determine the structure of the AQCs, they are spin-coated on an Au(111) surface at different rotational speeds in a two-step process, known to promote even drying and improve uniformity [213–215]. Among the different parameters used, only 10 s at a speed of 500 RPM followed by 10 s at a speed of 2500 RPM results in an ordered arrangement of $Cu_5[O_2]_n$, whose height can be reliably measured, as shown in Figure 5.1c. $Cu_5[O_2]_n$ AQCs form stripes arranged in a zig-zag pattern. The edges of the stripes, shown in Figure 5.1d, are blurred while the gold step edge is not, suggesting the clusters are diffusing and, hence, are not strongly interacting with each other or the gold surface. The average height of the AQCs in the stripes, shown in Figure 5.1e, is $z = 2.3 \pm 0.3$ Å. Furthermore, the line profile in Figure 5.1e shows that the stripes are approximately 5 nm apart and there is a 0.1 Å dip in the centre of each of them. These features are the fingerprints of the $22 \times \sqrt{3}$ herringbone reconstruction of the Au(111) surface [216], indicating that the AQCs preferentially bind in between face centred cubic (fcc) regions and on top of the

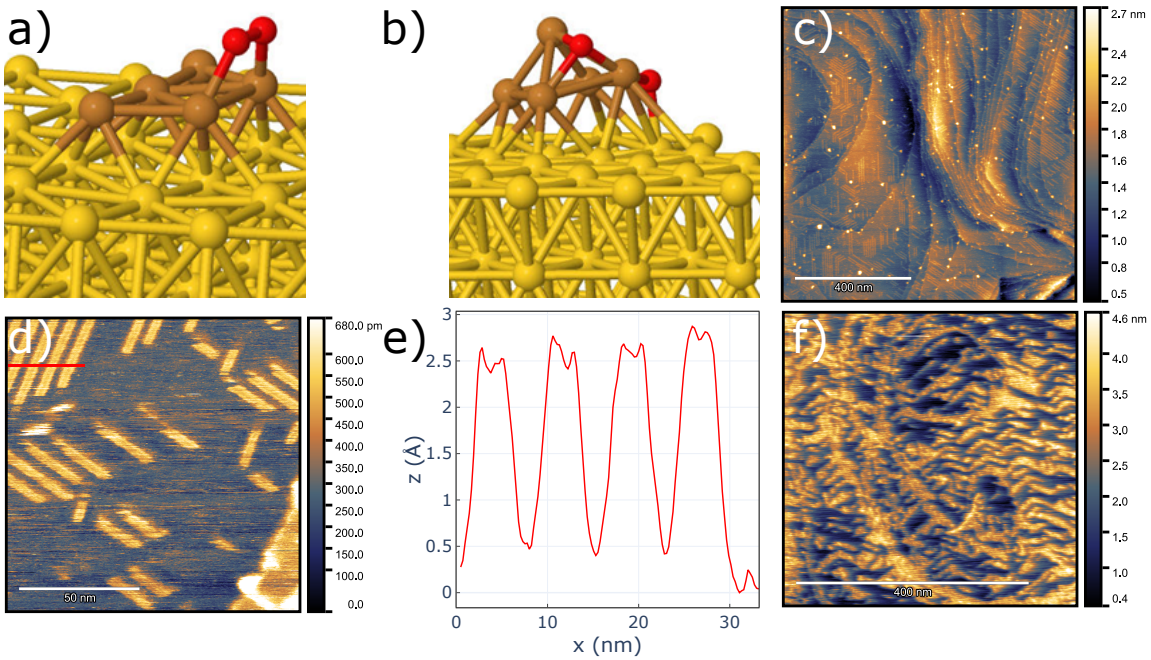

Figure 5.1: DFT simulation of (a) 2D and (b) 3D isomers of $Cu_5[O_2]_n$ on an ideal Au(111) surface. (c) AFM wide scan of $Cu_5[O_2]_n$ on Au(111) with (d) a small scan and (e) the corresponding line profile. (f) AFM wide scan of $Cu_5[O_2]_n$ after baking in the load-lock of the UHV chamber at 110 °C for 16 h. Panels a and b are courtesy of Dr. Qingqing Wu, panel d is courtesy of Leonardo Forcieri.

hexagonal close-packed (hcp) regions, as it is a highly reactive part of the surface.

Before conducting experiments in UHV such as NIXSW, the gold surface with the clusters needs to be baked to remove the water layer forming on it in ambient conditions, potentially disrupting the ordered structures of $Cu_5[O_2]_n$. Figure 5.1f shows that the stripes of AQCs survive the process of baking the gold surface on a sample plate 110 °C in the load-lock of the UHV chamber described in Section 3.4.1 for at least 16 h.

Identification of 2D $Cu_5[O_2]_n$ isomers

The information provided by the AFM is limited to small areas that might not be representative of the whole sample. Therefore, to provide more confidence in the results, NIXSW measurements are conducted at Diamond Light Source (beamline I09) since it is widely recognised as the most

accurate and precise method to determine the adsorption height in monolayers [176,204,217]. After spin-coating the AQCs on a high mosaicity Au(111) monocrystal following the method described above, the sample is cooled to liquid nitrogen temperature of 77 K for the NIXSW measurements. The position of the AQCs with respect to the non-reconstructed Au(111) surface, z, is schematically shown in Figure 5.2a. X-ray standing waves (XSW) with the same periodicity of the bulk Au(111) layer stacking, d_{111}, are generated by tuning the photon energy to match Au{111} Bragg energy of $E_{\mathrm{Bragg}} = 2.6386\,\mathrm{keV}$ (Figure 5.2a). The photoelectron intensity (relative adsorption) strongly depends on the adsorption height of the AQCs, such that an exact height above the Au(111) surface can be determined as described in Chapter 3.

The photoemission peak from the Cu $2p_{3/2}$ core-level (Figure 5.2b) is measured in different parts of the sample at different photon energies sweeping through the total reflectivity range between -5 and $+6\,\mathrm{eV}$ of E_{Bragg}. The resulting NIXSW profile, shown in Figure 5.2c, represents the change in the intensity of the Cu $2p_{3/2}$ photoemission as a function of the energy of the X-rays. The profile is best fitted to a coherent fraction and position of $Fc = 0.83 \pm 0.08$ and $Pc = 0.95 \pm 0.04$, respectively. The high coherent fraction indicates that most of the AQCs are at the same height above the Au(111) surface [176] consistent with AFM images, suggesting a uniform arrangement of $Cu_5[O_2]_n$ across the whole sample. Furthermore, this value of the coherent fraction indicates that the clusters are in a 2D configuration [218]. Indeed, if the AQCs were 3D (Figure 5.1b), the copper atoms would sit at remarkably different heights, resulting in a low coherent fraction [176]. For example, just two separate adsorption heights result in a $Fc < 0.6$ [185]. The height of the AQCs is calculated from the coherent position and $d_{111} = 2.355\,\text{Å}$ [219] using equation 3.6 resulting in $z = 2.2 \pm 0.1\,\text{Å}$. This calculation is based on the assumption that $n = 0$, as $n = 1$ would result in $z = 4.5 \pm 0.1\,\text{Å}$, which is completely different from the AFM measurements. Furthermore, the value obtained assuming $n = 0$ is more reasonable as it ranges between the spacing of the planes of Au(111) and Cu(111) bulk crystals [219]. The height derived from NIXSW measurements is the distance from a non-reconstructed Au(111) surface but the AFM measurements show that the AQCs align preferentially with the herringbone reconstruction which is at most 0.1 Å higher than the ideal surface. Hence, z is corrected by subtracting 0.1 Å, resulting in $z = 2.1 \pm 0.1\,\text{Å}$. The intense photon flux of the synchrotron light can cause damage to the sample. However, the Cu $2p_{3/2}$ core-level photoemission peaks collected before and after the NIXSW measurements shown in Figure 3.5d exhibit no changes, suggesting that the AQCs are undamaged.

In conclusion, the NIXSW measurements of the height of the clusters are in excellent agreement with the AFM data. Additionally, the high coherent fraction suggests that most of the copper atoms are at the same height indicating that the AQCs assume the structure of the 2D isomer.

Chemical composition

To determine the chemistry of the $Cu_5[O_2]_n$ AQCs on Au(111) and establish a benchmark to characterise them during the catalytic activity in Section 5.3.2, the AQCs are spin-coated on Au(111) on mica and analysed with XPS. Furthermore, DFT simulations suggest that oxygen molecules from a capping layer around the cluster [220] might influence their chemistry but the presence has not been experimentally confirmed yet.

Figure 5.3a shows the Cu 2p core-level photoemission spectrum exhibiting a sharp doublet with Cu $2p_{1/2}$ and Cu $2p_{3/2}$ components centred at 952.2 and 932.5 eV, respectively, and a weak shake-up feature around 945 eV. The position of the Cu 2p peaks is consistent with previous findings [65, 116, 221] and rules out the Cu^{+2} oxidation state [183], but it is insufficient to reliably distinguish between the Cu^{+1} and Cu^{+0} states due to the small energy difference of 0.2 eV [183]. To differentiate between the two oxidation states of copper, the Cu LMM Auger peak is measured as it is more sensitive to the bonding environment than the Cu 2p core-level [183]. Figure 5.3b shows a sharp Cu LMM peak centred at a kinetic energy of 918.4 eV with a smaller and broader peak between 920 and 922 eV. Any contributions from the Au(111) surface are ruled out as it does not exhibit a sharp peak in the same region, as shown in Figure 5.3c. However, the contribution of the substrate dominates in the region between 912 and 917 eV. A survey of the existing literature suggests that the Cu 2p and Cu LMM peak position shift depending on the size of the AQCs and the substrate they are supported by but no data are provided for Cu_5 supported on Au(111) [222]. The position of the LMM peak is in agreement with the value reported for copper Cu^{+0} films [183, 223, 224] and bulk crystals [222]. However, the shape of the Auger peak is more in line with Cu^{+1}. Based on the experimental observations, an oxidation state between Cu^{+0} and Cu^{+1} is most likely and it is referred to as $Cu^{+0/1}$. As AQCs exhibit collective orbitals similar to molecules [103, 220], the oxidation state must therefore be considered as an average across the entire cluster, and not on an atom-by-atom basis, resulting in fractional values.

The experimental results show that $Cu_5[O_2]_n$ are likely to be found in an oxidation state between Cu^{+0} and Cu^{+1} ($Cu^{+0/1}$). Furthermore, the XPS measurements indicate that the copper

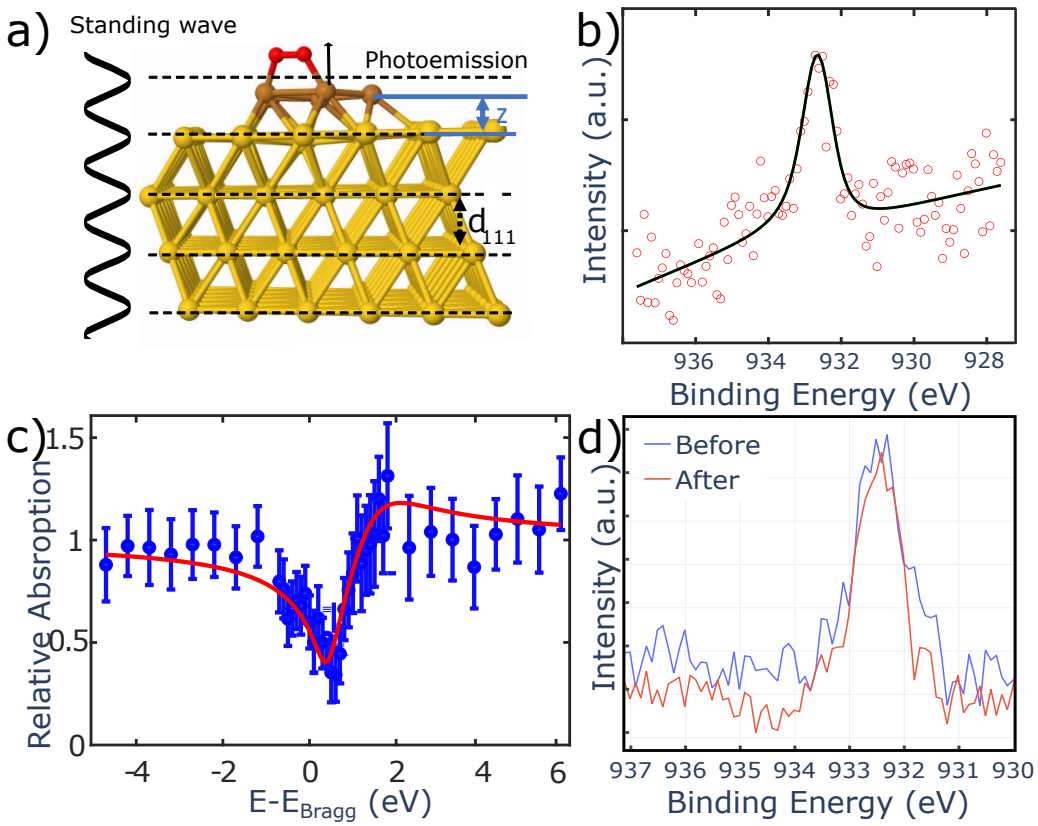

Figure 5.2: (a) Diagram of NIXSW showing the X-ray standing waves diffracted by the Au(111) surface when the X-ray energy $h\nu$ is close to the Bragg energy, E_{Bragg}. (b) Representative Cu $2p_{3/2}$ photoemission signal of $Cu_5[O_2]_n$ on Au(111) acquired at 77 K at Au{111} Bragg energy for the NIXSW measurement with the corresponding fit. (c) NIXWS of Cu $2p_{3/2}$ peak of $Cu_5[O_2]_n$ on Au(111) acquired at 77 K at Au{111} Bragg energy. Fitting analysis results in a coherent fraction and position of $Fc = 0.83 \pm 0.08$ and $Pc = 0.95 \pm 0.04$, respectively. The relative absorption error bars derive from the fits of the Cu $2p_{3/2}$ peak. (d) Cu 2p core-level photoemission spectrum of copper AQCs on Au(111) in the Cu $2p_{3/2}$ region measured at Au{111} Bragg energy before and after NIXSW measurements.

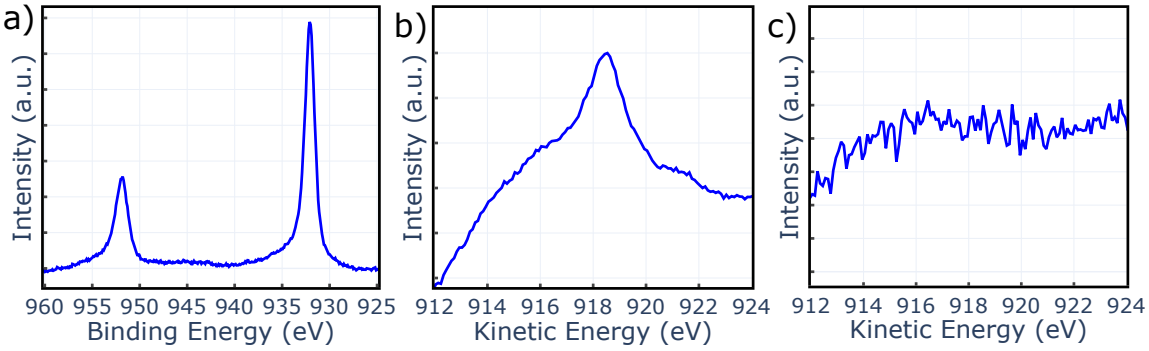

Figure 5.3: (a) Core-level photoemission spectrum of $Cu_5[O_2]_n$ AQCs on Au(111) in the Cu 2p region. Cu LMM Auger photoemission spectrum of (b) copper AQCs on Au(111) and (c) bare Au(111). Data collected at photon energy $h\nu = 1486.6\,\text{eV}$.

atoms are oxidised likely due to the absorption of less than three oxygen atoms, suggesting that a single oxygen molecule binds to each 2D cluster in agreement with the DFT simulations described above.

In conclusion, the XPS characterisation reveals that copper atoms of $Cu_5[O_2]_n$ cluster are in the oxidation state between Cu^{+0} and Cu^{+1} ($Cu^{+0/1}$), and the AFM and NIXSW that the height from the herringbone reconstruction of the Au(111) surface is $z = 2.1 \pm 0.1\,\text{Å}$.

5.3.2 2D-to-3D isomerisation of $Cu_5[O_2]_n$ AQCs during on-surface Ullmann coupling

To characterise the chemical composition and try to identify the transition to the 3D isomer of AQCs, $Cu_5[O_2]_n$ are used to catalyse the debromination of 4-(tetrabromophenyl) porphyrin (Br_4TPP). Although the Au(111) surface can catalyse the debromination, a previous study shows that $Cu_5[O_2]_n$ initiate the reaction at a significantly lower temperature such that the contribution of the surface can be neglected. This topic is discussed in the thesis of Leonardo Forcieri from Lancaster University, which is not yet published at the time of the writing of this thesis. In the following section, the Br_4TPP molecules (Figure 5.4a) are characterised to establish a baseline before studying the debromination reaction.

Characterisation of Br_4TPP

Br_4TPP molecules are thermally evaporated on a clean Au(111) surface as described in Section 3.4.1 to form a sub-monolayer coverage as shown in Figure 5.4b. The molecules arrange into flat islands approximately 4 Å in height as shown in Figure 5.4c. Furthermore, Br_4TPP are easily disturbed by AFM scanning at low set point forces as low as 125 pN as the island shape changes with each AFM scan, suggesting that the molecules are highly mobile on the Au(111) surface.

The quality of the Br_4TPP molecules is assessed using XPS. The C 1s core-level photoemission spectrum shown in Figure 5.4c exhibits a peak centred at 284.1 eV due to the phenyl rings (phenyl) with a contribution of C-C/H (sp^3 hybridisation) at 283.7 eV from the carbon atoms joining the rings of the macrocycle and the phenyl groups. The components at higher binding energy are assigned to the carbon-pyrrolic nitrogen (C=N) and carbon-phenyl bonds (C-Ph) at 284.7 eV, carbon-bromine (C-Br) and carbon-imidic nitrogen bonds (C-NH) at 285.1 eV, and the $\pi - \pi^*$ shake-up at 286.8 eV. The position of the components is in excellent agreement with references [225, 226] as the data are calibrated to the Fermi edge of gold in both cases.

The core-level photoemission spectrum collected in the Br 3p region shown in Figure 5.4d exhibits the bromine doublet with the Br $3p_{3/2}$ and Br $3p_{1/2}$ components at 183.5 and 190.5 eV, respectively. These binding energies are in agreement with the C-Br bonds reported in the literature [227].

The XPS data collected in the N 1s region shown in Figure 5.4f exhibits four different peaks: the two components at 399.3 and 400 eV are assigned to the pyrrolic nitrogen (=N-) and the pyrrolic nitrogen interacting with the Au surface (=N-Au); the two components at 397.2 and 397.7 eV are assigned to the imidic nitrogen (-NH-) and the imidic nitrogen interacting with the Au surface (-NH-Au). The structure and the binding energy of the nitrogen components are in excellent agreement with the literature [225] and confirm that the nitrogen environment of the porphyrin core is pristine. The presence of the N-Au signal in the XPS spectra is assigned to the interaction between the molecules and the gold adatoms freely diffusing from the step edges to the surface [225], confirming that there is a monolayer or sub-monolayer coverage of Br_4TPP.

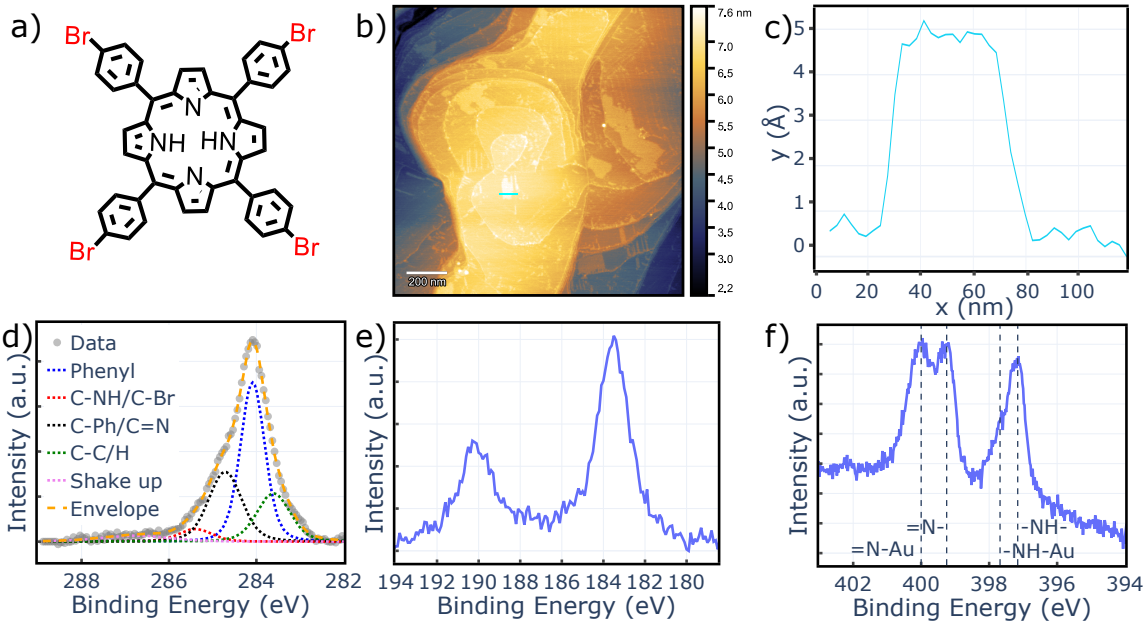

Figure 5.4: (a) Diagram of Br_4TPP structure. (b) AFM topographic image of Br_4TPP on Au(111) with (c) the respective line profile. Core-level photoemission spectrum of Br_4TPP on Au(111) in (d) C 1s, (e) Br 3p, and (f) N 1s region. The C 1s peak in panel d is fitted with five components: C-C/H (sp^3 hybridisation) at 283.7 eV, phenyl ring at 284.1 eV, C-Ph/C=N at 284.7 eV, C-NH/C-Br bonds at 285.1 eV, and the $\pi - \pi^*$ shake up at 286.8 eV. Vertical lines in panel f correspond to imidic (-NH-) and pyrrolic (=N-) components and the same components shifted by interaction with the gold surface, =N-Au and -NH-Au, respectively. Data in panels d and e is acquired at photon energy $h\nu = 900.0$ eV, data in panel f is acquired at photon energy $h\nu = 600.0$ eV.

2D-to-3D isomerisation of $Cu_5[O_2]_n$

To study the isomerisation of $Cu_5[O_2]_n$ during the debromination of Br_4TPP, the AQCs are spin-coated on top of a thermally evaporated Br_4TPP layer discussed in the section above. The sample is heated starting from an initial temperature of 290 K to induce the debromination while collecting Br $3p_{3/2}$ core-level photoemission spectra. Figure 5.5a shows that the Br $3p_{3/2}$ peak intensity progressively decreases and disappears completely at 380 K, indicating that the molecules are progressively debrominated and that bromine atoms desorb from the surface at 380 K. Furthermore, Figure 5.5b shows a shift of 0.15 eV in the C 1s peak at 380 K, suggesting a change in the phenyl groups of the Br_4TPP as previously reported in the literature [225]. This indicates that a reaction is occurring, however, this data is limited and the concept is further discussed in Chapter 6 where additional spectra on mica are shown. The Cu $2p_{3/2}$ core-level photoemission peak acquired at 290 and 380 K shown in 5.5c exhibits two well-separated components centred at 932.5 and 934.2 eV. The former is consistent with the $Cu^{+0/1}$ peak shown in Figure 5.3b, the latter is assigned to a fraction of copper in oxidation state Cu^{+2} [183]. The presence of Cu^{+2} at 290 K suggests an interaction between the molecules and the AQCs. When the sample is annealed until the debromination has been completed at 380 K, the Cu^{+2} signal intensifies. Based on the absence of bromine, the Cu^{+2} component is assigned to the formation of the C-Cu-C bonds between the $Cu_5[O_2]_n$ and the debrominated Br_4TPP, as established for the dehalogenation of aryl halides on Cu(111) [20, 167, 227, 228], namely the organometallic phase, schematically shown in Figure 5.5d. The change in the oxidation state of copper atoms indicates a charge transfer in agreement with DFT simulations of the reaction of aryl halides on Cu(111) and Au(111) surfaces as well as gold nanoparticles [91, 115]. However, the number of electrons of the surfaces is disproportionately bigger than the number of electrons in the aryl halides resulting in no change of the formal charge. The observed shift in the copper peak of the sub-nanometric AQCs is thought to derive from the limited availability of electrons in the $Cu_5[O_2]_n$ AQCs and the possibility of several molecules reacting with the same cluster.

The Cu^{+2} to $Cu^{+0/1}$ components are markers of organometallic and non-interacting copper AQCs, respectively. Consequently, it is possible to track the height of the AQCs in the two different chemical states by fitting the NIXSW data of each component individually as shown in Figure 5.6a. After completing the debromination at 380 K, the sample is cooled down at 77 K and the Cu $2p_{3/2}$ core-level photoemission peak is excited by X-rays at the Bragg energy of Au{111}, as described

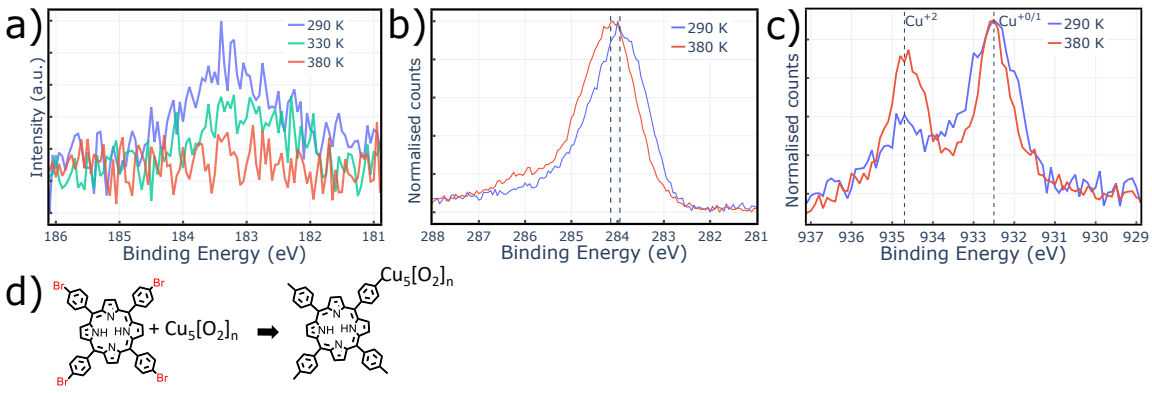

Figure 5.5: (a) Br 3p core-level photoemission spectrum of Br_4TPP on Au(111) with $Cu_5[O_2]_n$ AQCs at 290 K (blue), 330 K (green), and 380 K (red) (photon energy $h\nu$ = 900 eV). (b) C 1s core-level photoemission spectrum of Br_4TPP on Au(111) at 290 K (blue) and 380 K (red) with vertical line at 284.1 eV and 283.95 eV. (c) Normalised Cu $2p_{3/2}$ core-level photoemission spectrum of $Cu_5[O_2]_n$ AQCs on Br_4TPP on Au(111) at 290 K (blue) and 380 K (red) acquired at Au{111} Bragg energy showing two components corresponding to $Cu^{+0/1}$ (non-interacting) and Cu^{+2} (organometallic) at 932.5 eV and 934.2 eV, respectively. (d) Schematic of Br_4TPP debromination catalysed by $Cu_5[O_2]_n$.

for AQCs on Au(111) in Section 5.3.1. Figure 5.6b shows that the NIXSW profile of the $Cu^{+0/1}$ component is best fitted by $Fc = 0.8 \pm 0.1$ and $Pc = 0.97 \pm 0.05$, in excellent agreement with the surface-supported AQCs shown in Figure 5.2c. The results translate to a corrected height $z_{\text{non-interacting}} = 2.1 \pm 0.1$ Å.

The NIXSW profile of the Cu^{+2} component shown in Figure 5.6c is significantly different from the previous one. The data are best fitted by the parameters $Fc = 0.4 \pm 0.2$ and $Pc = 0.4 \pm 0.1$. The lower coherent fraction compared to the 2D AQCs suggests that the copper atoms are at different heights, in agreement with the three-dimensional structure hypothesis. The coherent positions differ significantly compared to the $Cu^{+0/1}$ component, indicating that the Cu atoms in the Cu^{+2} oxidation state are at a different height. Indeed, the organometallic copper atoms sit at $z_{\text{organometallic}} = 3.3 \pm 0.2$ Å above the Au(111) surface. This value is computed using equation 3.6 and assuming that $n = 1$, as the assumption that $n = 0$ would result in a height of 1.0 Å that is close enough to generate a significant repulsion from the underlying Au(111) surface. Furthermore, the low coherent fraction suggests $z_{\text{organometallic}}$ is the average of a height distribution with a wide variance, likely because AQCs assume a variety of 3D configurations and a different number of molecules are interacting with each cluster. The observation of a height change combined with the chemical shift in the Cu 2p spectrum is compatible with a 2D-to-3D isomerisation. Furthermore, the change in the oxidation state of copper suggests that a charge transfer from the clusters to the molecules is occurring. This experimental evidence is in agreement with DFT simulations in the literature showing that the removal of a single electron [105, 113, 114] and the interactions with other molecules, such as oxygen [103, 110], can induce a 2D-to-3D transition in AQCs. These findings highlight the correlation between the isomers and the catalytic activity of $Cu_5[O_2]_n$. The intense photon flux of the synchrotron radiation can cause damage to the sample. However, the Cu $2p_{3/2}$ core-level photoemission peaks collected before and after the NIXSW measurements shown in Figure 5.6d exhibit no changes, suggesting that the AQCs are undamaged.

DFT is used to simulate the interaction between $Cu_5[O_2]_1$ AQCs and phenyl radicals, which are proxies for the whole Br_4TPP molecules. Figure 5.7a shows two phenyl radicals attached to a 2D $Cu_5[O_2]_1$ AQCs before optimisation. Figure 5.7b shows that after the geometrical optimisation, the structure of the clusters becomes 3D, suggesting that the 2D isomer becomes unstable when interacting with the radicals. By removing the oxygen dimer from the structure, the case of bare

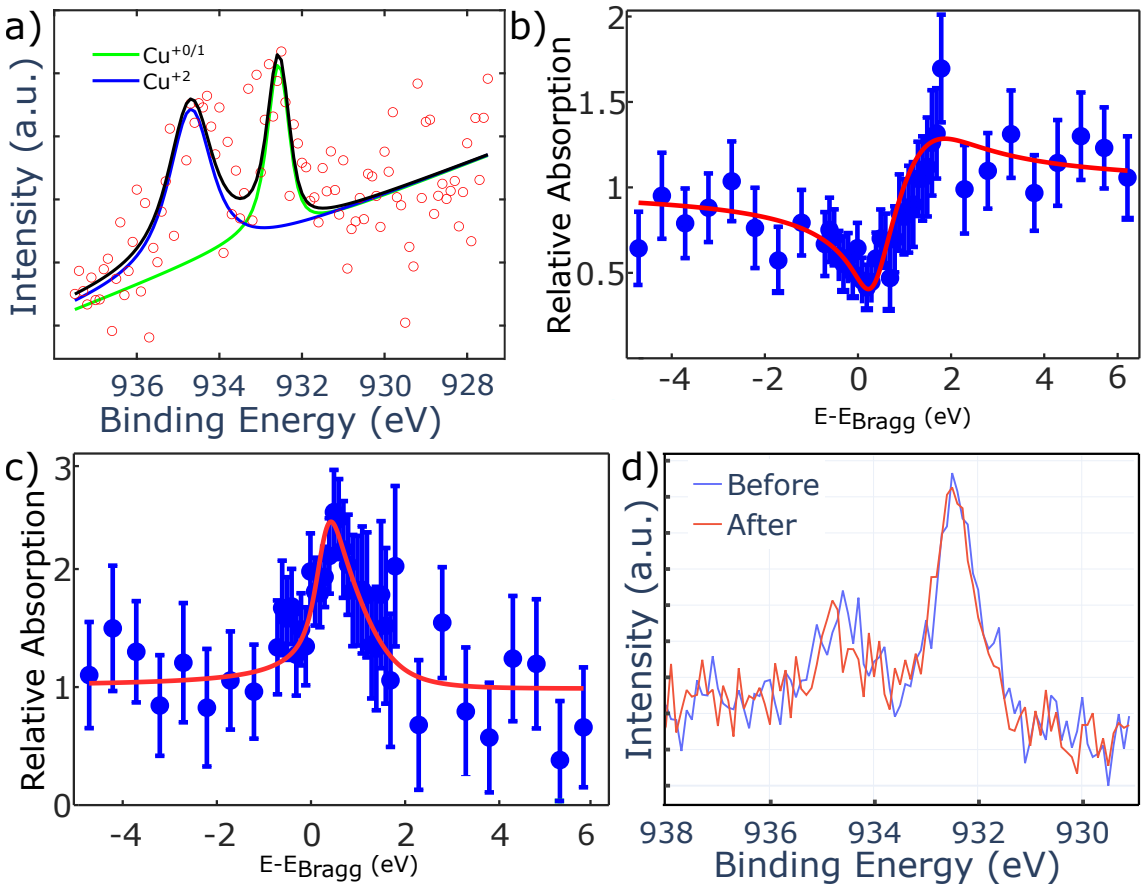

Figure 5.6: (a) Representative NIXSW data and corresponding fits of Cu $2p_{3/2}$ region on Au(111) acquired at 77 K at Au{111} Bragg energy. NIXWS of (b) $Cu^{+0/1}$ and (c) Cu^{+2} components of Cu $2p_{3/2}$ peak of $Cu_5[O_2]_n$ with Br_4TPP on (111) after annealing at 380 K. Data is acquired at 77 K at Au{111} Bragg energy and the fitting analysis results in a coherent fraction and position of $Fc = 0.8 \pm 0.1$ and $Pc = 0.97 \pm 0.05$ as well as $Fc = 0.4 \pm 0.24$ and $Pc = 0.4 \pm 0.1$, for panel b and c respectively. The relative absorption error bars derive from the fits of Cu 2p components. (d) Cu 2p core-level photoemission spectrum of copper AQCs on Au(111) in the Cu 2p region measured at Au{111} Bragg energy before and after NIXSW measurements.

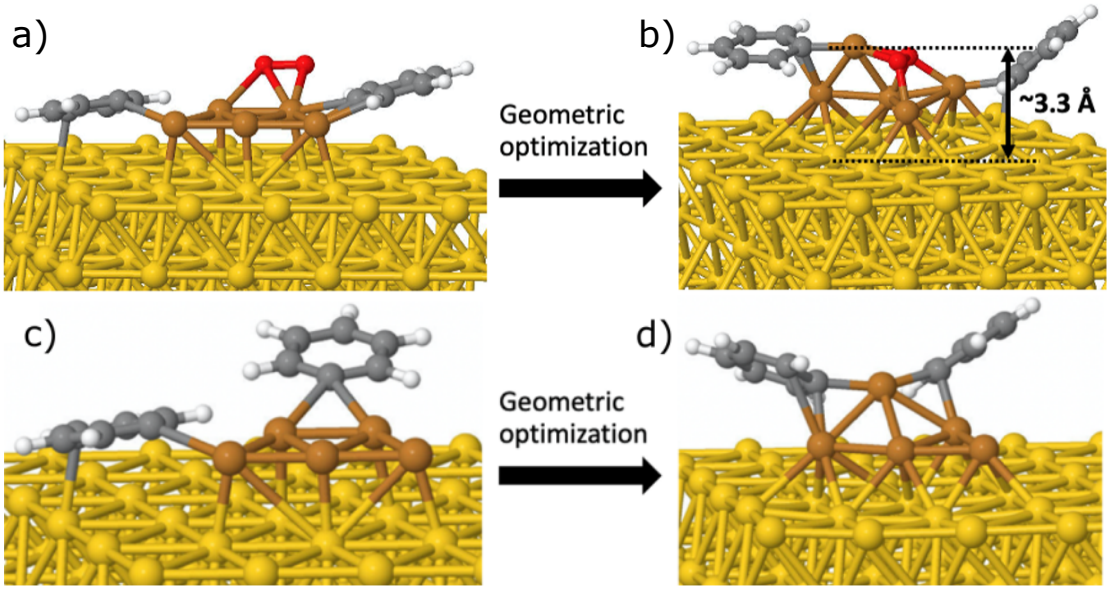

Figure 5.7: (a,b) 2D-to-3D transition of the organometallic phase of $Cu_5[O_2]_1$ AQC-phenyl radical simulated with DFT. (c,d) 2D-to-3D transition of the organometallic phase of Cu_5 AQC-phenyl radical simulated with DFT. Figure courtesy of Dr. Qingqing Wu.

Cu_5 with two phenyl rings is simulated to understand the effect of the absorbed oxygen molecules. First, the 2D to 3D transition still occurs as shown in Figure 5.7c and d. Second, the oxygen attracts a fraction of charges from Cu_5, therefore fewer electrons are transferred to the phenyl rings, weakening their coupling with the copper atoms. This phenomenon results in the promotion of the diffusion and recombination of the two phenyl rings, potentially favouring polymerisation.

In conclusion, the $Cu_5[O_2]_n$ oxidation state partially evolves from $Cu^{+0/1}$ to Cu^{+2} upon the debromination of Br_4TPP, likely due to the formation of Cu-C bonds between AQCs and molecules. At the same time, the copper atoms in the $Cu^{+0/1}$ oxidation state remain at the same height, $z_{\text{non-interacting}} = 2.1 \pm 0.1$ Å, uniformly across the sample as in the absence of Br_4TPP. On the other hand, the height of the copper atoms in the Cu^{+2} oxidation state becomes $z_{\text{organometallic}} = 3.3 \pm 0.2$ Å likely due to a 3D isomerisation caused by the interaction with the debrominated Br_4TPP. This point is supported by the low coherent fraction and by DFT simulations showing that the 2D $Cu_5[O_2]_1$ and Cu_5 AQCs become 3D upon interaction with two phenyl radicals.

5.4 Conclusions and future work

In the chapter, the presence of 2D and 3D isomers of $Cu_5[O_2]_n$ AQCs supported by an Au(111) surface was investigated. The correlation between the chemistry and isomeric structure during the catalytic debromination of Br_4TPP is studied using AFM, XPS, NIXSW, and DFT simulations.

For the first time, the height of $Cu_5[O_2]_n$, spin-coated on an Au(111) surface, is experimentally determined to be $z = 2.1 \pm 0.1$ Å using AFM and NIXSW. The high coherent fraction of 0.83 ± 0.08 suggests that most of the copper atoms sit at a similar height from the surface indicating that the AQCs are 2D. The structural and catalytic properties of the $Cu_5[O_2]_n$ AQCs are studied by catalysing the debromination of Br_4TPP molecules. When the reaction has completed, the chemistry of the copper atoms in the AQCs partially changes from $Cu^{+0/1}$ to Cu^{+2} suggesting an interaction between clusters and molecules. At the same time, the height of the AQCs interacting with the molecules becomes $z_{\text{organometallic}} = 3.3 \pm 0.2$ Å, suggesting a transition to a 3D structure, further confirmed by the reduced coherent fraction. The experimental evidence is substantiated by DFT simulations showing a 2D-to-3D transition of $Cu_5[O_2]_n$ AQCs upon interaction with phenyl radicals. These results highlight the role of isomers in determining the catalytic activity and the importance of allowing for structural changes in DFT simulations of AQCs reactions.

To further improve the understanding of the isomers, the AQCs could be decoupled from the Au(111) surface using an atomically flat insulating layer as interaction with gold cannot be neglected. It was not possible to study with NIXSW the next stage of the reaction between Br_4TPP molecules due to the limited time available at Diamond light source. However, it could be interesting in the future to anneal $Cu_5[O_2]_n$ AQCs and Br_4TPP molecules until the C-Cu bonds are cleaved to identify whether the clusters revert to the 2D structure after catalysing the reaction. Additionally, different catalytic processes involving AQCs could be studied on technologically relevant surfaces such as SiO_2, TiO_2, or hexagonal boron nitride.

The presence of a single oxygen molecule bound to the AQCs is predicted by DFT and inferred from XPS measurements. In the future, it could be of interest to count the number of oxygen on single clusters using qPlus AFM and study the effect of the absorbed oxygen on the band gap and electronic states of AQCs using low-temperature STM in imaging and spectroscopy mode.

Chapter 6

Polymerisation of Br_4TPP on inert surfaces using AQCs

6.1 Introduction

On-surface polymerisation on semiconductors and insulators is essential for better exploiting the polymers for applications but it is extremely challenging [14, 26, 55]. Without a catalyst, precursor molecules sooner desorb from surfaces before they can polymerise, greatly limiting the ability to prepare surface polymers on non-metal substrates. Several strategies have been designed to address this issue ranging from decoupling layers [51], light to activate the reaction [12] or anchor groups to strongly adsorb molecules on surface [56], and single metal atoms as extrinsic catalysts [50,60,61], as discussed in Section 2.1. However, a general strategy to grow polymers using a plethora of different molecules without the need for specialised structures or processes is missing.

The use of extrinsic metal catalysts, instead of coinage metal surfaces, offers the possibility to activate the polymerisation of a variety of molecules on different surfaces and avoid desorption at the same time. Moreover, it provides the possibility of controlling the activation, diffusion, and coupling barriers involved in Ullmann coupling discussed in Section 2.1. Single atoms have been reported to catalyse on-surface polymerisation but they can poison the polymer growth by sintering together [50]. The use of AQCs, $Cu_5[O_2]_n$ and $Ag_5[O_2]_n$, introduced in Section 2.2 to induce the on-surface polymerisation of tetra (4-bromophenyl) porphyrin (Br_4TPP) on inert surfaces is

explored. The interest in these clusters derives from the high catalytic activity combined with thermal stability and resistance to sintering [90, 110], thereby potentially overcoming the issues related to the use of single atoms. Copper and silver clusters are investigated as replacements for copper and silver surfaces since they are the most active towards Ullmann coupling [29].

The catalytic properties of $Cu_5[O_2]_n$ and $Ag_5[O_2]_n$ towards the Ullmann coupling of Br_4TPP on HOPG and mica are investigated in Section 6.3 and 6.4, respectively. The substrates are chosen as flat and non-catalytic surfaces, HOPG is a zero-band gap semiconductor, and mica is a bulk insulator. To this end, the catalytic activity of the clusters is studied with temperature-programmed XPS (TP-XPS) by comparing the reaction in the absence and presence of the clusters. Furthermore, the morphological properties of the Br_4TPP polymers produced using $Cu_5[O_2]_n$ are studied with AFM under ambient conditions.

6.2 Methodology

6.2.1 Sample preparation

Before sample preparation, the HOPG and mica surfaces were cleaned as discussed in Section 3.4.1. $Cu_5[O_2]_n$ AQCs, prepared following a previously reported method [65], are deposited before the molecular deposition as $4\,\mathrm{mg\,L^{-1}}$ solutions in Milli-Q water. Similarly, $Ag_5[O_2]_n$ AQCs, prepared following a previously reported method [71], were deposited before the molecular deposition as $4\,\mathrm{mg\,L^{-1}}$ and $96.8\,\mathrm{mg\,L^{-1}}$ solutions in Milli-Q water on mica and HOPG, respectively. The AQCs were first dispersed by ultrasonication for 10 min and then spin-coated for 10 s at a speed of 500 RPM followed by 10 s at a speed of 1500 RPM. HOPG and mica surfaces were then annealed at 130 °C in UHV conditions to remove contaminants and water. Br_4TPP molecules were deposited via thermal sublimation in UHV (better than 10^{-9} mbar) as discussed in Section 3.4.1. The preparation of samples without clusters followed the procedure described above but no cluster was spin-coated on the substrates.

6.2.2 Temperature-programmed XPS

Temperature-programmed XPS consist of collecting XPS spectra as the sample is heated in a specially designed sample bar with a PID system to control the temperature and the heating ramp. The samples are heated from $25 - 30\,^{\circ}\mathrm{C}$ to $400\,^{\circ}\mathrm{C}$ at a rate ranging from 0.1 to $0.4\,^{\circ}\mathrm{C/min}$, at a pressure below 10^{-9} mbar. All the measurements are performed using a Kratos AXIS Supra spectrometer with monochromatic Al K_α X-ray source, operating at 15 kV, 15 mA, and equipped with an electron gun for charge neutralisation.

TP-XPS data is displayed as a heat map with the temperature on the y-axis, the binding energy on the x-axis, and the counts per second (CPS) as the colour scale. Bright colours indicate high CPS and, thus, the presence of peaks; dark colours indicate low CPS, representing the background. The uncertainty in the temperature is estimated as the temperature difference between the start and the end of each XPS measurement, ranging from 10 to $20\,^{\circ}\mathrm{C}$.

6.2.3 AFM

AFM measurements are acquired with a Bruker MultiMode 8 equipped with a Nanoscope V controller in ambient conditions in an ultra-low-noise facility, IsoLab. These measurements are acquired in PeakForce mode using NuNano Scout 70 probes with a resonant frequency of approximately 70 kHz and nominal spring constant $2\,\mathrm{N\,m^{-1}}$ to minimise the interaction between the tip and samples.

6.3 Results and discussion: $Cu_5[O_2]_n$ AQCs

In the following sections, the use of $Cu_5[O_2]_n$ AQCs as extrinsic catalysts for the on-surface polymerisation of Br_4TPP on HOPG and mica is studied with TP-XPS and AFM.

6.3.1 Polymerisation on HOPG

To study the catalytic activity of $Cu_5[O_2]_n$ towards the on-surface polymerisation of Br_4TPP on HOPG (Figure 6.1a), the reaction between the molecules without and with $Cu_5[O_2]_n$ are compared. The TP-XPS results are shown in Figure 6.2. The first step of the Br_4TPP polymerisation is the

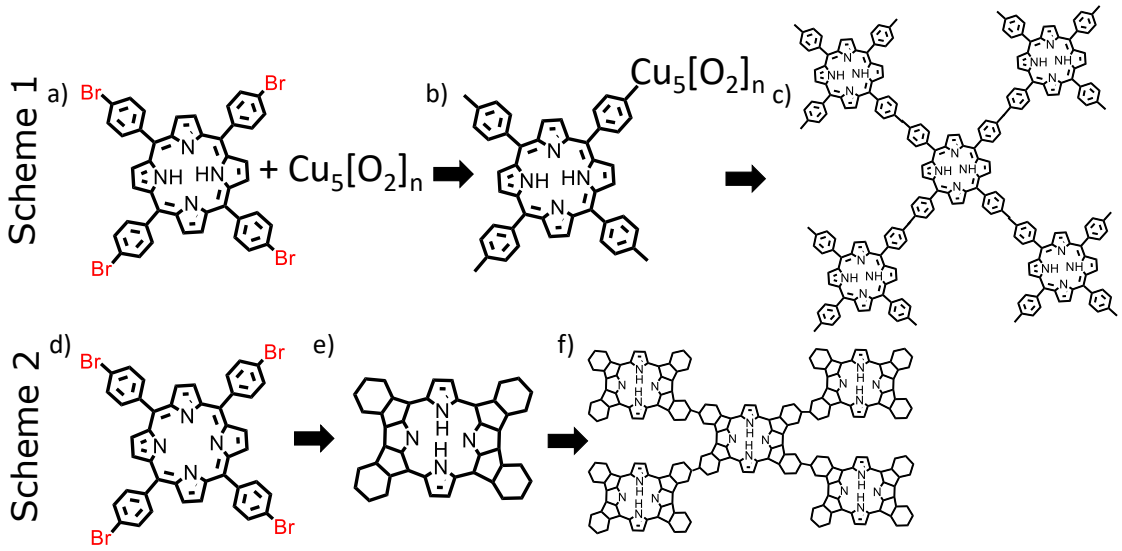

Figure 6.1: Scheme 1. (a) Br_4TPP and $Cu_5[O_2]_n$ clusters. (b) The first step of the Br_4TPP Ullmann coupling is the dehalogenation of the monomer resulting in the formation of the metalorganic phase (C-Cu bonds). (c) The molecules link into a polymer by ejecting the clusters. Scheme 2. (d) Damage to the imidic nitrogen (-NH-) of the porphyrin macrocycle results in the formation of pyrrolic nitrogen atoms (=N-). (e) Porphyrin molecules after ring-closing reaction due to the cyclodehydrogenation between phenyl groups and the porphyrin macrocycle. (f) Tentative schematic of a polymer of cyclodehydrogenated porphyrins.

activation through C-Br bond cleavage (Figure 6.1b) that is monitored through high-resolution XPS measurements in the Br 3p region. In the absence of clusters (Figure 6.2a), the Br 3p doublet is detected at temperatures as high as $300 \pm 10\,^{\circ}\mathrm{C}$. When $Cu_5[O_2]_n$ and Br_4TPP are present at the same time (Figure 6.2b), the bromine peaks are less intense at room temperature, whereby only the Br $3p_{3/2}$ component is distinguishable. The signal completely disappears at $125 \pm 20\,^{\circ}\mathrm{C}$, as shown in Figure 6.2c, pointing at the C-Br bond cleavage and the desorption of the halogen atoms. These results indicate that the $Cu_5[O_2]_n$ are effective catalysts for the debromination of Br_4TPP on HOPG.

The C-C coupling, the final step of Br_4TPP polymerisation, could be studied by analysing the C 1s peak but the signal is dominated by photoemission from the graphite substrate. Consequently, the presence of Br_4TPP on the surface is checked through the photoemission from the N 1s core-level of the porphyrin core. The presence of the N 1s peak of Br_4TPP without and with clusters provides indirect evidence of the polymerisation of Br_4TPP. Indeed, the polymer should be thermally stable and desorb at a higher temperature than the individual monomers do. TP-XPS data of Br_4TPP molecules on HOPG (Figure 6.2d) shows that the N 1s peak disappears at $310 \pm 10\,^{\circ}\mathrm{C}$, indicating that the molecules desorb from the surface. This observation shed light on the disappearance of the Br 3p peak reported in Figure 6.2a. The molecules desorb without the carbon-bromine bond cleavage, indicating that the activation of Ullmann coupling of Br_4TPP on HOPG is impossible without the use of a catalyst as the molecules desorb before the reaction starts, as reported before [41]. The TP-XPS data collected in the N 1s region when both molecules and the AQCs are deposited on HOPG is shown in Figure 6.2e. The nitrogen peak is detected at temperatures as high as $400 \pm 20\,^{\circ}\mathrm{C}$, well above the desorption temperature of the monomer as shown in Figure 6.2f by overlapping the spectra collected at $400\,^{\circ}\mathrm{C}$ in Figure 6.2d,e. Interestingly, the centre of the N 1s peak shifts from 399.3 eV to 398.5 eV while the width remains constant during the on-surface polymerisation with the clusters, pointing at a change in the core of the porphyrin macrocycle. Based on the literature [225, 229–231], the shift could be assigned to two different processes. First, the dehydrogenation of the pyrrolic nitrogen (-NH-) could be caused by the interaction with the metal clusters as shown in Figure 6.1d, namely self-metalation. Second, it could be caused by a transition from a multilayer to a monolayer of Br_4TPP molecules [231]. In the first case, the N 1s peak width decreases significantly because there is only a single bonding environment (=N- in Figure 6.1e) [225, 230, 231]; in the second case, the peaks shift to lower binding energies. Although

the resolution of the peaks acquired with a lab-based XPS is not good enough to resolve the pyrrolic (-NH- at 400.3 eV) and imidic (=N- at 398.3 eV) nitrogen components of the N 1s peak, the constant width of the peak suggests that the two components are still present, pointing at a transition to monolayer [231].

To investigate the role of $Cu_5[O_2]_n$ in the Br_4TPP on-surface polymerisation, the high-resolution XPS spectrum of Cu $2p_{3/2}$ core-level is acquired during the reaction, as shown in Figure 6.2h. The centre of the peak shift from 932.5 eV at room temperature to 933.0 eV in the temperature range of $125 - 300\,^{\circ}C$, and the back to 932.5 eV at higher temperatures, as shown in Figure 6.2i. The component at 932.5 eV could be assigned to both Cu^{+0} and Cu^{+1} due to the small energy difference but the findings of Chapter 5 suggest that a mixed state is most likely. The shift in the Cu $2p_{3/2}$ peak to 933.0 eV indicates a partial change of the oxidation state of the clusters to Cu^{+2} during the on-surface polymerisation, in agreement with the findings of Chapter 5. The onset of the shift coincides with the debromination temperature, suggesting that the clusters interact with the only species left on the surface, i.e. the debrominated Br_4TPP (Figure 6.1b). This conclusion is compatible with evidence of the formation of C-Cu bonds between the adatoms of the copper surface and the dehalogenated aryl halides in on-surface Ullmann coupling published in the literature [20, 41, 167]. Additionally, the shift at higher binding energy suggests a partial transfer of electrons from clusters to the monomers. At temperatures higher than $300\,^{\circ}C$, the Cu $2p_{3/2}$ peak shifts back to 932.5 eV, indicating that the clusters return to their initial chemical state, likely because the C-Cu bonds are replaced by C-C during the monomer polymerisation. These observations prove that $Cu_5[O_2]_n$ clusters indeed behave like catalysts in the Ullmann coupling of Br_4TPP as they revert to the initial chemical state.

To further study the reaction between Br_4TPP molecules, AFM images of the sample comprising Br_4TPP with $Cu_5[O_2]_n$ AQCs are compared to a set of controls consisting of HOPG only, $Cu_5[O_2]_n$ AQCs on HOPG, and Br_4TPP on HOPG (Figure 6.3). All the samples are compared at room temperature and after 30 min of annealing in UHV at $150\,^{\circ}C$, a temperature high enough to induce the monomer debromination as shown in Figure 6.2b.

The AFM images of HOPG at room temperature and after annealing (Figure 6.3a,e respectively) show no damage to the substrates as the roughness remains the same because the height fluctuations shown in the line profiles do not exceed 0.150 nm. The AFM image of the $Cu_5[O_2]_n$

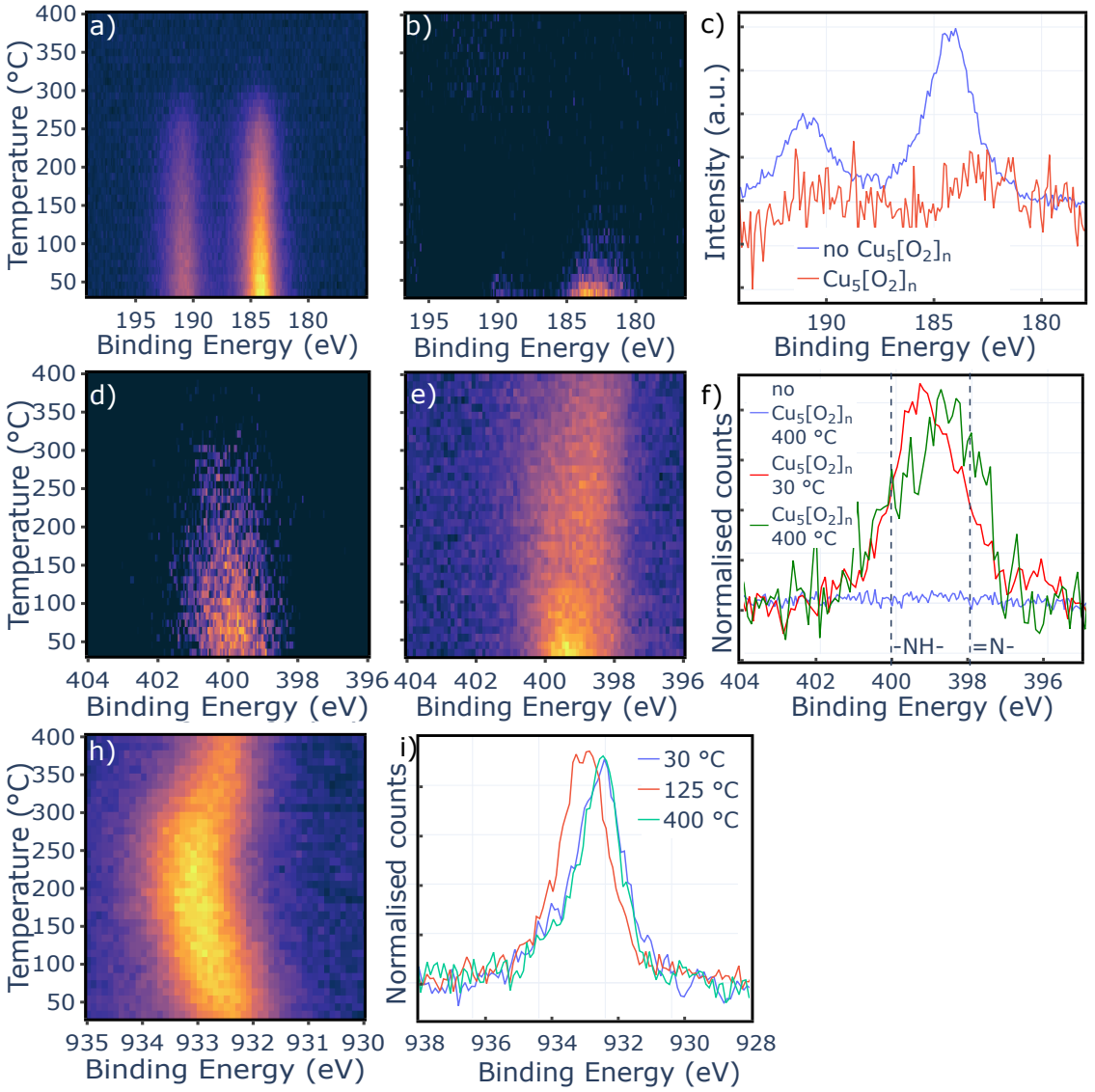

Figure 6.2: Temperature-programmed XPS in Br 3p region of Br_4TPP on HOPG (a) without and (b) with $Cu_5[O_2]_n$. (c) High-resolution XPS spectrum of Br_4TPP in Br 3p region without and with $Cu_5[O_2]_n$ showing the complete debromination at $125 \pm 20\,°C$ in presence of $Cu_5[O_2]_n$. Temperature-programmed XPS in N 1s region of Br_4TPP (d) without and (e) with $Cu_5[O_2]_n$. (f) High-resolution XPS spectrum of Br_4TPP in N 1s region at 400 °C without $Cu_5[O_2]_n$ as well as at 30 and 400 °C with $Cu_5[O_2]_n$. (h) Temperature-programmed XPS in Cu $2p_{3/2}$ region of Br_4TPP with $Cu_5[O_2]_n$. (i) High-resolution XPS spectrum of $Cu_5[O_2]_n$ in Cu 2p region at 30, 125, and 400 °C showing that shift in the peak. All data are referenced to C 1s s-p^2 at 284.5 eV.

clusters on HOPG at room temperature (Figure 6.3b) shows that they form agglomerates of approximately 0.8 nm in height, as shown in the line profile. This height exceeds the dimension of a single cluster, suggesting a preferential interaction with themselves rather than with the substrate (Volmer-Weber growth). After the annealing at 150 °C (Figure 6.3 f), the clusters are still found in agglomerates approximately between 0.3 and 0.8 nm in height as shown in the line profile. However, a significant amount of AQCs is located at the step edges of the HOPG likely because they are the most reactive sites of the substrate. These results indicate that the clusters are thermally stable at this temperature as discussed in Section 2.2. Br_4TPP molecules form flat islands on HOPG 0.5 nm in height, as shown in Figure 6.3c. Upon annealing at 150 °C, the molecules remain on the surface (Figure 6.3g) in accordance with the TP-XPS data in Figure 6.2d and are found in flat islands 0.5 nm in height as before the annealing. When both clusters and molecules are present on the surface at the same time (Figure 6.3d), only agglomerate of approximately 0.8 nm are found on the substrate but no islands, suggesting that the molecules are attached to the clusters. Upon annealing at 150 °C (Figure 6.3h), small disordered agglomerates of different heights are found on the surface. They are tentatively assigned to the metalorganic phase detected in the TP-XPS. Despite many attempts, only small amounts of material at the step edges of HOPG are observed upon annealing at 400 °C (Figure 6.3i), suggesting that the Br_4TPP do not form extended polymeric networks. It is, however, possible to speculate that the monomer couples into small oligomers, as reported in the literature [51, 232], because the N 1s signal is detected at 400 °C.

In conclusion, TP-XPS measurements prove that the debromination temperature of Br_4TPP on HOPG with $Cu_5[O_2]_n$ is 125 ± 20 °C and that the clusters interact with the debrominated molecules between 125 and 300 ± 20 °C, likely forming the metalorganic phase. Although it is not possible to provide direct evidence of the C-C coupling between the molecules, two indirect measurements suggest that the coupling is taking place. First, the N 1s signal is detected at temperatures as high as 400 °C only in presence of $Cu_5[O_2]_n$. Second, the AFM images reveal the formation of rough, disordered structures that could be assigned to small Br_4TPP oligomers.

6.3.2 Polymerisation on mica

To study the catalytic activity of $Cu_5[O_2]_n$ towards the on-surface polymerisation of Br_4TPP on mica, a bulk insulator, the reaction of the molecules without and with clusters are compared, fol-

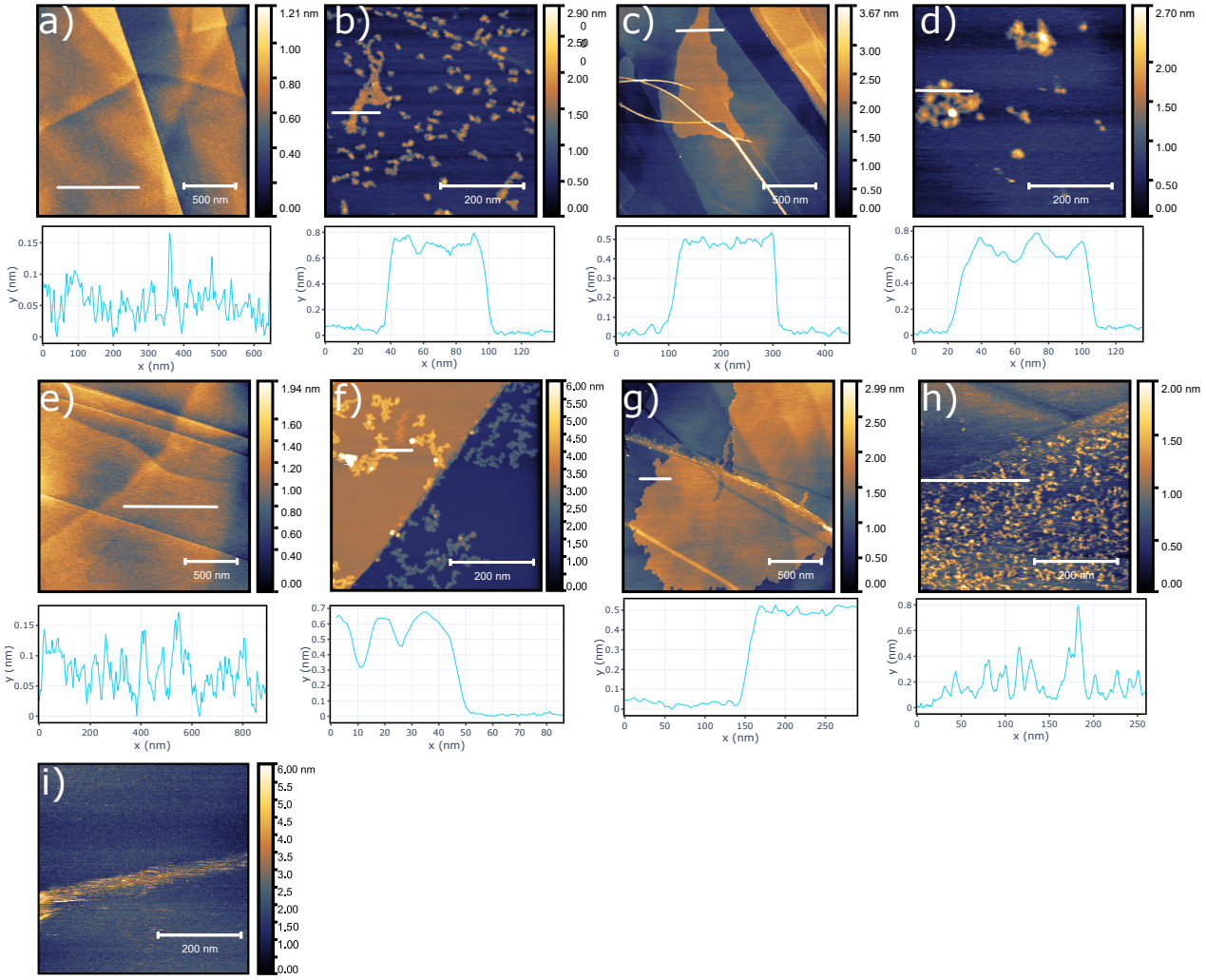

Figure 6.3: AFM topographic images of (a) HOPG, (b) $Cu_5[O_2]_n$ on HOPG, (c) Br_4TPP on HOPG, and (d) both $Cu_5[O_2]_n$ and Br_4TPP on HOPG at room temperature, shown with the corresponding line profiles. AFM topographic images of (e) HOPG, (f) $Cu_5[O_2]_n$ on HOPG, (g) Br_4TPP on HOPG, and (h) both $Cu_5[O_2]_n$ and Br_4TPP on HOPG annealed at 150 °C, shown with the corresponding line profiles. (i) AFM topographic image of $Cu_5[O_2]_n$ and Br_4TPP on HOPG annealed at 400 °C for 30 min. All measurements are performed in Peak Force mode under ambient conditions.

lowing the procedure described in the previous section. As all the XPS spectra are referenced to the Al 2p peak at 74.5 eV and not to C 1s to retain the possibility of measuring shifts in the carbon bonding environments, the binding energies as shifted by approximately 0.5 eV with respect to the section above.

The first step of the Br_4TPP polymerisation is the cleavage of the C-Br bond which is monitored through high-resolution XPS measurements in the Br $3p_{3/2}$ region. In the absence of clusters (Figure 6.4a), the Br $3p_{3/2}$ signal is detected at temperatures as high as $225 \pm 20\,^{\circ}$C. When both $Cu_5[O_2]_n$ and Br_4TPP are present (Figure 6.4b), the bromine peak is less intense at room temperature and disappears at $150 \pm 20\,^{\circ}$C, as shown in Figure 6.4c, pointing at the C-Br bond cleavage and the desorption of the halogen atoms. These results indicate that the $Cu_5[O_2]_n$ AQCs are effective catalysts for the debromination of Br_4TPP not only on HOPG but on mica, too.

It is not possible to monitor the N 1s XPS core-level spectrum of the Br_4TPP on mica as it overlaps with a peak from the substrate. It is thus impossible to prove that pristine molecules desorb from the surface in the absence of catalysts as shown for HOPG. However, the C-C coupling of Br_4TPP into a polymer in the presence of AQCs could be studied by analysing the C 1s peak as shown in Figure 6.4d. The peak is detected up to $400\,^{\circ}$C, suggesting the molecules in the presence of the catalysts remain on the substrate above the debromination temperature of the monomer. The C 1s spectra undergo a significant change from room temperature to the debromination temperature of $150\,^{\circ}$C as shown in Figure 6.4e. First, the $\pi - \pi^*$ shake-up peak at approximately 290 eV disappears. As this component is associated with the aromatic carbon atoms in the phenyl rings, the observed change suggests a chemical reaction is taking place in the phenyl groups of the Br_4TPP. Second, the centre of the peak, associated with the aromatic rings, shifts from 285 eV at $30\,^{\circ}$C to 284.5 eV at $400\,^{\circ}$C, suggesting a change in the phenyl groups [225]. The component at 286.6 eV (C-Br/C-NH) disappears completely at the debromination temperature suggesting a further change in the molecular structure. This component could not be univocally assigned as the binding energy is consistent with both C-Br bonds [53] and C-NH bonds [225, 231]. The observed change is likely caused by two reactions happening at the same time: the debromination and the ring-closing reaction shown in Figure 6.1e. The latter process can take place during the annealing of porphyrins on catalytically active substrates, such as Cu(111), and it is consistent with the change observed in the phenyl group as they undergo the cyclodehydrogenation reaction merging the phenyl rings

with the porphyrin macrocycle [225, 229, 233, 234]. These findings suggest that $Cu_5[O_2]_n$ AQCs are catalytically active towards the cleavage of C-H bonds.

To investigate the role of $Cu_5[O_2]_n$ in the Br_4TPP on-surface polymerisation, the high-resolution XPS spectrum of the Cu $2p_{3/2}$ core-level is acquired during the reaction, as shown in Figure 6.4f. The peak acquired at 50 °C (Figure 6.4e) is asymmetric peak and centred at 933.1 eV, suggesting a partial transition to the Cu^{+2} oxidation state [183]. The peak becomes sharper and shifts from 933.1 eV to 932.5 eV as the temperature reaches 400 °C, suggesting that copper progressively transitions to the Cu^{+0} or Cu^{+1} oxidation states. As discussed above, it is not possible to reliably assign the position of the peak to a precise oxidation state due to the small energy difference between the two. Analogously to the discussion of $Cu_5[O_2]_n$ on HOPG, the oxidised component of Cu $2p_{3/2}$ peak is assigned to the molecules-cluster interaction [20, 41, 167], suggesting a partial transfer of electrons from clusters to the monomers, although a contribution from the substrate could not be ruled out. The data suggest that C-Cu bonds are already present at room temperature and are completely broken when the temperature reaches 400 °C, implying that the debromination starts at room temperature on mica. The comparison between the TP-XPS of Cu $2p_{3/2}$ on HOPG and mica suggests that the substrate still has a minor influence on debromination as the reaction occurs at different temperatures, which is minor compared to the change from Au(111) reported in Chapter 5.

To further study the reaction between the Br_4TPP molecules, AFM images of the sample comprising Br_4TPP with $Cu_5[O_2]_n$ are compared to a set of controls consisting of mica only, $Cu_5[O_2]_n$ on mica, and Br_4TPP on mica, as shown in Figure 6.5. All the samples are compared at room temperature and after 30 min of annealing in UHV at 150 °C, a temperature high enough to induce the monomer debromination and the changes in the C 1s spectrum as shown in Figure 6.4b,e.

The AFM images of mica at room temperature and after annealing (Figure 6.5a, e respectively) show no damage as the roughness, measured through the height fluctuations from the line profiles, does not exceed 0.12 nm in both cases. The AFM image of the $Cu_5[O_2]_n$ clusters on mica at room temperature (Figure 6.5b) shows that they form agglomerates up to 2 nm in height. As noticed on HOPG, the clusters interact preferentially among themselves, giving rise to a Volmer-Weber growth of agglomerates. After the annealing at 150 °C (Figure 6.5 f), the clusters are still found in agglomerates of smaller size approximately 0.3 nm in height, indicating that they are unstable against temperature and can be dispersed. The Br_4TPP molecules form agglomerates as high as

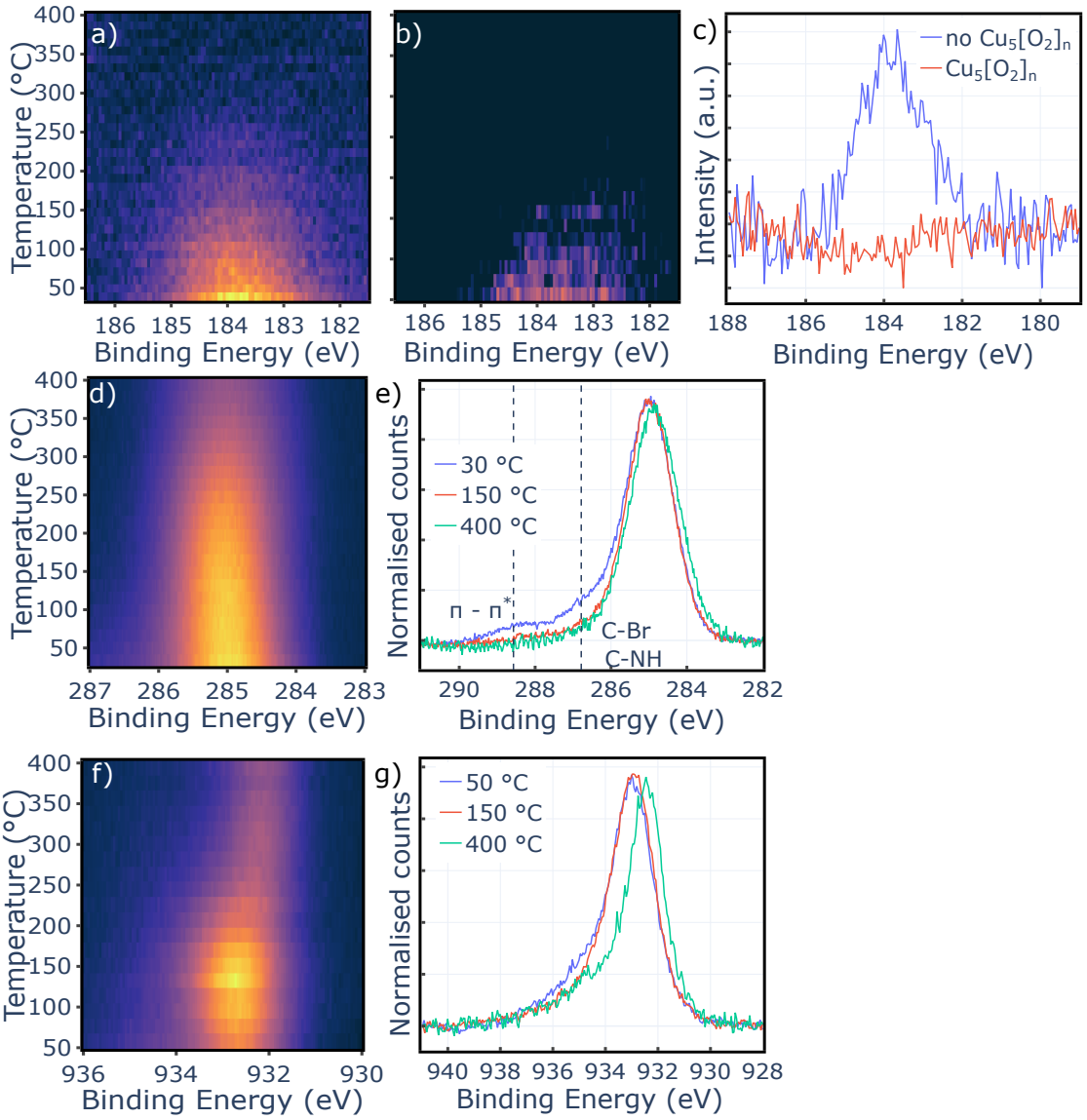

Figure 6.4: Temperature-programmed XPS in Br $3p_{3/2}$ region of Br_4TPP (a) without and (b) with $Cu_5[O_2]_n$ on mica. (c) High-resolution XPS spectra of Br_4TPP in Br $3p_{3/2}$ region without and with $Cu_5[O_2]_n$ showing the complete debromination at $150 \pm 20\,°C$ in presence of $Cu_5[O_2]_n$. (d) Temperature-programmed XPS in C 1s region of Br_4TPP with $Cu_5[O_2]_n$. (e) High-resolution XPS spectrum of Br_4TPP in C 1s region at 30,150, and 400 °C showing the evolution of the peak. (f) Temperature-programmed XPS in Cu $2p_{3/2}$ region of Br_4TPP with $Cu_5[O_2]_n$. (g) High-resolution XPS spectrum of $Cu_5[O_2]_n$ in Cu 2p region at 50, 150, and 400 °C showing that shift in the peak. All data are referenced to Al 2p at 74.5 eV of the muscovite mica.

6 nm (Volmer-Weber growth), as shown in Figure 6.5c. Upon annealing at 150 °C, the agglomerates break into smaller ones that reach a height of 1.8 nm from the surface (Figure 6.5g). When both clusters and molecules are present on the surface at the same time (Figure 6.5d), only agglomerate of approximately 1.5 nm are found on the substrate, suggesting that the molecules are attached to the AQCs. Upon annealing at 150 °C (Figure 6.5h), islands 0.5 nm high are found on the substrate, contrary to all the control samples, suggesting that they are a result of the reaction between clusters and molecules. The high-resolution measurement of the island (Figure 6.5i) shows long vertical rows of squares, each of them being a molecule. The assignment of these rows to polymerised Br_4TPP molecules is not straightforward. The molecule-to-molecule distance along the rows is 1.25 ± 0.1 nm and across them is 1.0 ± 0.1 nm, as shown in the line profile, which is lower than the value reported in the literature for Br_4TPP [24, 33, 164]. This difference could be attributed to the ring-closing reaction detected from the C 1s TP-XPS (Figure 6.4d) as the centre-to-centre distance is lower than the dimension of a single Br_4TPP. Furthermore, the two dimensions of the molecules could be asymmetric as shown in Figure 6.1e,f but further investigation would be needed to confirm it. The proposed molecular structure is based on the work of Wiengarten *et al* showing that this is the most stable configuration among the different possibilities studied with DFT and confirmed with STM measurements [235]. The molecule-to-molecule distance upon annealing in the presence of $Cu_5[O_2]_n$ could not be compared to the molecule without $Cu_5[O_2]_n$ as they do not grow into flat islands on mica.

In conclusion, TP-XPS measurements prove that the debromination temperature of Br_4TPP on mica and HOPG with $Cu_5[O_2]_n$ happens between 125 and 150 °C. The clusters interact with the debrominated molecules starting from room temperature and 50 °C up to a temperature of 300 ± 20 °C for mica and HOPG. The XPS data reveals that the molecules undergo the ring-closing reaction upon annealing, suggesting that the molecules remain on the surface, likely due to the coupling C-C. The AFM images provide evidence of the formation of flat islands with ordered molecular structure only in the presence of $Cu_5[O_2]_n$, suggesting that the cluster catalyses the on-surface polymerisation of Br_4TPP.

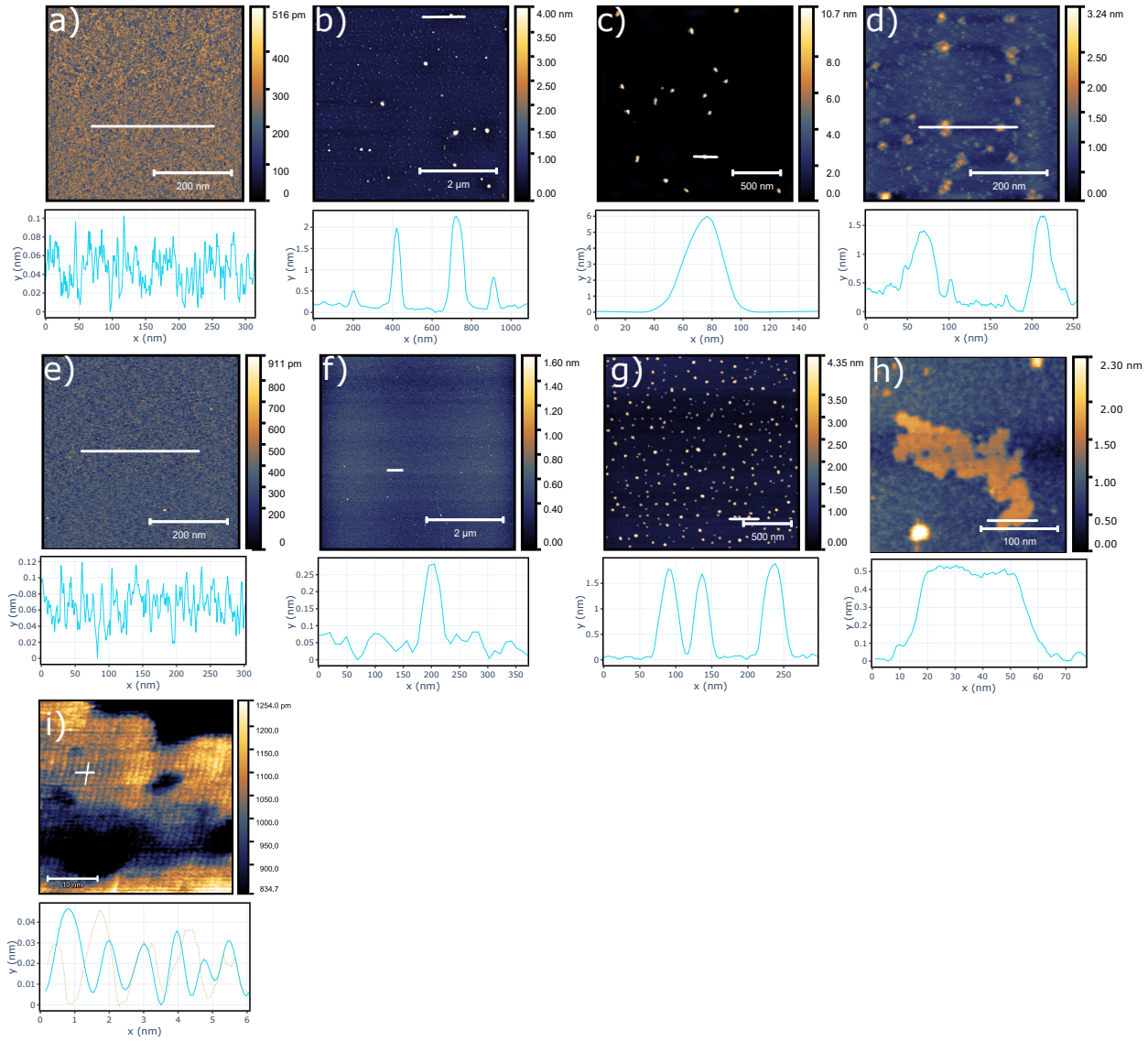

Figure 6.5: AFM topographic images of (a) mica, (b) $Cu_5[O_2]_n$ on mica, (c) Br_4TPP on mica, and (d) both $Cu_5[O_2]_n$ and Br_4TPP on mica at room temperature, shown with the corresponding line profiles. AFM topographic images of (e) mica, (f) $Cu_5[O_2]_n$ on mica, (g) Br_4TPP on mica, and (h) both $Cu_5[O_2]_n$ and Br_4TPP on mica annealed at 150 °C shown with the corresponding line profiles. (i) Molecular-resolution image of the island in panel h with the corresponding line profile along the x and y directions in brown and light blue, respectively. All the images are acquired in Peak Force mode under ambient conditions.

	Silver ($mg\,L^{-1}$)	Nitrates ($mg\,L^{-1}$)	Silicates ($mg\,L^{-1}$)
NG 14	45.8	9.4	25
NG 15	96.8	14.5	25
NG 21	92.3	14.2	25

Table 6.1: Concentration of silver, nitrates, and silicates in $Ag_5[O_2]_n$ NG 14, 15, 21 water solutions as provided by the manufacturer.

6.4 Results and discussion: $Ag_5[O_2]_n$ AQCs

In the following sections, the $Ag_5[O_2]_n$ AQCs powders and milli-Q water solution are first characterised with XPS and AFM. Then, the use of these AQCs as extrinsic catalysts for the polymerisation of Br_4TPP on inert surfaces, HOPG and mica, is studied with TP-XPS.

6.4.1 Characterisation of $Ag_5[O_2]_n$ AQCs powders and solutions

$Ag_5[O_2]_n$ AQCs powders and solutions, named NG 14, 15, and 21 and produced with different methods, are analysed with XPS to assess the purity level as the synthesis is still new and under optimisation. The solutions contain $Ag_5[O_2]_n$ AQCs and different salts used during the synthesis by the providers, mainly nitrates and silicates, as described in Table 6.1. The powders are produced by freeze-drying the corresponding solutions and the level of purity is unknown. Therefore, the presence of contaminants in the $Ag_5[O_2]_n$ AQCs is assessed and the possibility of purifying the solutions through spin-coating is tested.

Powders The XPS characterisation of the $Ag_5[O_2]_n$ AQCs NG 14, 15, 21 powders is presented in Figure 6.6a-d. The Ag 3d core-level photoemission spectrum shown in Figure 6.6a exhibits a sharp doublet consisting of Ag $3d_{3/2}$ and Ag $3d_{5/2}$ components centred at 374.5 and 368.8 eV for all the powders. The binding energy of the peak is in excellent agreement with the measurements of pure Ag_2O and $AgNO_3$ powders [236] suggesting that the AQCs are in the Ag^{+1} oxidation state. To further confirm the assignment, the Ag MNN Auger peak is measured as shown in Figure 6.6b. The spectrum comprises several peaks due to the Auger signal from the Ag $M_4N_{45}N_{45}$ peak ranging between 352 and 360 eV as well as the $M_5N_{45}N_{45}$ peak ranging between 343 and 352 eV. All the

spectra in Figure 6.6b consist of two peaks centred at 351 and 357 eV, respectively, in excellent agreement with the Ag^{+1} oxidation state [236]. It is, however, impossible to distinguish whether the clusters are oxidised in the form of Ag_2O, $AgNO_3$, or a mixture of the two, due to the small energy difference [236].

The presence of nitrates and silicates as contaminants as reported by the manufacturer is confirmed by core-level photoemission spectrum in the N 1s and Si 2p region reported in Figure 6.6c and d, respectively. The N 1s peak is centred at 407.4 eV in excellent agreement with the nitrate peak reported in the literature [237]. The Si 2p peak is centred between 103.2 and 103.6 eV depending on the samples, in agreement with the binding energy of silicate ions reported in the literature [237]. Additionally, sodium and calcium are detected as a result of the nitrate and silicate salts used in the production process. Due to the surface sensitivity of XPS, only the surface of the powders is analysed, it is therefore impossible to assess the contamination in the bulk.

$Ag_5[O_2]_n$ AQCs solutions on Au(111). To characterisation the $Ag_5[O_2]_n$ AQCs solution with XPS, several drops are spin-coated on Au(111) surface for 10 s at a speed of 500 RPM followed by 10 s at a speed of 1500 RPM. The results are presented in Figure 6.6e-h.

The Ag 3d core-level photoemission spectrum shown in Figure 6.6e exhibits a sharp doublet consisting of Ag $3d_{3/2}$ and Ag $3d_{5/2}$ components centred at 374.4 and 368.4 eV, respectively, for all the solutions. These binding energies are lower than the corresponding powders by 0.4 eV and are in excellent agreement with the measurements of pure Ag foil [236], suggesting that the AQCs in milli-Q water solution are in the Ag^{+0} oxidation state. To further confirm the difference between powders and solution, the Ag MNN Auger peak is measured as shown in Figure 6.6f. The spectrum comprises several peaks due to the Auger signal from the Ag $M_4N_{45}N_{45}$ and $M_5N_{45}N_{45}$ peaks. All the spectra in Figure 6.6f comprise several peaks, the most intense being centred at a kinetic energy of 358.1 and 351.2 eV, respectively, in excellent agreement with Ag^{+0} oxidation state [236]. The structure of the Auger peak changes completely from the powders to the spin-coated solutions suggesting that the process of freeze-drying and the exposure to air have a significant effect on the chemical composition of the AQCs and suggesting that water solution is suitable for long-term storage of the clusters. Furthermore, the presence of Ag^{+0} suggests that AQCs are resistant to oxidation caused by the oxygen molecules dissolved in the water solution, meaning that the molecular oxygen is not split into atomic oxygen bonded to the AQCs in agreement with DFT

simulation [103], as discussed for $Cu_5[O_2]_n$ in Chapter 5.

The contamination of nitrates and silicates is assessed by core-level photoemission spectrum in the N 1s and Si 2p region reported in Figure 6.6g and h, respectively. No signal is detected in the N 1s peak, suggesting that there are no nitrates salts. A peak is detected in the Si 2p region suggesting that there is silicon on the surface. The peak is centred at 102.5 eV and not 103.6 eV, as detected for the powders, suggesting that there are no silicates likely because silicon contamination derives from the storage of the gold surface. Additionally, XPS survey scans show no sodium or calcium peaks detected in the powder samples.

For the following experiments, the $Ag_5[O_2]_n$ AQCs NG 15 are chosen due to the lowest level of contaminations in the powders suggesting that the initial solution is the purest.

$Ag_5[O_2]_n$ NG 15 solution on HOPG and mica. The purity of $Ag_5[O_2]_n$ NG 15 solution upon spin-coating on both HOPG and mica is tested using XPS to establish a benchmark to investigate the on-surface polymerisation of Br_4TPP in the following sections.

The Ag 3d core-level photoemission spectra, shown in Figure 6.6i, exhibit a sharp doublet with the Ag $3d_{3/2}$ and Ag $3d_{5/2}$ components centred at 374.3 and 368.3 eV, respectively, on HOPG. These binding energies are in excellent agreement with the measurements on Au(111) and of pure Ag foil [236], suggesting that the AQCs in milli-Q water solution are in the Ag^{+0} oxidation state. On mica, the binding energy of the silver peaks is centred at 374.8 and 368.8 eV, respectively, overlapping with the photoemission peaks of mica at 378.8 eV. These binding energies suggest that the clusters deposited on mica are oxidised, likely because of the interaction with the ions on the surface.

To further confirm the oxidation state of silver, the Ag MNN Auger peak is measured. Figure 6.6j exhibits two peaks centred at 357.8 and 352.0 eV on HOPG as well as at 357.0 and 350.8 eV on mica. The position and the shape of the peak on HOPG are in excellent agreement with the Ag^{+0} oxidation state. However, the clusters deposited on mica are consistent with the Ag^{+1} oxidation state [236] suggesting that they are interacting with the oxygen atoms of the surface as nitrogen is not detected in the N 1s spectrum on both HOPG and mica (Figure 6.6k). The contamination of silicates is assessed by core-level photoemission spectrum Si 2p region reported in Figure 6.6l. A peak is detected in the Si 2p region suggesting that there is silicon on the surface. The peak is centred at 101.7 eV with a shoulder at higher binding energy on HOPG, suggesting that most of

the signal comes from silicon oxide likely due to the storage of the solution or the handling of the surface, as noticed on Au(111). The silicon peak is centred at 103.0 eV on mica as the substrate itself contains silicate ions.

These findings suggest that, although the powders exhibit contaminations that affect the chemistry of the AQCs, the spin-coated solutions are free from nitrate and silicate contamination and result in $Ag_5[O_2]_n$ AQCs in the Ag^{+0} oxidation state. However, $Ag_5[O_2]_n$ NG15 spin-coated on mica are found in the Ag^{+1} oxidation state, likely due to the interaction with the oxygen atoms of the substrate and not the contaminations from the solution as no nitrogen is detected. These observations are rationalised by assuming that the salts in the solution are dissociated into ions, given the high solubility of silver nitrate salts and the fair solubility of silicate salts. The clusters are thus mostly free from the contaminants in the solution. The ions are removed with the water droplet during the spin-coating process due to their affinity with water and the repulsion from the hydrophobic gold and HOPG surfaces. Although most of the clusters are removed with the drop, some of them preferentially absorb onto the substrates compared to the inorganic salts as shown by the AFM measurements presented below. It could be interesting to elucidate this point with more experiments in the future.

AFM of $Ag_5[O_2]_n$ NG 15 solution on Au(111). Similarly to the characterisation of $Cu_5[O_2]_n$ AQCs reported in Chapter 5, the order and the dimensions of the $Ag_5[O_2]_n$ AQCs NG 15 is studied using AFM. Milli-Q water solutions of the AQCs are spin-coated for 10 s at a speed of 500 RPM followed by 10 s at a speed of 2500 RPM on atomically flat Au(111) prepared as described in Section 3.4.1. Four different concentrations, 0.9, 4.0, 9.6, and 96.8 mg L^{-1} are studied and the results are shown in Figure 6.7.

Figure 6.7a shows that $Ag_5[O_2]_n$ AQCs at a 0.9 mg L^{-1} concentration form lines on the Au(111) surface, exceeding 100 nm in length. The AQCs appear blurred while the gold step edge is not, suggesting the clusters are diffusing and, hence, are not strongly interacting with each other or the gold surface. The line profile in Figure 6.7b shows that the clusters are 0.2 nm high.

At a concentration of 4.0 mg L^{-1}, the lines are replaced by rectangular islands, ranging from 10 to 60 nm in lateral size, as shown in Figure 6.7c, and 0.25 nm high, as shown in Figure 6.7d. This value is higher than the one measured at a lower concentration, likely because the height in Figure 6.7c is underestimated due to the diffusion of the cluster or the possible disruption caused

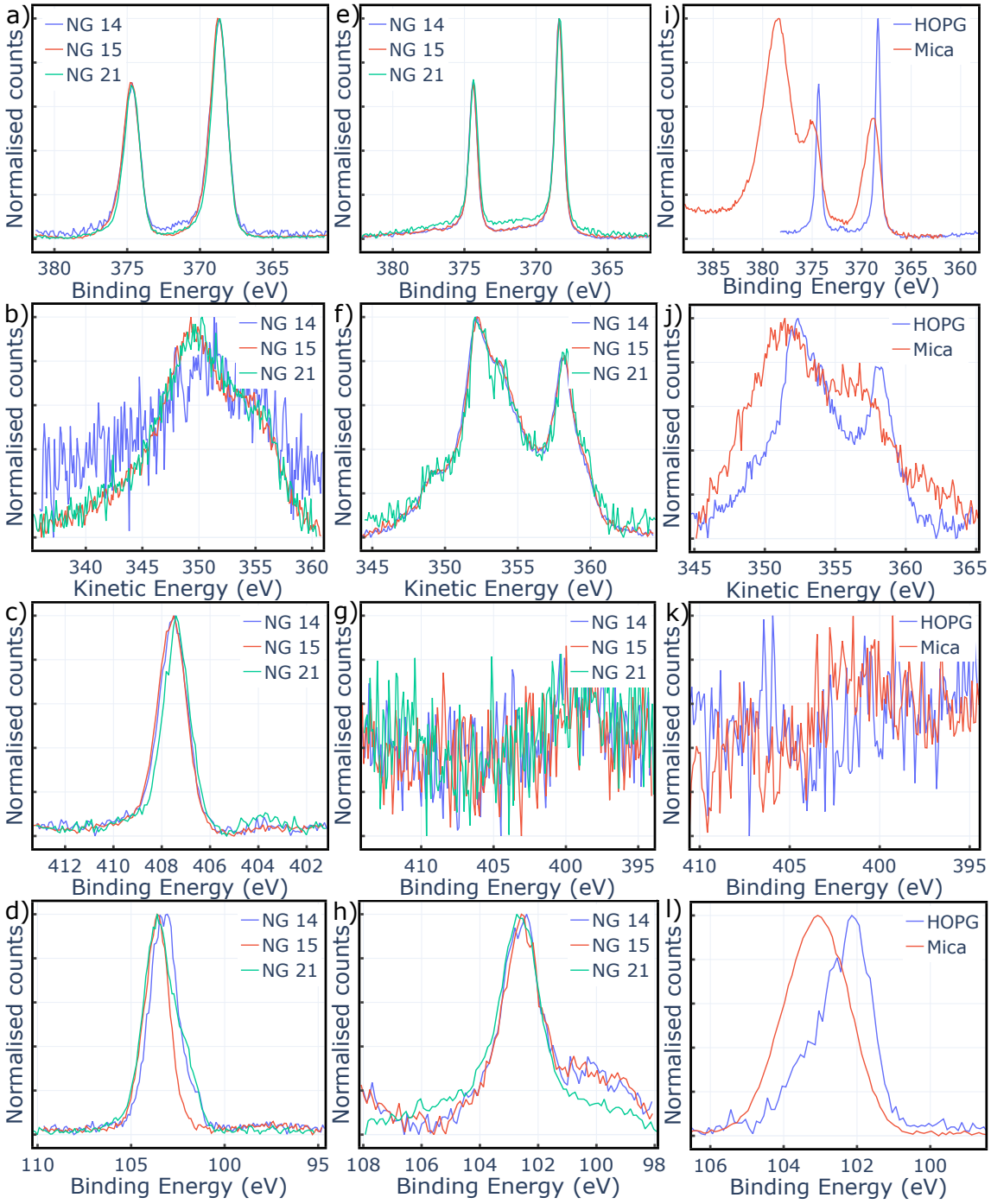

Figure 6.6: $Ag_5[O_2]_n$ AQCs NG 14, 15, 21 powders and solution. High-resolution photoemission spectrum of $Ag_5[O_2]_n$ AQCs powders NG 14, 15, 21 in the (a) Ag 3d, (b) Ag MNN, (c) N 1s, and (d) Si 2p regions. High-resolution photoemission spectrum of $Ag_5[O_2]_n$ AQCs solutions NG 14, 15, 21 spin-coated on Au(111) in the (e) Ag 3d, (f) Ag MNN, (g) N 1s, and (h) Si 2p regions. High-resolution photoemission spectrum of $Ag_5[O_2]_n$ AQCs solutions NG 15 spin-coated on HOPG and mica in the (i) Ag 3d, (j) Ag MNN, (k) N 1s, and (l) Si 2p regions. Data referenced to C 1s at 285.0 eV and C 1s sp^2 at 284.5 eV for HOPG.

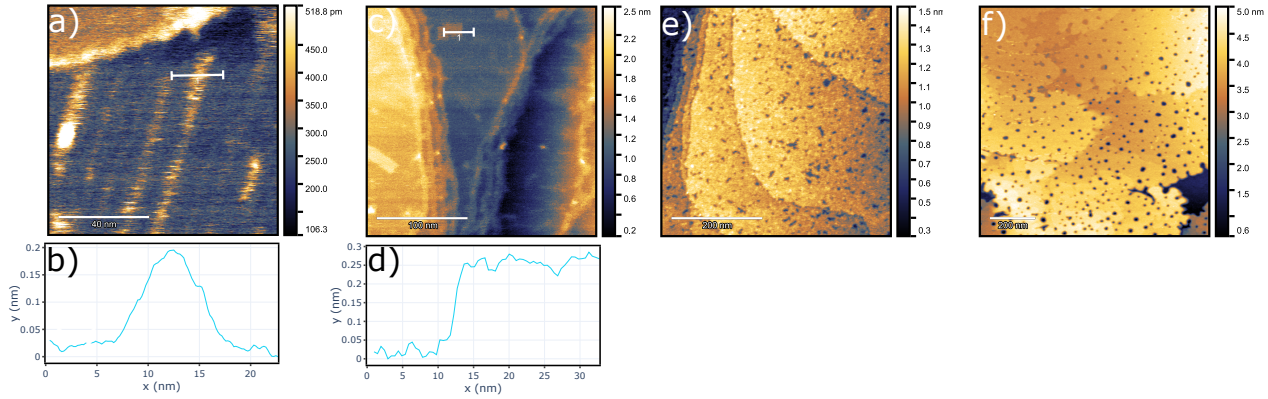

Figure 6.7: High-resolution topographic images of $Ag_5[O_2]_n$ NG 15 solutions spin-coated on Au(111) for 10 s at a speed of 500 RPM followed by 10 s at a speed of 2500 RPM. (a) High-resolution AFM topographic images of $Ag_5[O_2]_n$ NG 15 at a concentration of 0.9 mg L^{-1} with (b) line profile and (c) at a concentration of 4.0 mg L^{-1} with (d) line profile. High-resolution AFM topographic images of $Ag_5[O_2]_n$ NG 15 (e) 9.6 mg L^{-1} and (f) 96.8 mg L^{-1}.

by the tip to the not densely packed lines. However, the height of 0.25 nm is similar to the value measured for the $Cu_5[O_2]_n$ AQCs in Chapter 5, suggesting that the $Ag_5[O_2]_n$ AQCs could be 2D on Au(111), and is in good agreement with the value reported for Ag_3 clusters [238]. This result could be confirmed using NIXSW as shown in Chapter 5 or with qPlus AFM.

At a concentration of 4.0 mg L^{-1}, a layer of $Ag_5[O_2]_n$ AQCs with some holes in it covers the Au(111) terraces. Finally, at a concentration of 96.8 mg L^{-1}, several layers of $Ag_5[O_2]_n$ AQCs cover the surface as the features of the gold cannot be clearly distinguished. The AQCs layer, however, exhibits some holes suggesting that the growth is primed by the formation of the first layer.

In conclusion, the XPS characterisation reveals that spin-coating is a viable strategy to deposit pure $Ag_5[O_2]_n$ AQCs from milli-Q solutions as silver atoms are found in the oxidation state Ag^{+0} upon spin-coating on Au(111) and HOPG surfaces while they are in oxidation state Ag^{+1} in the powders and on mica. The $Ag_5[O_2]_n$ NG 15 AQCs, chosen for further characterisation due to the lowest level of contamination, are found to be 0.25 nm high, suggesting they have a 2D structure on Au(111), like $Cu_5[O_2]_n$ AQCs.

6.4.2 Polymerisation of Br_4TPP on HOPG

To study the catalytic activity of $Ag_5[O_2]_n$ NG 15 AQCs towards polymerisation of Br_4TPP on HOPG, the reaction between the molecules without and with $Ag_5[O_2]_n$ are compared, similarly to what is reported in Section 6.3. Because of the low sticking coefficient of $Ag_5[O_2]_n$ AQCs on HOPG, it is necessary to deposit 7 droplets of the milli-Q water solution at a concentration of $96.8\,\mathrm{mg\,L^{-1}}$ on the mica substrate and wait for 1 h before the spin-coating process. The TP-XPS results are shown in Figure 6.8.

The first step of the Br_4TPP polymerisation is the cleavage of the C-Br bond which is monitored through high-resolution XPS measurements in the Br 3p region shown in Figure 6.8a. In the absence of clusters (Figure 6.2a), the Br 3p double signal is detected at temperatures as high as $300 \pm 10\,^{\circ}\mathrm{C}$. Figure 6.8a shows that when both $Ag_5[O_2]_n$ and Br_4TPP are present at the same time, the bromine peaks become progressively less intense until they disappear at $220 \pm 10\,^{\circ}\mathrm{C}$. The spectra collected at 30 and $220\,^{\circ}\mathrm{C}$ are shown in Figure 6.8b. These findings point to the C-Br bond cleavage starting at room temperature and the complete desorption of the halogen atoms at $220\,^{\circ}\mathrm{C}$, indicating that the $Ag_5[O_2]_n$ are effective catalysts for the debromination of Br_4TPP molecules on HOPG. Interestingly, the debromination temperature in the presence of $Ag_5[O_2]_n$ is higher than in the presence of $Cu_5[O_2]_n$ by $100\,^{\circ}\mathrm{C}$, indicating the silver-based clusters are less reactive than copper-base ones. This trend is consistent with the experimental and theoretical evidence that copper is the best catalyst among the noble metals in Ullmann coupling [14, 20, 29].

The C-C coupling, the final step of Br_4TPP polymerisation, could not be studied by analysing the C 1s peak as the signal is dominated by photoemission from the graphite substrate. Consequently, the presence of Br_4TPP on the surface is checked through the photoemission from the N 1s core-level of the porphyrin core. The presence of the N 1s peak of Br_4TPP molecules without and with clusters provides indirect evidence of the polymerisation of Br_4TPP as the polymer should be thermally stable and desorb at a higher temperature than the individual monomers do. TP-XPS data of Br_4TPP molecules on HOPG shown in Figure 6.2d and discussed above indicate that the N 1s photoemission spectrum disappears at $310 \pm 10\,^{\circ}\mathrm{C}$ because the molecules desorb from the surface. TP-XPS data collected in the N 1s region when both molecules and the $Ag_5[O_2]_n$ AQCs are deposited on the HOPG substrate is shown in Figure 6.8c. The nitrogen peak is detected at temperatures as high as $400 \pm 10\,^{\circ}\mathrm{C}$, well above the desorption temperature of the monomer, suggesting that the molecules are polymerised. The XPS spectra collected at 30, 220, and $400\,^{\circ}\mathrm{C}$ shown

in Figure 6.8d show that the centre of the N 1s peak and the width remains constant during the on-surface polymerisation with the clusters, suggesting that no damage is occurring to the nitrogen atoms in the centre of the porphyrins, consistently with the reaction in presence of $Cu_5[O_2]_n$. It is thus possible to rule out the metalation of the porphyrin core. However, it is not possible to distinguish subtle changes in the imidic and pyrrolic nitrogen atoms due to the limited resolution of the data.

To investigate the role of $Ag_5[O_2]_n$ AQCs in the Br_4TPP on-surface polymerisation, the high-resolution XPS spectrum of Ag 3d core-level is acquired during the reaction, as shown in Figure 6.8e. The position of the doublet remains constant with the Ag $3d_{3/2}$ and Ag $3d_{5/2}$ at 374.1 eV and 368.2 eV, respectively. The position of the peaks is in good agreement with the Ag^{+0} oxidation state, as discussed in the characterisation of $Ag_5[O_2]_n$ powders and solutions. Figure 6.8f shows no significant change in the peak below and above the debromination temperature of 220 °C. These findings suggest a weak or negligible interaction between the bromine atoms or the molecules and the AQCs, consistent with the literature of Ullmann coupling on Ag surfaces where no organometallic phase is detected [20, 41]. The presence of C-Ag or Br-Ag bonds could be studied with low-temperature AFM.

The debromination temperature in the presence of $Ag_5[O_2]_n$ AQCs and the evolution of the chemical state of the catalysts during the reaction on HOPG is remarkably different from $Cu_5[O_2]_n$ AQCs, suggesting that the choice of the metal comprising the clusters has a strong effect on the overall activity, offering the possibility of fine-tuning the reaction.

6.4.3 Polymerisation of Br_4TPP on mica

To study the catalytic activity of $Ag_5[O_2]_n$ NG 15 AQCs towards the on-surface polymerisation of Br_4TPP on mica, a bulk insulator, the reaction of the molecules without and with clusters are compared, following the same procedure described for $Cu_5[O_2]_n$ AQCs. All the XPS spectra are referenced to the Al 2p peak at 74.5 eV and not to C 1s to retain the possibility of measuring shifts in the carbon bonding environments.

The first step of the Br_4TPP polymerisation is the activation of the C-Br bond, which is monitored through high-resolution XPS measurements in the Br $3p_{3/2}$ region. In the absence of clusters, the Br $3p_{3/2}$ signal is detected at temperatures as high as 225±20 °C as shown in Figure 6.4a. When

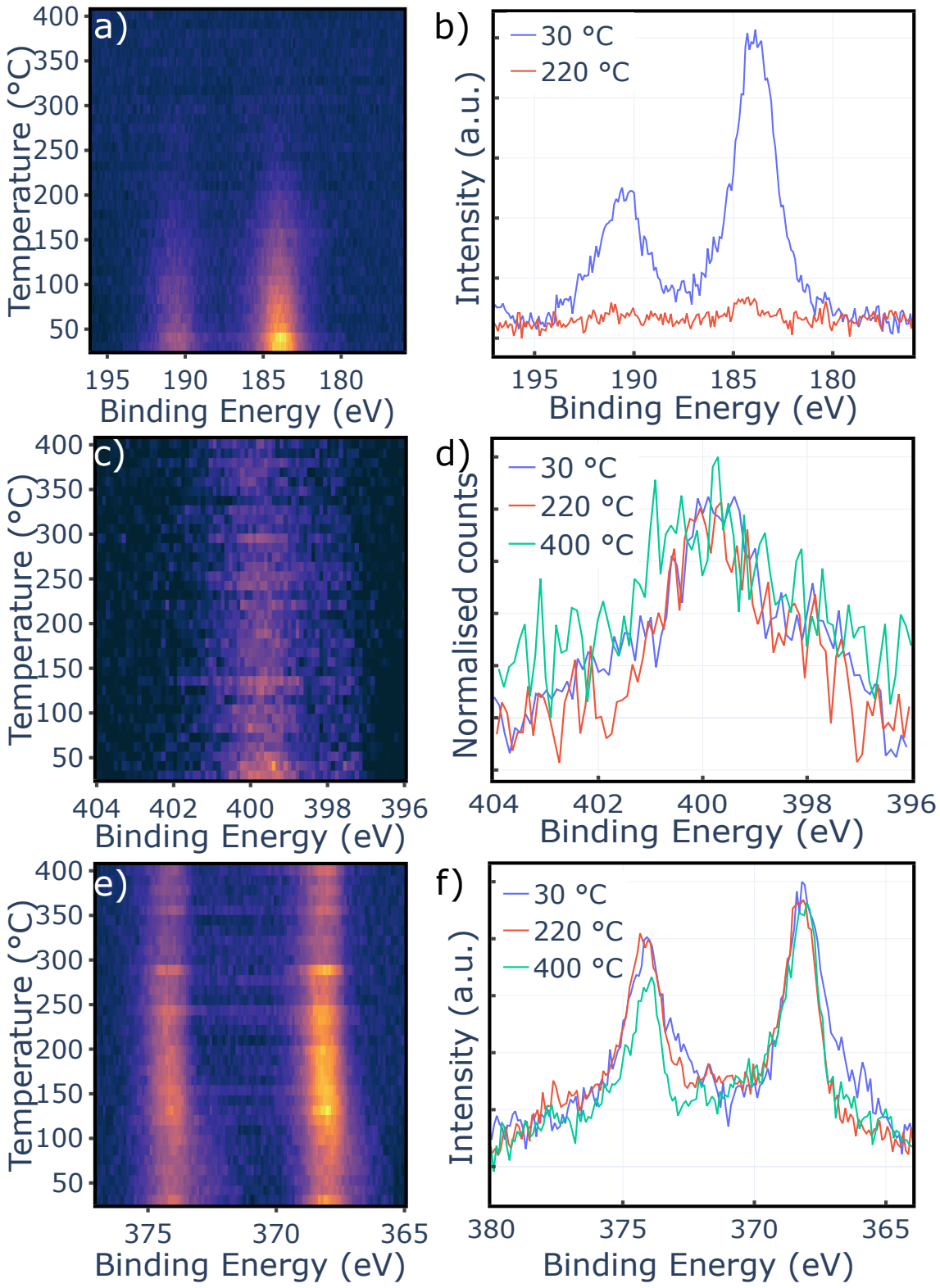

Figure 6.8: TP-XPS of $Ag_5[O_2]_n$ NG 15 solution and Br_4TPP molecules on HOPG. (a) TP-XPS in the Br 3p region with (b) data acquired at 30 and 220 °C. (c) TP-XPS in the N 1s region with (d) with the data acquired at 30, 220, and 400 °C. (e) TP-XPS in the Ag 3d region with (f) data collected at 30, 220, and 400 °C. Data referenced to C 1s sp^2 at 284.5 eV.

$Ag_5[O_2]_n$ are present alongside the Br_4TPP molecules, the bromine peak disappears at $200 \pm 10\,°C$, as shown in Figure 6.9b, in agreement with the results on HOPG. Although the debromination temperature on mica in the presence and the absence of $Ag_5[O_2]_n$ is similar, the interaction between Br and Ag atoms discussed below suggests that the clusters are catalysing the C-Br bond cleavage. The first measurement performed in the Br 3p region ('First data' in Figure 6.9b) shows the Br doublet with the Br $3p_{1/2}$ and Br $3p_{3/2}$ components at 191.5 and 184.0 eV, respectively. These binding energies are compatible with the C-Br bond as reported in the literature [227]. After the first measurement and before heating, the bromine doublets become broader due to a doublet at higher binding energies ('30 °C' in Figure 6.9b), associated with the formation of C-Ag bonds [239]. As the two measurements are conducted both at 30 °C, the split is likely to be caused by excess energy provided by the X-rays during the measurements. This finding indicates that $Ag_5[O_2]_n$ AQCS can probably initiate the debromination already at room temperature on mica. The behaviour of $Ag_5[O_2]_n$ AQCs is different from $Cu_5[O_2]_n$ clusters, where the splitting of the Br 3p peak is not detected at room temperature, suggesting that the choice of metal could be used to fine-tune chemical reactions. The measurements conducted at 220 and 400 °C show minimal changes suggesting that the debromination is completed.

It is not possible to monitor the N 1s XPS core-level spectrum of the Br_4TPP on mica as it overlaps with a peak from the substrate, as discussed above. However, the C-C coupling of Br_4TPP into a polymer in the presence of AQCs is studied by analysing the C 1s peak as shown in Figure 6.9c. The peak is detected up to 400 °C, suggesting the molecules remain on the substrate above the debromination temperature of the monomer in the presence of the catalysts. The C 1s spectra do not undergo a significant change from room temperature to 400 °C as shown in Figure 6.9d. However, the peaks measured before and after the X-ray induced debromination called 'First data' and '30 °C' respectively, are significantly different from the Br_4TPP with $Cu_5[O_2]_n$. First, the low intensity of the $\pi - \pi^*$ shake-up peak at approximately 288.7 eV associated with the aromatic carbon atoms in the phenyl rings suggests that a chemical reaction is taking place. Second, the centre of the peak, associated with the aromatic ring, shifts from 284.8 eV at 30 °C to 284.4 eV at 400 °C, suggesting a change in the phenyl groups [225]. The small C-Br/C-NH component at 286.6 eV disappears completely suggesting a further change in the molecular structure as discussed above, this component could not be univocally assigned to C-Br and C-NH bonds as the binding energies overlap. The observed change is likely caused by both the debromination

and the cyclodehydrogenation, as noticed for the reaction with $Cu_5[O_2]_n$ AQCs [225, 229, 233, 234]. These findings suggest that $Ag_5[O_2]_n$ AQCs, as $Cu_5[O_2]_n$ AQCs, can activate the C-H bond, but the former AQCs are more active than the latter ones as the reaction is activated by the X-rays at room temperature.

To investigate the role of $Ag_5[O_2]_n$ in the Br_4TPP on-surface polymerisation, the high-resolution XPS spectrum of the Ag $3d_{5/2}$ core-level is acquired during the reaction, as shown in Figure 6.9e. The Ag $3d_{3/2}$ component overlaps with a peak from the background, as shown in Figure 6.6, and could not be reliably measured. The peak acquired at 30 and 220 °C shown in Figure 6.4f exhibit a symmetric peak centred at 368.1 eV associated with the Ag^{+1} oxidation state likely due to the interaction with the substrate and the bromine atoms. The position of the Ag $3d_{5/2}$ components differs from the value reported in Figure 6.6 due to the different peaks used to reference the data. The peak becomes sharper and shifts from 368.1 eV to 367.7 eV above the debromination temperature. This finding suggests that silver transitions to the Ag^{+0} oxidation state, indicating that the clusters are not interacting with the bromine atoms and the surface. Contrary to $Cu_5[O_2]_n$ AQCs, the shift of Ag peak to Ag^{+0} above the debromination temperature suggests that there are no bonds between the $Ag_5[O_2]_n$ ACQs and the brominated molecules as noticed on HOPG. These findings indicate that are in good agreement with the literature on Ullmann coupling on Ag surface [14, 20, 41] where no C-Ag bonds are detected using XPS and STM.

In conclusion, $Ag_5[O_2]_n$ NG 15 AQCs are found to catalyse the debromination of Br_4TPP with complete desorption of the halogen atoms at 220 ± 10 °C on both HOPG and mica. The catalytic activity of $Ag_5[O_2]_n$ is lower than $Cu5_5[O_2]_n$ AQCs, suggesting that clusters follow the same trend reported copper and silver surfaces. The XPS measurements suggest that no stable molecule-cluster bonds form during the reaction with $Ag_5[O_2]_n$ while they are detected when using $Cu_5[O_2]_n$. These findings are in good agreement with the literature showing no bonds between the silver adatoms on Ag surfaces and molecules. Finally, $Ag_5[O_2]_n$ AQCs were found to be more catalytically active toward cyclodehydrogenation than Cu_5 AQCs as the reaction takes place already at 30 °C on mica. The same reaction occurs around 220 °C on Ag(111) [229], Ag(111) [34], and Au(111) [233] surfaces suggesting that AQCs are exceptionally active towards the C-H bond cleavage.

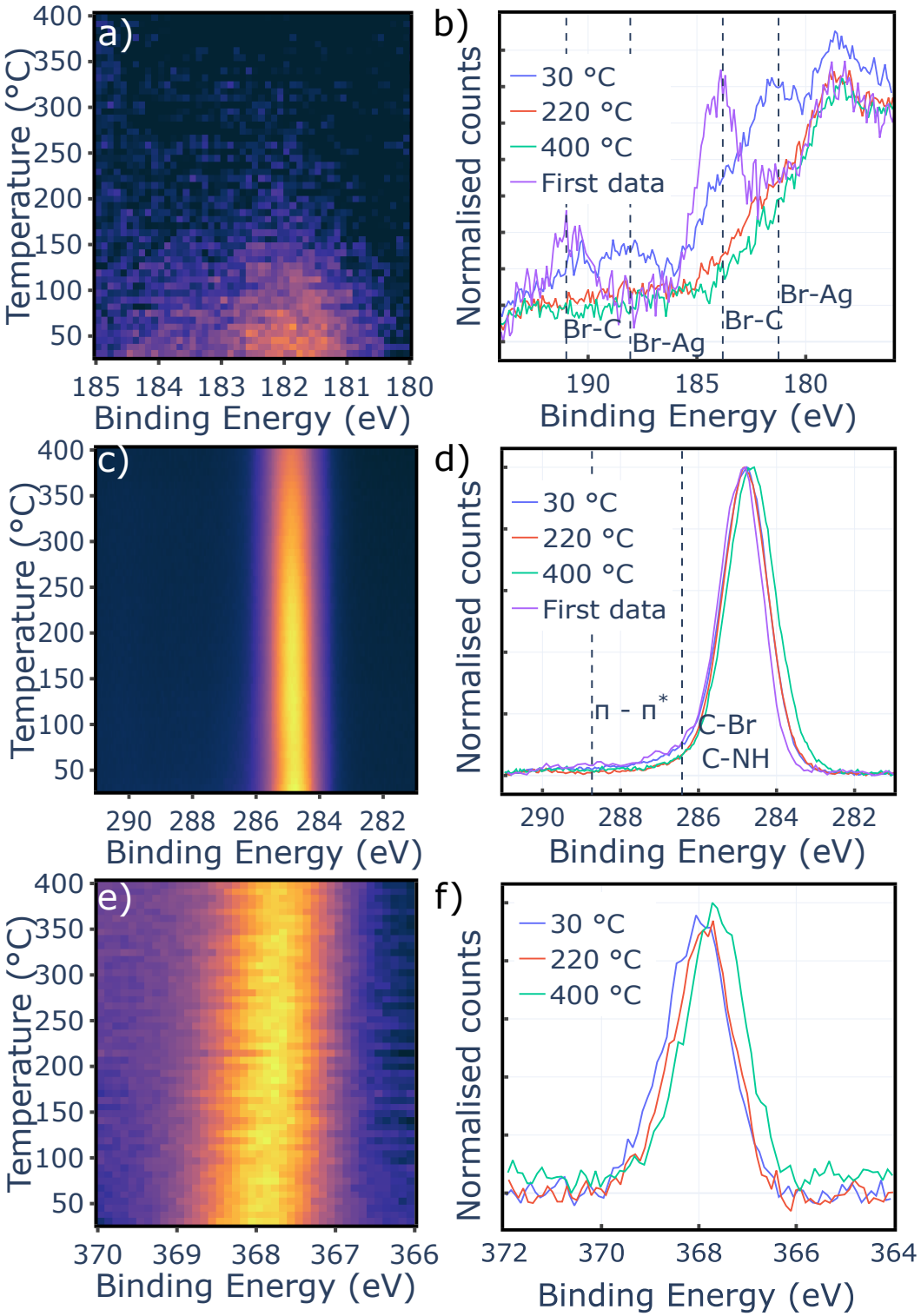

Figure 6.9: TP-XPS of $Ag_5[O_2]_n$ NG 15 solution and Br_4TPP on mica. (a) TP-XPS in the Br 3p region with (b) first bromine collected and data acquired at 30, 220, and 400 °C. (c) TP-XPS in the C 1s region with (d) the first spectra collected and data acquired at 30, 220, and 400 °C. (e) TP-XPS in the Ag $3d_{5/2}$ region with (f) spectra collected at 30, 220, and 400 °C. Data referenced to Al 2p at 74.5 eV.

6.5 Conclusions and future work

In this chapter, the possibility of using $Cu_5[O_2]_n$ and $Ag_5[O_2]_n$ AQCs as extrinsic catalysts for the polymerisation of Br_4TPP on inert surfaces, HOPG and mica, was explored through AFM and XPS. While the molecules sooner desorb from the surface before the C-Br bonds activation without a catalyst, both $Cu_5[O_2]_n$ and $Ag_5[O_2]_n$ AQCs are shown to activate the carbon-halogen bond of Br_4TPP molecules at mild temperatures, starting at room temperature up to 150 and 220 °C, respectively. The lower debromination temperature in the presence of $Cu_5[O_2]_n$ AQCs is found to be in agreement with the well-known fact that copper is the best catalyst for Ullmann coupling [14, 29, 232]. However, $Ag_5[O_2]_n$ clusters appear to initiate the debromination reaction at a lower temperature on mica due to the additional energy provided by the X-rays. It could be possible to prevent this phenomenon and measure the precise temperature to initiate the reaction by cooling the sample to liquid nitrogen temperature, as shown in the literature [53]. Furthermore, the excellent catalytic activity exhibited by both kinds of AQCs towards debromination could be exploited to cleave higher-energy bonds, such as C-Cl or C-F, at mild temperatures.

In the presence of both kinds of AQCs, porphyrins remain on the surface at a temperature as high as 400 °C suggesting that a coupling reaction has occurred between them. The AFM images show the growth of ordered islands on mica in the presence of $Cu_5[O_2]_n$, although the structure of each individual molecule could not be resolved. XPS data suggests that AQCs catalyse the cyclodehydrogenation reaction, which is well documented in the literature [225, 229, 230]. $Cu_5[O_2]_n$ and $Ag_5[O_2]_n$ are, thus, suitable to catalyse the activation of C-H bonds that would otherwise require higher temperatures, providing the opportunity of linking molecules thus far inaccessible to surface polymerisation on non-metal surfaces. The structure of the polymer and the cyclodehydrogenation could be further confirmed using qPlus AFM or low-temperature STM to resolve the structure of the polymer, as shown in the literature [164, 165, 225]. Furthermore, two or more species of clusters could be spin-coated on the surfaces to target specific parts of the reactions, which is not possible with noble metal surfaces alone. The results in this chapter suggest that $Ag_5[O_2]_n$ AQCs can be used to catalyse the debromination while $Cu_5[O_2]_n$ AQCs could be used to target the C-C coupling.

Although only $Cu_5[O_2]_n$ and $Ag_5[O_2]_n$ AQCs have been used in this thesis, it would be fascinating to explore the parameters space by choosing clusters with a different number of atoms, such

as Ag_3 or Cu_6, or with different chemical compositions, such as nickel or platinum. Finally, the results discussed in this chapter indicate that AQCs open the possibility of extending on-surface polymerisation to a broader selection of surfaces such as insulators and semiconductors, where the application of on-surface polymer can be better exploited. The possibility of growing molecular devices on technologically relevant substrates, such as transistors or heterojunctions directly on silicon wafers or conductive nanowires on insulators such as hexagonal boron nitride, could be explored.

Chapter 7

Conclusions and future work

This work aimed to investigate the properties of monolayer polymers grown on surfaces using two methods that are remarkably different: the atomically precise on-surface polymerisation catalysed by AQCs and the somewhat disruptive plasma polymerisation.

In Chapter 4, the widely-held belief that plasma polymerisation is surface-independent and that plasma polymers are inherently disordered was tested. By comparing the chemical composition and the morphology of TEMPO plasma polymers grown on SiO_2, Au(111), and HOPG, it was demonstrated that the surface is an essential factor, determining the final results up to a critical film thickness of approximately 30 nm. Beyond that point, the growth becomes surface-independent. The experiments conducted on HOPG showed for the first time that plasma polymerisation is suitable for growing monolayers of liquid organic molecules, that are incompatible with other methods of thin-film deposition, such as UHV deposition. The comparison between experimental data and DFT simulations highlighted that TEMPO monolayers on HOPG are ordered, in disagreement with the usual assumption that plasma polymers are always disordered, and showed that the order in the films can be controlled through annealing. These results indicate that there is a wealth of fascinating phenomena happening in the early stages of plasma polymerisation that are available for further investigation. Although simulations of plasma polymers are scarce as this research area is mainly driven by the applications, this work highlighted that DFT provides valuable information to interpret experimental results.

It was demonstrated that the anti-microbial activity of TEMPO plasma polymers deposited on PTFE against *S. epidermidis* can be improved by loading TEMPO molecules into the coating. These preliminary results could be expanded in the future by trying to incorporate more nitroxide radicals in the plasma polymer itself by increasing the monomer pressure, using pulsed plasma, or loading more TEMPO molecules into the coating. To aim for the use of TEMPO as an anti-biofouling coating in catheters and medical implants, the anti-bacterial performances should be tested against a variety of bacteria and the effects of the plasma polymers on cells should be explored.

In Chapter 5, the relationship between the catalytic activity and the isomers of $Cu_5[O_2]_n$ AQCs supported by an Au(111) surface was investigated using AFM, XPS, NIXSW, and DFT simulations. It was experimentally demonstrated for the first time that $Cu_5[O_2]_n$ AQCs have 2D and 3D isomers with different catalytic activities. The clusters are found in the 2D structure on Au(111) and become 3D when catalysing the debromination reaction of Br_4TPP molecules. However, it was not possible to investigate the next step of the Ullmann coupling of Br_4TPP, the C-C coupling, due to time limitations. It would be interesting in the future to understand if the clusters revert to the 2D isomers after the reaction is completed as XPS data suggest. Furthermore, the presence of oxygen molecules around the clusters was not directly proved but it could be substantiated through low-temperature measurements with STM or qPlus AFM.

The results presented in this chapter highlight the viability of NIXSW as a method to study the structural and chemical properties of AQCs supported by surfaces and the importance of allowing for changes in the structures of the AQCs when simulating their catalytic activity with DFT.

In Chapter 6, the use of $Cu_5[O_2]_n$ and $Ag_5[O_2]_n$ AQCs as extrinsic catalysts for the Ullmann coupling of Br_4TPP molecules on inert surfaces was investigated for the first time. It was demonstrated through AFM and XPS that AQCs can catalyse the on-surface polymerisation of the monomer on both HOPG and mica. These results are a major step towards extending the Ullmann coupling from noble metal to technologically relevant surfaces, such as SiO_2, as this approach is promising for the activation of a variety of chemical bonds, such as carbon-halogen and carbon-hydrogen. It is also possible to deposit two or more species of clusters on a surface at the same time to target specific parts of the polymerisation reactions, which is impossible when using noble metal surfaces.

In the future, it would be interesting to grow molecular devices, such as graphene nanoribbons, directly on SiO_2 by catalysing Ullmann coupling with AQCs as the transfer method currently used results in a low yield of usable nanostructures.

Appendix A

Sheath and ions in plasma polymerisation

The formation of the sheath around a substrate in contact with plasma and how it affects the flux of film-forming species are discussed in Section A.1 and A.2, respectively. In Section A.3, the effect of the monomer pressure on the collisions in the sheath is discussed and the consequences for functional group retention in plasma polymerisation are highlighted.

A.1 Sheath

When a substrate stands in the plasma, an interface, known as the sheath, develops around it, drastically changing the physics of the surrounding plasma. The fast-moving electrons impinging onto the substrate charge it to the floating voltage V_f, lower than the plasma potential V_p. In turn, the surface repels the electrons with lower kinetic energy than the potential barrier, creating a positively charged region around the substrate. At the same time, the voltage drop converts the potential energy of the ions into kinetic energy, accelerating them toward the surface. Eventually, the electron and ion fluxes at the surface, j_e and j_i respectively, reach equilibrium

$$j_i = j_e. \tag{A.1}$$

The fluxes read:

$$j_e = \frac{1}{4} n_e \bar{v}_e \tag{A.2}$$

and

$$j_i = \frac{1}{4} n_e \bar{v}_e \tag{A.3}$$

where

$$\bar{v} = \sqrt{\frac{8 k_B T}{\pi m}} \tag{A.4}$$

is the average velocity of a particle of mass m at temperature T in gas (k_B is the Boltzmann constant).

The electron density at the surface, n'_e, is the bulk electron density reduced by the Boltzmann weight that accounts for the depletion:

$$n'_e = n_e e^{-\frac{e(V_p - V_f)}{k_b T_e}}, \tag{A.5}$$

As the bulk plasma is neutral ($n_e = n_i$), and the electron density at the surface is known (eq. A.5), eq. A.1 reads:

$$\frac{1}{4} n_e \sqrt{\frac{8 k_B T_i}{\pi m_i}} = \frac{1}{4} n_e e^{\frac{e(V_p - V_f)}{k_b T_e}} \sqrt{\frac{8 k_B T_e}{\pi m_e}} \tag{A.6}$$

The potential difference between the surface and the plasma thus reads:

$$V_p - V_f = \frac{k_b T_e}{2e} \ln\left(\frac{m_i T_e}{m_e T_i}\right), \tag{A.7}$$

showing that it depends on the electron temperature.

It is possible to generalise the previous expression to compute the potential in all the points in space,$V(x)$, assuming that the Boltzmann distribution describes the electron density:

$$n_e(x) = n_e e^{-\frac{eV(x)}{k_b T_e}}. \tag{A.8}$$

The electrostatic potential generated by a charge density $\rho = e(n_i - n_e(x))$ is computed through Poisson's equation:

$$\nabla^2 V(x) = \frac{\rho}{\epsilon_0}, \tag{A.9}$$

where ϵ_0 is the permittivity of the vacuum. If $V(0) \ll k_B T_e$ the equation has an analytical solution:

$$V(x) = V_0 e^{-\frac{|x|}{\lambda_D}}, \tag{A.10}$$

where

$$\lambda_D = \sqrt{\frac{k_B T_e \epsilon_0}{n_e e^2}} \tag{A.11}$$

is the Debey length.

However, this assumption might not be realistic. Equation A.1 shows that the potential decreases exponentially from the substrate, becoming negligible after 3-4 λ_D, as the ions screen the negative charge build up. This phenomenon, known as Debey screening, is more effective at high electron temperatures and low densities.

A.2 Ion flux

At the edge of the sheath, the electron and ion densities are equal but lower than the bulk values. Indeed, electrons are repelled, while ions spread thin as their speed, $v_i(x)$, increases

$$\frac{1}{2} m_i v_i^2(x) = \frac{1}{2} m_i v_i^2(0) - eV(x), \tag{A.12}$$

where $v_i(0)$ is the speed in the bulk. So, there exists a minimum velocity such that the ions and electrons density is equal. It reads

$$v_B = \sqrt{\frac{k_B T_e}{m_i}}, \tag{A.13}$$

and it is known as Bohm velocity [240]. The area where the ions reach the Bohm velocity is the pre-sheath. It implies that a small electric field penetrates from the sheath into the pre-sheath. The computation of the Bohm velocity assumes the conservation of energy *i.e.* there are no collisions between the ions. It is a reasonable assumption only at low density.

Under the hypothesis that the ions enter the pre-sheath with negligible energy, the ion flux at the surface reads [120]:

$$j_i = e^{-\frac{1}{2}} n_i \sqrt{\frac{k_B T_e}{m_i}}. \tag{A.14}$$

It depends on the electron and not the ion temperature. The ratio between the ion flux due to the electric field in the sheath and the thermal motion, j_t is

$$\frac{j_i}{j_t} = \sqrt{2\pi} e^{-\frac{1}{2}} \sqrt{\frac{T_e}{T_i}}. \tag{A.15}$$

Assuming that the ions are at room temperature, the surfaces enhance the flux by a factor of approximately 15 [120]. This result contradicts the assumption that the ion flux is negligible compared to the radicals because their density in the bulk is lower [126]. In addition, each species has a different probability of sticking to the surface. An ion sticking probability ranges between 20 and 50% depending on the energy, as they interact with the surface electric field [120]. On the contrary, radicals and neutrals stick to the surface less than 0.1% of the time [120], further reducing their contribution to the deposited mass. There has been significant debate about the contribution of ions or radicals as film-forming species [131]. Short and colleagues have substantiated the role of the sheath at high pressure by showing that the ion mass flux at the surface, composed of intact or protonated monomers and dimers, is often sufficient to account for the whole of the mass flux [124, 127–129].

A.3 Functional groups retention

Retention of the moieties of the monomers is necessary to deposit functional coatings. However, the electrons in the plasma have enough energy to break the monomer bonds, causing damage to the molecules. Reducing the electron energy is thus the key to highly functionalised coatings. First, the lower the power provided to the plasma, the lower the energy of the electrons. Second, increasing the pressure results in a higher rate of collisions between electrons, reducing the average energy. Furthermore, ions accelerate in the sheath due to the potential difference and convert the kinetic energy into internal energy when landing on the surface, potentially causing damage to the molecule (hard-landing). If the voltage provided by the radiofrequency, V_{rf}, is much higher than $\frac{k_B T_e}{e}$, the potential difference between the plasma and the surface approaches V_{rf} that usually ranges between $5 - 40$ V. Reducing kinetic energy gained by the ions in the sheath is the key to retaining the monomer functional groups. First, decreasing the RF power reduces V_{rf}. Second, increasing the pressure causes the transition from a collisionless to a collisional sheath (α-γ transition). The ion-ion collision drastically reduces the kinetic energy of the ions and thus the fragmentation upon landing (soft-landing). Figure A.1 shows that the energy of TEMPO and protonated TEMPO ions centred at 30 eV at 5 Pa, drops to less than 15 eV at 25 Pa and the distribution centre is at 0 eV. Thus, low power and high pressure are ideal conditions for the deposition of pristine ions [127–129].

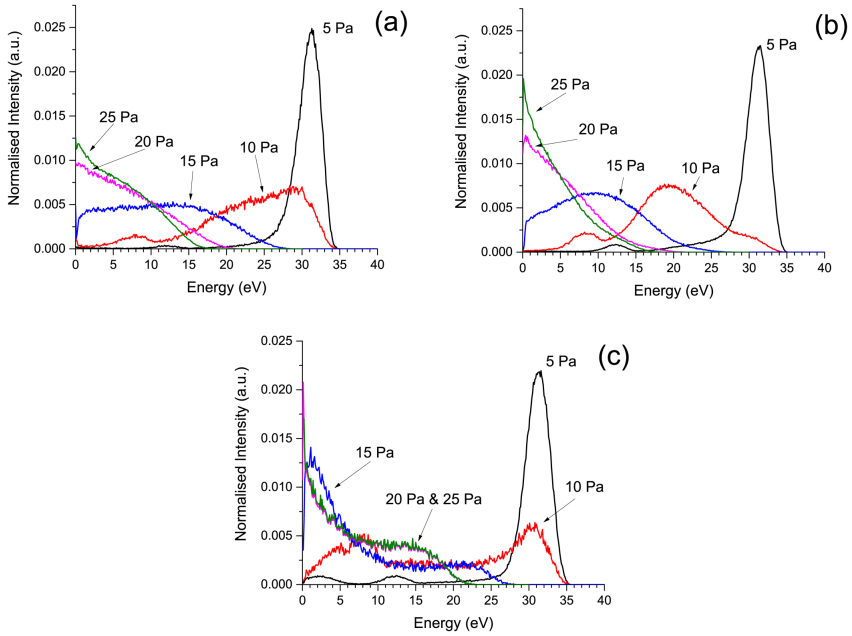

Figure A.1: Normalised ions energy distribution function of TEMPO ions of (a) 156, (b) 126 and (c) 58 a.m.u. as a function of the pressure when the power provided by the electric field is 5 W. Picture reproduced from reference [129].

Bibliography

[1] Christopher JL Murray, Kevin Shunji Ikuta, Fablina Sharara, Lucien Swetschinski, Gisela Robles Aguilar, Authia Gray, Chieh Han, Catherine Bisignano, Puja Rao, Eve Wool, Sarah C. Johnson, Annie J. Browne, Michael Give Chipeta, Frederick Fell, Sean Hackett, Georgina Haines-Woodhouse, Bahar H. Kashef Hamadani, Emmanuelle A.P. Kumaran, Barney McManigal, Ramesh Agarwal, Samuel Akech, Samuel Albertson, John Amuasi, Jason Andrews, Aleskandr Aravkin, Elizabeth Ashley, Freddie Bailey, Stephen Baker, Buddha Basnyat, Adrie Bekker, Rose Bender, Adhisivam Bethou, Julia Bielicki, Suppawat Boonkasidecha, James Bukosia, Cristina Carvalheiro, Carlos Castañeda-Orjuela, Vilada Chansamouth, Suman Chaurasia, Sara Chiurchiù, Fazle Chowdhury, Aislinn J. Cook, Ben Cooper, Tim R. Cressey, Elia Criollo-Mora, Matthew Cunningham, Saffiatou Darboe, Nicholas P.J. Day, Maia De Luca, Klara Dokova, Angela Dramowski, Susanna J. Dunachie, Tim Eckmanns, Daniel Eibach, Amir Emami, Nicholas Feasey, Natasha Fisher-Pearson, Karen Forrest, Denise Garrett, Petra Gastmeier, Ababi Zergaw Giref, Rachel Claire Greer, Vikas Gupta, Sebastian Haller, Andrea Haselbeck, Simon I. Hay, Marianne Holm, Susan Hopkins, Kenneth C. Iregbu, Jan Jacobs, Daniel Jarovsky, Fatemeh Javanmardi, Meera Khorana, Niranjan Kissoon, Elsa Kobeissi, Tomislav Kostyanev, Fiorella Krapp, Ralf Krumkamp, Ajay Kumar, Hmwe Hmwe Kyu, Cherry Lim, Direk Limmathurotsakul, Michael James Loftus, Miles Lunn, Jianing Ma, Neema Mturi, Tatiana Munera-Huertas, Patrick Musicha, Marisa Marcia Mussi-Pinhata, Tomoka Nakamura, Ruchi Nanavati, Sushma Nangia, Paul Newton, Chanpheaktra Ngoun, Amanda Novotney, Davis Nwakanma, Christina W. Obiero, Antonio Olivas-Martinez, Piero Olliaro, Ednah Ooko, Edgar Ortiz-Brizuela, Anton Yariv Peleg, Carlo Perrone, Nishad Plakkal, Alfredo Ponce-de Leon, Mathieu Raad, Tanusha Ramdin, Amy Riddell, Tamalee Roberts, Julie Victoria Robotham,

Anna Roca, Kristina E. Rudd, Neal Russell, Jesse Schnall, John Anthony Gerard Scott, Madhusudhan Shivamallappa, Jose Sifuentes-Osornio, Nicolas Steenkeste, Andrew James Stewardson, Temenuga Stoeva, Nidanuch Tasak, Areerat Thaiprakong, Guy Thwaites, Claudia Turner, Paul Turner, H. Rogier van Doorn, Sithembiso Velaphi, Avina Vongpradith, Huong Vu, Timothy Walsh, Seymour Waner, Tri Wangrangsimakul, Teresa Wozniak, Peng Zheng, Benn Sartorius, Alan D. Lopez, Andy Stergachis, Catrin Moore, Christiane Dolecek, and Mohsen Naghavi. Global burden of bacterial antimicrobial resistance in 2019: a systematic analysis. *The Lancet*, 399(10325):629–655, 2022.

[2] Francesca Prestinaci, Patrizio Pezzotti, and Annalisa Pantosti. Antimicrobial resistance: A global multifaceted phenomenon. *Pathogens and Global Health*, 109(7):309–318, 2015.

[3] Yue Wang, Yannan Yang, Yiru Shi, Hao Song, and Chengzhong Yu. Antibiotic-Free Antibacterial Strategies Enabled by Nanomaterials: Progress and Perspectives. *Advanced Materials*, 32(18):1–21, 2020.

[4] Hirotsugu Yasuda and Yasuo Matsuzawa. Economical advantages of low-pressure plasma polymerization coating. *Plasma Processes and Polymers*, 2(6):507–512, 2005.

[5] Melanie Macgregor and Krasimir Vasilev. Perspective on plasma polymers for applied biomaterials nanoengineering and the recent rise of oxazolines. *Materials*, 12(1), 2019.

[6] Yaqi Wo, Li-Chong Xu, Zi Li, Adam J Matzger, Mark E Meyerhoff, and Christopher A Siedlecki. Antimicrobial nitric oxide releasing surfaces based on S-nitroso-N-acetylpenicillamine impregnated polymers combined with submicron-textured surface topography. *Biomaterials Science*, 5(7):1265–1278, 2017.

[7] Rong Ye, Wen Chi Liu, Hui Ling Han, and Gabor A. Somorjai. Development and Elucidation of Superior Turnover Rates and Selectivity of Supported Molecular Catalysts. *ChemCatChem*, 10(8):1666–1685, 2018.

[8] Rong Ye, Tyler J. Hurlburt, Kairat Sabyrov, Selim Alayoglu, and Gabor A. Somorjai. Molecular catalysis science: Perspective on unifying the fields of catalysis. *Proceedings of the National Academy of Sciences of the United States of America*, 113(19):5159–5166, 2016.

[9] Eric C. Tyo and Stefan Vajda. Catalysis by clusters with precise numbers of atoms. *Nature Nanotechnology*, 10(7):577–588, 2015.

[10] Yugen Zhang and Siti Nurhanna Riduan. Functional porous organic polymers for heterogeneous catalysis. *Chemical Society Reviews*, 41(6):2083–2094, 2012.

[11] Qi Sun, Zhifeng Dai, Xiangju Meng, Liang Wang, and Feng Shou Xiao. Task-Specific Design of Porous Polymer Heterogeneous Catalysts beyond Homogeneous Counterparts. *ACS Catalysis*, 5(8):4556–4567, 2015.

[12] Markus Lackinger. Synthesis on inert surfaces. *Dalton Transactions*, 50(29):10020–10027, 2021.

[13] Johannes V. Barth, Giovanni Costantini, and Klaus Kern. Engineering atomic and molecular nanostructures at surfaces. *Nature*, 2005.

[14] Leonhard Grill and Stefan Hecht. Covalent on-surface polymerization. *Nature Chemistry*, 12(2):115–130, 2020.

[15] Tibor Kudernac, Shengbin Lei, Johannes A.A.W. Elemans, and Steven De Feyter. Two-dimensional supramolecular self-assembly: Nanoporous networks on surfaces. *Chemical Society Reviews*, 38(2):402–421, 2009.

[16] H Spillmann, A Kiebele, M Stöhr, T.A. Jung, D Bonifazi, F Cheng, and F Diederich. A Two-Dimensional Porphyrin-Based Porous Network Featuring Communicating Cavities for the Templated Complexation of Fullerenes. *Advanced Materials*, 18(3):275–279, feb 2006.

[17] Jean-Marie Lehn. Supramolecular chemistry. *Science*, 260:1762+, oct 1993.

[18] A Dmitriev, N Lin, J Weckesser, J V Barth, and K Kern. Supramolecular Assemblies of Trimesic Acid on a Cu(100) Surface. *The Journal of Physical Chemistry B*, 106(27):6907–6912, jul 2002.

[19] Stefan Griessl, Markus Lackinger, Michael Edelwirth, Michael Hietschold, and Wolfgang M Heckl. Self-Assembled Two-Dimensional Molecular Host-Guest Architectures From Trimesic Acid. *Single Molecules*, 3(1):25–31, apr 2002.

[20] Hermann Walch, Rico Gutzler, Thomas Sirtl, Georg Eder, and Markus Lackinger. Material- and orientation-dependent reactivity for heterogeneously catalyzed carbon-bromine bond homolysis. *Journal of Physical Chemistry C*, 114(29):12604–12609, jul 2010.

[21] U Schlickum, R Decker, F Klappenberger, G Zoppellaro, S Klyatskaya, M Ruben, I Silanes, A Arnau, K Kern, H Brune, and J V Barth. MetalOrganic Honeycomb Nanomeshes with Tunable Cavity Size. *Nano Letters*, 7(12):3813–3817, dec 2007.

[22] Jacob N. Israelachvili. *Strong Intermolecular Forces: Covalent and Coulomb Interactions*. 2011.

[23] Alexander Langner, Steven L Tait, Nian Lin, Chandrasekar Rajadurai, Mario Ruben, and Klaus Kern. Self-recognition and self-selection in multicomponent supramolecular coordination networks on surfaces. *Proceedings of the National Academy of Sciences*, 104(46):17927 LP – 17930, nov 2007.

[24] L. Lafferentz, V. Eberhardt, C. Dri, C. Africh, G. Comelli, F. Esch, S. Hecht, and L. Grill. Controlling on-surface polymerization by hierarchical and substrate-directed growth. *Nature Chemistry*, 4(3):215–220, 2012.

[25] Pascal Ruffieux, Shiyong Wang, Bo Yang, Carlos Sanchez-Sanchez, Jia Liu, Thomas Dienel, Leopold Talirz, Prashant Shinde, Carlo A. Pignedoli, Daniele Passerone, Tim Dumslaff, Xinliang Feng, Klaus Müllen, and Roman Fasel. On-surface synthesis of graphene nanoribbons with zigzag edge topology. *Nature*, 531(7595):489–492, 2016.

[26] Sylvain Clair and Dimas G. De Oteyza. Controlling a Chemical Coupling Reaction on a Surface: Tools and Strategies for On-Surface Synthesis. *Chemical Reviews*, 119(7):4717–4776, 2019.

[27] R Lloyd Carroll and Christopher B Gorman. The Genesis of Molecular Electronics. *Angewandte Chemie International Edition*, 41(23):4378–4400, dec 2002.

[28] Philipp Alexander Held, Harald Fuchs, and Armido Studer. Covalent-Bond Formation via On-Surface Chemistry. *Chemistry - A European Journal*, 23(25):5874–5892, 2017.

[29] Jonas Björk, Felix Hanke, and Sven Stafström. Mechanisms of halogen-based covalent self-assembly on metal surfaces. *Journal of the American Chemical Society*, 135(15):5768–5775, 2013.

[30] Marco Di Giovannantonio, Massimo Tomellini, Josh Lipton-Duffin, Gianluca Galeotti, Maryam Ebrahimi, Albano Cossaro, Alberto Verdini, Neerav Kharche, Vincent Meunier, Guillaume Vasseur, Yannick Fagot-Revurat, Dmitrii F. Perepichka, Federico Rosei, and Giorgio Contini. Mechanistic Picture and Kinetic Analysis of Surface-Confined Ullmann Polymerization. *Journal of the American Chemical Society*, 138(51):16696–16702, 2016.

[31] Sigrid Weigelt, Carsten Busse, Christian Bombis, MartinM. Knudsen, KurtV. Gothelf, Thomas Strunskus, Christof Wöll, Mats Dahlbom, Bjørk Hammer, Erik Lægsgaard, Flemming Besenbacher, and TrolleR. Linderoth. Covalent Interlinking of an Aldehyde and an Amine on a Au(111) Surface in Ultrahigh Vacuum. *Angewandte Chemie International Edition*, 46(48):9227–9230, dec 2007.

[32] Sigrid Weigelt, Christian Bombis, Carsten Busse, Martin M Knudsen, Kurt V Gothelf, Erik Lægsgaard, Flemming Besenbacher, and Trolle R Linderoth. Molecular Self-Assembly from Building Blocks Synthesized on a Surface in Ultrahigh Vacuum: Kinetic Control and Topo-Chemical Reactions. *ACS Nano*, 2(4):651–660, apr 2008.

[33] Leonhard Grill, Matthew Dyer, Leif Lafferentz, Mats Persson, Maike V Peters, and Stefan Hecht. Nano-architectures by covalent assembly of molecular building blocks. *Nature Nanotechnology*, 2(11):687–691, 2007.

[34] Alissa Wiengarten, Knud Seufert, Willi Auwärter, David Ecija, Katharina Diller, Francesco Allegretti, Felix Bischoff, Sybille Fischer, David A Duncan, Anthoula C Papageorgiou, Florian Klappenberger, Robert G Acres, Thien H Ngo, and Johannes V Barth. Surface-assisted Dehydrogenative Homocoupling of Porphine Molecules. *Journal of the American Chemical Society*, 136(26):9346–9354, jul 2014.

[35] Hong-Ying Gao, Philipp Alexander Held, Marek Knor, Christian Mück-Lichtenfeld, Johannes Neugebauer, Armido Studer, and Harald Fuchs. Decarboxylative Polymerization of 2,6-Naphthalenedicarboxylic Acid at Surfaces. *Journal of the American Chemical Society*, 136(27):9658–9663, jul 2014.

[36] Tao Lin, Xue Song Shang, Jinne Adisoejoso, Pei Nian Liu, and Nian Lin. Steering On-Surface Polymerization with Metal-Directed Template. *Chemistry - A European Journal*, pages 3576–3582, 2013.

[37] de Oteyza Dimas G., Gorman Patrick, Chen Yen-Chia, Wickenburg Sebastian, Riss Alexander, Mowbray Duncan J., Etkin Grisha, Pedramrazi Zahra, Tsai Hsin-Zon, Rubio Angel, Crommie Michael F., and Fischer Felix R. Direct Imaging of Covalent Bond Structure in Single-Molecule Chemical Reactions. *Science*, 340(6139):1434–1437, jun 2013.

[38] Oscar Díaz Arado, Harry Mönig, Jörn-Holger Franke, Alexander Timmer, Philipp Alexander Held, Armido Studer, and Harald Fuchs. On-surface reductive coupling of aldehydes on Au(111). *Chemical Communications*, 51(23):4887–4890, 2015.

[39] Biao Yang, Jonas Björk, Haiping Lin, Xiaoqing Zhang, Haiming Zhang, Youyong Li, Jian Fan, Qing Li, and Lifeng Chi. Synthesis of Surface Covalent Organic Frameworks via Dimerization and Cyclotrimerization of Acetyls. *Journal of the American Chemical Society*, 137(15):4904–4907, apr 2015.

[40] Marco Bieri, Matthias Treier, Jinming Cai, Kamel Aït-Mansour, Pascal Ruffieux, Oliver Gröning, Pierangelo Gröning, Marcel Kastler, Ralph Rieger, Xinliang Feng, Klaus Müllen, and Roman Fasel. Porous graphenes: Two-dimensional polymer synthesis with atomic precision. *Chemical Communications*, (45):6919–6921, 2009.

[41] Rico Gutzler, Hermann Walch, Georg Eder, Stephan Kloft, Wolfgang M. Heckl, and Markus Lackinger. Surface mediated synthesis of 2D covalent organic frameworks: 1,3,5-tris(4-bromophenyl)benzene on graphite(001), Cu(111), and Ag(110). *Chemical Communications*, (29):4456–4458, 2009.

[42] Marco Di Giovannantonio, Mohamed El Garah, Josh Lipton-Duffin, Vincent Meunier, Luis Cardenas, Yannick Fagot-Revurat, Albano Cossaro, Alberto Verdini, Dmitrii F. Perepichka, Federico Rosei, and Giorgio Contini. Reply to "comment on 'Insight into Organometallic Intermediate and Its Evolution to Covalent Bonding in Surface-Confined Ullmann Polymerization'". *ACS Nano*, 8(3):1969–1971, 2014.

[43] Marco Bieri, Manh Thuong Nguyen, Oliver Gröning, Jinming Cai, Matthias Treier, Kamel Aït-Mansour, Pascal Ruffieux, Carlo A. Pignedoli, Daniele Passerone, Marcel Kastler, Klaus

Müllen, and Roman Fasel. Two-dimensional polymer formation on surfaces: Insight into the roles of precursor mobility and reactivity. *Journal of the American Chemical Society*, 132(46):16669–16676, 2010.

[44] César Moreno, Manuel Vilas-Varela, Bernhard Kretz, Aran Garcia-Lekue, Marius V. Costache, Markos Paradinas, Mirko Panighel, Gustavo Ceballos, Sergio O. Valenzuela, Diego Peña, and Aitor Mugarza. Bottom-up synthesis of multifunctional nanoporous graphene. *Science*, 360(6385):199–203, 2018.

[45] Alex Saywell, Jutta Schwarz, Stefan Hecht, and Leonhard Grill. Polymerization on Stepped Surfaces: Alignment of Polymers and Identification of Catalytic Sites. *Angewandte Chemie International Edition*, 51(21):5096–5100, may 2012.

[46] Qitang Fan, Cici Wang, Yong Han, Junfa Zhu, Wolfgang Hieringer, Julian Kuttner, Gerhard Hilt, and J Michael Gottfried. Surface-Assisted Organic Synthesis of Hyperbenzene Nanotroughs. *Angewandte Chemie International Edition*, 52(17):4668–4672, apr 2013.

[47] F Ullmann and Jean Bielecki. Ueber Synthesen in der Biphenylreihe. *Berichte der deutschen chemischen Gesellschaft*, 34(2):2174–2185, may 1901.

[48] Catherine M. Doyle, Cormac McGuinness, Anna P. Lawless, Alexei B. Preobrajenski, Nikolay A. Vinogradov, and Attilio A. Cafolla. Surface Mediated Synthesis of 2D Covalent Organic Networks: 1,3,5-Tris(4-bromophenyl)benzene on Au(111). *Physica Status Solidi (B) Basic Research*, 256(2):1–11, 2019.

[49] Zhenliang Hao, Lingling Song, Cuixia Yan, Hui Zhang, Zilin Ruan, Shijie Sun, Jianchen Lu, and Jinming Cai. On-surface synthesis of one-type pore single-crystal porous covalent organic frameworks. *Chemical Communications*, 55(72):10800–10803, 2019.

[50] Ke Ji Shi, Xin Zhang, Chen Hui Shu, Deng Yuan Li, Xin Yan Wu, and Pei Nian Liu. Ullmann coupling reaction of aryl chlorides on Au(111) using dosed Cu as a catalyst and the programmed growth of 2D covalent organic frameworks. *Chemical Communications*, 52(56):8726–8729, 2016.

[51] Claudius Morchutt, Jonas Björk, Sören Krotzky, Rico Gutzler, and Klaus Kern. Covalent coupling via dehalogenation on Ni(111) supported boron nitride and graphene. *Chemical Communications*, 51(12):2440–2443, 2015.

[52] M. Lackinger. Surface-assisted Ullmann coupling. *Chemical Communications*, 53(56):7872–7885, 2017.

[53] Massimo Fritton, David A. Duncan, Peter S. Deimel, Atena Rastgoo-Lahrood, Francesco Allegretti, Johannes V. Barth, Wolfgang M. Heckl, Jonas Björk, and Markus Lackinger. The Role of Kinetics versus Thermodynamics in Surface-Assisted Ullmann Coupling on Gold and Silver Surfaces. *Journal of the American Chemical Society*, 141(12):4824–4832, 2019.

[54] Markus Kittelmann, Philipp Rahe, Markus Nimmrich, Christopher M. Hauke, André Gourdon, and Angelika Kühnle. On-surface covalent linking of organic building blocks on a bulk insulator. *ACS Nano*, 5(10):8420–8425, 2011.

[55] Markus Kittelmann, Robert Lindner, and Angelika Kühnle. On-Surfaces Synthesis on Insulating Substrates BT - On-Surface Synthesis. pages 181–197, Cham, 2016. Springer International Publishing.

[56] Markus Kittelmann, Markus Nimmrich, Robert Lindner, André Gourdon, and Angelika Kühnle. Sequential and site-specific on-surface synthesis on a bulk insulator. *ACS Nano*, 7(6):5614–5620, 2013.

[57] Teng Zhang, Renyi Li, Xiaoyu Hao, Quanzhen Zhang, Huixia Yang, Yanhui Hou, Baofei Hou, Liangguang Jia, Kaiyue Jiang, Yu Zhang, Xu Wu, Xiaodong Zhuang, Liwei Liu, Yugui Yao, Wei Guo, and Yeliang Wang. Ullmann-Like Covalent Bond Coupling without Participation of Metal Atoms. *ACS Nano*, 17(5):4387–4395, 2023.

[58] Christian Bombis, Francisco Ample, Leif Lafferentz, Hao Yu, Stefan Hecht, Christian Joachim, and Leonhard Grill. Single molecular wires connecting metallic and insulating surface areas. *Angewandte Chemie - International Edition*, 48(52):9966–9970, 2009.

[59] Atena Rastgoo-Lahrood, Jonas Björk, Matthias Lischka, Johanna Eichhorn, Stephan Kloft, Massimo Fritton, Thomas Strunskus, Debabrata Samanta, Michael Schmittel, Wolfgang M. Heckl, and Markus Lackinger. Post-Synthetic Decoupling of On-Surface-Synthesized Covalent

Nanostructures from Ag(111). *Angewandte Chemie - International Edition*, 55(27):7650–7654, 2016.

[60] Jinne Adisoejoso, Tao Lin, Xue Song Shang, Ke Ji Shi, Aditi Gupta, Pei Nian Liu, and Nian Lin. A single-molecule-level mechanistic study of pd-catalyzed and cu-catalyzed homocoupling of aryl bromide on an au(111) surface. *Chemistry - A European Journal*, 20(14):4111–4116, 2014.

[61] B. Cirera, J. Björk, R. Otero, J. M. Gallego, R. Miranda, and D. Ecija. Efficient Lanthanide Catalyzed Debromination and Oligomeric Length-Controlled Ullmann Coupling of Aryl Halides. *Journal of Physical Chemistry C*, 121(14):8033–8041, 2017.

[62] Xu Zhao, Jiehe Sui, Fei Li, Haitao Fang, Hongen Wang, Jiangyu Li, Wei Cai, and Guozhong Cao. ion batteries †. pages 17902–17910, 2016.

[63] Vanesa Porto, Erea Borrajo, David Buceta, Carmen Carneiro, Shahana Huseyinova, Blanca Domínguez, Kyra J.E. Borgman, Melike Lakadamyali, Maria F. Garcia-Parajo, José Neissa, Tomás García-Caballero, Giampaolo Barone, M. Carmen Blanco, Natalia Busto, Begoña García, José Maria Leal, José Blanco, José Rivas, M. Arturo López-Quintela, and Fernando Domínguez. Silver Atomic Quantum Clusters of Three Atoms for Cancer Therapy: Targeting Chromatin Compaction to Increase the Therapeutic Index of Chemotherapy. *Advanced Materials*, 30(33):1–8, 2018.

[64] Takane Imaoka, Tetsuya Toyonaga, Mari Morita, Naoki Haruta, and Kimihisa Yamamoto. Isomerizations of a Pt4 cluster revealed by spatiotemporal microscopic analysis. *Chemical Communications*, 55(33):4753–4756, 2019.

[65] Shahana Huseyinova, José Blanco, Félix G. Requejo, José M. Ramallo-López, M. Carmen Blanco, David Buceta, and M. Arturo López-Quintela. Synthesis of Highly Stable Surfactant-free Cu5 Clusters in Water. *Journal of Physical Chemistry C*, 120(29):15902–15908, 2016.

[66] Caroline M Krauter, Jochen Schirmer, Christoph R Jacob, Markus Pernpointner, and Andreas Dreuw. Plasmons in molecules: Microscopic characterization based on orbital transitions and momentum conservation. *The Journal of Chemical Physics*, 141(10):104101, sep 2014.

[67] Yizhong Lu and Wei Chen. Sub-nanometre sized metal clusters: From synthetic challenges to the unique property discoveries. *Chemical Society Reviews*, 41(9):3594–3623, 2012.

[68] Xiang Liu and Didier Astruc. Atomically precise copper nanoclusters and their applications. *Coordination Chemistry Reviews*, 359:112–126, 2018.

[69] Avik Halder, Larry A. Curtiss, Alessandro Fortunelli, and Stefan Vajda. Perspective: Size selected clusters for catalysis and electrochemistry. *Journal of Chemical Physics*, 148(11), 2018.

[70] Estefanía Fernández and Mercedes Boronat. Sub nanometer clusters in catalysis. *Journal of Physics: Condensed Matter*, 31(1):013002, jan 2019.

[71] Vanesa Porto, David Buceta, Blanca Domínguez, Carmen Carneiro, Erea Borrajo, María Fraile, Nerea Davila-Ferreira, Iria R. Arias, José M. Blanco, Maria C. Blanco, Juan M. Devida, Lisandro J. Giovanetti, Félix G. Requejo, Juan C. Hernández-Garrido, José J. Calvino, Miguel López-Haro, Giampaolo Barone, Andrew M. James, Tomás García-Caballero, Diego M. González-Castaño, Martin Treder, Wolfgang Huber, Anxo Vidal, Michael P. Murphy, M. Arturo López-Quintela, and Fernando Domínguez. Silver Clusters of Five Atoms as Highly Selective Antitumoral Agents Through Irreversible Oxidation of Thiols. *Advanced Functional Materials*, 32(29), 2022.

[72] Xiangchun Zhang, Zhichao Zhang, Qingming Shu, Chao Xu, Qinqin Zheng, Zhao Guo, Chen Wang, Zhenxia Hao, Xin Liu, Guoqing Wang, Wangjun Yan, Hongping Chen, and Chengyin Lu. Copper Clusters: An Effective Antibacterial for Eradicating Multidrug-Resistant Bacterial Infection In Vitro and In Vivo. *Advanced Functional Materials*, 31(14), 2021.

[73] Youkun Zheng, Lanmei Lai, Weiwei Liu, Hui Jiang, and Xuemei Wang. Recent advances in biomedical applications of fluorescent gold nanoclusters. *Advances in Colloid and Interface Science*, 242:1–16, 2017.

[74] Carlos Vázquez-Vázquez, Manuel Bañobre-López, Atanu Mitra, M. Arturo López-Quintela, and José Rivas. Synthesis of small atomic copper clusters in microemulsions. *Langmuir*, 25(14):8208–8216, 2009.

[75] W. D. Knight, Keith Clemenger, Walt A. De Heer, Winston A. Saunders, M. Y. Chou, and Marvin L. Cohen. Electronic shell structure and abundances of sodium clusters. *Physical Review Letters*, 52(24):2141–2143, 1984.

[76] W Ekardt. Photoabsorption Photoemission. *Physical Review B*, 31(10):6360–6370, 1985.

[77] W. Ekardt. Collective multipole excitations in small metal particles: Critical angular momentum lcr for the existence of collective surface modes. *Physical Review B*, 32(4):1961–1970, 1985.

[78] A. W. Castleman and S. N. Khanna. Clusters, superatoms, and building blocks of new materials. *Journal of Physical Chemistry C*, 113(7):2664–2675, 2009.

[79] Dennis Bonatsos, N. Karoussos, D. Lenis, P. P. Raychev, R. P. Roussev, and P. A. Terziev. Unified description of magic numbers of metal clusters in terms of the three-dimensional q-deformed harmonic oscillator. *Physical Review A - Atomic, Molecular, and Optical Physics*, 62(1):13, 2000.

[80] Dennis Bonatsos, D. Lenis, P. P. Raychev, and P. A. Terziev. Deformed harmonic oscillators for metal clusters: Analytic properties and supershells. *Physical Review A - Atomic, Molecular, and Optical Physics*, 65(3):1–12, 2002.

[81] Matthias Emmrich, Ferdinand Huber, Florian Pielmeier, Joachim Welker, Thomas Hofmann, Maximilian Schneiderbauer, Daniel Meuer, Svitlana Polesya, Sergiy Mankovsky, Diemo Ködderitzsch, Hubert Ebert, and Franz J. Giessibl. Subatomic resolution force microscopy reveals internal structure and adsorption sites of small iron clusters. *Science*, 348(6232):308–311, 2015.

[82] David Buceta, Yolanda Piñeiro, Carlos Vázquez-Vázquez, José Rivas, and Manuel Arturo López-Quintela. Metallic clusters: Theoretical background, properties and synthesis in microemulsions. *Catalysts*, 4(4):356–374, 2014.

[83] Noelia Vilar-Vidal, José Rivas, and M. Arturo López-Quintela. Size dependent catalytic activity of reusable subnanometer copper(0) clusters. *ACS Catalysis*, 2(8):1693–1697, 2012.

[84] E. William Kaden, Wu Tianpin, A. William Kunkel, and Scott L. Anderson. Electronic Structure Controls Reactivity of Size-Selected Pd Clusters Adsorbed on TiO2 Surfaces. *Science (New York, N.Y.)*, 326(November):826–830, 2009.

[85] Takane Imaoka, Yuki Akanuma, Naoki Haruta, Shogo Tsuchiya, Kentaro Ishihara, Takeshi Okayasu, Wang Jae Chun, Masaki Takahashi, and Kimihisa Yamamoto. Platinum clusters with precise numbers of atoms for preparative-scale catalysis. *Nature Communications*, 8(1):1–8, 2017.

[86] A. Jafarzadeh, K. M. Bal, A. Bogaerts, and E. C. Neyts. CO2 Activation on TiO2-Supported Cu5 and Ni5 Nanoclusters: Effect of Plasma-Induced Surface Charging. *Journal of Physical Chemistry C*, 123(11):6516–6525, 2019.

[87] Lichen Liu and Avelino Corma. Confining isolated atoms and clusters in crystalline porous materials for catalysis. *Nature Reviews Materials*, 6(3):244–263, 2021.

[88] Michael Walter, Jaakko Akola, Olga Lopez-Acevedo, Pablo D Jadzinsky, Guillermo Calero, Christopher J Ackerson, Robert L Whetten, Henrik Grönbeck, and Hannu Häkkinen. A unified view of ligand-protected gold clusters as superatom complexes. *Proceedings of the National Academy of Sciences*, 105(27):9157 LP – 9162, jul 2008.

[89] Estefania Fernández and Mercedes Boronat. Sub nanometer clusters in catalysis. *Journal of Physics Condensed Matter*, 31(1), 2019.

[90] Alexandre Zanchet, Patricia López-Caballero, Alexander O. Mitrushchenkov, David Buceta, Manuel Arturo López-Quintela, Andreas W. Hauser, and Mariá Pilar De Lara-Castells. On the Stability of Cu5 Catalysts in Air Using Multireference Perturbation Theory. *Journal of Physical Chemistry C*, 123(44):27064–27072, 2019.

[91] Mercedes Boronat, Tirso López-Ausens, and Avelino Corma. Making C–C Bonds with Gold Catalysts: A Theoretical Study of the Influence of Gold Particle Size on the Dissociation of the C–X Bond in Aryl Halides. *The Journal of Physical Chemistry C*, 118(17):9018–9029, may 2014.

[92] Andrew A. Herzing, Christopher J. Kiely, Albert F. Carley, Philip Landon, and Graham J. Hutchings. Identification of active gold nanoclusters on iron oxide supports for CO oxidation. *Science*, 321(5894):1331–1335, 2008.

[93] Stefan Vajda, Michael J. Pellin, Jeffrey P. Greeley, Christopher L. Marshall, Larry A. Curtiss, Gregory A. Ballentine, Jeffrey W. Elam, Stephanie Catillon-Mucherie, Paul C. Redfern, Faisal Mehmood, and Peter Zapol. Subnanometre platinum clusters as highly active and selective catalysts for the oxidative dehydrogenation of propane. *Nature Materials*, 8(3):213–216, 2009.

[94] Kimihisa Yamamoto, Takane Imaoka, Wang-Jae Chun, Osamu Enoki, Hideaki Katoh, Masahiro Takenaga, and Atsunori Sonoi. Size-specific catalytic activity of platinum clusters enhances oxygen reduction reactions. *Nature Chemistry*, 1(5):397–402, 2009.

[95] Judit Oliver-Meseguer, Jose R. Cabrero-Antonino, Irene Domínguez, Antonio Leyva-Pérez, and Avelino Corma. Small gold clusters formed in solution give reaction turnover numbers of 107at room temperature. *Science*, 338(6113):1452–1455, 2012.

[96] Alexander Okrut, Ron C Runnebaum, Xiaoying Ouyang, Jing Lu, Ceren Aydin, Son-Jong Hwang, Shengjie Zhang, Olayinka A Olatunji-Ojo, Kathleen A Durkin, David A Dixon, Bruce C Gates, and Alexander Katz. Selective molecular recognition by nanoscale environments in a supported iridium cluster catalyst. *Nature Nanotechnology*, 9(6):459–465, 2014.

[97] Prasenjit Maity, Seiji Yamazoe, and Tatsuya Tsukuda. Erratum: Dendrimer encapsulated copper cluster as a chemoselective and regenerable hydrogenation catalyst (ACS Catalysis (2013) 3 (182-185)). *ACS Catalysis*, 3(4):554, 2013.

[98] Yongmei Liu, Hironori Tsunoyama, Tomoki Akita, Songhai Xie, and Tatsuya Tsukuda. Aerobic Oxidation of Cyclohexane Catalyzed by Size-Controlled Au. *ACS Catalysis*, pages 2–6, 2011.

[99] Gao Li, Chao Liu, Yu Lei, and Rongchao Jin. Au25 nanocluster-catalyzed Ullmann-type homocoupling reaction of aryl iodides. *Chemical Communications*, 48(98):12005–12007, 2012.

[100] Zhen An Qiao, Pengfei Zhang, Song Hai Chai, Miaofang Chi, Gabriel M. Veith, Nidia C. Gallego, Michelle Kidder, and Sheng Dai. Lab-in-a-shell: Encapsulating metal clusters for size sieving catalysis. *Journal of the American Chemical Society*, 136(32):11260–11263, 2014.

[101] Avelino Corma, Patricia Concepción, Mercedes Boronat, Maria J Sabater, Javier Navas, Miguel José Yacaman, Eduardo Larios, Alvaro Posadas, M Arturo López-Quintela, David Buceta, Ernest Mendoza, Gemma Guilera, and Alvaro Mayoral. Exceptional oxidation activity with size-controlled supported gold clusters of low atomicity. *Nature Chemistry*, 5(9):775–781, 2013.

[102] Antonio Leyva-Pérez, Judit Oliver-Meseguer, Paula Rubio-Marqués, and Avelino Corma. Water-stabilized three- and four-atom palladium clusters as highly active catalytic species in ligand-free C-C cross-coupling reactions. *Angewandte Chemie - International Edition*, 52(44):11554–11559, 2013.

[103] Qingqing Wu, Songjun Hou, David Buceta, Hector J L Ordoñez, M Arturo López-Quintela, and Colin J Lambert. Tuning the surface states of TiO2 using Cu5 atomic clusters. *Applied Surface Science*, 594:153455, 2022.

[104] Moteb Alotaibi, Qingqing Wu, and Colin Lambert. Computational studies of Ag5 atomic quantum clusters deposited on anatase and rutile TiO2 surfaces. *Applied Surface Science*, 613:156054, 2023.

[105] Anderson S. Chaves, Gustavo G. Rondina, Maurício J. Piotrowski, Polina Tereshchuk, and Juarez L.F. Da Silva. The role of charge states in the atomic structure of Cun and Ptn (n = 2-14 atoms) clusters: A DFT investigation. *Journal of Physical Chemistry A*, 118(45):10813–10821, 2014.

[106] Yuuki Adachi, Yasuhiro Sugawara, and Yan Jun Li. Atomic Scale Three-Dimensional Au Nanocluster on a Rutile TiO2(110) Surface Resolved by Atomic Force Microscopy. *Journal of Physical Chemistry Letters*, 11(17):7153–7158, 2020.

[107] P Calaminici, A M Köster, N Russo, and D R Salahub. A density functional study of small copper clusters: Cun (n5). *The Journal of Chemical Physics*, 105(21):9546–9556, dec 1996.

[108] Xi Kang and Manzhou Zhu. Structural Isomerism in Atomically Precise Nanoclusters. *Chemistry of Materials*, 33(1):39–62, 2021.

[109] Jiale Shi, Shanghui Huang, François Gygi, and Jonathan K. Whitmer. Free-Energy Landscape and Isomerization Rates of Au4Clusters at Finite Temperatures. *Journal of Physical Chemistry A*, 126(21):3392–3400, 2022.

[110] Estefanía Fernández, Mercedes Boronat, and Avelino Corma. Trends in the Reactivity of Molecular O2 with Copper Clusters: Influence of Size and Shape. *Journal of Physical Chemistry C*, 119(34):19832–19846, 2015.

[111] Estefania Fernandez, Mercedes Boronat, and Avelino Corma. The Crucial Role of Cluster Morphology on the Epoxidation of Propene Catalyzed by Cu5: A DFT Study. *Journal of Physical Chemistry C*, 124(39):21549–21558, 2020.

[112] Estefanía Fernández, Mercedes Boronat, and Avelino Corma. The 2D or 3D morphology of sub-nanometer Cu5and Cu8clusters changes the mechanism of CO oxidation. *Physical Chemistry Chemical Physics*, 24(7):4504–4514, 2022.

[113] Xiang Chu, Mingli Xiang, Qun Zeng, Wenhai Zhu, and Mingli Yang. Competition between monomer and dimer fragmentation pathways of cationic CuN clusters of N = 2-20. *Journal of Physics B: Atomic, Molecular and Optical Physics*, 44(20), 2011.

[114] Karl Jug, Bernd Zimmermann, Patrizia Calaminici, and Andreas M. Köster. Structure and stability of small copper clusters. *Journal of Chemical Physics*, 116(11):4497–4507, 2002.

[115] Manh Thuong Nguyen, Carlo A. Pignedoli, and Daniele Passerone. An ab initio insight into the Cu(111)-mediated Ullmann reaction. *Physical Chemistry Chemical Physics*, 13(1):154–160, 2011.

[116] Patricia Concepción, Mercedes Boronat, Saray García-García, Estefanía Fernández, and Avelino Corma. Enhanced Stability of Cu Clusters of Low Atomicity against Oxidation. Effect on the Catalytic Redox Process. *ACS Catalysis*, 7(5):3560–3568, 2017.

[117] Francisco L Tabares and Ita Junkar. Cold Plasma Systems and their Application in Surface Treatments for Medicine. *Molecules (Basel, Switzerland)*, 26(7), mar 2021.

[118] J R Hollahan, B B Stafford, R D Falb, and S T Payne. Attachment of amino groups to polymer surfaces by radiofrequency plasmas. *Journal of Applied Polymer Science*, 13(4):807–816, apr 1969.

[119] H K Yasuda. *Plasma Polymerization*. Academic Press, 1985.

[120] Andrew Michelmore, David A. Steele, Jason D. Whittle, James W. Bradley, and Robert D. Short. Nanoscale deposition of chemically functionalised films via plasma polymerisation. *RSC Advances*, 3(33):13540–13557, 2013.

[121] Hasan D Hazrati, Jason D Whittle, and Krasimir Vasilev. A Mechanistic Study of the Plasma Polymerization of Ethanol. *Plasma Processes and Polymers*, 11(2):149–157, feb 2014.

[122] Andrew Michelmore, Petr Martinek, Vasu Sah, Robert D. Short, and Krasimir Vasilev. Surface morphology in the early stages of plasma polymer film growth from amine-containing monomers. *Plasma Processes and Polymers*, 8(5):367–372, 2011.

[123] Krasimir Vasilev, Andrew Michelmore, Petr Martinek, Joseph Chan, Vasu Sah, Hans J. Griesser, and Robert D. Short. Early stages of growth of plasma polymer coatings deposited from nitrogen- and oxygen-containing monomers. *Plasma Processes and Polymers*, 7(9-10):824–835, 2010.

[124] Thomas D. Michl, Jakob Barz, Carla Giles, Michael Haupt, Jan Hinnerk Henze, Joachim Mayer, Kathryn Futrega, Michael Robert Doran, Christian Oehr, Krasimir Vasilev, Bryan R. Coad, and Hans Joerg Griesser. Plasma Polymerization of TEMPO Yields Coatings Containing Stable Nitroxide Radicals for Controlling Interactions with Prokaryotic and Eukaryotic Cells. *ACS Applied Nano Materials*, 1(12):6587–6595, 2018.

[125] Thomas Danny Michl, Dung Thuy Thi Tran, Hannah Frederike Kuckling, Aigerim Zhalgasbaikyzy, Barbora Ivanovská, Laura Elena González García, Rahul Madathiparambil Visalakshan, and Krasimir Vasilev. It takes two for chronic wounds to heal: dispersing bacterial biofilm and modulating inflammation with dual action plasma coatings. *RSC Advances*, 10(13):7368–7376, 2020.

[126] Dirk Hegemann, Mohammad Mokbul Hossain, Enrico Körner, and Dawn J. Balazs. Macroscopic description of plasma polymerization. *Plasma Processes and Polymers*, 4(3):229–238, 2007.

[127] Solmaz Saboohi, Marek Jasieniak, Bryan R. Coad, Hans J. Griesser, Robert D. Short, and Andrew Michelmore. Comparison of Plasma Polymerization under Collisional and Collision-Less Pressure Regimes. *Journal of Physical Chemistry B*, 119(49):15359–15369, 2015.

[128] Solmaz Saboohi, Bryan R. Coad, Andrew Michelmore, Robert D. Short, and Hans J. Griesser. Hyperthermal Intact Molecular Ions Play Key Role in Retention of ATRP Surface Initiation Capability of Plasma Polymer Films from Ethyl α-Bromoisobutyrate. *ACS Applied Materials and Interfaces*, 8(25):16493–16502, 2016.

[129] Michael J. Barnes, Alexander J. Robson, Javad Naderi, Robert D. Short, and James W. Bradley. Plasma polymerization of (2,2,6,6-tetramethylpiperidin-1-yl)oxyl in a collisional, capacitively coupled radio frequency discharge. *Biointerphases*, 15(6):061007, 2020.

[130] Dirk Hegemann. Macroscopic control of plasma polymerization processes. *Pure and Applied Chemistry*, 80(9):1893–1900, 2008.

[131] Achim Von Keudell and Jan Benedikt. A Physicist's perspective on "Views on macroscopic kinetics of plasma polymerisation". *Plasma Processes and Polymers*, 7(5):376–379, 2010.

[132] www.altrika.com.

[133] www.bdbiosciences.com/purecoat.

[134] www.liquipel.com.

[135] www.p2i.com.

[136] Jason D. Whittle, Robert D. Short, David A. Steele, James W. Bradley, Paul M. Bryant, Faiq Jan, Hynek Biederman, Anton A. Serov, Andrei Choukurov, Andrew L. Hook, Winston A. Ciridon, Giacomo Ceccone, Dirk Hegemann, Enrico Körner, and Andrew Michelmore. Variability in plasma polymerization processes - An international round-robin study. *Plasma Processes and Polymers*, 10(9):767–778, 2013.

[137] Bryan R. Coad, Pietro Favia, Krasimir Vasilev, and Hans J. Griesser. Plasma polymerization for biomedical applications: A review. *Plasma Processes and Polymers*, 19(11):1–16, 2022.

[138] Shengxia Duan, Xia Liu, Yanan Wang, Yuedong Meng, Ahmed Alsaedi, Tasawar Hayat, and Jiaxing Li. Plasma surface modification of materials and their entrapment of water contaminant: A review. *Plasma Processes and Polymers*, 14(9), 2017.

[139] Jesús Idígoras, Francisco J. Aparicio, Lidia Contreras-Bernal, Susana Ramos-Terrón, María Alcaire, Juan Ramón Sánchez-Valencia, Ana Borras, Ángel Barranco, and Juan A. Anta. Enhancing Moisture and Water Resistance in Perovskite Solar Cells by Encapsulation with Ultrathin Plasma Polymers. *ACS Applied Materials and Interfaces*, 10(14):11587–11594, 2018.

[140] Mohan V. Jacob, Natalie S. Olsen, Liam J. Anderson, Kateryna Bazaka, and Robert A. Shanks. Plasma polymerised thin films for flexible electronic applications. *Thin Solid Films*, 546:167–170, 2013.

[141] www.biofilms.ac.uk.

[142] D. R.M. Smith, K. B. Pouwels, S. Hopkins, N. R. Naylor, T. Smieszek, and J. V. Robotham. Epidemiology and health-economic burden of urinary-catheter-associated infection in English NHS hospitals: a probabilistic modelling study. *Journal of Hospital Infection*, 103(1):44–54, 2019.

[143] K. Bazaka, M. V. Jacob, W. Chrzanowski, and K. Ostrikov. Anti-bacterial surfaces: Natural agents, mechanisms of action, and plasma surface modification. *RSC Advances*, 5(60):48739–48759, 2015.

[144] Lucy M. Watkins, Adam F. Lee, James W.B. Moir, and Karen Wilson. Plasma-generated poly(allyl alcohol) antifouling coatings for cellular attachment. *ACS Biomaterials Science and Engineering*, 3(1):88–94, 2017.

[145] Evan M. Hetrick and Mark H. Schoenfisch. Reducing implant-related infections: Active release strategies. *Chemical Society Reviews*, 35(9):780–789, 2006.

[146] Stefanie Ann Alexander, Caroline Kyi, and Carl H. Schiesser. Nitroxides as anti-biofilm compounds for the treatment of Pseudomonas aeruginosa and mixed-culture biofilms. *Organic and Biomolecular Chemistry*, 13(16):4751–4759, 2015.

[147] Thomas D. Michl, Bryan R. Coad, Michael Doran, Michael Osiecki, Morteza Hasanzadeh Kafshgari, Nicolas H. Voelcker, Amanda Hüsler, Krasimir Vasilev, and Hans J. Griesser.

Nitric oxide releasing plasma polymer coating with bacteriostatic properties and no cytotoxic side effects. *Chemical Communications*, 51(32):7058–7060, 2015.

[148] Zahra Sadrearhami, Thuy Khanh Nguyen, Rashin Namivandi-Zangeneh, Kenward Jung, Edgar H.H. Wong, and Cyrille Boyer. Recent advances in nitric oxide delivery for antimicrobial applications using polymer-based systems. *Journal of Materials Chemistry B*, 6(19):2945–2959, 2018.

[149] Nicolas Barraud, Michael V Storey, Zoe P Moore, Jeremy S Webb, Scott A Rice, and Staffan Kjelleberg. Nitric oxide-mediated dispersal in single- and multi-species biofilms of clinically and industrially relevant microorganisms. *Microbial Biotechnology*, 2(3):370–378, may 2009.

[150] Niu Liu, Yueming Xu, Sajjad Hossain, Nick Huang, Dan Coursolle, Jeffrey A Gralnick, and Elizabeth M Boon. Nitric Oxide Regulation of Cyclic di-GMP Synthesis and Hydrolysis in Shewanella woodyi. *Biochemistry*, 51(10):2087–2099, mar 2012.

[151] Dhruv P Arora, Sajjad Hossain, Yueming Xu, and Elizabeth M Boon. Nitric Oxide Regulation of Bacterial Biofilms. *Biochemistry*, 54(24):3717–3728, jun 2015.

[152] Salvatore Sortino. Light-controlled nitric oxide delivering molecular assemblies. *Chemical Society Reviews*, 39(8):2903–2913, 2010.

[153] César De La Fuente-Núñez, Fany Reffuveille, Kathryn E. Fairfull-Smith, and Robert E.W. Hancock. Effect of nitroxides on swarming motility and biofilm formation, multicellular behaviors in pseudomonas aeruginosa. *Antimicrobial Agents and Chemotherapy*, 57(10):4877–4881, 2013.

[154] Robert P Howlin, Katrina Cathie, Luanne Hall-Stoodley, Victoria Cornelius, Caroline Duignan, Raymond N Allan, Bernadette O Fernandez, Nicolas Barraud, Ken D Bruce, Johanna Jefferies, Michael Kelso, Staffan Kjelleberg, Scott A Rice, Geraint B Rogers, Sandra Pink, Caroline Smith, Priya S Sukhtankar, Rami Salib, Julian Legg, Mary Carroll, Thomas Daniels, Martin Feelisch, Paul Stoodley, Stuart C Clarke, Gary Connett, Saul N Faust, and Jeremy S Webb. Low-Dose Nitric Oxide as Targeted Anti-biofilm Adjunctive Therapy to Treat Chronic Pseudomonas aeruginosa Infection in Cystic Fibrosis. *Molecular Therapy*, 25(9):2104–2116, 2017.

[155] Behnam Akhavan, Karyn Jarvis, and Peter Majewski. Evolution of hydrophobicity in plasma polymerised 1,7-octadiene films. *Plasma Processes and Polymers*, 10(11):1018–1029, 2013.

[156] Behnam Akhavan, Bernhard Menges, and Renate Förch. Inhomogeneous Growth of Micrometer Thick Plasma Polymerized Films. *Langmuir*, 32(19):4792–4799, 2016.

[157] Nghia H. Le, Magali Bonne, Aissam Airoudj, Philippe Fioux, Rémi Boubon, Diane Rebiscoul, Florence Bally-Le Gall, Bénédicte Lebeau, and Vincent Roucoules. When chemistry of the substrate drastically controls morphogenesis of plasma polymer thin films. *Plasma Processes and Polymers*, (August), 2020.

[158] Michel M. Brioude, Marie Pierre Laborie, Hamidou Haidara, and Vincent Roucoules. Understanding the Morphogenesis of Nanostructures in Maleic Anhydride Plasma Polymer Films via Growth Kinetics and Chemical Force Titration. *Plasma Processes and Polymers*, 12(11):1220–1230, 2015.

[159] Marianne Vandenbossche, Maria Isabel Butron Garcia, Urs Schütz, Patrick Rupper, Martin Amberg, and Dirk Hegemann. Initial Growth of Functional Plasma Polymer Nanofilms. *Plasma Chemistry and Plasma Processing*, 36(2):667–677, 2016.

[160] D. Hegemann, B. Hanselmann, N. Blanchard, and M. Amberg. Plasma-Substrate Interaction during Plasma Deposition on Polymers. *Contributions to Plasma Physics*, 54(2):162–169, 2014.

[161] Raphael Victor Foureaux Paulino, Solmaz Saboohi, and Andrew Michelmore. The chemistry of organophosphate thin film coatings from low pressure plasma and the effect of the substrate on adhesion. *Plasma Processes and Polymers*, 14(11):1–8, 2017.

[162] Yali Li, Benjamin W. Muir, Christopher D. Easton, Lars Thomsen, David R. Nisbet, and John S. Forsythe. A study of the initial film growth of PEG-like plasma polymer films via XPS and NEXAFS. *Applied Surface Science*, 288:288–294, 2014.

[163] Nghia H. Le, Magali Bonne, Aissam Airoudj, Philippe Fioux, Rémi Boubon, Diane Rebiscoul, Florence Bally-Le Gall, Bénédicte Lebeau, and Vincent Roucoules. When chemistry of the substrate drastically controls morphogenesis of plasma polymer thin films. *Plasma Processes and Polymers*, 18(2), 2021.

[164] S. P. Jarvis, S. Taylor, J. D. Baran, N. R. Champness, J. A. Larsson, and P. Moriarty. Measuring the mechanical properties of molecular conformers. *Nature Communications*, 6, 2015.

[165] Leo Gross, Bruno Schuler, Niko Pavliček, Shadi Fatayer, Zsolt Majzik, Nikolaj Moll, Diego Peña, and Gerhard Meyer. Atomic Force Microscopy for Molecular Structure Elucidation. *Angewandte Chemie - International Edition*, 57(15):3888–3908, 2018.

[166] Andrei Choukourov, Ivan Gordeev, Dmitry Arzhakov, Anna Artemenko, Jaroslav Kousal, Ondřej Kylián, Danka Slavínská, and Hynek Biederman. Does cross-link density of PEO-like plasma polymers influence their resistance to adsorption of fibrinogen? *Plasma Processes and Polymers*, 9(1):48–58, 2012.

[167] Yixiu Wang, Hongtao Lin, Wenzhuo Wu, and Juejun Hu. Tellurene: A Multifunctional Material for Midinfrared Optoelectronics. 2019.

[168] Kenji Furuya, Ryoichi Nakanishi, Hiroshi Okumura, Makoto Makita, and Akira Harata. Influence of substrate type on surface structure of polymeric perfluorocarbon in the initial stage of deposition in Ar/c-C4F8 plasmas. *Thin Solid Films*, 516(18):6028–6032, 2008.

[169] Renee V Goreham, Robert D Short, and Krasimir Vasilev. Method for the Generation of Surface-Bound Nanoparticle Density Gradients. *The Journal of Physical Chemistry C*, 115(8):3429–3433, mar 2011.

[170] Andrei Choukourov, Hynek Biederman, Danka Slavinska, Luke Hanley, Andrey Grinevich, Hanna Boldyryeva, and Anna Mackova. Mechanistic studies of plasma polymerization of allylamine. *Journal of Physical Chemistry B*, 109(48):23086–23095, 2005.

[171] J B Nebe, Henrike Rebl, Michael Schlosser, Susanne Staehlke, Martina Gruening, Klaus-Dieter Weltmann, Uwe Walschus, and Birgit Finke. Plasma Polymerized Allylamine—The Unique Cell-Attractive Nanolayer for Dental Implant Materials, 2019.

[172] Paul van der Heide. *X-Ray Photoelectron Spectroscopy: An Introduction to Principles and Practices*. 2011.

[173] Fred A. Stevie and Carrie L. Donley. Introduction to x-ray photoelectron spectroscopy. *Journal of Vacuum Science Technology A*, 38(6):063204, 2020.

[174] George H. Major, Neal Fairley, Peter M. A. Sherwood, Matthew R. Linford, Jeff Terry, Vincent Fernandez, and Kateryna Artyushkova. Practical guide for curve fitting in x-ray photoelectron spectroscopy. *Journal of Vacuum Science Technology A*, 38(6):061203, 2020.

[175] Alexander G. Shard. Practical guides for x-ray photoelectron spectroscopy: Quantitative XPS. *Journal of Vacuum Science Technology A*, 38(4):041201, 2020.

[176] D. P. Woodruff. Surface structure determination using x-ray standing waves. *Reports on Progress in Physics*, 68(4):743–798, 2005.

[177] Ricardo García. *Amplitude Modulation Atomic Force Microscopy*. Wiley-VCH Verlag GmbH Co. KGaA, Weinheim, Germany, oct 2010.

[178] Ricardo Garcia. Nanomechanical mapping of soft materials with the atomic force microscope: Methods, theory and applications. *Chemical Society Reviews*, 49(16):5850–5884, 2020.

[179] K Siegbahn and K Edvarson. β-Ray spectroscopy in the precision range of 1 : 105. *Nuclear Physics*, 1(8):137–159, 1956.

[180] John Wolstenholme. Procedure which allows the performance and calibration of an XPS instrument to be checked rapidly and frequently. *Journal of Vacuum Science Technology A*, 38(4):43206, jun 2020.

[181] Peter M A Sherwood. Rapid evaluation of the Voigt function and its use for interpreting X-ray photoelectron spectroscopic data. *Surface and Interface Analysis*, 51(2):254–274, feb 2019.

[182] Mark H Engelhard, Donald R Baer, Alberto Herrera-Gomez, and Peter M A Sherwood. Introductory guide to backgrounds in XPS spectra and their impact on determining peak intensities. *Journal of Vacuum Science Technology A*, 38(6):63203, sep 2020.

[183] Mark C. Biesinger. Advanced analysis of copper X-ray photoelectron spectra. *Surface and Interface Analysis*, 49(13):1325–1334, 2017.

[184] Lukas Grossmann, David A. Duncan, Samuel P. Jarvis, Robert G. Jones, Soumen De, Johanna Rosen, Michael Schmittel, Wolfgang M. Heckl, Jonas Björk, and Markus Lackinger. Evolution

of adsorption heights in the on-surface synthesis and decoupling of covalent organic networks on Ag(111) by normal-incidence X-ray standing wave. *Nanoscale Horizons*, 7(1):51–62, 2022.

[185] Samuel P. Jarvis, Hongqian Sang, Filipe Junqueira, Oliver Gordon, Jo E.A. Hodgkinson, Alex Saywell, Philipp Rahe, Salvatore Mamone, Simon Taylor, Adam Sweetman, Jeremy Leaf, David A. Duncan, Tien Lin Lee, Pardeep K. Thakur, Gabriella Hoffman, Richard J. Whitby, Malcolm H. Levitt, Georg Held, Lev Kantorovich, Philip Moriarty, and Robert G. Jones. Chemical shielding of H2O and HF encapsulated inside a C60 cage. *Communications Chemistry*, 4(1):1–7, 2021.

[186] Donald H. Bilderback, Pascal Elleaume, and Edgar Weckert. Review of third and next generation synchrotron light sources. *Journal of Physics B: Atomic, Molecular and Optical Physics*, 38(9), 2005.

[187] https://www.diamond.ac.uk/Science/Machine.html.

[188] B Krässig, M Jung, D S Gemmell, E P Kanter, T LeBrun, S H Southworth, and L Young. Nondipolar Asymmetries of Photoelectron Angular Distributions. *Physical Review Letters*, 75(26):4736–4739, dec 1995.

[189] G Binnig and H Rohrer. Scanning tunneling microscopy. *Surface Science*, 126(1):236–244, 1983.

[190] G Binnig, C F Quate, and Ch. Gerber. Atomic Force Microscope. *Physical Review Letters*, 56(9):930–933, mar 1986.

[191] V.L. Mironov. *Fundamentals of Scanning Probe Microscopy*. 2004.

[192] Bharat Bhushan. *Springer Handbook of Nanotechnology, 3rd ed.* Sprin, 2010.

[193] Leo Gross, Z L Wang, D Ugarte, Fabian Mohn, Nikolaj Moll, W a Heer, P Vincent, Peter Liljeroth, C Journet, Gerhard Meyer, V T Binh, M Poot, H S J Van Der Zant, a Aguasca, a Bachtold, K Kim, a Zettl, P Hung, H W C Postma, M Bockrath, X Blase, and S Roche. only appears when looking at the I. *Science*, 325(August):1110–4, 2009.

[194] Vladimir V. Korolkov, Alex Summerfield, Alanna Murphy, David B. Amabilino, Kenji Watanabe, Takashi Taniguchi, and Peter H. Beton. Ultra-high resolution imaging of thin films

and single strands of polythiophene using atomic force microscopy. *Nature Communications*, 10(1):1–8, 2019.

[195] Stefan B. Kaemmer. Application Note # 133 Introduction to Bruker ' s ScanAsyst and PeakForce Tapping AFM Technology. *Bruker Application Note*, pages 1–12, 2011.

[196] Sheetal Korde Choudhari, Minal Chaudhary, Sachin Bagde, Amol R. Gadbail, and Vaishali Joshi. Nitric oxide and cancer: A review. *World Journal of Surgical Oncology*, 11:1–11, 2013.

[197] Anthony D. Verderosa, Sarah C. Mansour, César De La Fuente-Núñez, Robert E.W. Hancock, and Kathryn E. Fairfull-Smith. Synthesis and evaluation of ciprofloxacin-nitroxide conjugates as anti-biofilm agents. *Molecules*, 21(7):1–16, 2016.

[198] Jörg Friedrich. Mechanisms of plasma polymerization - Reviewed from a chemical point of view. *Plasma Processes and Polymers*, 8(9):783–802, 2011.

[199] Li Chong Xu and Christopher A. Siedlecki. Staphylococcus epidermidis adhesion on hydrophobic and hydrophilic textured biomaterial surfaces. *Biomedical Materials (Bristol)*, 9(3), 2014.

[200] Iker De-la Pinta, Mónica Cobos, Julen Ibarretxe, Elizabeth Montoya, Elena Eraso, Teresa Guraya, and Guillermo Quindós. Effect of biomaterials hydrophobicity and roughness on biofilm development. *Journal of Materials Science: Materials in Medicine*, 30(7), 2019.

[201] Judit Oliver-Messeguer, Lichen Liu, Saray García-García, Claudia Canós-Giménez, Irene Domínguez, Rafael Gavara, Antonio Doménech-Carbó, Patricia Concepción, Antonio Leyva-Pérez, and Avelino Corma. Stabilized naked Sub-nanometric Cu clusters within a polymeric film catalyze C-N, C-C, C-O, C-S, and C-P bond-forming reactions. *Journal of the American Chemical Society*, 137(11):3894–3900, 2015.

[202] Barbara A.J. Lechner, Fabian Knoller, Alexander Bourgund, Ueli Heiz, and Friedrich Esch. A Microscopy Approach to Investigating the Energetics of Small Supported Metal Clusters. *Journal of Physical Chemistry C*, 122(39):22569–22576, 2018.

[203] Koen Schouteden, Koen Lauwaet, Ewald Janssens, Giovanni Barcaro, Alessandro Fortunelli, Chris Van Haesendonck, and Peter Lievens. Probing the atomic structure of metallic nanoclusters with the tip of a scanning tunneling microscope. *Nanoscale*, 6(4):2170–2176, 2014.

[204] J Zegenhagen. Surface structure determination with X-ray standing waves. *Surface Science Reports*, 18(7):202–271, 1993.

[205] M Dion, H Rydberg, E Schröder, D C Langreth, and B I Lundqvist. van der Waals density functional for general geometries. *Physical review letters*, 92(24):246401, jun 2004.

[206] Jiří Klimeš, David R Bowler, and Angelos Michaelides. Van der Waals density functionals applied to solids. *Physical Review B*, 83(19):195131, may 2011.

[207] Stefan Grimme, Jens Antony, Stephan Ehrlich, and Helge Krieg. A consistent and accurate ab initio parametrization of density functional dispersion correction (DFT-D) for the 94 elements H-Pu. *The Journal of Chemical Physics*, 132(15):154104, apr 2010.

[208] R F W Bader. Atoms in molecules : a quantum theory. 1990.

[209] Graeme Henkelman, Andri Arnaldsson, and Hannes Jónsson. A fast and robust algorithm for Bader decomposition of charge density. *Computational Materials Science*, 36(3):354–360, 2006.

[210] Edward Sanville, Steven D Kenny, Roger Smith, and Graeme Henkelman. Improved grid-based algorithm for Bader charge allocation. *Journal of Computational Chemistry*, 28(5):899–908, apr 2007.

[211] Koichi Momma and Fujio Izumi. *VESTA3* for three-dimensional visualization of crystal, volumetric and morphology data. *Journal of Applied Crystallography*, 44(6):1272–1276, dec 2011.

[212] Ali Alavi, Peijun Hu, Thierry Deutsch, Pier Luigi Silvestrelli, and Jürg Hutter. CO Oxidation on Pt(111): An Ab Initio Density Functional Theory Study. *Physical Review Letters*, 80(16):3650–3653, apr 1998.

[213] Takashi Ogi, Luis Balam Modesto-Lopez, Ferry Iskandar, and Kikuo Okuyama. Fabrication of a large area monolayer of silica particles on a sapphire substrate by a spin coating method. *Colloids and Surfaces A: Physicochemical and Engineering Aspects*, 297(1-3):71–78, 2007.

[214] Kazutoshi Sekiguchi, Takayuki Nakanishi, Hiroyo Segawa, and Atsuo Yasumori. Fabrication of Silica Nanoparticle Monolayer Arrays Using an Anodic Aluminum Oxide Template. *ACS Omega*, 4(10):14333–14339, 2019.

[215] Xiaofei Sheng, Jing Wang, Yajuan Cheng, and Zhe Zhao. Controllable fabrication of large-size defect-free domains of 2D colloidal crystal masks guided by statistical experimental design. *Coatings*, 11(1):1–9, 2021.

[216] Felix Hanke and Jonas Björk. Structure and local reactivity of the Au(111) surface reconstruction. *Physical Review B - Condensed Matter and Materials Physics*, 87(23):1–6, 2013.

[217] Robert G. Jones, A. S.Y. Chan, M. G. Roper, M. P. Skegg, I. G. Shuttleworth, C. J. Fisher, G. J. Jackson, J. J. Lee, D. P. Woodruff, N. K. Singh, and B. C.C. Cowie. X-ray standing waves at surfaces. *Journal of Physics Condensed Matter*, 14(16):4059–4074, 2002.

[218] D. P. Woodruff and D. A. Duncan. X-ray standing wave studies of molecular adsorption: why coherent fractions matter. *New Journal of Physics*, 22(11), 2020.

[219] M Zehner and Doon Gibbs. Au(111) surface: X-ray-scattering. *Physical Review B*, 43(6), 1991.

[220] Wenzhuo Wu, Gang Qiu, Yixiu Wang, Ruoxing Wang, and Peide Ye. Chem Soc Rev nanomanufacturing , and device applications. (d):7203–7212, 2018.

[221] Matthew C. Patterson, Xiaowa Nie, Fei Wang, Richard L. Kurtz, Susan B. Sinnott, Aravind Asthagiri, and Phillip T. Sprunger. Growth and structure of Cu and Au on the nonpolar ZnO(1010) surface: STM, XPS, and DFT studies. *Journal of Physical Chemistry C*, 117(36):18386–18397, 2013.

[222] Giuliano Moretti, Amedeo Palma, Ernesto Paparazzo, and Mauro Satta. Auger parameter and Wagner plot studies of small copper clusters. *Surface Science*, 646:298–305, 2016.

[223] I. Lyubinetsky, S. Thevuthasan, D. E. McCready, and D. R. Baer. Formation of single-phase oxide nanoclusters: Cu 2O on SrTiO 3(100). *Journal of Applied Physics*, 94(12):7926–7928, 2003.

[224] S. Peters, S. Peredkov, N. Ferretti, A. Savci, and M. Neeb. Core level photoionization spectroscopy of supported metal clusters: Cu55 on silica. *Journal of Electron Spectroscopy and Related Phenomena*, 181(2-3):140–144, 2010.

[225] Matthew Edmondson, Eleanor S. Frampton, Chris J. Judd, Neil R. Champness, Robert G. Jones, and Alex Saywell. Order, disorder, and metalation of tetraphenylporphyrin (2H-TPP) on Au(111). *Chemical Communications*, 58(42):6247–6250, 2022.

[226] G. Galeotti, F. De Marchi, E. Hamzehpoor, O. MacLean, M. Rajeswara Rao, Y. Chen, L. V. Besteiro, D. Dettmann, L. Ferrari, F. Frezza, P. M. Sheverdyaeva, R. Liu, A. K. Kundu, P. Moras, M. Ebrahimi, M. C. Gallagher, F. Rosei, D. F. Perepichka, and G. Contini. Synthesis of mesoscale ordered two-dimensional π-conjugated polymers with semiconducting properties. *Nature Materials*, 19(8):874–880, 2020.

[227] Min Chen, Jie Xiao, Hans Peter Steinrück, Shiyong Wang, Weihua Wang, Nian Lin, Wolfgang Hieringer, and J. Michael Gottfried. Combined photoemission and scanning tunneling microscopy study of the surface-assisted ullmann coupling reaction. *Journal of Physical Chemistry C*, 118(13):6820–6830, 2014.

[228] Qitang Fan, Tao Wang, Liming Liu, Jin Zhao, Junfa Zhu, and J. Michael Gottfried. Tribromobenzene on Cu(111): Temperature-dependent formation of halogen-bonded, organometallic, and covalent nanostructures. *Journal of Chemical Physics*, 142(10), 2015.

[229] Jie Xiao, Stefanie Ditze, Min Chen, Florian Buchner, Michael Stark, Martin Drost, Hans Peter Steinrück, J. Michael Gottfried, and Hubertus Marbach. Temperature-dependent chemical and structural transformations from 2H-tetraphenylporphyrin to copper(II)-tetraphenylporphyrin on Cu(111). *Journal of Physical Chemistry C*, 116(22):12275–12282, 2012.

[230] Alisson Ceccatto Dos Santos, Nataly Herrera-Reinoza, Alejandro Pérez Paz, Duncan John Mowbray, and Abner De Siervo. Reassessing the Adsorption Behavior and on-Surface Reactivity of a Brominated Porphyrin on Cu(111). *Journal of Physical Chemistry C*, 125(31):17164–17173, 2021.

[231] K. Diller, F. Klappenberger, M. Marschall, K. Hermann, A. Nefedov, Ch Wöll, and J. V. Barth. Self-metalation of 2H-tetraphenylporphyrin on Cu(111): An x-ray spectroscopy study. *Journal of Chemical Physics*, 136(1), 2012.

[232] Rico Gutzler, Wolfgang M. Heckl, and Markus Lackinger. Combination of a Knudsen effusion cell with a quartz crystal microbalance: In situ measurement of molecular evaporation rates with a fully functional deposition source. *Review of Scientific Instruments*, 81(1), 2010.

[233] Borja Cirera, Bruno De La Torre, Daniel Moreno, Martin Ondráček, Radek Zbořil, Rodolfo Miranda, Pavel Jelínek, and David Écija. On-Surface Synthesis of Gold Porphyrin Derivatives via a Cascade of Chemical Interactions: Planarization, Self-Metalation, and Intermolecular Coupling. *Chemistry of Materials*, 31(9):3248–3256, 2019.

[234] Jianchen Lu, Binbin Da, Wei Xiong, Renjun Du, Zhenliang Hao, Zilin Ruan, Yong Zhang, Shijie Sun, Lei Gao, and Jinming Cai. Identification and electronic characterization of four cyclodehydrogenation products of H2TPP molecules on Au(111). *Physical Chemistry Chemical Physics*, 23(20):11784–11788, 2021.

[235] Alissa Wiengarten, Julian A. Lloyd, Knud Seufert, Joachim Reichert, Willi Auwärter, Runyuan Han, David A. Duncan, Francesco Allegretti, Sybille Fischer, Seung Cheol Oh, Özge Salam, Li Jiang, Saranyan Vijayaraghavan, David Écija, Anthoula C. Papageorgiou, and Johannes V. Barth. Surface-Assisted Cyclodehydrogenation; Break the Symmetry, Enhance the Selectivity. *Chemistry - A European Journal*, 21(35):12285–12290, 2015.

[236] Ana Maria Ferraria, Ana Patrícia Carapeto, and Ana Maria Botelho Do Rego. X-ray photoelectron spectroscopy: Silver salts revisited. *Vacuum*, 86(12):1988–1991, 2012.

[237] J F Moulder, J Chastain, and R C King. *Handbook of X-ray Photoelectron Spectroscopy: A Reference Book of Standard Spectra for Identification and Interpretation of XPS Data*. Physical Electronics, 1995.

[238] David Buceta, Natalia Busto, Giampaolo Barone, José M. Leal, Fernando Domínguez, Lisandro J. Giovanetti, Félix G. Requejo, Begoña García, and M. Arturo Lõpez-Quintela. Ag2 and Ag3 Clusters: Synthesis, Characterization, and Interaction with DNA. *Angewandte Chemie - International Edition*, 54(26):7612–7616, 2015.

[239] Matthias Lischka, Massimo Fritton, Johanna Eichhorn, Vijay S Vyas, Thomas Strunskus, Bettina V Lotsch, Jonas Björk, Wolfgang M Heckl, and Markus Lackinger. On-Surface Polymerization of 1,6-Dibromo-3,8-diiodpyrene—A Comparative Study on Au(111) Versus Ag(111)

by STM, XPS, and NEXAFS. *The Journal of Physical Chemistry C*, 122(11):5967–5977, mar 2018.

[240] Andrew Guthrie and R. K. Wakerling. Bohm, in the characteristics of electrical discharges in magnetic fields, 1949.